EPHD

COMPREHENSIVE ASSESSMENT OF GaAs SUBSTRATES FOR INTEGRATED CIRCUIT APPLICATIONS

Stephen Clark, BA, MA.

A thesis submitted in partial fulfilment of the requirements of the Council for National Academic Awards for the degree of Doctor of Philosophy.

February 1990

Department of Electrical and Electronic Engineering.
Nottingham Polytechnic, Burton Street, Nottingham.

Collaborating Establishment: Plessey Research (Caswell),
Caswell, Towcester, Northamptonshire.

This thesis is dedicated to the many people who have made it possible; in particular: Derek for starting it off, Brian and Lawrence for interfering, and Lynn for her constant support.

COMPREHENSIVE ASSESSMENT OF GaAs SUBSTRATES FOR INTEGRATED CIRCUIT APPLICATIONS

S.Clark.

ABSTRACT

It is known that dislocations in GaAs substrates can affect the uniformity of the parameters of devices grown on them. It is thought that this is due to the influence of defects (such as EL2) which associate with dislocations. Efforts to improve substrate quality usually involve producing dislocation free material (by indium–doping), or alternatively, heat treating dislocated material to remove the association of defects with dislocations.

In this work, dislocation structures, their associated precipitates and defect atmospheres are investigated by A/B etching; EL2 is investigated using its characteristic near–infrared absorption band; the electrical properties of the material are determined by Hall effect measurements; and some heat treated material is investigated by cathodoluminescence imaging. In addition, a new system for producing EL2 concentration ([EL2]) line–scans is described. This is based around a near–infrared silicon vidicon imaging apparatus, which images variations in EL2 using its characteristic absorption band.

New investigations of defects in indium–doped GaAs are detailed, with emphasis on those dislocations, and their associated defects, in the central region of the ingot. The effects of annealing on these defects is described and discussed.

Novel results of heat treatments followed by rapid cooling (quenching) on bulk material (large blocks) are described. Quenching from 1100°C, or above, produces superior uniformity to conventionally annealed material. However, [EL2] drops, dislocation density is increased and some samples display p–type conversion. After re–annealing quenched material at 950°C, [EL2] and semi–insulating nature are restored, without affecting the superior quenched uniformity.

Subsequently, an entire ingot was quenched from 1100°C and re–annealed at 950°C. This ingot quenched material was semi–insulating and displayed superior uniformity, although dislocation densities were high (at about $10^6 cm^{-2}$). Initial processing results carried out on this material are promising. Ingot quenching and re–annealing has great potential for providing uniform semi–insulating GaAs substrates.

CONTENTS

LIST OF FIGURES

following page

1. INTRODUCTION.

1.1 GaAs Overview and Project Aims.

GaAs has promised much as a substrate material for semiconductor devices over the past few decades. This applies in particular to the field of high speed, low power devices, where it has developed a significant commercial niche. However its future development will depend on the material continuing to meet market requirements, where factors like costs and yields are more important than the potential benefits indicated by one–off research device properties and theoretical performance. In part, this will require stronger collaboration between crystal growers, assessment groups and production facilities and an awareness by all of the needs of the customer.

The main aims of the project were to improve the assessment techniques used to qualify Liquid Encapsulated Czochralski (LEC) grown, GaAs substrate material and if possible improve the quality of the substrates themselves. Since the quality of substrates clearly influences the properties of the devices grown on them, it is hoped this will lead to improvement of device results, in particular improved yields through improved uniformity.

1.2 GaAs for Semiconductor Devices.

The general properties of GaAs which make it an important commercial semiconductor, together with its relative merits compared to Si are discussed below. This is followed by a brief summary of the main device applications of GaAs.

1.2.1 Comparison of GaAs with Si.

Advantages of GaAs over Si as a substrate material.

1) GaAs has a higher mobility, lower electron effective mass and can achieve higher electron velocities than Si (although the saturation velocity mobility at high electric fields is not significantly greater than that of Si)

2) Intrinsic Semi–Insulating (SI) GaAs substrates of high resistivity ($\sim 10^8$ohm.cm) obviate the need for device isolation from the substrate resulting in reduction of parasitic capacitances.

3) GaAs is a direct band–gap material hence opto–electronic devices can be made on GaAs with the further possibility of integrated electro–optical IC's.

4) GaAs is more radiation hard than Si.

5) GaAs devices can operate at higher temperatures than Si devices due to the wider GaAs band–gap.

6) The limitations on FET gate lengths are less stringent for GaAs than for silicon (partly due to reduced parasitics) with a corresponding increase in possible packing densities and speed.

7) At high electric fields conduction electrons are transferred from the main conduction band to one of the side valleys with an associated drop in electron velocity. Hence increasing the field in this region gives rise to a decrease in conduction or negative resistance. This property is known as the Gunn effect and its main application is the production of micro–wave oscillators.

Advantages of Si over GaAs as a substrate material.

1) The cost of the raw materials (and the raw material processing costs) of GaAs are higher than those of Si.

2) It is harder to grow large diameter GaAs crystals than silicon. This has further increased substrate costs and also delayed the introduction of GaAs technology.

3) GaAs is more brittle than silicon, hence more care must be taken with GaAs during processing.

4) GaAs substrates have non–uniform electrical properties which arise from non–uniform defect distributions.

5) It is difficult to produce zero dislocation density GaAs.

6) The thermal conductivity of GaAs is lower than Si and hence overheating is more of a problem, despite the wider band–gap of GaAs.

7) An insulating oxide layer cannot be grown on GaAs.

8) It is difficult to carry out n–type diffusions as this causes surface degradation due to As loss.

9) Si technology had several decades "head–start" over GaAs.

1.2.2 GaAs devices; the state of the art.

The competition with Si devices.

In the area of high speed digital devices, Si is ahead of GaAs at present, and holds the majority of the market. This is at the expense of increasing complexity (especially in terms of the number of masking levels during fabrication) and higher power consumption but with much lower cost and higher levels of integration. In the area of high speed analogue (or microwave) devices and in the area of opto–electronic devices, GaAs has the main market share. However, in the near future, there will be extra competition for conventional GaAs devices from silicon on insulator, GaAs on silicon, III–V heterojunction transistors, or other III–V's (especially InP).

The main applications of GaAs:

Analogue devices:

This mainly consists of discrete devices and MMIC's (Monolithic Microwave IC's), operating at microwave frequencies. The market share of discrete microwave devices is likely to drop with respect to that of IC's, as circuit construction and interfacing at microwave frequencies is difficult. For further information on these devices see for example the articles by Spadaro (001) and Gagnon (002).

Opto–electronic devices:

The area of opto–electronics was always a natural niche market for GaAs because of its direct band–gap. The main applications at present are for substrates for LED's and laser diodes used in optical fibre communication systems. In the future, the market share of GaAs is likely to drop compared to InP substrates. This is because of the lower loss "windows" in fibre optic cables at the higher wavelengths which can be exploited by devices on InP substrates. At present

development work is being carried out on combined optoelectronic–electronic IC's to remove much of the need for interfacing between electronic and opto–electronic circuits.

Digital devices:

At the very high speed low power end of the market GaAs digital circuits have a small market share but at present the performance levels of silicon are not far behind at a lower cost. At this time, Depletion mode FET (D–FET) or combined Depletion/Enhancement mode FET (E/D–FET) circuits are available at MSI and LSI complexity. 16k RAMs operating with about 1ns access times are currently available in GaAs. In the future as threshold voltage variations are reduced and the technology matures, Enhancement mode FET (E–FET), VLSI circuits may be produced. For more information on digital devices and the technologies used to produce them, see the articles by Ohmori (003), Cole (004), Tomasetta (001), Spadaro (005), Schappacher (006), Lewis (007), Eden (008) and Sugeta et al (009).

1.3 SI LEC GaAs Substrates for Ion Implantation.

1.3.1 Device technology.

The active regions of devices of interest to this project are produced by ion–implantation of impurities into the substrate material. At present, this technique is mainly used for the production of MMIC's but the number of digital devices manufactured is likely to increase strongly over the next few years. A discussion of the technology of ion–implantation and device manufacture is beyond the scope of this thesis. For further information on GaAs device technology see the articles by Eden (008), Sealy (010), Sugeta et al (009), Tomasetta (005), Ohmori (003) and the references therein. For more information on ion implantation see the article by Blunt (011) and the references therein.

Undoped SI LEC substrates are used because the material must maintain its SI properties throughout the implantation and processing stages. The traditional SI Horizontal Bridgman (HB) material where shallow donor impurities are compensated by chromium deep acceptors is unsuitable, as the highly mobile chromium ions cause significant device degradation during post–implant anneals.

1.3.2 Defects in GaAs substrates.

Defect types, distribution and compensation.

The main defect types found in undoped SI LEC GaAs are listed below; they will be discussed in more detail in chapter 2.

Dislocations:

Typical dislocation densities in undoped LEC GaAs are around 10^4–$10^5 cm^{-2}$. Dislocations are non–uniformly distributed with usually a "w" shape distribution across a diameter of an ingot. There is much evidence of dislocation interaction which gives rise to complicated dislocation structures such as cellular structure and lineage.

Precipitates:

There are (very) approximately $10^8 cm^{-3}$ sub–micron arsenic (or As–rich) precipitates, of micron

or sub–micron dimensions, in LEC GaAs. They are nearly always associated with dislocations.

Impurities:

The main electrically active impurities in undoped LEC GaAs are shallow acceptors (predominantly carbon) and shallow donors (predominantly silicon or sulphur), usually with shallow acceptors in excess by about $10^{15}cm^{-3}$. In addition there is a high concentration (up to $10^{17}cm^{-3}$) of boron, which mainly acts as an isoelectronic impurity. This is due to the boric oxide encapsulant used in LEC growth. These impurities are usually assumed to be nearly radially uniform across ingot diameters. Axial variations are produced by impurity segregation during growth.

Native deep level defects:

These are dominated by the so called Electron Level 2 (EL2) with an energy level at mid–gap and concentrations of around $10^{16}cm^{-3}$. The distribution of EL2 generally follows that of dislocations across ingot diameters (particularly on a microscopic scale). EL2 compensates the excess of shallow acceptors over shallow donors giving rise to the SI properties of undoped LEC crystals by pinning the Fermi–level near mid–gap. Concentrations of other native deep level donor defects (such as EL3 or EL6) are usually below $10^{15}cm^{-3}$. Little is known about native deep acceptor concentrations in undoped SI LEC material.

The effect of substrate defects on devices.

Substrate effects on devices are still not fully understood. However, in some cases a correlation has been demonstrated between the variations of substrate properties and device properties (Miyazawa 012). As the processing technology matures, process related deviations are likely to be reduced, making substrate induced fluctuations more significant. At present, both effects are usually significant (Koyama 013).

For a long time it was thought that dislocations were the most important substrate property affecting device uniformity. It is now thought that they are more likely to have an indirect effect and that the associated defect atmosphere is a more important factor. If this is the case, then we would expect to see strong improvements in device uniformity if the defect distribution in the substrate can be homogenised in some way, even if the dislocation structure is unchanged. This is one of the key possibilities underlying the work in this thesis.

1.3.3 Substrate assessment.

The Importance of Assessment.

There are two distinct aims of assessment:

The first is to provide a rapid, preferably non–destructive assessment routine, through which the quality of substrates used for subsequent device fabrication can be judged.

The second is to improve the scientific understanding of the material, in particular with reference to those processes which influence subsequent device uniformity. Gaining this understanding is important in the case of undoped SI GaAs. This is because the identities of many technologically important defect identifications are contentious or unknown, as are the effects of these defects on device properties.

The Assessment of EL2 in SI LEC GaAs.

Because of the crucial role of EL2 in compensation of undoped LEC GaAs, the investigation of EL2 (especially its distribution) is of vital importance. EL2 was initially characterised by Deep Level Transient Spectroscopy (DLTS) in n–type material. Unfortunately, DLTS is unsuitable for the assessment of deep levels in SI material. Hence, the assessment of EL2 through its characteristic mid–band–gap Near Infra–Red (NIR) absorption has become an important technique. The absorption coefficient in this region is proportional to the EL2 concentration, [EL2]. Thus an investigation of the spatial variations of NIR absorption gives the distribution of [EL2]. Much of the work in this thesis involves the assessment of EL2, via its NIR absorption, using various techniques.

1.3.4 Improvement of substrate uniformity.

Present efforts at improving substrate uniformity follow two main directions:

The first involves advances in crystal growth techniques, the aim usually being to reduce dislocation densities. This can give either a direct or indirect effect on improved device uniformity. One of the major methods of reducing dislocation densities is by the use of isoelectronic doping (usually In–doping) to "harden" the lattice. Dislocation free or "nearly" dislocation free crystals can be produced by this method. An advantage of low dislocation density In–doped material is that the point defect atmospheres associated with dislocations do not overlap to the same extent as in undoped LEC material. This factor was exploited in this present work, as the form of the defect atmospheres, their relationship with the host dislocations and the effects of heat treatments on them are more easily investigated than in heavily dislocated, undoped, GaAs.

The second effort is an attempt to remove the correlation between dislocation structures and those defect distributions which most affect device uniformity. This can be achieved by post–growth thermal treatments (or anneals). Recently there has been a strong interest in heat treatments followed by fast cooling (or quenching). To date, interest in quenching has been mainly academic in nature. In this work we examine potential commercial implications of quenching as well as the scientific implications. In particular, the resulting improvement in substrate uniformity, after quenching, and the stability of the quenched material during subsequent anneals, has been investigated.

1.4 Thesis Content.

Chapter 1: Introduction.

Chapter 2: The properties of semi–insulating GaAs.

The main properties of undoped SI GaAs are described with particular emphasis on the properties of the deep donor EL2. Crystal non–stoichiometry, dislocation structures, arsenic precipitates, crystal growth (with emphasis on the LEC technique and indium doping), annealing and defect dynamics, electrical properties and compensation, and substrate effects on device properties, are also discussed.

Chapter 3: Assessment of semi–insulating GaAs substrates.

The main techniques used to assess SI GaAs are described. Emphasis is given to those which have been used in this work or that are closely related to them. The main sections are involved with: the assessment of dislocations and precipitates (mainly by etching, X–ray topography and electron microscopy); the assessment of EL2 (using DLTS, NIR absorption and various other techniques); electrical assessment (mainly by the Hall effect); the assessment of stoichiometry; and the assessment of non–radiative recombination centres (mainly by Photoluminescence and Cathodoluminescence).

Chapter 4: Assessment techniques used in this work.

The experimental details of the assessment techniques used in this work are described. The main techniques used are: mapping of the Near Infra–Red (NIR) absorption of EL2 (using a NIR video camera for imaging or a quantitative spectrophotometer to produce [EL2] line–scans); and the investigation of dislocations and precipitates (using A/B etching or X–ray topography). The flexibility of the qualitative, imaging system is contrasted with the inflexible but quantitative spectrophotometer system with the conclusion that some method of quantifying the imaging system is desirable.

Chapter 5: The [EL2] line–scan system.

A method of producing semi–quantitative [EL2] from the imaging system described in Chapter 4 is detailed. The system is based around a vidicon camera NIR absorption imaging system. Intensity information is taken from a line in the camera field using a video digitiser. It is then transferred into a small microcomputer, averaged, and processed to give [EL2] line–scans, using a calibration from a spectrophotometer. The applications of this system are described and its limitations are discussed.

Chapter 6: Defect assessment in In–doped material.

Results on In–doped material are presented and discussed. Emphasis is given to the investigation of threading dislocations in the central region of In–doped ingots and their associated defect atmospheres. Also the effects of annealing on In–doped crystals are shown. The results are discussed together with their implications for undoped material regarding the formation of defect distributions around dislocations.

Chapter 7: Bulk quenching and annealing studies.

Ingot, and large block sample anneals are studied as a function of various anneal temperatures, with both slow and fast cooling rates. Particular emphasis is given to the effects of anneals with fast cooling rates (quenches) on the concentration and uniformity of EL2, dislocation densities and distributions, and on subsequent electrical properties.

Chapter 8: Conclusions and further work.

The main conclusions of this work are given together with suggestions for useful further work.

1.5 Acronyms, Abbreviations and Notation.

1.5.1 Acronyms and abbreviations.

A list of the abbreviations and acronyms used in this work is given in appendix 1.1.

1.5.2 Notation.

Wherever possible the author will use the standard conventions used in the literature. However, to avoid confusion, the following notations and their associated meanings are defined for this work:

The levels $EL2^{o}$ and $EL2^{+}$ will be identified with the neutral (filled) and ionised (empty) charge states, of the $EL2^{+/o}$ level, respectively. $EL2^{o}$ is the uncompensated charge state normally seen in SI or n–type material and is that charge state which gives rise to the characteristic mid–band NIR absorption of undoped SI GaAs. $EL2^{+}$ will also be regarded as the filled charge state of the second donor level of EL2 (the $EL2^{++/+}$ level). The details of these charge state assignments, or any discussion on the charge states of any constituent point defects in the EL2 model, are beyond the scope of this thesis.

Photoquenching will be used to denote the removal of the properties of EL2 by light in the region of 1.1um at low temperatures (T<140K). Photoquenching of the EL2 optical absorption spectrum may also be denoted by bleaching.

Quenching will be used to denote the rapid cooling of a sample from high temperatures to low temperatures after an anneal.

Crystallographic directions and planes will be defined with the assumption that the growth direction is along [001]. To clarify dislocation structures, for a vector [xyz], or plane (xyz) the x and y components (undistinguished) will be distinguished from the z component, unless preceded by the word "standard". For example, the two sets of vectors <110> and <101> (including <011>) will be regarded as separate, unless described as the "standard <110>" in which case no distinction will be made.

1.6 References.

For the readers convenience, each reference in the text is given a three figure number and the surname of the first author. The complete references are listed in the references section (section 10), in numerical order. Each reference number is followed by a second number in brackets, which refers to an alternate filing system. This second number has no significance in this thesis and is retained for the convenience of the author. References from conference proceedings are given in abbreviated form; the full details of conference proceedings are given at the end of section 10.

2 THE PROPERTIES OF SEMI-INSULATING GaAs.

2.1 Introduction.

This chapter is intended to review part of the relevant literature to the work in this thesis. It gives an overview of the main properties of bulk, undoped, Semi-Insulating (SI) GaAs with particular emphasis on the main defects in material grown using the LEC technique. The techniques used to assess SI GaAs will be discussed in the next chapter.

2.2 Crystal Growth, Dislocations, and Mechanical Properties.

2.2.1 Stoichiometry and the phase diagram.

A possible (schematic) phase diagram for GaAs showing the region near stoichiometry is given in fig.2.1. It is drawn to be consistent with the work of Hurle et al (014 and 015) and is discussed in more detail there. An important feature shown on the diagram involves the retrograde solidus on the As-rich side; whereby a solid of the composition shown in the diagram becomes supersaturated with respect to precipitation of an As-rich liquid. This gives a mechanism for the formation of As precipitates. These precipitates will be discussed in more detail in section 2.2.4. Experimental data on the solidus phase boundary on the As-rich side was obtained by Terashima (016). A magnetic field was used to reduce temperature fluctuations in the melt, enabling accurate determination of the changes in crystal composition down a crystal to be made. The results clearly showed the effect of the retrograde solidus on the As-rich side. A second important feature in fig.2.1, is the relatively large phase extent indicating a high number of equilibrium point defects at high temperature in GaAs. The likely nature and concentration of these point defects will be discussed below.

Early work suggested that vacancies were likely to be the main point defect in GaAs near the melting point. Logan and Hurle (017) calculated point defect concentrations and non-stoichiometry with the assumption that Schottky (vacancy) disorder was dominant. Van Vechten (018) also proposed a model where nonstoichiometry was mainly due to vacancies, with vacancy and antisite complexes forming as the crystal cools. More recently this received support from positron annhilation results (Dannefaer 019) which suggest that vacancy-antisite complexes are predominant in undoped SI GaAs at room temperature (with a concentration of about $3x10^{17}cm^{-3}$).

Recent results from lattice parameter experiments are contradictory. Several groups (Nakajima 020, 021, Terashima 022, Takano 023) measured a significant increase of lattice parameter with increasing As mole fraction, indicating the dominant presence of As interstitals, which dilate the lattice. However another group (Okada 024) noted only a slight increase in lattice parameter, when the samples were diced to avoid residual strains originating from crystal growth. Combined lattice parameter and density measurements (Bublik 025, Aref'ev 026), on diced specimens show that As-rich material must contain a large number of As interstitials. The results only showed a small small increase in lattice parameter but a large increase in density as the material became more As-rich. The stoichiometric composition was found to correspond to

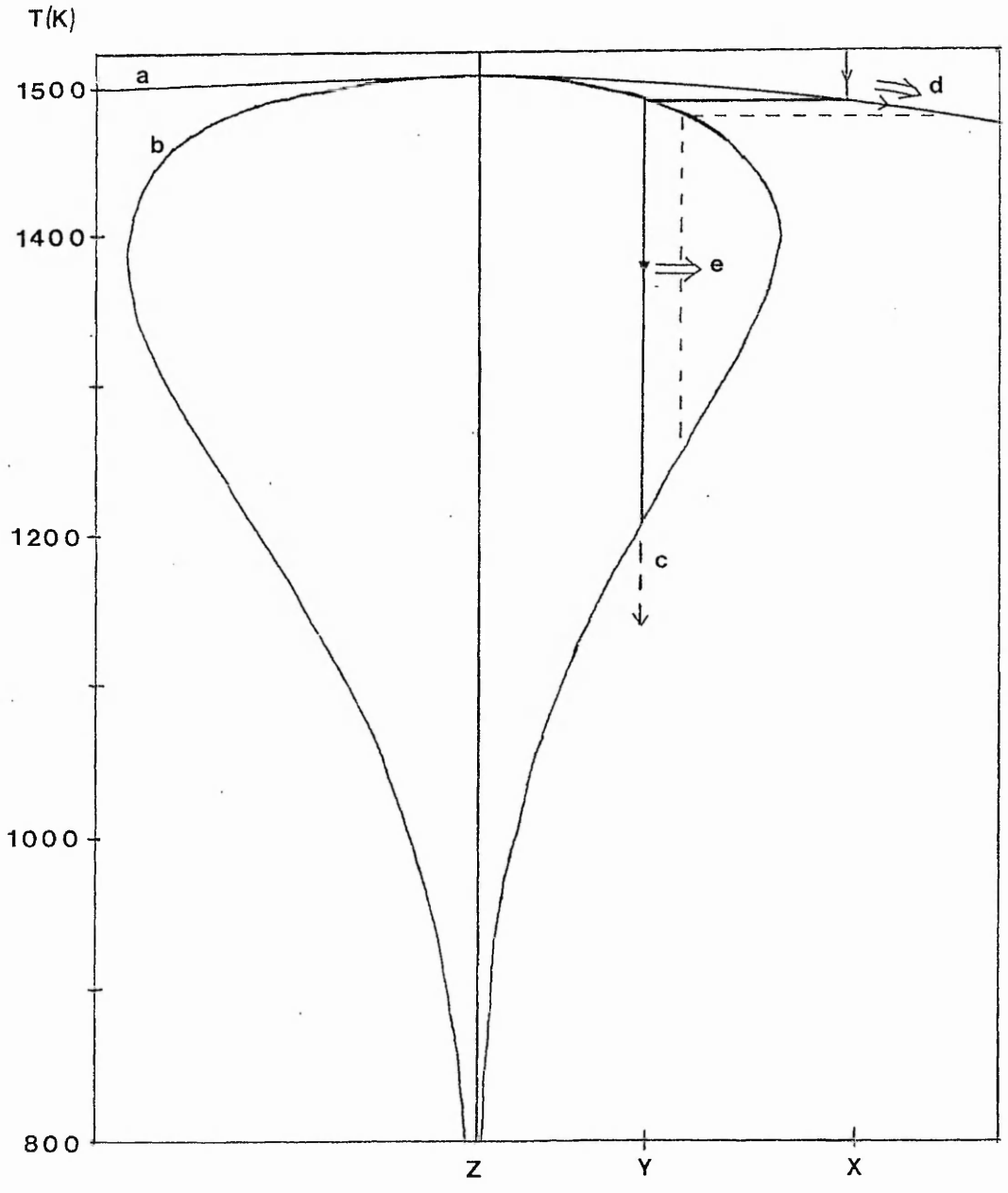

Fig.2.1. Schemetic of the GaAs phase diagram in the region near stoichiometry. The stoichiometric composition is marked as Z. The Ga–rich liquidus is shown at a, the Ga–rich solidus at b.

Indicated on the diagram: GaAs melt of composition X cools through the arsenic rich liquidus resulting in the initial formation of GaAs solid, of composition Y. The remaining melt becomes more As–rich as precipitation continues (d), resulting in solidification of GaAs of increasing As–richness (e). When the solid of composition Y cools, eventually it drops through the retrograde solidus (c). This results in the precipitation of an As rich phase (probably the "As precipitates seen on dislocations in GaAs)

0.505 As atom fraction in the melt.

Experimental irradiation studies (Pons 027) and recent theoretical binding energy studies (Baraff 028) both indicate that Frenkel disorder on the As sublattice is likely to dominate. The As vacancy and interstitial are both likely to be positively charged while the Ga vacancy and interstitial are likely to have opposite charge (with the interstitial positive) and hence will attract and annihilate each other.

In view of the work by Bublik et al, amongst others, Hurle revised his model to include Frenkel disorder (Hurle 014). The main conclusion of his work is that nonstoichiometry was probably dominated by the As Frenkel reaction. Hence As vacancies would be in excess on the Ga–rich side of stoichiometry and As interstitials would be in excess on the As–rich side.

The electrical importance of stoichiometry was shown by Holmes, Elliott et al (Holmes 031, 032, Elliott 033, 034, 035, 036). They studied the effect of changes of stoichiometry on, the concentrations of EL2 centres (associated with the As_{Ga} antisite) and the "A" centre (or 78meV/ 203meV double acceptor, thought to be associated with the Ga_{As} antisite). Also, the effect of stoichiometry on the conduction type, resistivity, mobility and carrier concentration was demonstrated. Their results are summarised in fig.2.2. Note the sharp change in electrical properties at the critical melt composition of 0.475 As mole fraction in the melt. The effect of stoichiometry on electrical properties is discused further in section 2.5.3.

Morrow (029, 030) suggested that during cooling defect reactions run to completion, without affecting the net grown in non–stoichiometry, leaving either EL2 or the double acceptor as the dominant defect, in As–rich or Ga–rich material respectively. This model can be used to explain the electrical data in fig.2.2. However, this model is unlikely to be correct as the experimental results described above indicate dominance of one type of native defect with concentrations of the order of $10^{18}cm^{-3}$ near the melting point and about $3x10^{17}cm^{-3}$ at room temperature (from positron annihilation). Also, the melt compositions for minimum non–stoichiometry and the large change in electrical properties do not correspond. To solve these problems Hurle (015) suggested that As Frenkel disorder gives the predominant non–stoichiometry whereas the Ga Frenkel disorder, which is two to three orders of magnitude lower, is responsible for the obseved EL2 or "A" centre concentrations. Annihilation of Ga Frenkel pairs will leave a net excess of Ga vacancies or Ga interstitials depending on stoichiometry. As_{Ga} antisites (related to EL2) are formed by the reaction of the net Ga vacancies with an excess of As interstitials, whereas Ga_{As} antisites (thought to be related to the "A" centre) are formed by the reaction of Ga interstitials with an excess of As vacancies. The high concentration of As interstitials or vacancies remaining after these reactions are expected either to precipitate out or form dislocation loops as the crystal cools. Alternatively, they could be still be present as point defects, but must be electrically and optically inactive at room temperature.

The Hurle model provides a good explanation for the main electrical and physical changes seen with changing melt composition. However it cannot be used to explain the positron annhilation results, which indicate the presence of a large concentration of vacancies in SI LEC GaAs. Hopefully this problem will soon be solved but at present we cannot really say with any certainty what the main point defects, or what their concentrations are, at any particular temperature, in undoped bulk GaAs.

Fig.2.2 The dependance of electrical properties of LEC GaAs on the As atom fraction in the melt.

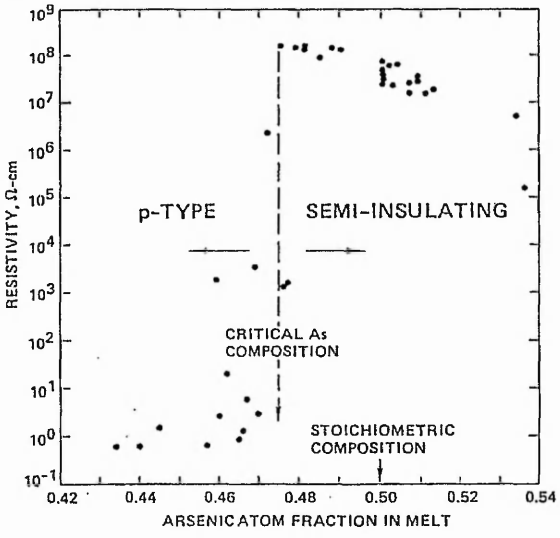

Fig.2.2(a) The effect of stoichiometry on resistivity (after Holmes 031)

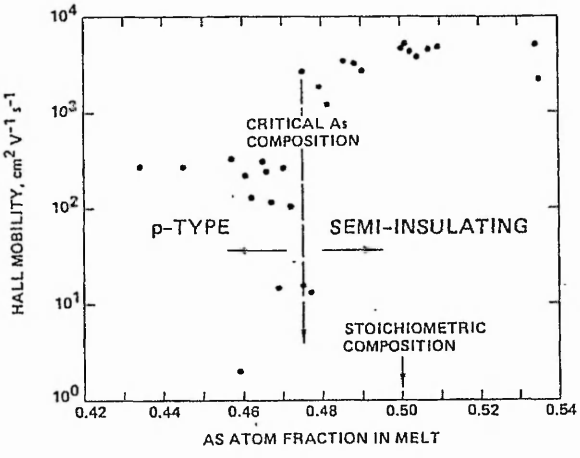

Fig2.2(b) The Effect of melt stoichiometry on mobility (after Holmes 031)

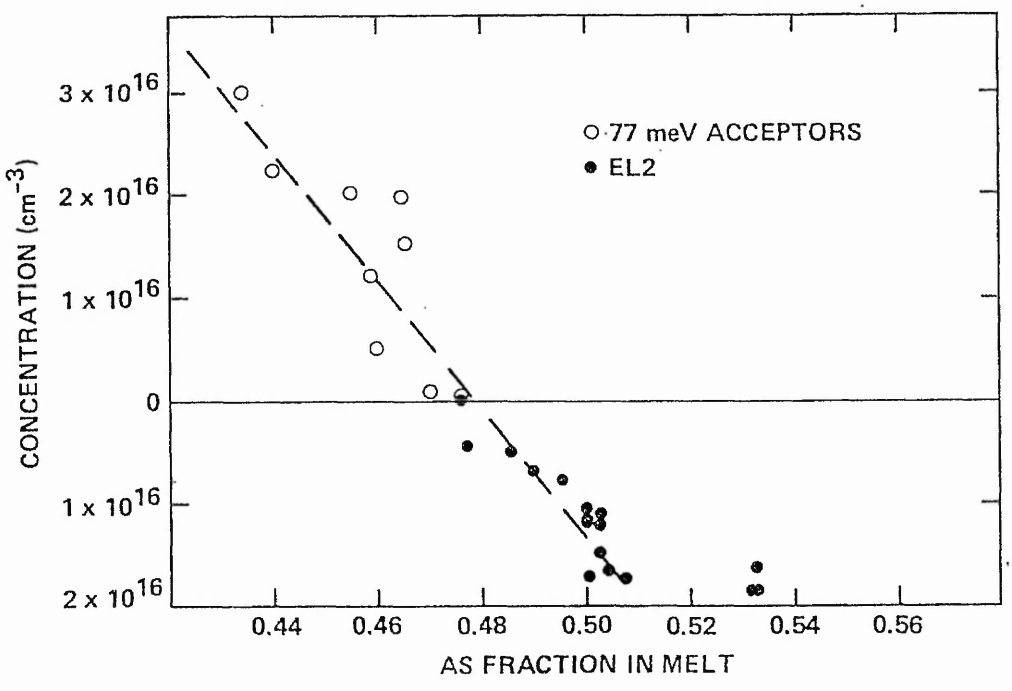

Fig.2.2(c) The effect of melt stoichiometry on the dominant native defect concentration; 77meV double acceptor concentrations in p–type GaAs above the axis, EL2 concentrations in n–type GaAs below the axis. (after Elliott 033)

2.2.2 Dislocation generation mechanisms.

Three main mechanisms are likely to be dominant in LEC grown GaAs. They will be discussed in turn below:

1) Stress induced dislocations;

When the thermal stress in the crystal exceeds the critically resolved shear stress (CRSS) for a particular slip system, slip dislocations will be induced in the material. A model for predicting dislocation densities (and their distribution) produced in this way, in LEC GaAs, was reviewed and developed by Jordan and co-workers (037, 038). Although it does not take into account dislocation interactions or other dislocation generation mechanisms, it still gives a very good quantitative prediction of experimental dislocation densities in LEC GaAs and their macroscopic variation (Clark 039, Jordan 080).

2) Grown in dislocations;

These can be divided into two main types: those which have propagated from the seed during growth and those which have been produced by another mechanism but have reached the growth interface and henceforth have propagated with the growth front. Evidence for the former type is very clear, especially in In-doped GaAs where the number of dislocations produced by other mechanisms have been reduced to near zero (Yamada 040, Stirland 041).

3) Condensation of point defects;

The condensation of point defects and subsequent formation of dislocation loops is clearly very important in HB growth as shown by Lagowski and co-workers (Parsey-Jr 042, 043, Lagowski 044, 045). They demonstrated a strong minima in dislocation density as the crystal stoichiometry was altered from Ga to As-rich. Its importance in LEC GaAs is less certain but according to Lagowski (045) it may be significant, particularly in p-type material, due to fermi energy enhanced vacancy condensation.

The relative importance of the three mechanisms of dislocation formation, given above, is unclear in SI LEC GaAs; although the stress induced glide dislocations are likely to be the most important, from the good correlation of dislocation densities with the Jordan model. The situation is further complicated by secondary generation of dislocations by dislocation multiplication under the influence of stress (or perhaps point defect supersaturations) and by dislocation interactions with other dislocations, point defects or precipitates.

2.2.3 Dislocations structures in LEC GaAs.

Atomic dislocation structures in the GaAs lattice are discussed by Hirth and Lothe (046), Hornstra (047) and Sumino (048). The main types of dislocation are of standard $a_o/2<110>$ burgers vector and usually lie on {111} slip planes with standard $a_o/2<101>$ (or occasionally $a_o<100>$) directions giving a variety of screw, 60° and less commonly, 90° dislocations. Because of the polar nature of the zinc-blende structure of GaAs the 60° and 90° dislocations are further subdivided into α and β dislocations. The terms α and β dislocations are used to denote those 60° (or 90°) dislocations with Ga or As atoms at the core, respectively. This different core structure can give rise to different dislocation properties (Sumino 048, 049).

Recent evidence also suggests that dislocations in GaAs are often dissociated into their corresponding standard $a_o/6<211>$ burgers vector partials (Feuillet 050, Jimenez–Melendo 051).

The mechanisms of dislocation formation were discussed in section 2.2.2. On cooling, dislocations interact strongly with each other and with point defects to give the well known dislocation configurations (Clark 039, Stirland 052, Wehyer 053) and associated impurity atmospheres (Skolnick 054) seen in SI LEC GaAs. These are commonly known as cell structure and lineage, the latter of which was divided by Skolnick and co–workers (054) into sheets and streamers.

Because of the association of defects with dislocations in cell walls, techniques which image this defect distribution (in particular that of EL2) can be used as an indirect method for visualising dislocation structures, as the more direct methods, in particular etching, are destructive. The distribution of EL2 and its relation to dislocations and cell structure will be discussed in more detail in section 2.3.4. In addition to EL2, impurity atoms (in particular carbon) and native defects have also been seen to associate with cell walls using various techniques. These include; CL (Chin 055, and Leigh 056), combined CL and SIMS (Kamejima 057), PL (Kitahara 058), combined PL and resistivity profiles (Kikuta 059) and resistivity and mobility profiles (Bonnet 060). However in contradiction with the above results, Bourret (061) has shown, by using autoradiography of a ^{14}C doped crystal, that carbon is distriubuted homogeneously on the microscopic scale.

The dislocations in the cell walls are generally referred to as "grown in" whereas those in the cell centre or those which lie along slip planes and have clearly not interacted strongly with other dislocations are known as "slip" or "glide" dislocations. The "slip" dislocations, formed at a lower temperature, often lack impurity atmospheres and genrally occur in much lower densities than the dislocations in cell walls.

Various models exist for the grown in dislocations and their surrounding "impurity atmospheres". One set of models is based on the assumption that dislocations produced at high temperature, move, interact, multiply and become tangled during post–growth cooling. Then they either getter (Brozel 062) and/or generate defect atmospheres by climb (Weber 063, Stirland 236) to form cell structure. A different model, suggested by Wehyer et al (064, 065), attributes the cell structure and associated impurity atmospheres to the first stage in Constitutional Supercooling. In this model, the point defect imbalance, giving rise to cell structure, is grown in. Dislocations then form from point defect condensation as the crystal cools.

More information on dislocation structures, in particular those in In–doped crystals, will be given in section 6.2.

2.2.4 Precipitates and associated defects in GaAs.

This section deals with the precipitates seen in stoichiometric or As–rich material. Ga precipitates which are not dealt with here, are seen in Ga–rich material and the shoulder regions of some nominally As–rich LEC ingots, due to As loss during growth (Brozel, 066).

Precipitate identification.

In As–rich and stoichiometric GaAs the precipitates seen are nearly always associated with dislocations (Cullis 067, Cornier 068). They are typically about 20nm to 100nm in size (from TEM studies: Cullis 067), with observable densities from 10^6 up to $10^{10}cm^{-3}$ (Cullis 067, Suchet 069). The identification of these precipitates is still in doubt. The earliest identification using TEM on HB Cr–doped GaAs (Cullis 067), was hexagonal As. More recent TEM work on undoped material confirmed this identification (Stirland 052). However another group (Cornier 068) identified one precipitate as poly–crystalline GaAs. This identification was later confirmed on other precipitates, although a second type of precipitate in the same sample, found in similar numbers, were identified as hexagonal As (Duseaux 070). In a more recent study (Lee 071), precipitates were again identified as hexagonal As with a simple orientation relationship with the GaAs matrix. A combined TEM and Energy Dispersive X–ray analysis (EDX) study of In–doped GaAs by the same group (Lee 072) also showed As precipitates of the same type along with a precipitate of an As–rich GaAs phase. Barrett et al (073) using EDX on In–doped material also identified precipitates as an As–rich GaAs phase in In–doped material. Finally, Suchet et al (069) has suggested that some As precipitates getter impurities while others are pure As.

Analysis of "As precipitates" in In–doped GaAs indicate that they contain no In (Lee 072, Barret 073, Nakajima 074). For the purpose of this work it will be assumed that the precipitates in In–doped material are of the same nature as those in undoped GaAs.

It is clear that there are several types of precipitates, some of which may even co–exist in a particular sample. The identities, distribution and sizes of precipitates seen could depend on the growth technique, dopants and post growth heat treatments used. In this work, for convenience, all precipitates of this type will be referred to as As precipitates. More information on precipitates related to their scattering of NIR light is given in section 2.3.6

Precipitate formation.

The formation of As precipitates is probably due to the crystal cooling through the retrograde solidus, giving a supersaturation of As interstitials, as discussed in section 2.2.1 and illustrated in fig.2.1. From different annealing studies, their formation temperature is thought by some (Suchet 069, Yamada 075) to be around 1000°C and by others (Lee 077) to be around 650°C. The effect of annealing on precipitates will be discussed in more detail in sections 2.4.4.

Other micro–defects.

In addition to As precipitates various other micro–defects have been seen in GaAs crystals. High Resolution TEM (HRTEM) studies (Ponce 076) show precipitates of 2 to 20nm in size which appear mainly in cell walls. They appear to be coherent with the matrix, with minimal associated lattice strain and hence are not thought to be decorated dislocation loops. They appear to be amorphous in HRTEM but unfortunately no chemical analysis could be performed and hence their nature is unclear. Dislocation loops of interstitial and occasionally vacancy–type from 2 to 3 nm in size were also seen in the interior of cells. TEM studies of GaAs which contained As precipitates also showed dislocation loops probably associated with As interstitials (Lee 071, 077). Other workers (Lessof 078) have noted a large density of stacking faults and partial dislocation loops in "dislocation free" regions of In–doped GaAs using TEM and etching

studies.

2.2.5 Crystal growth techniques.

A brief review of the main bulk crystal growth techniques for GaAs is given below. Emphasis is given to the LEC process for the growth of undoped SI ingots and the main methods of reducing dislocation density in these crystals. For more detailed reviews see the work by Willardson (079), Jordan (080), Hurle (081) and Hollan et al (082).

LEC Growth and its variants.

The historical development of the LEC technique (along with some speculation on its future) is reviewed by Hurle (081). LEC material has come to dominate the market for undoped SI substrates because of advantages over its major competitor, the Horizontal Bridgman (HB) technique. The main advantages are the growth of (001) circular cross section, undoped, SI material with a high yield. The ability to grow undoped SI crystals is due to reduced silicon (donor) contamination, mainly by the use of a high purity pyrolytic boron nitride crucible instead of a cheaper quartz crucible. The compensation mechanism is controlled by native deep donors (mainly EL2) and an excess of shallow residual acceptor impurities (mainly carbon) over donor impurities (see section 2.5).

An outline of the LEC process is as follows: A GaAs seed crystal is dipped into a GaAs melt and slowly pulled back through a boric oxide encapsulant. The encapsulant, which prevents As loss from the melt is usually wet boric oxide (approximately 2000ppm water), as impurity concentrations (in particular carbon and boron) are reduced compared to crystals grown under dry (approximately 100 ppm water) boric oxide (Hunter 083, Kikuta 084, Emori 085, Baumgartner 086). The seed and crucible are both rotated, usually in opposite directions, to improve growth uniformity and stirring of the melt. Growth is usually carried out in a high pressure container with inert gas (about 60 atmospheres of argon). The GaAs melt is produced by direct in–situ synthesis from the elements. An alternative form of growth is at low pressure (about 5 atmospheres) with a polycrystalline GaAs starting charge (Elliot 087). The majority of crystals are grown using the high pressure technique mainly because of the increased risk of contamination from the polycrystalline charge. However, recent developments with low pressure growth using As injection also allows direct, in–situ synthesis of GaAs from its elements (Duncan 088). At present, mainly three inch crystals are grown, although there is still some two inch growth and the growth of four inch crystals has been reported (for example: Orito 089).

One of the major disadvatages of "standard" undoped SI LEC GaAs is the relatively high dislocation density (typically from 10^4 to $10^5 cm^{-2}$). Advances in LEC growth are mainly designed to reduce dislocation densities. One method of achieving this is to reduce thermal gradients in the crystal by reducing the difference between the melt temperature and the ambient temperature. Various attempts have been used to reduce thermal gradients (Elliot 090). These result in lower dislocation densities but often with poor diameter control, hence a trade off is required (Jordan 080). One attempt to improve LEC growth by thickening the boric oxide encapsulant and hence reduce thermal gradients, is called the Fully Encapsulated Czochralski (FEC) technique (Yamada 040, Kohda 091). Its variants include heating the boric oxide

(Shimada 092), and the inclusion of thermal baffles (Shimada 093). Another method of growth is known as the Liquid Encapsulated Kyropoulos technique (LEK) where the crystal is not withdrawn from the boric oxide (Duseaux 094, Jacob 095, 096). An adaption of the LEK technique is the Liquid Encapsulated Freeze (LEF) technique (Mo 097). These techniques can give dislocation densities as low as $10^2 cm^{-2}$.

The use of isoelectronic dopants, especially indium, to reduce dislocation densities is described in the next section. State of the art In–doped GaAs is dislocation free. Various workers have used a stong magnetic field in conjunction with In–doping for LEC growth (see for example, Osaka 098). Magnetic fields reduce convection and hence reduce temperature fluctuations in the melt. This also gives more stable solid–melt interface conditions. The main advantages of this technique are the removal of growth striations and the improved uniformity of various substrate properties (Kawase 099, Kimura 100, Terashima 101). In fact, one group using the FEC technique along with In–doping, a dislocation free lattice matched seed and a strong vertical magnetic field, have produced dislocation and striation free, two and three inch GaAs (Yamada 040, Kohda 091). More recently the system was developed to produce four inch ingots (Orito 089). Another advantage of magnetic fields is the possibility of high speed pulling of LEC crystals. One group have demonstrated this (Kimura 102) and have shown excellent uniformity of various substrate properties after a post growth anneal.

Other growth techniques.

The Horizontal Bridgman (HB) technique involves moving the crucible containing the melt from a hot zone in a furnace to a cooler zone. The melt gradually solidifies at the interface between these two zones as the crucible moves. Advantages of the HB technique include lower dislocation density with tight stoichiometry control (Parsey Jr. 043) and subsequent good uniformity of substrate properties (Gray 103). The main disadvantages are that the crystals are not circular and the difficulty of growing undoped SI GaAs due to the use of quartz boats with subequent silicon contamination. SI HB crystals are usually produced by chromium doping. However Recent developments have allowed the reduction of silicon concentrations and the production of SI undoped ingots (Parsey Jr. 042).

The Horizontal Gradient Freeze (HGF) technique is similer to the HB technique but involves moving the heat zone rather than moving the crucible. The results and limitations are very similar to those of HB growth.

The heat exchanger method (HEM), unlike the other methods described here, involves growth without built in temperature gradients in the heat zone (Khattak 104). This gives very low thermal stresses and correspondingly low dislocation densities. The compensation mechanism is the same as in LEC crystals and electrical properties are highly uniform, as the ingot is annealed in–situ (Khattak 105).

The most promising of the alternatives to the LEC type growth is the Vertical Gradient Freeze (VGF) technique, where undoped, low dislocation density, near cylindrical ingots can be grown without diameter control (Gray 106, Gault 107). Recently the improved uniformity of various parameters (including V_{th}) over LEC material has been demonstrated (Gray 106, Clemans 108, Reynolds 109). In addition to this, the adaptation of the technique to the growth of four inch diameter crystals should be less of a problem than for competing growth techniques.

Possible Future Trends.

In–doped, dislocation and striation–free GaAs has been grown. Unfortunately, there are still several problems which must be solved if the market share of In–doped material is to be increased. These problems include, the small segregation coefficient of indium (Effective segragation k_{eff}~0.13, McGuigan 110) which results in the indium concentration increasing strongly towards the tail end of the crystal, leading to constitutional supercooling and twinning. This limits the length of useful crystal that can be grown. In–doping also shifts the lattice constant of GaAs, causing problems when the material is to be used for epitaxial applications. In–doping makes GaAs more brittle which can cause problems during cutting, polishing and proccessing. These factors are particularly important for dislocation free material where the In content at the seed end must be high. In–doped crystals are also more expensive than their undoped counterparts because of these problems.

Low thermal gradient LEC growth and its close relatives (LEK and FEC) cannot produce dislocation free undoped GaAs and diameter control is still a problem. However yields are higher and costs are lower than for In–doped material. Also, with the advances in post growth annealing, the effect of dislocations on device uniformity may become unimportant (see section 2.6.3).

Both of the above methods are likely to be strongly challenged by the VGF technique with its advantages of very low dislocation density, preset "cylindrical" shape and ease of modification to four inch growth.

Various crystal growers are working on four inch diameter GaAs, which will give higher yields per slice and compatibility with silicon processing equipment. Problems include the ability to meet smaller diameter crystal quality control specifications and the increased cost of growth.

2.2.6 Isoelectronic doping.

The most effective isoelectronic dopant utilised for SI GaAs is indium (Hobgood 111). The reason for its inclusion is an attempt to harden the lattice and hence reduce dislocation densities (Ehrenreich 112) without effecting electrical properties. Experimentally, dislocation densities are seen to drop rapidly when the indium concentation exceeds $10^{18}cm^{-3}$ (Kimura 113). In fact, in some crystals, large dislocation free regions are seen, where slip is reduced to zero. Only "grown–in" dislocations from the seed–crystal interface mismatch are seen along the crystal axis (Yamada 040). By using lattice–matched, In–doped, dislocation free seeds and necking procedures, dislocation free SI GaAs can be grown (Orito 089, Kohda 091).

The mechanism of dislocation reduction brought about by In–doping is still not fully understood as the theoretically required increase in CRSS to give dislocation free GaAs is not acheived according to many experiments (Tabache 114, Bourret 115). However, many of these experiments involve extrapolation from temperatures well below the melting point of GaAs. Hence, this problem awaits new mechanisms or more experimental data fron higher temperatures. Jordan's (038, 080) theoretical study of lattice hardening, shows a good tie in with experiment. However, his study assumes a CRSS near the melting point which may be unrealistic, for the reasons described above. Lagowski and Gatos (045) suggested an alternative view of dislocation reduction based on the modification of point defect

concentrations and reduced dislocation loop formation by vacancy condensation. Other workers (Jimenez 116) suggest that because of the dissociated nature of dislocations in GaAs, In–doping could effect the stacking fault width between partials and hence reduce cross–slip and climb. This would reduce dislocation mobility and dislocation multiplication. The effects of In–doping on dislocation generation and subsequent mobility are reviewed by Sumino (048, 049).

One alternative to In–doping which shows promise is indium and phosphorus co–doping (Kimura 117). The segregation coefficient of phosphorus is greater than one hence the amount of indium required for reducing dislocation densities at the seed end is reduced. Also, part of the crystal can be lattice matched to GaAs. This technique would benefit if some method of phosphorus injection can be developed.

2.3 EL2 and GaAs Near–Infrared Optical Properties.

EL2 is the dominant native deep level in undoped GaAs. It is the deep donor level which is responsible for the SI nature of undoped material. In this section, the main properties of EL2 will be discussed, followed by possible atomic models for the defect. The characteristic Near–Infra–Red (NIR) absorption band of EL2 will then be described along with its use to measure the concentration and distribution of EL2. Finally the contribution of absorption and scattering, from other defects, to the NIR properties of GaAs will be discussed.

2.3.1 EL2 properties.

For several general reviews on the properties of EL2 see the papers by: Martin (118, 119) Makram Ebeid (120), Lagowski and Gatos (121, 122), Weber and Omling (123), Kaminska (124), and Von Bardeleben (125).

The main properties of EL2 are summarised below:

1) The defect is a deep donor (Martin 118) with an energy level (corresponding to $EL2^{+/0}$) at about Ec–0.76 eV (Martin 118). Its characteristic emission rate, e_n measured from DLTS is given by the Arrhenius type relationship:

$$e_n = a_n T^2 . \exp(-E_n/kT)\ s^{-1}$$

where a_n and E_n are $3.42 \times 10^7 s^{-1} K^{-2}$ and 0.825eV (Martin 126). These values were recently modified by Gatos and Lagowski (121) to $2.83 \times 10^7 s^{-1} K^{-2}$ and 0.814eV. The sensitivity of the emission to an electric field suggests a Frank–Condon shift of 140meV (+/–10) for this level (Makram Ebeid 127, Chantre 128). Recently a second donor state (corresponding to $EL2^{++/+}$) situated at Ev+0.52eV has been ascribed to EL2 (Lagowski 129, Bencherifa 130). Fig.2.3 illustrates the level schematically and also shows a possible configuration coordinate diagram.

2) The defect gives rise to an broad absorption band in the near infra–red (Martin 131). The absorption band is shown in fig.2.4, It extends from 0.8eV, to the band gap, at 1.45eV. This absorption band is discussed in more detail in section 2.3.3.

3) The defect exhibits a zero phonon line (ZPL) at 1.04eV, corresponding to a A_1 to T_2 intracentre transition (Kaminska 132). This ZPL is visible in near infrared absorption,

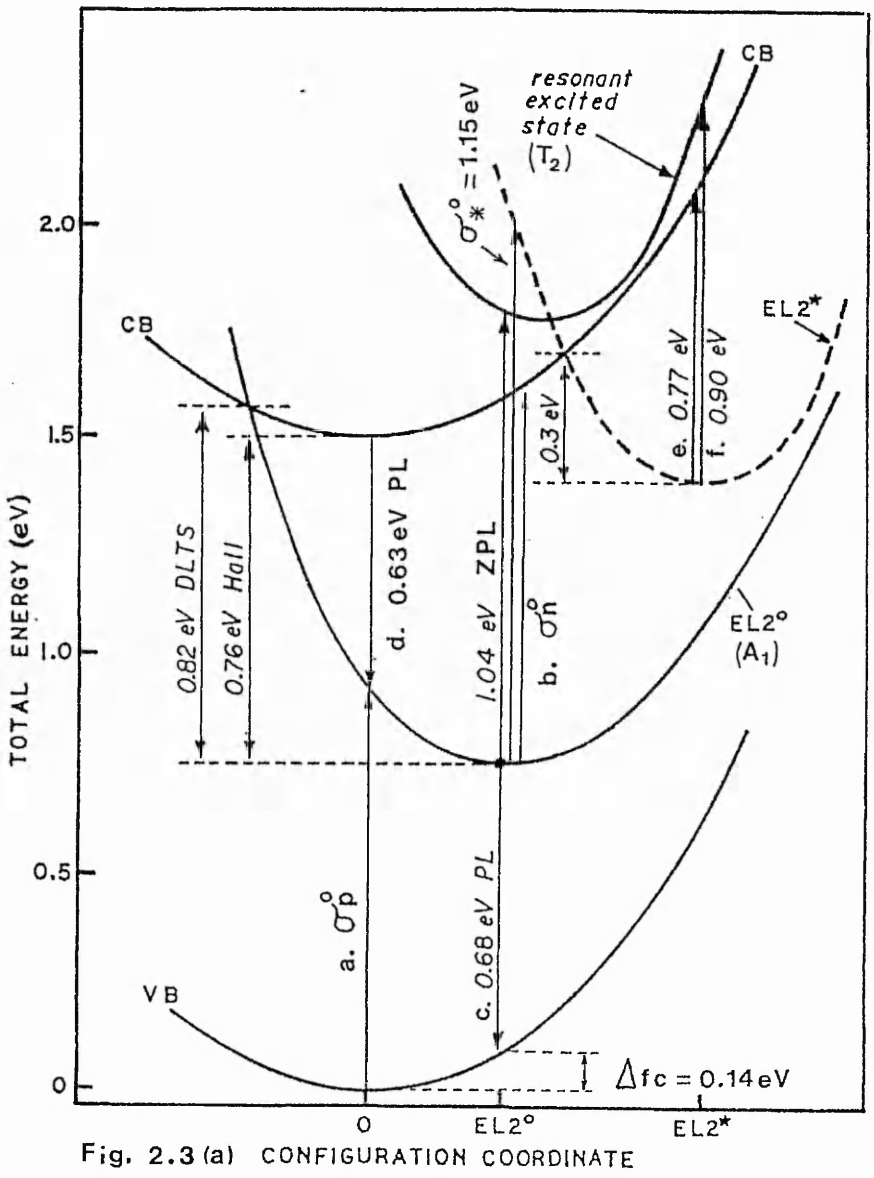

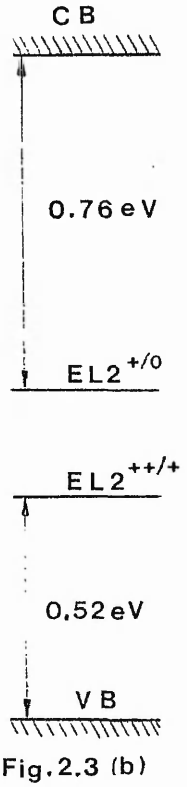

Fig.2.3 (b)

Fig.2.3(a) A possible configuration coordinate diagram for the EL2 defect in GaAs. This shows the relationship of the main donor level of EL2 ($EL2^{+/o}$) to the conduction band and the valence band. The parabolic curves represent the variation of Total Energy with configuration coordinate. Also shown in the diagram are the excited state of EL2 which is resonant with the conduction band and the metastable state ($EL2^{*}$) which displays a large lattice relaxation illustrated by the shift in its energy minima with configuration coordinate. Transitions a and b show the onsets of optical excitation from the valence band to EL2 (σ_p) or from EL2 to the conduction band (σ_n) respectively. Transitions c and d represent the EL2 related PL bands (Tajima 463). Transitions e and f represent photo-enhanced recovery from the metastable state (Fisher 544). All other transitions are detailed in the text in section 2.3.1.

Fig.2.3(b) A schematic of the EL2 level positions in the GaAs band gap including the second donor level of EL2 ($EL2^{++/+}$).

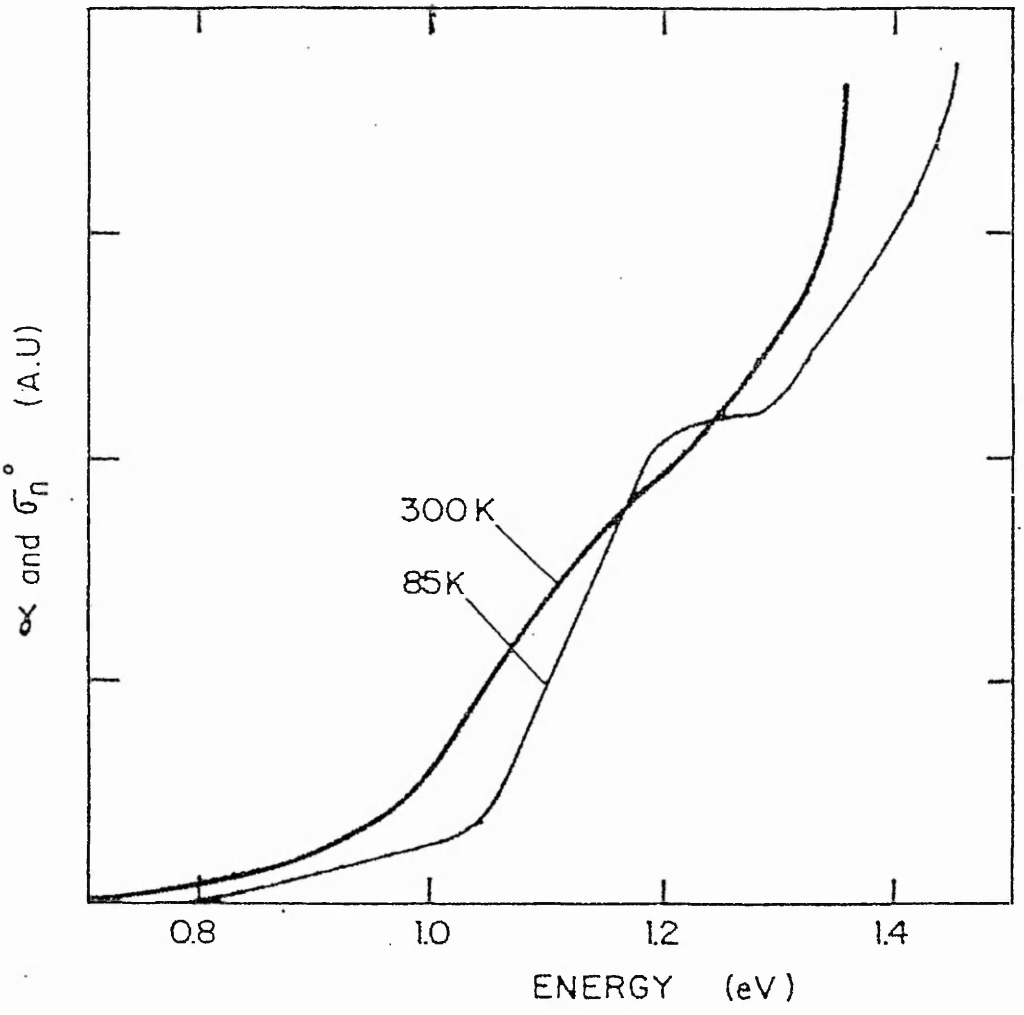

Fig.2.4. Optical absorption coefficient versus photon energy, at 85K and 300K, for the EL2 defect in undoped SI GaAs.

photocapacitance (Mochizuki 133) and photocurrent (Tsukada 134). The excited state of EL2 is resonant with the conduction band.

4) The defect displays a metastable state which can be reached by optical exitation at low temperatures. The characteristic EL2 optical absorption band and photo-capacitance signals disappear when the defect is photo-quenched (Vincent 135). The wavelength dependance of the light capable of transferring EL2 to its metastable state shows a gaussian peak with maximum efficiency for 1.15 eV light. The normal state of EL2 can be recovered by heating the sample to above 140K with an associated activation energy of about 0.3eV (Vincent 135). This process can be accelerated by the presence of electrons with an activation energy, for the thermally activated electron cross section, of about 0.1eV (Vincent 135). Transfer to the metastable state occurs via the intracentre transition from the neutral (occupied, $EL2^{o}$) state (Skowronski 136, Manasreh 167). Investigations of the "EL2" defect in the GaAsP alloy system demonstrate that the metastable property is lost when the excited state is no longer resonant with the conduction band (Samuelson 137). The metastable state is shown on the configuration coordinate diagram in fig.2.3.

5) EPR studies, along with other techniques, show that the ionised $EL2^{+}$ defect is associated with the EPR spectrum of the As_{Ga}^{+} defect (Weber 063) and hence almost certainly identifies EL2 as the isolated neutral As antisite defect (As_{Ga}^{o}), or a complex of it (Martin 118). Additional evidence for the EL2 defect containing As_{Ga} includes the following: photo-enhancement spectra for the ZPL anti-correlates with the photoresponse of the $(As_{Ga})^{+}$ EPR signal (Tsukada 134, 138); combined EPR and ZPL studies on material, with the degree of compensation altered by photoquenching and annealing, shows that the sum of the $[EL2^{o}]$ and $[As_{GA}^{+}]$, as the charge state is altered, is constant (Lagowski 139). See section 2.3.2 for more discussion on the possible atomic models of EL2.

6) The concentration of the defect increases as the stoichiometry of the bulk material is moved to As-richness (Holmes 031, Walukiewicz 140).

7) The defect is thermally stable up to at least 850°C (Kitagawa 141, 142, Kaufmann 143, Weber 144)

Individually the properties described above do not distinquish EL2 from other possible defects. This particularly applies to the El2 NIR absorption band, as other absorption bands occur in this wavelength region (see section 2.3.3). Hence the question remains, how do we know that we are dealing with EL2? The most obvious method of confiming this is to look for the EL2 DLTS signature (Gatos 121). Unfortunately, the material must be n-type for DLTS and most investigations of EL2 are in SI material. Also care must be taken in interpreting DLTS data (Gatos 121), otherwise artifacts of the technique may be confused with EL2 properties. Another commonly used method is to look for EL2 related photo-quenching. Unfortunately, this is often unreliable, as characteristics of other defects may be affected by photo-quenching, either directly or indirectly (for example by changes in fermi level), when EL2 is transformed to its metastable state.

The EL2 "family".

There is considerable evidence indicating that EL2 is not a single defect but a family of closely related levels.

DLTS evidence has clearly shown the existence of the "oxygen related" level, ELO (Lagowski 145, Gatos 146). Other DLTS results show the three level system EO1, EO2 and EO3 (Yahata 147), where EO3 correlates with the NIR absorption, but the other two levels do not (EO1 is assigned to EL2 and EO2 is possibly ELO). Another three level system involves the ETX–1, ETX–2 and ETX–3 DLTS peaks (Taniguchi 148). ETX–3 is stable under reverse bias and resembles the EL2 level in HB material and hence is identified as such.

Some workers have noted different spectral photoquenching cross–sections and photo–capacitance quenching behaviour of GaAs grown using different techniques (Taniguchi 149, 150, Mita 151). Other workers have shown two stages in the thermal recovery from the metastable state, with (Parker 152) and without (Vignaud 153) optical assistance. The relative efficiency of the first stage is again material dependent.

The arguments for the existence of an EL2 family are reviewed by Mochizuchi and Ikoma (154, 155). Recently, in addition to the above results, a Local Vibration Mode (LVM) has been seen which is claimed to exhibit some "EL2 like properties" including a frequency shift after photoquenching but whose concentration appears to be well below that of EL2 in the material (Zhong 156). The authors tentatively assign this LVM to ELO.

2.3.2 EL2 models.

Numerous atomic models for EL2 have been proposed but the confirmation of the "correct" model has proved to be a particularly difficult and often controversial task as none of the techniques available for elucidating its structure can give a definite identification. However progress is being made as the amount of experimental data available increases and the quality of theoretical predictions improve.

A list of the atomic models for EL2 is given in table 2.1. A full discussion of these different atomic models and their relative merits is beyond the scope of this thesis. However, a summary of the main information pertaining to the identification of EL2 will be given, concentrating on those models which are thought to be most likely in the current literature. Further discussion of the possible models for EL2 can be found in the following references: Aref'ev (026), Martin (118), Gatos (121), Lagowski (122), Weber (123, 157), Kaminska (124), Von–Bardeleben (125), Ikoma (154), Kennedy (158) and Bourgoin (159).

As discussed in section 2.3.1, it is fairly clear that EL2 contains the As_{Ga} defect. Is EL2 the isolated antisite or is it a complex containing the antisite? Evidence suggesting the antisite–complex model includes the following:

1) ENDOR results (Meyer 160, 161), suggest trigonal symmetry (and hence favour the As_{Ga}–As_i model, amongst others).

2) There is difficulty in explaining how the isolated antisite forms a metastable state.

3) Plastic deformation, ion implantation, and electron or neutron irradiation introduces

EPR detectable antisites in concentrations larger than [EL2] (Weber 162). The majority of these antisites anneal out at a much lower temperature than EL2 (Weber 144, Omling 163). The argument that acceptors are created which compensate constant [As_{Ga}] (Skowronski 164) cannot be correct as the introduced [As_{Ga}] far exceeds that of the initial [$EL2^{o}$] in the material.

4) The absorption in plastically deformed material does not all bleach (Samuelson 165) and antisites in neutron irradiated GaAs do not display persistent photoquenching (Wosik 166, Manesreh 167).

5) In recent quenching experiments, involving heat treatments with fast cooling rates (Von Bardeleben 125), the photoquenchable (and hence EL2 related) As_{Ga} EPR signal and the characteristic DLTS emmision signature of EL2, are both changed significantly. The EPR signal remains at the same magnitude and no longer photo–quenches, whereas the magnitude of the EL2 related DLTS signal drops by an order of magnitude. After re–annealing (followed by a slow cool), the level of the DLTS signal and the photosensitivity of the EPR signal are retreived.

6) Experimental techniques which point towards the assignment of tetrahedral symmetry to EL2 (for example the splitting of ZPL under uniaxial stress, Kaminska 168) are mainly sensitive to the four nearest arsenic neighbours of the antisite. Any changes in the second or further shells of neighbours may not be seen by these techniques.

7) Anomalous outdiffusion profiles of EL2 at a sample surface after annealing indicates that EL2 is unlikely to be a simple point defect (Wada 169, Makram–Ebeid 170).

Unfortunately, much of the above information is controversial. The ENDOR results rely on a complicated interpretation and may have an alternative explanation but they are as yet undisputed. Recent theoretical calculations (Mauger 171, Dabrowski 172, Chadi 173) show that it is possible for the antisite to have a metastable state. The plastic deformation and irradiation studies can be explained by saying the EPR signal NOT related to EL2 is due to a defect interaction, as indeed seems to be the case with the "U–band" of related defects (see section 2.4.2). The combined DLTS and EPR studies are controversial (Gatos 174, Von Bardeleben 175). The ZPL data cannot easily distinguish either model. The outdiffusion data has been shown by other workers (Martin 176) to follow the expected "erf" (or error function) distribution for an outdiffusing (previously uniformly distributed) point defect. Moreover, the DLTS technique which is used to determine this distribution may be suspect (Gatos 121) and there is an alternative model for annomalous out–diffusion of the antisite based on As loss at the surface (Matsui 177).

However assuming that EL2 is a complex the following facts can be used to distinguish the likely models:

1) Positron annihilation studies (Dannefaer 178) show that EL2 is not associated with vacancies unless they are in a positive charge state. This tends to eliminate any defect containing V_{Ga} as it is likely to be either in a neutral or negative charge state in n–type or SI material (Stucky 179).

2) The EL2 concentration shows a clear increase as the crystal becomes more As rich

(Holmes 031). This eliminates any defects which are not As rich (for example the As_{Ga}–Ga_{As} defect).

3) Symmetry studies of ENDOR (Meyer 160, 161) and ZPL (Kaminska 168) indicate tetrahedral symmetry for the antisite nearest neighbours. Hence it is surrounded by four As atoms. This eliminates the nearest neighbour As_{Ga}–V_{As} defect.

4) Calculations of the concentrations of antisites and EL2 defects in the same material show very similar concentrations (Lagowski 139). This would tend to eliminate the As_{Ga} cluster models unless most antisites in a cluster display EL2–like character.

If EL2 is a complex, the As_{Ga}–As_i model and the various As aggregate models are the most likely candidates. The trigonal As_{Ga}–As_i model is also supported by: DLTS results on the regeneration kinetics of EL2 after quenching (Von–Bardeleben 125); evidence of a supersaturation of As interstitials in As rich material (as was discussed in section 2.3.2); the symmetry results of ENDOR (Meyer 160, 161) and ballistic phonon scattering (Culbertson 180) and photocapacitance quenching under uniaxial stress (Levinson 181); and on the stress splitting of the ZPL (Manasreh 182, 183).

The main model for the As_{Ga}–As_i defect places the interstitial at the second nearest site along o (Von–Bardeleben 125). The metastable properties of EL2 can then be easily explained by a simple site switch of the interstitial from the second nearest to first nearest neighbour site, where it interacts with the antisite giving a large lattice relaxation. Theoretical calculations show that this defect should be bound in intrinsic or n–type GaAs (Baraff 184). However these calculations (Baraff 185) also show that there should be an acceptor level at 0.2 to 0.5 eV above the main donor level (which is at E_c–0.8eV); this level has never been seen. Note also that several groups have recently questioned the association of an interstitial with EL2 on the grounds that it does not explain a wide variety of experimental results (Wosinski 186, Gatos 174).

Several other points of caution should be mentioned. The above arguments apply only to the main electrically active defect in the material; other defects which are not electrically active could exist undetected, in large concentrations, in the same material. Also the arguments above often involve dismissing a model on a single piece of evidence. Finally the material being used by various experimenters around the world, which is assumed to be the same, may have different dominant defect concentrations. Hence, no definite identification of EL2 can yet be made. However, the isolated As_{Ga} antisite or its complex with an As interstitial look to be the most likely of those models discussed here.

Table 2.1. Atomic models for EL2

As_{Ga}	(Weber 063, Kaminska 168, Lagowski 187, Johnson 188)
As_{Ga}–V_{As}	(Gatos 121 ,Walukiewicz 140, 189, Lagowski 190)
As_{Ga}–As_i	(Von–Bardeleben 125, 175, 191, 192, 193, Steivenard 194)
As_{Ga}–V_{Ga}–V_{As}	(Zou 195, 196, 197, Wu 198, 199, Wager 200)
V_{Ga}–As_{Ga}–V_{Ga}	(Van–Vechten 201, Suezewa 202)
As_{Ga}–V_{Ga}	(also As_{Ga}–impurity, Goltzene 203)
As_{Ga}–As_{Ga}	(Figielski 204, 205)
As_{Ga}–As_i–As_{Ga}	(Figielski 206, 207, 208)
As aggregate	(Taniguchi 143, 149, 150, Wada 169, Ikoma 154, 209, Jimenez 210, Mita 211)
As_{Ga}–acceptor	(Hariu 212, 213)
As_i–V_{As}	(Aref'ev 026)
As_{Ga}–Ga_{As}	(Schneider 214)
Oxygen related	(for a review see Martin 118 or Gatos 146)
C^o–D^+	(Levinson 215, Fillard 216, 217; where C^o is a multi–charge state defect (As_{Ga}^o, for example) and D is a donor level)

(NB the last of these models is really a phenomelogical model rather than an atomic model)

2.3.3 EL2 absorption and calibration.

Fig.2.4 shows the characteristic near infra–red absorption band of EL2 at room temperature and 77K. The band is thought to include contributions from several competing processes. Firstly there are transitions to the three conduction band minima, Γ, L and X. These transitions give the characteristic absorption thresholds at 0.7, 1.0 and 1.3eV respectively (Martin 131, Chantre 128). Superimposed on this is an intra–center transition with its associated ZPL (Kaminska, 132). The intracentre contribution is quite large but was not noticed for a long period as it overlays the predicted L conduction band transition. However its presence was clearly demonstrated by comparing optical absorption and photocurrent spectra (Kaminska, 132). The ZPL is situated at 1.039 eV at 4K, and is seen to have several phonon replicas (Kuszko 218). In addition, there are lesser contributions from other processes such as hole photo–ionisation; these will be discussed below.

Work by Martin (131) showed that the [EL2] as measured by DLTS, was proportional to the absorption coefficient of the sample, that is:

$$[EL2] = f.\alpha = f.\ln(T_2/T_1)/d$$

where, α is the absorption coefficient, d is the sample thickness and T_2 and T_1 are the sample transmissions where there is no EL2 absorption and at the calibration wavelength respectively.

The values of f, the calibration factor, at the two most commonly used wavelengths, 1μm (1.24eV) and 1.1μm (1.13eV), are $7x10^{15}$ and $12.5x10^{15}$ cm^{-3} respectively. Martin's calibration is shown in fig.2.5.

Other contributions to the absorption cross section from the EL2 level are:

1) The hole photo–ionisation cross section from the ionised level, $EL2^+$, to the valence band (σ^o_P): The spectral form of this has been given by several workers (Chantre 128, Silverberg 219, 220). Generally the contribution from the hole photo–ionisation is ignored as it is assumed that EL2 is nearly fully occupied and that $\sigma^o_N > \sigma^o_P$ for the wavelengths where the concentration is measured. At room temperature and 1μm σ^o_N exceeds σ^o_P by about a factor of 8 (Silverberg 219). Fig.2.6. shows σ^o_P for $EL2^+$ as obtained from DLOS (Chantre 128) and photo–capacitence (Siverberg 219).

2) The double donor level electron and hole photoionisation cross sections (Silverberg 220): In SI or n–type material the double donor state will be occupied hence the hole photo–ionisation contribution which is relatively large, will not be seen. However, the electron photo–ionisation cross section of the double donor state should contribute giving a very small threshold at about 1.1eV (its magnitude is nearly two orders of magnitude down on that of σ^o_N). Fig.2.6 shows the electron and hole photo–ionisation cross sections taken from the work by Silverberg et al (220).

In this work we assume that the compensation ratio is high and ignore any contributions other than σ^o_N to the optical absorption unless otherwise stated.

Recently a calibration was given for the absorption coefficient of the ZPL (Skowronski 221, Lagowski 222). An absorption coefficient of 0.06 cm^{-1} was found to correspond to an [EL2] of $5x10^{16}cm^{-3}$ by comparing with DLTS results. By using a multi–stage technique, the authors claim that concentrations of both charge states of the singly ionised charge states of EL2 can be determined. The procedure is as follows: firstly, cool the sample from room temperature to about 6K in the dark and measure the ZPL absorption coefficient with weak illumination (to avoid transfer to the metastable state); secondly, bleach the sample with white light; thirdly, anneal the sample at about 140K in the dark and return the sample to 6K and re–measure the ZPL absorption coefficient. Using the calibration given above, the first stage gives the [$EL2^o$] and the third stage gives [EL2] and hence the difference between the first and third stages gives [$EL2^+$]. This technique is difficult to understand as it seems to rely on the acceptor compensating EL2 being thermally unionised at 140K. This will not by true when compensation by shallow C or Zn acceptors dominates, as is normally expected to be the case.

The problems associated with Martin's calibration (as used in this work) are described below. Some of these can be avoided by measuring the absorption at one wavelength before and after bleaching, preferably at about 4K. Otherwise by use of the ZPL calibration, which requires a high resolution FTIR spectro–photometer.

Problems with calculating [EL2] from NIR absorption.

1) Martin's calibration (131) may not be accurate. Certainly the work requires repeating, as the number of data points is small and the error bars are quite large. The calibration for 1μm and 1.1μm light is shown in Fig.2.5. Recently the calibration has been repeated by Skowronski et al

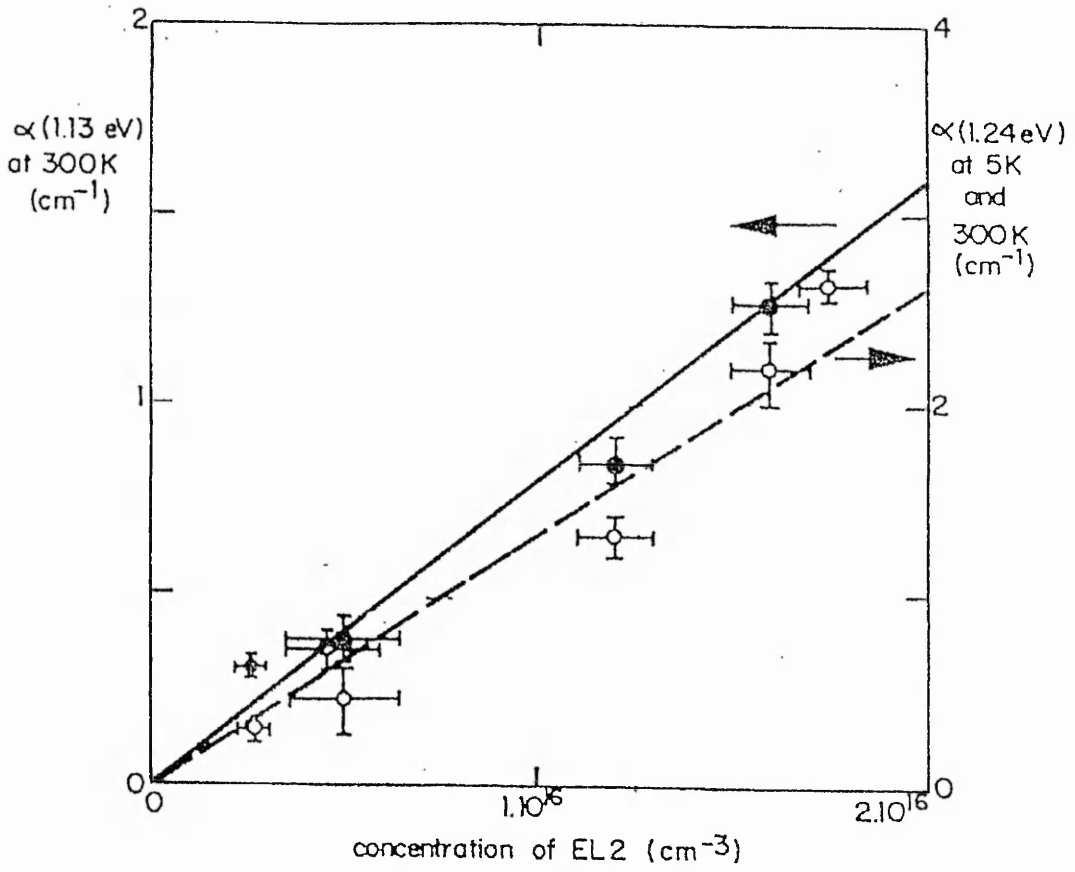

Fig.2.5. Martin's calibration (Martin 131) of the optical absorption coefficient of EL2 at wavelengths of 1μm (1.24eV) and 1.1μm (1.13eV): "Variation of the optical absorption coefficient in undoped n–type materials as a function of the concentration of EL2 determined by capacitance methods in the same materials. Measurements at 5K (open circles) and at room temperature (full circles)".

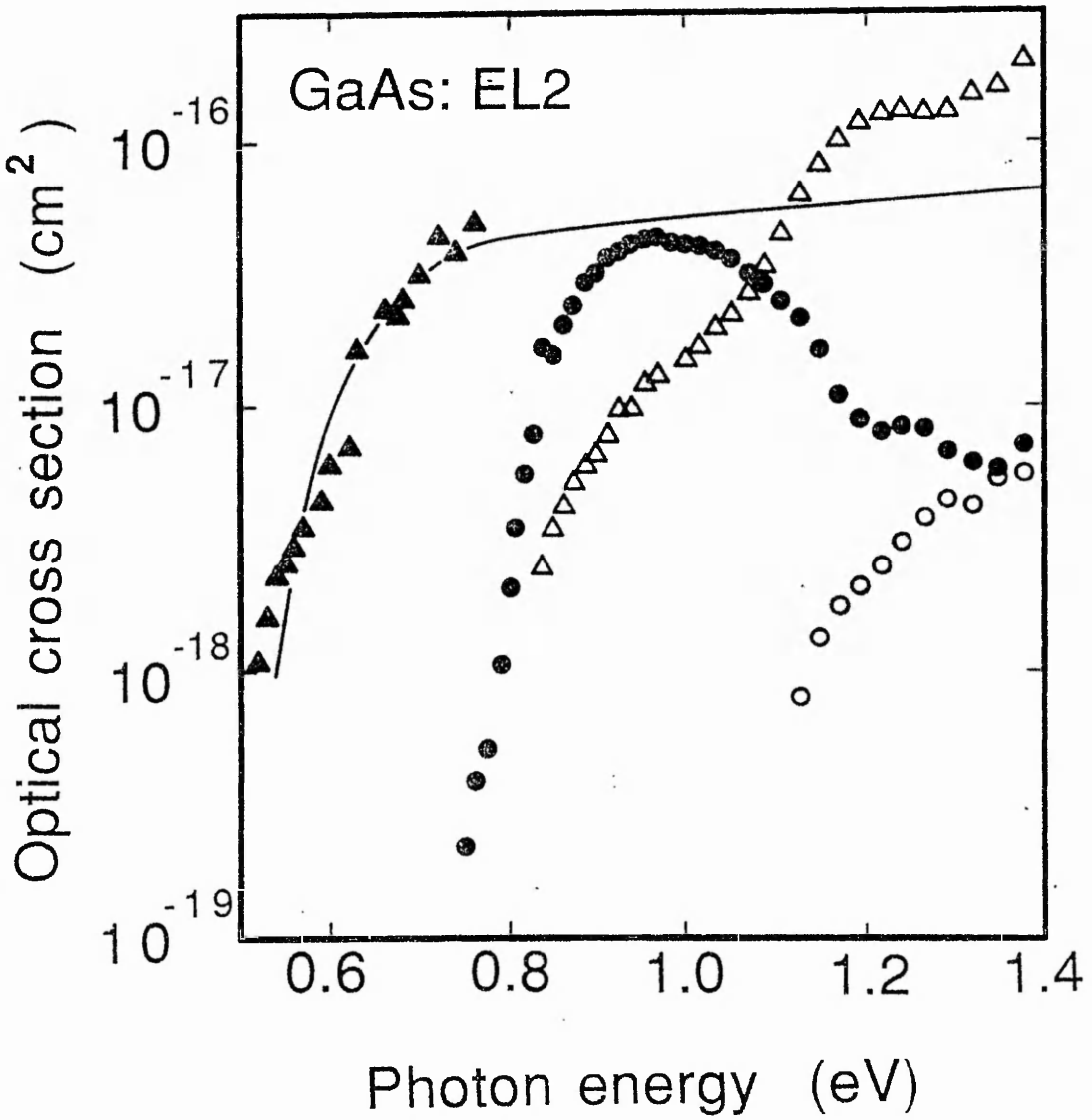

Fig.2.6. The variation with photon energy of the electron and hole photo–ionisation cross–sections for both EL2 levels ($EL2^{+/o}$ and $EL2^{++/+}$). Open triangles represent the electron optical cross–section for $EL2^{o}$(at 78K); filled circles, the hole optical cross–section for $EL2^{+}$(at 78K); open circles, the electron optical cross–section for $EL2^{+}$ (at 150K); and filled triangles, the hole optical cross–section for $EL2^{++}$ (at 85K). Also included are results on the optical cross–section of p–type material (Lagowski 129). Taken from the work by Silverberg et al (220).

(221) who calculated that the calibration factor for room temperature and 1.06μm light, should be increased from Martin's value of $1.25x10^{16}$ to $2x10^{16}cm^{-3}$.

2) Several groups have shown that the absorption coefficient in their material is not proportional to [EL2] as measured by DLTS (Yahata 147, Ishida 223, Tajima 224). This result, if universally correct, invalidates the use of the NIR absorption coefficent for the evaluation of [EL2]. However, it is to be noted that DLTS can be a problematical technique and various precautions must be taken if the results are to be beleived. In addition more information on the GaAs samples used in these experiments is required before these results are regarded as being typical for "state of the art" undoped LEC GaAs. However it is important that this problem is solved soon, preferably by workers using several different sources of material.

3) There is a contribution from hole photo–ionisation of $EL2^+$ and hole and electron photo–ionisation cross sections for the double donor state (see above).

4) If EL2 is indeed a family of defects then the individual components may have different absorption cross sections. In this work we assume that EL2 is one defect.

5) The effect of scattering on the measured transmission: although present this is expected to be small and hence can be ignored (see section 2.3.4).

6) Absorption from other deep levels, in particular those antisite defects in plastically deformed and irradiated material which are non bleachable or deep–level transition–metal impurities. (see section 2.3.5)

7) Variation of refractive index and reflectivity (R) with wavelength: this gives an error in the background transmission which is taken at 2μm and often assumed to be the same at 1μm. The reflectivity changes from 0.29 to 0.31 between these two points (Blakemore 225) giving an error (from changes in $(1-R)^2$) of approximately 5.8% in the assumed background transmission.

8) Absorption by electronic states associated with dislocations: this is likely to be important in the near band gap region (Bahzhenov, 226).

2.3.4 EL2 distribution.

The conventional view of the distribution of NIR absorption in GaAs is that of a fluctuating concentration of EL2 compensated by a uniform residual concentration of shallow acceptor impurities, usually carbon (Alt 227, 228). The nature of the distribution will be discussed in three parts. The first will deal with the seed to tail distribution of EL2, the second with the macroscopic distribution across a slice and the third will deal with microscopic fluctuations on the scale of dislocation cell structure. Following this the distribution of NIR absorption in In–doped material will be discussed and finally a other models which could give the observed NIR fluctuations assuming a near constant [EL2] and changes in other defects will be described.

Seed–Tail variations.

The axial seed–tail variation of [EL2] in a wafer is apparently not directly related to dislocation density but more to the melt composition (Katsumata 229). Hence, with As–rich melts, the [EL2]

increases towards the tail and with Ga–rich melts, it decreases towards the tail, whereas the dislocation density tends to increase towards the tail in both cases. There will also be an effect due to post growth thermal history as the tail end will cool faster than the seed (Holmes 230). In addition the distribution will be affected by the pulling rate and the magnetic field strength, if present (Kimura 100, Katsumata 229).

Radial variations.

At the seed end of the crystal the radial variation of EL2 tends to follow the form of the macroscopic dislocation density, giving the characteristic "W" shape distribution seen in most undoped LEC crystals (Martin 231). Absolute maxima are found at the edge along d and absolute minima at about 0.6 of the radius along n . At the tail end of the crystal, the EL2 concentration often does not follow the dislocation density variations. Both distributions are not neccesarily "W" shaped (Holmes 232). It has been noticed that slices taken from the seed and tail ends of an ingot can often give a misleading impression of the majority of wafers taken from in between (Dobrilla 233).

Kuhn and Sigmon (235) noted the correlation between the EL2 distribution and predicted thermal stress patterns and suggested that the formation of EL2 may be by some stress enhanced mechanism. The stress field could generate an electric field in the crystal which interacts with defects (probably interstitials) causing diffusion and subsequent non–uniform formation of EL2.

Holmes and Chen (234) proposed that the distribution of EL2 comprised of a constant level, determined by melt stoichiometry, with a superimposed distribution (usually w shaped) from either stress enhanced production of EL2, dislocation climb or gettering of EL2. The authors favoured the gettering model for the production of the microscale variations and the climb model for the macroscopic "w" shape distribution. The seed to tail variation of the radial distribution would be determined by a change in the constant [EL2] level by changes in melt stoichiometry, plus the differing post growth thermal history of different parts of the ingot, in which the tail end cools faster, reducing gettering and climb (Holmes 230).

Microscopic variations.

On a microscopic scale, EL2 fluctuations always follow the dislocation structure in as–grown crystals. In particular, cell walls and lineage features display high concentrations of EL2. Some lineage features, with high [EL2], are surrounded by extended denuded zones (or EDZ's), which display a low [EL2] (Stirland 052). The correlation of EL2 with dislocations can be removed by various annealing treatments (This will be discussed further in section 2.4.2).

Various models have been suggested for fluctuations of EL2 on a microscopic scale. Weber (063) and Stirland (236) independently proposed a dislocation climb model for production of EL2. Mechanisms for the production of EL2 by climb have also been given by Figielski (205, 237, 238). Alternatively Brozel and co–workers (Brozel 062) proposed a gettering model.

Examination of slip bands (Alt 239, 240) has show that peak concentrations are associated with local drops in the "background" [EL2], supporting the gettering model for microscopic fluctuations. This was backed up by Dobrilla and Blakemore (241) who found that [EL2] at the cell centre and cell wall displayed the same macroscopic variations, again consistent with the

gettering model but not the climb model. This was further supported by a combined etching and NIR absorption study (Dobrilla 242) which show a three zone structure to large cells; indicating that EL2 had been gettered by the cell walls from the outer region of the cell interior, but not from the cell centre.

NIR absorption in In–doped material.

A "U" shaped radial variation of EL2 has been seen in dislocation free In–doped crystals (Miyairi 243, Katsumata 244). This proves that some mechanism other than dislocation climb or gettering is operating here, and probably also in undoped crystals. The stress enhanced model would not explain these results as it would predict a "w" distribution. The effect is probably due to changing stoichiomety of the melt as growth proceeds along with a non–planar growth front.

Not all In–doped crystals are dislocation free. In these crystals, the EL2 distribution follows that of the dislocations on a microscopic scale, as in undoped material. In particular, the effect of axial single dislocations can be investigated, where groups of isolated grown–in dislocations are often seen. The effects of lineage can also be investigated at the edge of the sample, where slip dislocation are seen, but with lower densities and with less complicated interactions than in undoped material. Hence low dislocation density In–doped material provides an excellent research tool for the study of dislocation effects on local defect distributions.

Other models for NIR absorption fluctuations.

Various groups have questioned the model of fluctuations in NIR absorption being due to fluctuations in [EL2]. Other models for the distribution include the following:

1) A near constant [EL2] with a non–uniform acceptor distribution, based on the mapping of both charge states of EL2 (Skowronski 164, Bray 245, Kuma 246, Windscheif 247, Heinemann 248, Spaeth 249 and Asom 250).

2) The variation of native donors shallower than EL2 (Walukiewicz 251, Abernathy 252), which alter compensation. This cannot happen universally as some GaAs often has a total [acceptor] which is less than the fluctuations seen in [EL2°].

3) The variation of impurity concentrations and hence a variations in $[N_A–N_D]$. This model is unlikely as the magnitude of fluctuations of [EL2°] usually exceeds the total concentrations of shallow impurity levels.

4) The EL2 absorption is uniform and that variations in transmission are due to a large non–uniform scattering contribution. This model was suggested by Fillard et al (Fillard 253, Castagne 254, 255, Gall 256), based on the evidence that very little of the non–uniform "absorption" photo–quenched at 77K. Unfortunatly as pointed out by Skolnick et al (257, 258), EL2 does not bleach completely at this temperature. The sample transmission is uniform in the same samples after photo–quenching at 4K. It follows that the model is erroneous. The contribution of the non–uniform scattering component to the infra–red transmission has not yet been measured but is clearly insignificant in this case.

2.3.5 Other near–infrared absorption.

Both plastically deformed material and irradiated material, display non–bleachable absorption which is related to As_{Ga} antisites but clearly not to EL2. This could be relevant to the idea of the EL2 family as discussed in section 2.3.1. In particular, to the assignment of EO1 to EL2, when EO3 is the only level which correlates with the NIR absorption (Yahata 147). In the work descibed in this thesis, the contribution of As antisites, EO3, ELO or any other members of the EL2 family which do not have bleachable absorption are assumed to be insignificant, as material grown in the same way in the past has shown no significant absorption after bleaching.

The spectral form and magnitude of the optical cross section of EL6 at 77K is very similar to that of EL2 (Chantre 128). As optical measurements were carried out at room temperature where EL6 would be thermally ionised, this contribution can be ignored.

The material in this work contained no deliberate additions of chromium or other transition metal impurities and their contribution to the optical cross section can be ignored. However, in general, if the GaAs is doped with chromium or any other impurity which introduces deep levels then Their optical cross sections must be considered. Optical cross sections for chromium and copper were given by Chantre and Bois (128).

2.3.6 Scattering

Katsumata et al (259) investigated precipitates in crystal grown from different melt compositions. The scattering was shown to be of Rayleigh type and the scattering centres were always found to be associated with dislocations. The scatterers were divided into the following three types according to their behaviour under light of different polarisations:

1) Large As precipitates in As–rich material.

2) Small As clusters (possibly related to clusters of EL2) in As–rich and stoichiometric material.

3) Large Ga precipitates in Ga–rich material.

Scattering intensity increases as the material becomes more As–rich and is strongly reduced (often to zero in some areas) for growth under a strong magnetic field (Katsumata 260).

The distribution of scattering centres nearly always follows the dislocation cell structure and lineage (Suchet 069, Castagne 254, Gall 256, Katsumata 260, Ogawa 261, 262, Moriya 263, 264). In addition, the 3–D distribution of scattering at cell walls has been demonstrated by Kuma et al (265). Scattering in In–doped material is also associated with dislocations; in particular, with the threading dislocations at the center of the crystal (Ogawa 262, 266, 267, Moriya 263)

The contribution of scattering to NIR transmission images was shown to be negligible (Skolnick 257, 258) for the optical equipment which is standard for mapping [EL2].

2.4 Annealing and Defect Dynamics.

Post–growth cooling will be discussed briefly in section 2.4.1. Section 2.4.2 is concerned with high temperature (T>700°C) bulk anneals, followed by a slow cool to room temperature. Wafer

anneals will be discussed briefly in section 2.4.3 and anneals with fast cooling rates or quenches will be discussed seperatly in section 2.4.4.

2.4.1 Post growth cooling.

The post growth cooling curves for various parts of the crystal during LEC growth was discussed by Holmes et al (230). In particular, the tail end of the crystal cools much faster than the seed and the degree of thermodynamic versus kinetic control, of defect formation and diffusion, will be different in these regions.

It is desirable in LEC growth to make the rate of cooling low, to reduce thermal gradients and dislocation densities. However, this may give concentrations and distributions of defects which are undesirable. If a compromise is not possible, which is often the case, some form of post–growth heat treatment is required.

2.4.2 Standard bulk anneals.

There are several aims of post growth heat treatment: to increase the uniformity of various substrate properties and hopefully reduce variations in device properties; to stabilise the semi–insulating properties by the removal of native acceptors and donors other than EL2; and to reduce in–built stresses, which will result in less wafer breakage during cutting, polishing and processing.

The main recent investigations of bulk annealing of GaAs will be described below together with the optimum conditions (if any) discovered by each group. After the anneal the ingots were allowed to cool slowly to room temperature either by just turning the furnace off or by a programmed slow cool.

Rumsby et al (268, 269) investigated ingot annealing in the 650–1000°C temperature range for between 3 and 15 hours. They found that the optimum anneal was 950°C for 5 hours. Radial variations of resistivity and mobility could be reduced to less than 10%. Seed–tail variations in electrical properties were also reduced, the EL2 distribution was smoothed out and the dislocation distribution was unaffected in this temperature range. However some arsenic precipitation was seen at the tail end of a crystal after a 15hour 1000°C anneal. The 950°C 5 hour anneal will be taken to be the standard conventional anneal in this work.

Martin, Duseaux and co–workers (Martin 270 and 271, Duseaux 070) investigated anneals in the 700–1000°C temperature range for between 0.5 and 60 hours. They showed that there was usually an increase in both EL2 concentration and uniformity with time, for anneals over 700°C. The exception to this was the 800°C anneals where long anneals showed a decrease in homogeneity. The optimum uniformity was achieved for the 1000°C 15 hour anneal. All samples tend to same final value of [EL2] at same temperature which suggests a thermodynamically controlled mechanism for annealing rather than a diffusion mechanism.

Lohnert et al (272) investigated the effect of 1000°C anneals for between 3 and 30 hours and showed that the uniformity of various substrate properties was improved. They suggested that this was due to an increase in [EL2] along with an increase in its uniformity.

Wu et al (199) demonstrated the dependence of EL2 on As pressure during annealing (1000°C,

5 hour). All samples saturated at the same [EL2] at high As pressure. Those samples which were annealed under zero As overpressure displayed lower concentrations than this saturation value. Those with an initial value lower than the saturation value, displayed a monotonic increase with As overpressure, up to saturation. Those which displayed a higher concentration for zero As overpressure showed an increase up to a vapour pressure of about 1 atmosphere of As, followed by a steady decrease to saturation.

Obokata et al (273) demonstrated the effect of As over–pressure for 950°C, 16 hour anneals. The best uniformity of EL2 and resistivity was seen in the range 50–530 torr.

Improvement of uniformity.

The uniformity of the following properties has been demonstrated to improve by annealing:

1) NIR absorption (Duseaux 070, Holmes 230, Alt 239, Katsumata 244, Windscheif 247, Rumsby 268, 269, Martin 270, 271, Lohnert 272, Obokata 273, Inada 274, Abernathy 275)

2) Photoluminescence (Lohnert 272, Yokogawa 276, Noto 277, Obokata 278, Hovel 279, Mikoshiba 280, Koteles 281)

3) Cathodoluminescence (Lohnert 272, Sekiguchi 282, Dussac 283, Chin 284)

4) Resistivity (Rumsby 268, 269, Lohnert 272, Obokata 273, 278, Yokogawa 276, Otoki 285, Bonnet 286)

5) Mobility (Otoki 285, Bonnet 286)

6) Leakage curent (Bonnet 286, Matsumoto 287)

7) FET threshold voltage (Miyazawa 288, 289, Egawa 290, Packeiser 291)

8) FET pinch–off voltage (Yokogawa 276)

9) Lattice strain (Okada 024)

10) Photo–thermal reflection (Mikoshiba 280)

11) Photoconductance (Abernathy 275)

Effects of annealing on other native defects.

One of the key advantages of bulk high temperature annealing is the reduction of native defect concentrations, particularly donor levels shallower than EL2 (other than EL2). This ensures that the fermi level remains close to the EL2 level giving SI GaAs. Ogawa et al (292) demonstrated that 500°C anneals degraded electrical performance, mainly because of an increase of EL3 and EL6. The semi–insulating properties were retrieved by an 800°C anneal. Auret et al (293) have shown that annealing above 700°C reduces the concentrations of EL3 and EL6 (situated at about E_c–0.55eV and E_c–0.35eV respectively) whereas EL2 was stable. Kitagawa et al (142) showed using DLTS that In–doped as–grown n–type GaAs could be converted to SI GaAs by the removal of native donors (mainly EL6) other than EL2 after a 950°C 2 hour anneal.

Native donors and their interactions have been studied in irradiated material where their concentrations are higher and interactions occur, causing defect levels to overlap and giving rise to defect bands. The most important of these is the "U–band" of donor defects at about E_C–0.5eV. The U–band is seen to anneal at above 500°C (Martin 118). This is thought to be due

to an interaction between EL2 and another associated defect (Goltzene 203, Martin 294), perhaps EL6 (Samitier 295, 296, 297, 298). A similar annealing stage has been observed in positron annihilation studies (Dannefaer 019) and annealing of the arsenic antisite EPR signal in deformed or irradiated material (Weber 144, Omling 163). This indicates that a defect reaction with the As_{Ga} antisite occurs at this temperature.

Annealing of In–doped material.

The bulk annealing behaviour of In–doped material was studied by Osaka et al (191,558) who used 5 hour anneals between 800 and 1000°C. In–doped material was found to behave in a similar manner to undoped material when annealed; EL2 concentrations increased to much the same levels as in undoped annealed material. At the same time silicon activation was seen to increase and NIR scattering intensity decreased. The key result from In–doped GaAs is that EL2 concentrations rise even in dislocation free regions of the crystal (see also the results in section 6.4.2) This gives further evidence for some thermodynamic control of EL2 concentrations as diffusion effects of this magnitude are highly unlikely (see section 2.4.6). However the increase of EL2 through the dissolution of precipitates, as suggested by Osaka, is possible.

2.4.3 Wafer anneals.

An alternative to bulk annealing is wafer annealing before implantation. The uniformity improvements are much the same as for bulk annealing with the possibility of faster cooling rates due to smaller sample size. The disadvantages are the additional cost compared to bulk annealing, and the need for protection to prevent surface degradation due to As loss. In a comparative study of ingot and wafer annealing, Lohnert et al (272) concluded that wafer annealing was of negligible benefit.

Various methods are used to prevent As loss from the surface, the most common being annealing under As pressure, face to face annealing or the use of an encapsulant. The latter process is shown to give variable results in particular depending on the encapsulant or substrate used (Kuzuhara 301, Hasagawa 302).

With the rapidly increasing interest in the use of fast cooling rates to control material properties (see section 2.4.3), annealing processes with fast cooling rates, such as rapid thermal annealing or flash annealing may become more important. An additional advantage is the short annealing time and correspondingly low surface arsenic loss and defect diffusion lengths.

After ion–implantation all wafers are annealed to activate the implant. These anneals use much the same conditions as pre–implant homogenising wafer anneals. Post–implant activation anneals are reviewed by Blunt (011).

2.4.4 Quenching.

Recent experimental results have recalled an interest in anneals with fast cooling rates or "quenches". The use of fast cooling rates is an attempt to move defect formation from the regime of thermodynamic control to that of kinetic control. The results of the various groups involved will be discussed in turn below:

Stoakes and co–workers (Stoakes 303) annealed 5cm diameter 400μm undoped SI LEC samples in an ampoule at 950°C for 5 or 25 hours with different As overpressures. After the anneal, the samples were quenched by removing the ampoule into air. The samples remained semi–insulating after this treatment. The lattice parameter of the material was studied before and after annealing. From the changes in lattice parameter with time, after annealing, it was clear that some atomic re–arrangement was taking place, even at room temperature. Changes were noted after one day and had stabilised after about two weeks. For samples annealed for 25 hours with 1 atmosphere of As overpressure, and 5 hours at 2.5 atmospheres, a strong dilatation of the lattice is seen. Whereas, the sample annealed for 25 hours with 2.5 atmospheres showed a slight contraction.

Lagowski and co–workers (Lagowski 304, Kang 305) annealed small (10mmx10mmx5mm), GaAs samples in an ampoule at between 1100 and 1200°C for 6 to 10 hours, under equilibrium As pressure (to prevent surface degradation). The samples were of conventional SI HB (lightly Cr–doped), lightly doped n–type conducting LEC (for DLTS studies), and undoped SI LEC material. The anneal was followed by a quench which consisted of removing the sample ampoule from the furnace and placing it in water at room temperature. The SI samples had converted to conducting p–type after the quench whilst the conducting n–type crystals retained this state. DLTS showed that the [EL2] had dropped from $2x10^{16}$ to $1x10^{15}$ cm^{-3} in all samples. A near removal of the characteristic absorption spectra and ZPL occurred in the n–type material, indicating that the EL2 had been destroyed (Lagowski 304). The p–type converted material then exhibited what the authors termed Inverted Thermal Conversion (ITC); during subsequent annealing at 850°C for 30 minutes, it recovered its n–type SI properties and as–grown [EL2]. By altering the time and temperature of the subsequent anneal the degree of compensation of the EL2 could be tailored as required (Kang 305). In particular, the theoretical maximum in resistivity of 10^9ohm.cm at near 80% compensation could be achieved for substrates, after ion implantation into the ITC material. In addition, dislocation–free material remained dislocation–free and conventional material retained a constant dislocation density during the heat treatments. Also, ITC GaAs was found to have the same activation efficiency as conventional material after ion–implantation.

Ford and co–workers (Ford 306, Look 307), grew low pressure LEC ingots of about 75mm diameter and 50 to 125mm length. The ingots were annealed at 950°C for 5 hours, in a sealed evacuated quartz ampoule. Following this, the ingots were either quenched by removing the ampoule from the furnace to cool in air, or cooled slowly by turning the furnace off and allowing the ingot cool, to room temperature, in–situ. The as–grown crystals displayed n–type behaviour with variable resistivity and mobility. After a quench they were universally n–type, with high resistivity and high mobility. After a subsequent anneal and slow cool, the samples retained their high mobility but became conducting n–type. The samples could be cycled, from SI to conducting, by repeating these quench and slow–cool cycles. Analysis of the samples, using PL and temperature dependent Hall effect measurements, show that this conversion phenomenon is controlled by native acceptors. Both quenched and slow–cooled material contain EL2 and other native donors, but the quenched material also contains native acceptors in greater

concentrations than the native donors. Hence the fermi energy is pinned at the EL2 level in quenched material. In the slowly cooled material the native acceptors, which are thermodynamically unstable, are not seen and the fermi energy is pinned at the native donor levels (Look 307). The standard deviation of the pinch–off voltage for FETs was seen to be improved for the quenched material over the as–grown material (Ford 306).

Von–Bardeleben et al (125) annealed lightly n–type silicon–doped HB slices (presumably of approximate dimensions, 50mm diameter and 350μm thickness), at 850°C for 10 minutes, with a Si_3N_4 cap. This was followed by a quench, consisting of removing the samples from the oven and allowing them to cool in air. This results in a very fast, uncontrolled cooling rate, as the sample is not contained in near vacuum conditions in an ampoule, as with all of the other quenching results presented here. The primary results from this treatment are as follows: the As_{Ga} antisite concentration (measured by EPR) is unchanged but now does not show the photoquenching behaviour characteristic of EL2. The surface [EL2] measured by DLTS is reduced from 0.5–1x10^{15}, to 0.5–5x$10^{14}$$cm^{-3}$. Subsequent anneals at low temperatures (90–150°C) are seen to regenerate both surface [EL2] and the characteristic photo–quenching behavoir of the As_{Ga} antisite.

Kitagawara et al (308), annealed slices of 50mm diameter In–doped, lightly n–type, conducting, dislocation free material. The anneal was at 950°C, for 2 hours, followed by an undefined fast cool with an estimated cooling rate of 100–200°C/min. This treatment caused the crystal to convert to SI behaviour. A further anneal of 450°C for 100 hours caused the return of conducting behaviour. This behaviour was studed by DLTS and was seen to be due to the removal and re–introduction of native donors, during the quench and reanneal respectively.

Kazuno and co–workers (309) used a similar quenching procedure to Lagowski except that the As pressure was varied and the samples of dimensions 5x5x25mm were lapped and etched (to 4x4x24mm) after the quench. The material exhibited p–type conversion after the quench. Using EPR, the [As_{Ga}] was found to decrease in a similar way to the [EL2] in Lagowski's work. However, lightly doped conducting n–type material also exhibited p–type conversion, indicating the creation of over $10^{16}cm^{-3}$ acceptors during the quench. Increasing As pressure stongly suppressed the creation of acceptors and slightly suppressed the destruction of EL2.

Asom et al (250), annealed samples (5x5x10mm) of n–type HB crystals grown from different melt–compositions. Anneal temperatures were 850, 950 and 1050°C, with As over–pressures of 1.0, 2.2 and 4.4x10^{-4} atmosphere, respectively. Anneal times varied from 30 minutes to 192 hours. The anneal was followed by a fast cool in air (at about 30°C/s). Measurements were taken from the centre of the samples to eliminate surface effects. The treatments showed a two stage process. The first stage was a rapid removal of acceptors (which occured for up to about 1 hour at 950°C). The second stage was a slow introduction of acceptors. The first stage was seen to be more dominant at low temperature and in Ga–rich material. It was speculated that the acceptors which were removed and those which were introduced were the same defect. It was postulated that the initial decrease was due to defect homogenisation, whilst the slow introduction,

occured at all times.

Sekiguchi and co–workers (282) annealed silicon–doped (at about $10^{16}cm^{-3}$) samples to investigate the effect on CL uniformity. Heat treatments were at 650, 750 800 and 1050°C for 24 hours followed by a quench of about 1000°C/minute. No sample size was given but samples must have been small as the cooling rate given is very rapid. The CL uniformity was improved for quenches from 750°C and above. The CL contrast was "homogenised" by the quench from 1050°C but as–grown distributions were restored by a subsequent anneal above 700°C with a slow cool.

More recently, Lee and co–workers (077) annealed SiO_2 encapsulated as–grown HB samples ($10x10x25mm^3$) and plastically deformed, high dislocation density, HB samples ($4x4x8mm^3$). Anneal temperatures were in the range 500–900°C for 1, 2, 24 or 72 hours. Quenching was achieved by removing the encapsulated samples from the furnace into air. In addition, an even faster quench was achieved by dropping one of the smaller samples directly from the furnace into an oil bath! The authors used these heat treatments to investigate As precipitate formation in GaAs. They concluded that precipitate formation depends critically on the sample cooling rate and on the number of nucleation sites (dislocations). These results will be discussed in more detail in section 2.4.5.

One important factor in quenching studies is the true cooling rate of the sample. This is obviously strongly dependent on the sample geometry and the mechanism of quenching. A second is the electrical stability of the sample to implant processing which involves an anneal usually equivalent to several minutes at 850°C.

The quenching of GaAs, and the relevance of these papers, will be discussed further in section 7.4.

2.4.5 Precipitates and annealing.

A study of the effect of annealing temperature and duration on precipitate formation was made by Suchet et al (Suchet 069). They used A/B etching and high resolution infra–red scattering tomography to investigate precipitates (previously identified as pure As or As–rich) in various types of GaAs. This study included Ga–rich crystals and dislocation free regions of In–doped cystals with initially no observable precipitates. With one exception, all crystals used (As–rich, stoichiometric, undoped, dislocated In–doped) showed the typical dislocation associated "network" arrangement of precipitates. The exception was an LEC crystal which had been quenched after growth. This displayed a low density of isolated precipitates. Anneals were carried out at 700, 800, 900 and 1000°C for 0.5, 3, 15 and 60 hours. The primary scattering results after 900 and 1000°C, 60 hour anneals were as follows:

After the 900°C anneal the Ga–rich material displayed a low intensity network pattern, the In–doped material (both dislocated and dislocation free) was unchanged. All other samples displayed a high density "milky way" pattern which was composed of a network of bright dots, superimposed on a background of large numbers of homogeneously distributed dots of lower intensity.

After the 1000°C anneal the Ga–rich material again displayed a low intensity network pattern, the In–doped material was unchanged and all other samples displayed a network pattern.

The A/B etching results on the density of precipitates were as follows:

No precipitates were observed for Ga–rich material and dislocation free regions of In doped material. The density of precipitates in dislocated regions of In–doped material was unchanged by the anneal.

No precipitates were seen in the quenched sample before anneal or after a 1000°C anneal but a low density was seen after a 900°C anneal

For the other samples the density of precipitates was increased by the 900°C anneal but reduced by the 1000°C anneal compared to the as–grown condition. The precipitate density was higher for the As–rich material than the stoichiometric material.

In addition the surface relief of the A/B etched samples was studied using a Talystep probe, with the following results:

Dislocations etched as ridges with a groove in the centre assumed to be associated with precipitates or impurity decoration.

Low temperature anneals (700 and 800°C) caused an increase in dislocation etch relief interpreted as increased gettering of impurities.

Increasing the time of a 900°C anneal causes an increase in the depth of the groove. This was interpreted as precipitates on the dislocations trapping impurities, introducing large electrical inhomgeneities in the lattice and a corresponding large etching profile.

At 1000°C dislocation profiles decrease with time indicating a more homogeneous distribution of impurities.

The authors concluded that precipitate formation occurs at about 1000°C and that between 950 and 800°C there is a strong interaction between the precipitates and the surrounding impurities in the lattice.

A more recent study of the effect of annealing on precipitates and As–rich dislocation loops in as–grown and plastically deformed (highly dislocated) GaAs was carried out by Lee et al (077). They carried out heat treatments, followed by quenches, as described in section 2.4.4 above. The main results of their study were as follows:

As–rich dislocation loops and precipitates were no longer observed in material after long term anneals above 700°C, but were observed after short term anneals of up to 800°C.

[EL2] increases for anneals above 600°C, with a maximum increase at about 800°C. This was assumed to be due to the dissolution of As precipitates.

The formation of point defects, is favoured by a fast cooling rate. A slow cooling rate will give precipitates (or dislocation loops in dislocation free regions).

All of the samples which were plastically deformed, to give higher dislocation densities, contained precipitates after quenching. Even the sample which was very rapidly

quenched by dropping into an oil bath.

They concluded that precipitate formation occured at between 600 and 700°C when the material cools through the retrograde solidus. Precipitation will only occur if the cooling rate is resonably slow and if dislocation nucleation sites are available.

Other investigations on the effects of annealing on the scattering intensity from precipitates in In–doped material have given contadictory results. Osaka et al (299, 300) observed a drop in precipitate scattering intensity for 5 hour, 800 to 1000°C anneals. Otoki et al (285) noticed an increase in scattering for 850°C anneals from 6 hour to 48 hour duration. Yamada et al (075) demonstrated that below 1000°C the precipitate size was strongly affected by the cooling rate.

2.4.6 Defect dynamics and diffusion.

This section contains a short review on the diffusion rates of defects in SI GaAs and the temperatures at which they become mobile. This information has relevance to defect models and annealing results. In particular, the quenching of GaAs from high temperatures can give defect concentrations which are not thermodynamically stable; the subsequent annealing temperatures can give information on the nature of the defects involved.

Firstly it should be noted that atomic self–diffusion in GaAs is very slow. For As self diffusion, the diffusion depth is only about 0.5μm after 24h at 1025°C (Palfrey 310). Ga diffuses slightly faster giving a diffusion depth of 1μm for the same conditions (Palfrey 311). The associated activation energies for As and Ga diffusion are 3.0eV and 2.6eV respectively.

Newman et al (312) have reported information on the mobility of point defects in irradiated material. As vacancies are mobile at 200°C, Ga vacancies at 300°C and As interstitials at temperatures as low as 100K in intrinsic or p–type material.

Pons and Bourgoin (027) have studied the annealing of radiation induced defects. They concluded that the As Frenkel reaction dominates defect production. All traps anneal with about the same activation energy 1.5 to 1.7 eV. Hence, it was postulated that all are limited by the mobility of the same defect, the As interstitial. The different annealing temperatures (230K, 280K and 500K) are thought to be due to different defect interactions and defect separations.

Several defect annealing stages are observed at around 500°C. Examples include: the annealing of the U band (Martin 119); the annealing of the deformation or radiation induced antisite EPR signal (Weber 144, Omling 163); and the annealing of vacancy–like positron annihilation signals (Dannefaer 019). This annealing stage is thought to be associated with the splitting of defect pairs or perhaps even the destruction of isolated As_{Ga} antisites probably by reaction with another point defect.

For temperatures above 850°C, EL2 related signals, in particular the EL2 related EPR antisite signal, anneal.

Chin et al (284) have seen diffusion fronts 200μm from the surface of wafer annealed material (at 550°C for 4 hours) using CL. They were not seen when an encapsulant or As overpressure was used with the anneal. This very high rate of diffusion is difficult to explain considering the low self diffusion rate of Ga and As, and may have been due to a contaminant. Similar high diffusion rates were observed by Ding et al (313) again using CL. They back damaged a wafer

(bead blasted) to getter defects from the front surface. Dislocation enhanced diffusion was sugested as a possible mechanism.

Diffusion of impurities.

For imformation on the diffusion rates of various impurities in GaAs see the INSPEC publication "Properties of gallium arsenide" (314). It should be noted that diffusion rates for some transition metal impurities can be very fast. In particular, chromium (which is commonly used as a dopant to give SI properties when donor impurity contamination is high) and copper, which can be a contaminant in quartz crucibles used for annealing experiments (Tin 315), are rapidly diffusing species.

2.5 Electrical Properties and Compensation.

The "conventional" view of compensation in SI GaAs is of the deep donor level EL2 compensating the net shallow acceptor concentration (mainly carbon) which is left after conpensating the smaller concentration of shallow donors. That is:

$N_{EL2} > N_{SA} > N_{SD}$

Where N denotes the concentration and the subscripts correspond to EL2, shallow acceptors and shallow donors respectively. The dominant acceptor is usually carbon, in the 10^{15}–$10^{16}cm^{-3}$ range. The dominant shallow donors are silicon or sulphur, usually in the low $10^{15}cm^{-3}$ range. All other impurities in the material are usually below $10^{15}cm^{-3}$ with the total concentration rarely exceeding a few $10^{15}cm^{-3}$. This compensation model is illustrated by a Shockley diagram in fig.2.7. It has been used to calculate the expected electrical properties of GaAs with different defect concentrations (Martin 316, Johnson 317). The model can be used to explain the variation of electrical properties with changes in carbon concentration (Holmes 031, Baumgartner 087, Chichibu 318) and changes in [EL2] with stoichiometry (Holmes 031, 032). Additional evidence for the validity of this compensation scheme was provided by Elliott and co–workers (035), who demonstrated that the EPR signal of the compensated, EL2 related, As_{Ga} antisite correlated with carbon concentration.

2.5.1 Impurities involved in compensation.

Impurity types and concentrations found in various types of GaAs have been reviewed by Clegg (319) and Brozel (320). However, it should be pointed out that their data refers to pre–1980 material. Recently, raman scattering results (Wagner 321) have indicated that zinc acceptors may be important in more recent material, especially in samples with low carbon concentrations. The main shallow donors are silicon and sulphur. The main deep level impurities seen in GaAs are chromium, iron, copper and manganese, all acceptors.

2.5.2 Native defects other than EL2 involved in compensation.

Native donors:

There have been several reports of compensation by native donor defects, shallower than EL2, in as–grown GaAs. These include compensation by a donor at 0.13eV (Ford 306, Look 307), at 0.22eV (Hunter 322), at 0.33eV (EL6: Kitagawara 142, Ogawa 292), at about 0.4eV (possibly

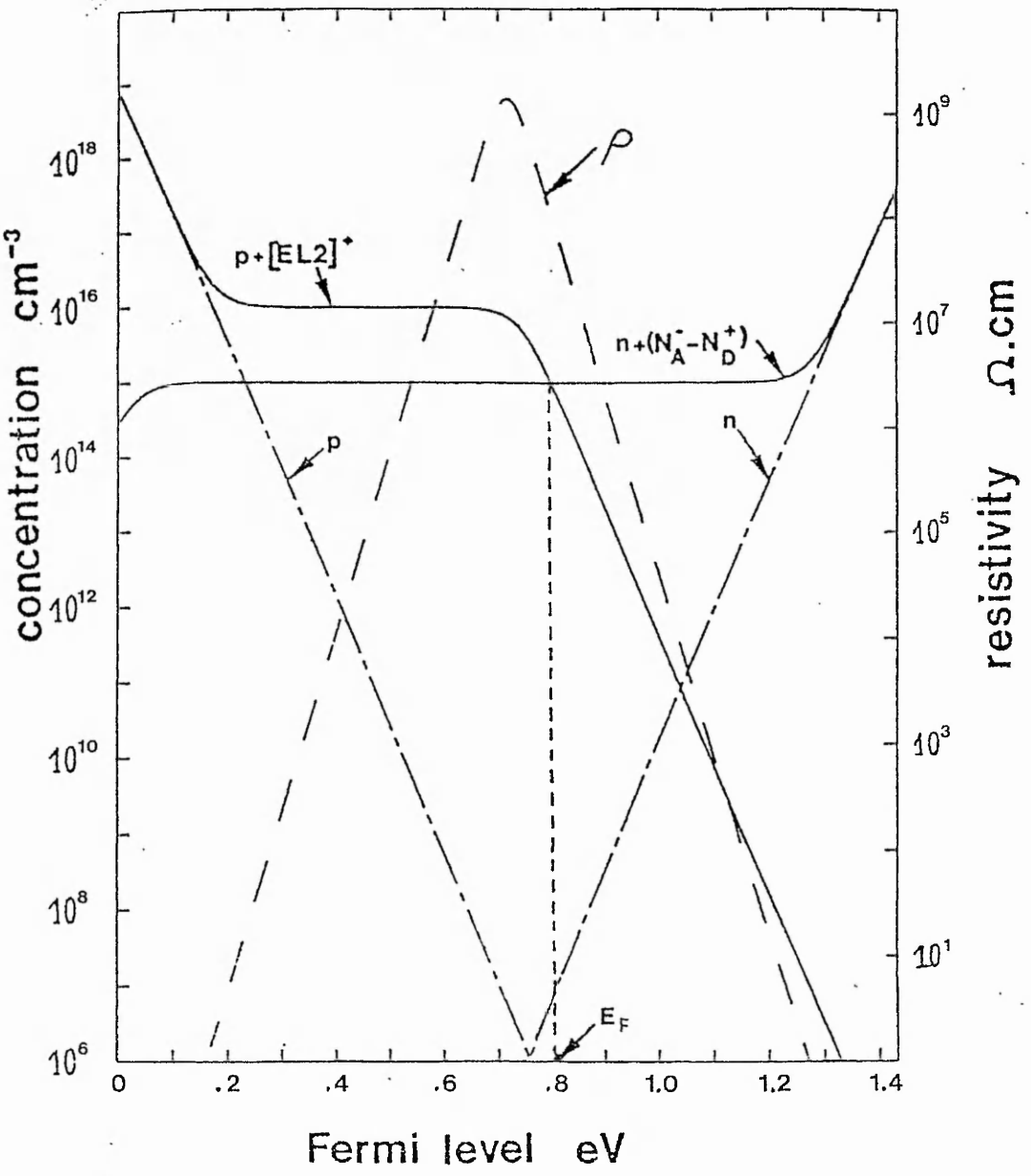

Fig.2.7. Shockley diagram for [EL2]=10^{16}cm^{-3} and [N_A-N_D]=10^{15}cm^{-3} (at 23°C).

EL5: Ikuta 323, Young 324) at about 0.6eV (EL3: Ogawa 292, Hunter 322) or with no reported activation energy (Hunter 083, Walukiewicz 251).

In addition, Walukiewicz et al (189) identified a native shallow donor at 20–30meV as a second donor state of EL2. This has strong implications for compensation scheme in SI GaAs as the residual acceptor would have to exceed the [EL2] concentration but be less than twice this concentration. This identification was disputed by Hunter (322) and is unlikely to be correct as these concentrations of acceptors have not been seen in SI material.

Native acceptors:

The effects of native acceptors on compensation in GaAs have been indentified by many groups working on a wide variety of materials (Skowronski 164, Kuma 241, Bray 245, Windscheif 247, Heinemann 248, Spaeth 249, Ikuta 323). In addition to as–grown material, acceptors have been created in material which has been quenched (Asom 250, Ford 306, Look 307, Kazuno 309). The main acceptor identified in as–grown GaAs is the "A" centre (or 78meV/203meV double acceptor) which is usually seen in p–type material (Mitchel 325, Moore 326, Wagner 327). However, an acceptor level of this energy was recently seen in quenched material (Ford 306, Look 307). Another group demonstrated the presense of an acceptor, at an energy of about 3meV, in quenched material (Asom 250). Other workers have shown the presence of deeper native acceptors (Kuma 241, Kazuno 309, Ikuta 323).

2.5.3 The stoichiometry dependence of compensation.

Holmes, Elliott and co–workers (Holmes 031, 032, Elliott 033, 034, 035, 036) produced considerable data on the stoichiometry dependence of electrical properties and the concentrations of the "A" centre and EL2. Their results were summarised in fig.2.2. At a critical As mole fraction of 0.475 the resistivity displayed a sharp increase, the carrier concentration displayed a sharp drop and the mobility increased by an order of magnitude. In addition, the dominant defect in the material changed over from the "A" centre to EL2 at this composition. This data was recently re–analysed by Walukiewicz et al (140) who concluded that the sharp drop in infra–red absorption below an arsenic composition of 0.5 was due to compensation of EL2 not a decrease in [EL2]. Taking into account the hole cross section of compensated EL2, they concluded that EL2 displayed a linear decrease with decreasing As mole fraction, giving [EL2] $>10^{16}cm^{-3}$ instead of near zero at the critical composition (0.475).

Ta et al (328) investigated the change in the thermal stability of GaAs of various stoichiometries after annealing. Unlike Holmes they found that the critical compositions for resistivity and mobility were found at different values (As mole fractions of 0.47 and 0.50 respectively). They also found that material with initial high mobility was thermally stable under 860°C wafer annealing but the more Ga–rich material with initial high resistivity and low mobility was not stable. The thermal conversion was demonstrated to be due to a reduction in surface [EL2]. This behaviour was also seen by Baumgartner et al (086).

2.5.4 Compensation mechanisms in other SI GaAs.

Genrally the compensation mechanism for undoped LEC material is the same as for GaAs grown by various other methods. Undoped SI material results provided the silicon

contamination level is less than the net acceptor concentration. This is the case for In–doped LEC GaAs (Osaka 098, Hobgood 111), with or without a magnetic field (Osaka 098), HEM GaAs (Wohlgemuth 329), HB GaAs (Parsey Jr 042) and VGF GaAs (Clemans 108). However LEF GaAs is not controlled by EL2 but by a deep donor at E_C–0.65eV (Mo 097), HGF by a donor at E_C–0.46eV (Abernathy 252) and a contradictory report of VGF controlled by a donor at E_C–0.54eV (Abernathy 252).

2.6 Implantation and Device Results.

2.6.1 Ion implantation.

A discussion of this topic is beyond the scope of this thesis. For more information on the ion–implantation process for SI GaAs substrates see the review of ion–implantation and post–implant annealing by Blunt (011), and references therein.

2.6.2 Device uniformity.

This review will ignore processing effects on device yield (which are likely to be important if not dominant: Koyama 013, McGuigan 330), and will only examine those variations caused by substrate properties. The parameters most commonly used to measure device uniformity are the threshold voltage (V_{th}) and the saturation drain–source current (I_{DSS}). Factors affecting the uniformity of these parameters are:

for V_{th}:

EL2 (Johannessen 331, Inada 247, 332, Fujisaki 333, Dobrilla 334, 335)

Dislocations (Miyazawa 288, 289, 336, 337, 338, 339, 400, Nanishi 341, 342, 343, Ishii 344, 345)

Carbon (Chen 346)

Lattice strain (Takano 347)

Substrate orientation (Deconinck 348)

Striations (Fujisaki 349)

for I_{DSS}:

EL2 (Johannessen 331, Dobrilla 335)

Dislocations (Nanishi 341, 342, 343)

The association of local fluctuations of V_{th} with dislocations was questioned by various workers who found no correlations between these two parameters (Winston 350, 351, 352, Yamazaki 353). In fact, Winston et al (352) reported that their most uniform substrate had a high dislocation density of $10^5 cm^{-2}$. Other workers did find a correlation but suggested that it was due to an indirect effect. This indirect effect could include the association of EL2 with dislocations (Dobrilla 334, 335) or a generalised As–rich defect atmosphere around dislocations (Miyazawa 288, 289, 336). The electrical effect of EL2 on V_{th} was modelled by Anholt and Sigmon (354).

The correlation of device properties with dislocations or defect distributions is further complicated by the ingot and wafer annealing processes used to improve substrate uniformity. The effect of dislocations has been shown to be removed by annealing (Miyazawa 289, 337); although for wafer anneals this sometimes depends on the type of encapsulant used, or the As over–pressure (Egawa 290). Inada et al (332) demostrated that annealing can improve V_{th} uniformity for dislocated GaAs but not for dislocation free In–doped GaAs. For Cr–doped material, the V_{th} distribution was seen to form two clusters of values (Kasahara 355). Uniformity was improved by the removal of one of these clusters after annealing. Fluctuations in V_{th} in the remaining cluster were associated with dislocations whereas within the annealing removed cluster, no correlation was seen.

Miyazawa and Hyuga (340) concluded that there were three regions of dislocation effect, the magnitude of the effect, for a particular region, increasing with proximity of the dislocation. The region above 50–60μm from the nearest dislocation etch pit showed no correlation. The region down to 30μm showed a moderate drop in V_{th} with proximity. The region below 30μm showed a higher magnitude of V_{th} drop with proximity. The weakness of this analysis is that it only takes into account the nearest dislocation and not all nearby dislocations. This fault was rectified in the model used by Suchet et al (356), who defined an influence zone for dislocations. They found a very good fit between the distribution of overlapping influence zones and V_{th} fluctuations on a local scale. It is the opinion of this author that this kind of statistical treatment must be carried out if dislocation effects are to be investigated sensibly. The weakness of the model at present is that it assumes all dislocations behave in the same way and also that the dislocation distribution does not change significantly, within the region under the surface, in which they influence V_{th}.

The material dependence of threshold voltage standard deviations compared to "standard" undoped material, is summarised below:

The standard deviation is high in Cr–doped GaAs (Packeiser 291, Kasahara 355).

The standard deviation is lower in VGF GaAs (Reynolds 109).

The standard deviation is lower in In–doped material (Miyazawa 288, Packeiser 291, Mcguigan 330, Nanishi 341, Yamazaki 353, Kuwamoto 357, Schink 358, Maluenda 359, Hunter 360, Rocher 361).

The standard deviation is lower in MLEC In–doped compared to standard In–doped GaAs (Terashima 101).

In conclusion, In–doped, lattice matched dislocation free seed, VM–FEC GaAs gives the best uniformity of threshold voltage at present.

For further information on the importance of substrate quality for GaAs IC's consult the following reviews: Di–Lorenzo (362), Martin (363), Miyazawa (288, 289), Packeiser (291)

2.7 General Properties of GaAs.

For other properties of GaAs not relevant to this work see the INSPEC publication "Properties of GaAs" (314) or the review given by Blakemore (364), and the references therein.

3 ASSESSMENT OF SEMI-INSULATING GaAs SUBSTRATES.

3.1 Introduction.

The main assessment techniques used to investigate defects in SI GaAs substrates are discussed below, along with their relative advantages and disadvantages. The chapter is split into sections on: dislocation assessment (including etching, X-ray topography and TEM); precipitate assessment; stoichiometry assessment; crystal strain assessment; NIR assessment (with emphasis on the NIR absorption assessment of EL2); DLTS and related space-charge techniques; electrical measurements; luminescent techniques (including CL and PL); device assessment (especially the mapping of FET properties); magnetic resonance techniques; and impurity assessment. Finally, a section describing other important techniques not included in those above is given.

Assessment of materials other than SI GaAs substrates, and the assessment of implanted layers or devices are beyond the scope of this thesis and are only discussed when they give information relevant to SI GaAs substrates.

3.2 Dislocation Assessment.

The different techniques used to assess dislocations tend to fall into several different groups. X-Ray Topography (XRT) or TEM are used to investigate the nature of dislocations, in particular their burgers vectors. XRT and the assessment etches (such as molten KOH or A/B etchants), are used to determine dislocation densities and distributions. The interaction of dislocations with other defects, especially the formation of impurity or native defect atmospheres, is investigated by the experimental etchants (such as A/B and DS(L) etchants), NIR topography or by luminescence techniques. NIR and luminescence assessment will be discussed separately in sections 3.6 and 3.9 respectively.

3.2.1 Etching.

Etching is inexpensive. On a macroscopic scale, it gives information on whole slice variations, and at the same time, details a few microns in size can be resolved. However, it is destructive and can be fairly time consuming.

The main etchants used for GaAs can be divided into two groups. The first group is used mainly for production assessment, to find dislocation densities. The main etch in this group is molten KOH (Grabmair 356, Miyazawa 366) which produces etch pits where dislocations intersect surfaces. More recently the A/B etch (described below) has been used for this purpose as it removes some of the under-counting problems associated with molten KOH (Stirland 367, Rees 368) and also reveals dislocations parallel with surfaces. The second group of etchants are the experimental etchants, which also include the A/B etch in its various forms along with similar defect atmosphere sensitive etchants, in particular the DS(L) etch. These etches are used mainly to investigate precipitates and defect atmospheres around dislocations. They are detailed and compared below:

The A/B etch, developed by Abrahams and Buiocchi (369) and advanced by Stirland (370), is based on a HF–$HCrO_3$–$AgNO_3$ solution. Dislocations are revealed as grooves or ridges depending on the position of the fermi level (Brown 371). Precipitates are revealed as pits. Defect atmospheres are also detected. This etch also displays a strong memory effect where dislocation or other defect traces are maintained as the etch depth is increased. Hence, this etch is highly suitable for investigating volume effects (for depths of up to about 50μm). The A/B etch is described in more detail in chapter 4.

The dilute Sirtl–like etch, used with or without light (DS(L)), is based on a CrO_3–HF solution (Weyher 053, 064, 372, Giling 373, Bunod 374, De Raedt 375, Gleichmann 376). It reveals more information than the A/B etch, on the interaction of dislocations with point defects, especially when used in conjunction with light (for photosensitive defects). However, because of its slow etch rate, compared to the A/B etch, it is less suitable for depth studies and dislocation density counts.

The DC(L) etch is based on CrO_3–HCl solutions (van de Ven 377). Similar results to DS(L) are claimed without the requirement of HF.

The diluted or modified A/B etches (Saitoh 378, Munoz–Yague 379, Dobrilla 242, 380) are claimed to give higher sensitivity than the conventional A/B etch.

A combination of molten KOH and NaOH (Yamada 075, Lessof 381, Miyairi 382) shows defect structures other than dislocations and is easier to use than the molten KOH etch.

Illuminated 8–1–1 or 6–1–1 H_2SO_4–H_2O_2–H_2O solutions are also used to give information on defects other than dislocations, such as growth striations. An example of this type of etchant is the HIL–PC (High Intensity Light Photo–Chemical) etch (Wang 383).

The early etchants developed for GaAs, including the Schell etch which is based on an HNO_3 solution (Schell 384), the RC (Richards– Crocker) etch, based on a HF/HNO_3 solution with added Ag ions (Richards 385) and its modification, the RC–1 etch (Abrahams 386) are no longer commonly used.

A strong need exists to compare and contrast in detail the various types of modern etchants. So far this has only been carried out by Wehyer et al (053) for the DS(L), A/B, Schell and RC etchants.

3.2.2 X–ray topography.

A review of X–ray topograpy (XRT) and diffraction imaging was given by Scott (387). Several types of XRT exist. Emphasis will be given here to the Lang camera (Lang 388) as it is one of the most common methods and is also the technique used in this work. In the Lang camera, the X–rays are focused into a line source which illuminates a carefully oriented sample. The photographic plate is then illuminated through a slit with a selected X–ray reflection line from the sample. The sample is then slowly scanned through the beam with the plate scanned at the same rate, building up a full topograph of the sample. Further experimental details are given in chapter 4. An alternative technique is the Hirst topography camera (Leigh 056) where flexing of a sample allows the whole transmission X–ray topograph to be taken at once. Hence, it is much faster than the Lang camera but only suitable for thin samples such as 300μm wafers.

XRT is essentially non–destructive but is time consuming and fairly expensive. It gives information on burgers vectors (using the extinction property, g.b=0) and hence dislocation types (that is, edge, screw etc.) can be determined. It can be used to provide details from whole slice dislocation distributions with a resolution of better than 10μm.

Topographs can be obtained in transmission or reflection modes. Transmission XRT (TXRT) gives information on dislocation arrangements throughout the volume of a sample. It is useful for comparing with bulk techniques (eg NIR absorption), but the samples investigated must be double polished. Reflection XRT (RXRT) examines only the top few microns of the sample. It can be compared with other surface techniques such as etching and only requires singly polished samples.

An alternative form of XRT is synchrotron radiation topography. This is a very expensive technique but the facility of variable X–ray wavelength removes some problems of sample alignment. It is particularly useful for in–situ investigations of dislocation generation and motion under stress (Tohno 389, 390, 391, Matsui 392).

3.2.3 Transmission electron microscopy.

Transmission Electron Microscopy (TEM) is the only method for investigating dislocations, precipitates and other defects at high resolution. It can be used in the identification of precipitate structures, and in burgers vector determinations, for line and loop dislocations. Problems occur with this technique because the sample volume investigated is very small and hence defects are often difficult to locate. TEM investigations are both time consuming and expensive, require very large concentrations of defects, and careful location and sample preparation techniques.

3.3 Precipitate Assessment.

The type of assessment technique used for investigating precipitates relies strongly on the information required. The exact location and identification (using electron diffraction) of a precipitate is usually carried out in an electron microscope. In addition, Energy Dispersive X–ray analysis (EDX)is sometimes used for identification purposes. Investigations of the concentration and distribution of precipitates are usually carried out using etching or NIR scattering studies. Size assessment of precipitates is difficult as the resolution of techniques such as optically inspected etching and NIR scattering are limited by diffraction to about 1μm; it is known that the particles are smaller than this. It is also difficult to judge the average size of precipitates using TEM as this technique preferentially detects small precipitates (up to about 100nm in size) because large precipitates will usually be removed in the thinning process. However, it may be possible to assess the size of precipitates above this size using the fact that the scattering mechanism changes as the particle size nears that of the scattering wavelength. For light of wavelength of approximately 1μm, Rayleigh scattering will be seen for particles of size below about 0.1μm. It should be possible to find whether some precipitates are larger than this by carefully studying the wavelength and polarisation dependence of the scattering intensity (Katsumata 259).

3.4 Stoichiometry Assessment.

The various techniques used to investigate stoichiometry variations are detailed below. Because of the presence of precipitates the "stoichiometry" of a sample will be different from the stoichiometry of the sample matrix. In addition, it is often difficult to fully distinguish between stoichiometry and strain effects. Another problem is the lack of an LEC grown stoichoimetric standard; at present HB material grown with an arsenic over–pressure corresponding to the minimum dislocation density is used, as such.

3.4.1 Lattice parameter.

Various workers have tried to use the variation in lattice parameter, with changes in melt composition, to measure changes in stoichiometry (Nakajima 020, 021, Terashima 022, Takano 023, Okada 024, Sato 393). Unfortunately, the results, as discussed in section 2.2.1, are not consistent and are likely in some cases to be strongly affected by crystal strain. This was clearly demonstrated by Okada et al (024) by taking the lattice parameter at various points across a wafer before and after dicing it. The results showed that the main radial variations were due to the lattice strain, which was relieved almost fully by dicing. A clear warning exists here: lattice parameter stoichiometry measurements should only be taken on diced samples. Another alternative is to combine density measurements (taken by hydrostatic weighing), with lattice parameter results (Aref'ev 026). This technique will determine the sample "stoichiometry" including that taken up in precipitates.

3.4.2 X–ray quasi–forbidden reflection.

Certain X–ray reflections from GaAs (eg 200,400,600) have very low intensities because the contributions from the two sublattices are in antiphase. For equal occupancy on the sublattices the intensity is given mainly by the difference in the atomic scattering factors of the As and Ga atoms. This is very small since their atomic masses are similar. Hence, differences in occupancy on the two sublattices, given by changes in stoichiometry, can easily be monitored by this technique (Fujimoto 394, 395, 396). The limit of accuracy for the technique is a deviation from stoichiometry of 3×10^{-5}. Experimentally, deviations of 10^{-4} have been seen for LEC GaAs, with higher occupancy on the As sub–lattice. The technique has the advantage that maps of stoichiometry changes can be produced. This technique can also be used to monitor the incorporation of dopants and to produce images of growth striations in doped crystals.

3.4.3 Titration.

This technique has the advantage that it is not affected by strain and also takes into account the contribution of precipitates. Unfortunately, it is the least sensitive of the three main techniques discussed here. However, large improvements in accuracy, to 1 part in 10^5, have been demonstrated recently by an improved experimental technique (Terashima 016, 022).

3.5 Crystal Strain Assessment.

Crystal strain assessment can be split into two main sections, either involving X–ray techniques (including lattice parameter measurements) or the optical technique of strain birefringence.

Double crystal X–ray topography can be used to map crystal strains and lattice tilts (Brown 397, Kitano 398). The technique has been semi–automated by Forman et al (399, 400) for fast wafer inspection. Double crystal topography utilises medium intensity reflections for their strong sensitivity to crystal strain and micro–cracks. Synchrotron radiation sources are generally used to reduce exposure times. Another X–ray technique is Digital Automated Rocking Curve (DARC) topography (Ananthanarayanan 401). This monitors the change of the rocking curve position across a slice and hence determines surface and sub–surface lattice strains. These X–ray topography techniques are non–destructive but are expensive and time consuming. Lattice parameter measurements can also be used to measure crystal strain providing the effects of stoichiometry are separated. This is achieved by taking the difference of the lattice parameter results before and after dicing the sample (Okada 024). Hence the technique is destructive.

The optical technique of NIR strain birefringence is faster, easier to use and cheaper than X–ray methods and is also non–destructive. However, the results are difficult to interpret. The technique is described in more detail in section 3.6.7.

3.6 Near Infra–Red Assessment.

The GaAs bandgap is at a wavelength of 0.88μm at room temperature. Above this wavelength, GaAs is transparent and can be assessed by NIR transmission techniques. A wide range of substrate properties affect the NIR optical properties of GaAs crystals. These include: optical absorption by deep levels (especially EL2); scattering due to precipitates; optical path differences due to growth striations, or stress induced modulation of the refractive index. In addition, changes in magnetic circular dichroism can be induced by spin resonance techniques. Although the properties being assessed differ greatly, the techniques are discussed together in this section because they have many features in common. Particular emphasis is given to the NIR absorption assessment of EL2.

For experimental details of the NIR assessment techniques used in this work, see section 4.2. For more information on the NIR absorption of EL2 see section 2.3. NIR assessment techniques have also been reviewed by Brozel (54), Stirland (53) and Skolnick (10).

3.6.1 Assessment of EL2.

The evaluation of [EL2] from its characteristic NIR absorption spectrum, using Martin's calibration (131), has become one of the most important assessment techniques for SI GaAs. This is mainly due to the critical importance of EL2 in electrical compensation combined with the difficulty of obtaining accurate [EL2] results using more traditional deep level assessment techniques such as DLTS (see section 3.7). Hence, many methods of NIR absorption assessment have been developed to investigate the EL2 distribution in GaAs ingots.

Early work involved the use of a spectrophotometer to take point measurements of [EL2] across a slice (Martin 231). Brozel and co–workers adapted this technique, using a simple sample scanning system, to produce high spatial resolution line–scans of EL2 absorption across a slice (Stirland 236, Brozel 405).

Brozel and co–workers (Stirland 236, Brozel 405) also carried out two dimensional imaging of EL2 absorption using a silicon vidicon closed circuit television (CCTV) camera. They compared

the results with those produced using the spectrophotometer linescan system. The GaAs sample was illuminated by an infra-red source and viewed in transmission by the NIR sensitive camera. Unlike the spectrophotometer, the imaging system in its basic form was not monochromatic; it was sensitive to light from the bandgap of GaAs to the cut-off of the vidicon camera at about 1.1μm. In this region the absorption cross section of EL2 is high, hence the sensitivity of this technique to a non-uniform distribution of EL2. To produce a monochromatic image a 1.065μm narrow band pass filter could be placed in the system. No qualitative differences were seen between the image produced with the filter in place or with it removed (Skolnick 054). Hence, imaging was carried out without the filter to increase the transmitted intensity and thus reduce noise on the vidicon image. Records of the vidicon image were taken by directly photographing the monitor on which the image was displayed. The vidicon system was soon adapted to produce full slice images (Skolnick 054) and later, "three dimensional" images by tilting the specimen and producing stereo pairs (Brozel 12). Recently, image processing has been used to normalise against variations in illumination intensity in absorption images, and to improve signal-to-noise ratios by image integration (Katsumata 244, 406, Castagne 254).

Instead of recording the image with a CCTV camera Kaufmann et al (153) used a similar experimental set-up to the NIR imaging system, but replaced the CCTV camera with a photographic arrangement using a camera with infra-red sensitive film. The same group developed a mapping system based on a linear array of 256 photo-diode detectors and compared the results they obtained with that of the photographic system (Windscheif 407, 408). They later extended the system to enable near band edge PL maps to be made using the same apparatus (Windscheif 247, 409). The system takes about 30 seconds to produce an absorption map (Wettling 410). Alt and co-workers used a similar system with improved resolution (using an array of 1024 photodiodes) to produce microscopic maps of EL2 absorption, illustrating cell structure (Alt 228, 239, 240).

Another approach to EL2 mapping is to use point measurements in conjunction with a scanning apparatus. The most advanced system of this type is that developed and improved by Dobrilla and Blakemore (Dobrilla 241, 411, 412). It produces an EL2 map, based on a 100x100 grid with variable magnification, in about 20 minutes, with a maximum resolution of 50μm. Many similar systems exist with lower resolutions (Holmes 232, 234, Abernathy 275, Gouteraux 413, Visentin 414)

Silverberg and co-workers were the first to develop a computer based mapping system for producing EL2 maps from vidicon imaging. The EL2 maps were obtained by processing the absorption images before and after bleaching the EL2 absorption (Silverberg 415). They later extended this system, using measurements at two different wavelengths, to produce maps of EL2 occupation in addition to the [EL2] maps (Silverberg 416). Unfortunately, this system of EL2 occupation mapping suffers from severe errors as it produces impossible occupancies for EL2 (less than zero and greater than one!) over much of the image. Recently, a similar system for obtaining EL2 maps from absorption images taken before and after bleaching was demonstrated by Fillard et al (253).

An alternative to using the wide NIR absorption band of EL2 for assessment is to use the

absorption due to the intra–centre transition, or more particularly its associated Zero Phonon Line (ZPL). The absorption coefficient of the ZPL was calibrated recently (Skowronski 221, Lagowski 222). Using this in conjunction with bleaching, concentrations of both charge states of EL2 can be calculated (Skowronski 221, Lagowski 222). This technique requires a high resolution FTIR spectrophotometer and liquid helium cryostats and to date has only been used for point measurements. For more details on the intra–centre transition, the ZPL absorption and its calibration, see section 2.3.3.

3.6.2 Monitoring of ion–implantation.

Ion–implantation causes lattice damage which increases the near band edge absorption of GaAs. The amount of absorption increases with implantation energy and dose. Hence, the standard NIR absorption techniques described above can also be used to moniter the magnitude of the implantation damage (Windscheif 247, Stirland 403).

3.6.3 Scattering.

NIR scattering gives information on the concentrations and distributions of precipitates in the scattering plane. Information on their size can be obtained from their polarisation behaviour (Katsumata 259) or the type of scattering (Raleigh scattering will occur if the particle size is much smaller than the scattering wavelength). Because the scattering is caused by precipitates which are nearly always associated with dislocations, the technique can also be used to give dislocation arrangements. This was beautifully demonstrated by Kuma et al (265) who built up a picture of the dislocation structure in three dimensions by overlaying the results from different scattering planes.

Various tomography systems exist for investigating NIR scattering. Most of these image the light scattered perpendicularly by scattering centres. The laser beam is then scanned across the sample to produce a two dimensional scattering image. The various experimental arrangements are similar but use different laser sources: the 1.06μm YAG (Moriya 263, 264, Fillard 417, Suchet 418); the 1.32μm YAG (Ogawa 267); or the 1.15μm He–Ne laser (Ogawa 261, 266, 267, Kuma 265).

3.6.4 The scanning infrared microscope.

The infrared laser scanning microscope (Kidd 419, 420) has several advantages over transmission imaging and light scattering tomography as both scattering and light absorption information can be obtained throughout the depth of the sample at high resolution (up to x1000). The sample is illuminated by a 1.15μm scanning He–Ne laser beam and light is detected by a Ge detector. The scanned output signal is used to produce a standard video image. The detector is either placed along the optical axis of the system, where a bright field image with contributions reduced by absorption and scattering is obtained, or at right angles to the optical axis, where a dark field image containing only scattered light is obtained. The limitations of the technique are that it cannot be used to provide macroscopic wafer images and that the samples need to be polished on at least three sides if bright and dark field images are both to be obtained.

3.6.5 Reverse contrast imaging.

Using near band gap light, that an image with reverse contrast to the normal EL2 absorption image is seen after the bleaching of EL2 absorption (Skolnick et al 404, 545, 546). To date, no definite explanation has been given for this effect but it has proved a useful assessment tool (Brozel et al 547). In particular, annealed wafers usually have uniform 1μm absorption but the near band edge images show clear cell structure in reverse contrast to that normally seen in unannealed wafers. Note that In–doped wafers show similar near band edge images but with positive contrast.

3.6.6 Growth striation imaging.

This technique was developed to image growth striations and dopant segregation at dislocations (Brozel 421, 422). It is an adaptation of the vidicon imaging system described in section 3.6.1. The sample is viewed slightly away from the focus of the camera lens with a near parallel light source. In this setup, light travelling through areas of differing refractive index will undergo different deflections, giving an image of the changes in refractive index across the sample. This technique is useful for imaging striations in In–doped material, which in turn gives information on the growth interface shape and the degree of segregation at dislocations (very little in the case of In–doping).

3.6.7 Stress mapping.

This technique relies on the rotation of the optical polarization axis by crystal strain. In its most basic form, a crystal is simply placed between crossed polarisers and is viewed with an NIR sensitive camera (Katsumata 406). For GaAs, the image produced, although caused by the stress field of the sample, is given mainly by the relationship of the refractive index ellipsoid of GaAs with that of the optical axis. Hence, there is no local correlation between the transmitted light intensity and the local stress field (Dobrilla 233, 423). Therefore, the technique cannot easily be quantified to map local stress distribution. To get over this problem Dobrilla and Blakemore (233, 423) developed a system of sensitive transmittance mapping that uses unpolarised light and examines the weak interference fringes which are due to local stress (demonstrated by the wavelength dependence of the fringes). Although the changes in transmittance are a very small, they do relate to local stress, and hence quantitative stress maps can be produced.

3.6.8 Magnetic circular dichroism.

The Magnetic Circular Dichroism (MCD) method of NIR assessment measures the difference in absorption of left and right hand circularly polarised light in a magnetic field. It is caused by the different populations of the two spin split levels (of the unpaired electrons) of a paramagnetic defect such as the ionised As_{Ga} antisite defect. It is mainly used in association with spin resonance techniques and its application will be discussed in section 3.11. The variation of EL2+ in a wafer has recently been mapped using the variation of MCD of its ionised antisite component (Heinmann 248 , Winnacker 424).

3.7 Deep Level Transient Spectroscopy and Related Techniques.

The principle aim of the techniques described here is to obtain information on deep levels; namely, concentrations, energy levels, thermal emission cross sections and optical cross sections. These are derived from the transients of electrical parameters such as capacitance or current, when the deep levels are emptied or filled.

3.7.1 Deep level transient spectroscopy.

Deep Level Transient Spectroscopy (DLTS) is one of the most commonly used techniques for investigating deep levels in semiconductors. Unfortunately, it cannot be used to characterise SI GaAs, as it is not quantitative (when the carrier concentration in the sample does not exceed the deep level concentration under investigation). Hence, DLTS assessment generally involves growing lightly n–type or p–type crystals and assuming that these doped crystals will otherwise behave in the same way as a SI crystal grown in the same manner. The other main limitations of DLTS are the requirement for contacts and that the basic technique is only sensitive to majority carrier traps.

The DLTS technique, as first used by Lang (425), is described below:

> A Schottky diode is formed on the sample and it is cooled down to a low temperature. The DLTS signal is then obtained in the following manner: the diode is reverse biased to fill the deep levels, the bias is then removed and as the traps empty, the capacitance transient produced is sampled at two fixed times after removing the bias. The DLTS signal is the difference in capacitance between the two sample times. This process is repeated as the sample is slowly heated. The DLTS signal is plotted against temperature and displays a series of peaks corresponding to the successive emptying of traps of increasing activation energies. By repeating the process with a different separation between the sample times (more commonly known as different rate windows), deep level cross sections, energies and concentrations can be obtained.

Details of various deep levels in GaAs are reviewed by Martin et al (119). Thermal emission signatures were also summarised in a separate paper (Martin 126). Care is required when using DLTS particularly for the assessment of EL2 (Gatos 121, Zohta 426). Firstly there is evidence that EL2 may be a family of defects (see section 2.3.1). In addition, DLTS can give different results when different metals are used for Schottky contacts (Yahata 427) and may give erroneous results at large reverse bias due to field enhanced emission.

The different behaviour of deep levels with similar emission signatures under high fields has been used to distinguish between them. This involved using a variation of DLTS known as RDLTS where emission pulses rather than capture pulses are used (Li 428). Another method of splitting peaks of similar activation energy was demonstrated by Lagowski et al (145, 429). By shortening the length of the filling pulse and utilising the higher electron capture cross section of ELO, the "EL2 family" peak shifts from that position characteristic of EL2 to that of ELO,.

Information on minority carrier traps can be obtained either by minority carrier injection using a p+ layer on an n–type substrate (Auret 293, Lang 425) or by optical excitation in Optical DLTS or ODLTS (Martin 119, Skowronski 164, 430, Wosinski 431). Unfortunately, it is difficult to

quantify these techniques to obtain minority trap concentrations.

The spatial distribution of traps can be studied either by taking a series of point measurements or by the use of scanning DLTS (Ikuta 323, Wosinski 431, Wada 432, Breitenstein 433, 434, Sporon–Fiedler 435). Scanning DLTS uses the capacitance or current transients induced by an electron beam in an SEM, to produce the DLTS signal. The technique is sensitive to both majority and minority carrier traps and has high spatial resolution. Hence it can be used to map the association of various deep levels with dislocations. Unfortunately this technique is also difficult to quantify.

3.7.2 Optical isothermal transient spectroscopy.

Optical isothermal Transient Spectroscopy (OITS) is based on the analysis of isothermal photocapacitance transients (Samitier 295, 296, 297, 298, Morante 436). It can be used to characterise hole traps as well as electron levels and can be used to assess SI material. Information on optical properties of the levels can also be obtained by varying the excitation wavelength.

3.7.3 Photo–induced transient spectroscopy.

Photo–Induced Transient Spectroscopy (PITS) is a similar technique to current sampled DLTS. The current transients produced after illumination are analysed using the rate window technique (Kremer 437, Abele 438, Tin 315, 439, Teh 440). The technique is sometimes known by other names: Photo Induced Current Transient Spectroscopy or PICTS (Yoshie 441, Balland 442, Tapiero 443); Photo–Deep Level Fourier Spectroscopy, or Photo–DLFS (Ikeda 444); Optical Transient Current Spectroscopy or OTCS and Photo–Electric Relaxation Spectroscopy, or PERS (Omeljanovsky 445). Ikeda et al (444) studied the effect of varying the excitation wavelength on Photo–DLFS. Yoshie et al (441) produced a scanning PICTS system and used it for mapping deep levels in various samples. They also investigated the use of the PICTS technique on the rising current transient during illumination.

Another variant of this technique is known as PR–DLTS where the ac resistance decay produced after photo–excitation is analysed (Seabaugh 446).

3.7.4 Thermally stimulated current and capacitance.

The Thermally Stimulated Current (TSC) technique has the advantage that information on traps can be obtained in high resistivity material where standard DLTS or ODLTS are not applicable. Unfortunately, it is difficult to distinguish between hole and electron traps, and as with DLTS, contacts are required. To obtain a TSC spectrum, the sample is cooled to low temperatures and illuminated to fill the traps. The illumination is then removed and the current is monitored as the temperature increases. The plot of TSC against temperature shows peaks, as successive traps of increasing activation energy empty. Trap energies and approximate concentrations can be calculated from the peaks. The technique has been used recently by several workers (Tsukada 134, Skowronski 164, Fillard 216, 217, Kuszko 447 and Walczac 448).

Thermally Stimulated Capacitance (TSCap) is a similar technique to TSC but capacitance transients are measured instead of current transients (Von Neida 449, Bencherifa 130, 450,

Hasegawa 451).

3.7.5 Photocapacitance and optical cross-sections.

Knowledge of optical cross-sections is important for the optical assessment of deep levels. This information can be obtained using various methods. Optical absorption allows direct measurements of optical cross-sections. Unfortunately, thick samples are required due to the low sensitivity of the technique, also different cross sections or contributions from different energy levels are not separated. Luminescence techniques can also be used although they are strongly affected by competition between different radiative or non-radiative levels. This can be overcome to a large extent by the use of photoluminescence excitation spectroscopy where the luminescence due to a particular level is monitored with changing excitation wavelength (see section 3.9). Photoconductivity can be used on SI material. It has high sensitivity but cross-sections are difficult to extract from the data. By far the best method is the use of photocapacitance; it has high sensitivity, it can be carried out on the same diode structures used for thermal emission analysis (as for example in DLTS), and contributions from the different cross-sections can be easily separated. Optical cross-sections are derived from the initial slope of the photocapacitance transient; electron or hole optical cross sections are obtained for traps initially filled or empty respectively. Several variants of photocapacitance spectroscopy are described below:

The Deep Level Optical Spectroscopy or DLOS technique (Chantre 128) is based on measuring the initial slope of the photo-stimulated capacitance transient produced after electrical (electrical DLOS), thermal (thermal DLOS) or optical (optical DLOS) excitation of a diode structure. The technique allows direct independent measurement of both electron and hole optical cross sections. The main disadvantage of the technique is that it is very time consuming.

The OITS technique (Samitier 295, 296, 297, 298, Morante 436) described in section 3.7.3 can also be used to determine optical cross sections, by monitoring the initial gradient of the capacitance transients.

By manipulating the occupation of EL2 using primary optical excitation and monitoring the photocapacitance transients after selective secondary optical excitation, Silverberg and co-workers (Silverberg 219, 220) have measured electron and hole cross sections for both charge states of EL2 ($EL2^{o/+}$ and $EL2^{+/++}$), for use in EL2 mapping techniques.

3.8 Electrical Assessment.

This section deals with the evaluation of the electrical properties of SI substrates such as the resistivity, resistance, carrier concentration, mobility and Hall constant. The subject was included in several recent reviews (Bonnet 286, Look 452) which also discussed the assessment of implanted layers and devices.

The Hall effect is a very powerful technique in that resistivities, mobilities and carrier types can be evaluated. In addition, temperature dependent results give information on the activation energies of compensating defects. Unfortunately, the technique is destructive. The information that can be obtained using the Hall effect was reviewed by Anderson (453). Experimental

systems for Hall effect mapping have been described by several authors (Bonnet 060, Visentin 414, Hyuga 454). The technique has been used to map resistivity and mobility (Bonnet 060, Visentin 414, Hyuga 454, Honda 455).

One of the most popular techniques for quantitatively mapping resistivity in GaAs is the three electrode guard technique (Obokata 278, Bonnet 286). Unfortunately, the technique is also destructive. Various workers have demonstrated resistivity maps using this technique (Kikuta 058, Shimada 093, Alt 228, Katsumata 244, Obokata 273, 278, Inada 332, Tomizawa 456).

The dark spot method of measuring sheet resistance was developed by Blunt (457). The technique is not quantitative but is largely non–destructive in that contacts are only required around the edge of the wafer. A strip of the wafer surface is illuminated to give photo–generated carriers, greatly reducing the surface resistivity in this region. A dark spot is then scanned along this illuminated strip, whilst the resistance of the strip is monitored. Since the resistance of the illuminated portion is negligible compared to that of the dark spot, the technique effectively maps the dark sheet resistance of the wafer. This technique was improved by Kitahara and Ozeki (458) and a "similar" technique was developed by Wang et al (459) called the Optically Assisted Imperfection Profile or OAIP. Look and co–workers (Look 452, 460, Pimentel 461) suggested several variations on the theme of the use of light strips. These included a Greek cross arrangement of illumination, with a dark spot at the intersection giving a form of four point probe measurement or alternately, with no dark spot for photo–resistivity and the photo–Hall effect.

The leakage current technique involves scanning a probe across an illuminated wafer surface with the probe biased with respect to the back of the substrate. It has the advantage of being non–destructive but interpretation is difficult, although often the signal is just assumed to be proportional to the conductivity of the sample (Matsumoto 287). Scanning leakage current results have been given by several workers (Kamejima 057, Mo 097, Matsumoto 287).

Many other techniques give information on substrate electrical properties. In particular, see the sections on microwave mapping (3.14.6), photo–refractive imaging (3.14.7) and electrochemical techniques (3.14.9) in this chapter.

3.9 Luminescence Techniques.

The emphasis here is on the information which can be obtained, from luminescent techniques, on deep level and non–radiative recombination centres. Impurity luminescence will be discussed very briefly in section 3.12. The two types of luminecence techniques commonly used to assess SI GaAs are Photo–Luminescence (PL) and Cathodo–Luminescence (CL). Information common to both techniques is discussed here whereas details of the two techniques are discussed in separate sections below.

The characteristic luminescent spectrum of SI GaAs displays sharp near band edge lines due to impurity and/or excitonic levels and several broad mid gap bands. Both luminescent intensity and spectral resolution increase with decreasing temperature. Low temperatures are required to distinguish between the mid gap bands. Tajima (462 and 463) has reviewed the identification of the mid–gap bands, mainly involving his own work using PL Excitation or PLE (see below). He has shown that the 0.63 and 0.68eV mid gap luminescence bands are due to the neutral and

ionised charge states of EL2 respectively. It is postulated that the large amount of contradictory identifications in the literature (see for example: Samuelson 165, 464, Yu 465, 466, Tajima 462, 466, 467 and Paget 469; other references are given in Tajima's review 462) are due to other deep levels which are sometimes present, especially the 0.65eV and the 0.8eV ("arsenic–rich related") luminescence. Unfortunately, this identification does not mean that the EL2 related lines can be used to map the two charge states of the defect. Hunter et al (470) have shown that electron–hole recombination, after excitation, is very fast and could not possibly be due to EL2 or impurity luminescence but is primarily determined by competition with non–radiative recombination. Hence the distribution of the EL2 related lines give a map with a direct contribution from EL2 and a competitive contribution from non–radiative recombination centres.

3.9.1 Photoluminescence

Standard PL utilises intrinsic (above band–gap) light excitation, usually with a laser to increase PL efficiency. The PL output is detected, split into a spectrum, and the magnitudes of the various bands are monitored. In scanning PL the spatial distribution of the magnitude of a particular band is investigated by scanning the excitation beam.

PLE moniters the variation of the luminescence of a particular band with the excitation wavelength (either intrinsic or extrinsic) and hence provides spectral information on the optical cross section of the level. PLE must be carried out at low temperature to resolve the different bands and provide reasonable luminescent intensity.

A selection of PL mapping studies, together with the sample temperature and light detected, are given below:

4K profiles of the 0.8,1.44,1.49 and 1.51eV bands (Watanabe 471).

4K profiles of the 0.65, 0.8 and 1.49eV bands (Kikuta 472, Tajima 473).

4K and 77K profiles of the 0.63eV band (Tajima 224).

Room temperature, near–band–edge profiles and maps (Windscheif 247, 409, Lohnert 272, Hovel 279, Mikoshiba 280, Wettling 410).

80K near–band–edge high resolution scanning PL (Hunter 360, 474, 475).

10K 1.51eV high resolution scanning PL (Hunter 360).

77K 1.49eV and 0.8eV maps (Kuma 246).

77K near–band–edge and 1.23 eV 1.35eV and 0.8eV maps (Kallel 476).

10K 1.514eV and 1.493eV PL maps (Kallel 476).

A selection of PLE studies are detailed below:

PLE of the 0.64eV and 0.8eV bands from 1.55eV (0.8μm) to 1.44eV (0.86μm) (Paget 469).

11K PLE of 0.63 and 0.68 bands from 0.7 to 1.7eV taken at luminescent frequencies where no overlap of the two bands occurs (Tajima 462, 467, 468).

2K PLE of the 0.63eV band from 0.8eV to 1.6eV (Samuelson 165, 464).

4K PLE from 1.4 to 2.0eV of the 0.77eV band (Yu 465) and of the 0.63 eV band (Yu 466).

3.9.2 Cathodoluminescence.

In the CL technique, excitation is produced by the electron beam in an SEM. Otherwise the luminescent mechanism, and the luminescent spectra produced, are much the same as for PL. Various CL mapping systems exist; a selection of results with the sample temperature and CL bands detected are given below:

Room temperature mapping with either CL from all bands or near–band–edge CL (Chin 055, 284, 477, Kamejima 057, Sekiguchi 282, Ding 313, Hunter 360, Watanabe 471).

80K mapping of band–edge (Lohnert 272, Hunter 470) and mid–gap CL (Hunter 470).

10K mapping of 1.51, 1.49 and 0.7eV bands (Dussac 283).

6K mapping of the 0.68, 0.8 and 1.51 bands (Brown 371, Warwick 478).

4K mapping of the 1.49 and 1.514eV bands (Leigh 056, Wakefield 479).

3.10 Device Mapping.

The ultimate test of the quality of SI GaAs substrates is to produce devices and to assess how well they perform. In particular uniform behaviour of devices is important if large scale integration is to become feasible on GaAs. To investigate device uniformity, arrays of FET's are usually produced on the SI substrates. Various FET parameters are then measured including threshold voltage (V_{Th}), drain–source saturation current (I_{DSS}), pinch–off voltage (V_{PO}) and transconductance (g_m). The uniformity of these parameters are then used to assess the substrates. Two different approaches to this problem can be taken:

Firstly, an overall uniformity of a particular device property can be used to assess substrates grown by different techniques. Standard deviations for a particular slice, batch, ingot or ingot type are usually quoted. A better approach, containing more information, was given by Packeiser and co–workers (Packeiser 291, Deconinck 348). They produced plots of "yield limitation factor" against standard deviation of threshold voltage for a particular ingot. The yield limitation factor being the probability of finding a dense row pattern of FETs (Schink 358, Maluenda 359) with a standard deviation better than a certain limit.

Secondly, correlation between the uniformity of devices and particular substrate properties can be assessed. Most effort has been put into the correlation (or not!) of dislocations with threshold voltage. Early work relied on correlating the distance of the nearest dislocation to a FET gate with threshold voltage. More recently a sophisticated statistical analysis of contributions from all nearby dislocations to particular FETs has been carried out (Suchet 356), again using dense row patterns (Schink 358, Maluenda 359). This technique involved defining an "influence zone" function for a dislocation which decreases with distance from a FET. Fitting parameters were used to produce the best form for the function.

The information obtained from FET mapping and its implications for the quality of substrates was discussed in section 2.6.2.

3.11 Spin Resonance Techniques.

Several review's of spin resonance techniques and their applicability to the characterisation of point defects in GaAs have been produced (Kennedy 158, Spaeth 480, 481, Gilason 482). The investigation of native defects, with emphasis on the As_{Ga} antisite and EL2, are discussed here.

Spin resonance techniques can be used for structure determination of point defects by analysing the interaction of unpaired electrons with the magnetic moments of lattice nuclei. The interaction with the host nuclei of the unpaired electron is known as the hyperfine (hf) interaction. The interactions with the surrounding lattice nuclei are known as super hyperfine (shf) interactions.

3.11.1 Electron paramagnetic resonance.

Electron Paramagnetic Resonance (EPR) is otherwise known as Electron Spin Resonance (ESR). By placing the sample in a magnetic field the two spin states of the unpaired electrons are split in energy. Transitions between the two states can then be induced by applying microwave excitation. The microwave absorption signal plotted against microwave wavelength is the EPR spectrum.

In GaAs only the hf interaction is resolved, hence information on the nearest neighbours cannot be directly obtained by this technique, although the symmetry of the defect can still be obtained from orientation studies. The EPR technique was first used to demonstrate the presence of the As_{Ga} antisite in GaAs (in its singly ionised paramagnetic state) by comparing the hypefine constants with those of the P_{Ga} antisite in GaP where the shf interaction is resolved (Wagner 483).

Optically detected investigations of GaAs utilise the MCD spectrum of the paramagnetic antisite. MCD relies on different populations of the two spin states of the unpaired electrons. EPR tends to equalise the two populations and hence by monitoring the microwave induced changes of the MCD the EPR spectrum can be obtained. Because the changes in MCD are large the sensitivity of the EPR technique is greatly improved (Meyer 484). ODEPR is also known as EPR tagged MCD, or as ODESR.

Since EPR detects the ionised charge state (As_{Ga}^{+}) of the As_{Ga} antisite, the use of photoexcitation to alter the charge state of the defect whilst monitoring the EPR spectrum can give information on the concentration of the neutral charge state and of the position of the defect energy in the gap. By using photo–EPR on a combination of SI and p–type GaAs the double donor nature of the antisite can be investigated (Weber 063, 123).

The tentative identifications of other native defects, investigated by EPR, are detailed below:

As_{Ga}–V_{As} complex (Von Bardeleben 485, 486).

As_{Ga}–V_{Ga} complex (Goltzene 203, 487).

Off centre As_{Ga}–V_{Ga} complex (Kaufmann 488).

As_{Ga} aggregates (Kaczmarek 489).

V_{As}–As_i complex (Von Bardeleben 490).

As interstitial complexes (Von Bardeleben 491).

3.11.2 Electron double nuclear resonance.

In the Electron double nuclear resonance, or ENDOR technique, the radio frequency induced change of the EPR signal, due to Nuclear Magnetic Resonance (NMR) transitions, is measured. ENDOR is a much more sensitive technique than EPR and hence enables information on the shf interaction to be obtained. Unfortunately the EPR signal–to–noise ratio is too low for standard ENDOR measurements in GaAs. This problem can be solved by using optically detected ENDOR (ODENDOR), monitoring changes of MCD as described, for ODEPR, above. The sensitivity of the technique is improved using ODENDOR, and shf interactions of several neighbour shells are resolved. By monitoring the angular dependence of the ODENDOR lines the EL2 defect was recently "identified" as the As antisite–As interstitial (As_{Ga}–As_i) pair (Meyer 160, 161, Spaeth 249).

3.12 Impurity Analysis.

Information on impurities in GaAs and their assessment techniques is covered well elsewhere (INSPEC, 314) and will only be outlined here. The impurities assumed to be important for the purpose of this thesis are shallow donors (especially silicon), shallow acceptors (especially carbon), the isoelectronic elements (In, used to harden the lattice to reduce dislocation densities; and boron, arising from the boric oxide encapsulant), and various transition metals. The most important assessment techniques for these impurities are briefly outlined below:

Mass Spectroscopy is quantitative but is generally not as sensitive to light elements. This is a problem because of the importance of carbon, boron, silicon and oxygen in SI GaAs. The main types of mass spectroscopy are: Secondary ion Mass Spectroscopy (SIMS), Spark Source Mass Spectroscopy (SSMS) and Glow Discharge Mass Spectroscopy (GDMS)

"Light" elements can be assessed using the characteristic infrared absorption due to Local Vibrational Modes (LVM) of impurity atoms (with atomic mass significantly less than the atoms of the host matrix) in GaAs. This technique is particularly important for the assessment of carbon, boron and silicon. It can be used to calculate impurity concentrations, provided a calibration for the absorption exists (Brozel 492). It can also give information on the impurity site and impurity pair interactions, as this gives a different peak frequency. Unfortunately thick samples and expensive FTIR spectrometers are required for good sensitivity. Also the concentration values obtained are often only approximate because the calibrations available are far from certain and the presence of the peak depends on the charge state of the defect.

PL is very useful for detecting the presence of shallow donor and acceptor impurities in GaAs (Harris 493, Skolnick 494). It is difficult to quantify the technique, although a rough comparison can be obtained by comparing the magnitude of impurity peaks with exciton peaks.

Raman spectroscopy is useful for the assessment of acceptor impurities particularly carbon and zinc (Wagner 321, 495, 496, 497, Harris 493). The zinc defect is found to be

important in the compensation mechanism of low [carbon] samples (Wagner 321). In addition, Raman spectroscopy can be adapted for impurity mapping, unlike many of its competitive techniques.

3.13 Other Assessment Techniques.

3.13.1 Positron annihilation.

Positron Annihilation measures the increased positron lifetimes in GaAs due to neutral or negatively charge defect sites (Dannefaer 019, 178, Stucky 179, Mascher 498, Dlubek 499, 500, Puska 501). In addition, an idea of the defect concentration can be obtained from the positron trapping rate. The technique is useful for studying vacancies and vacancy complexes.

3.13.2 Internal friction and ultrasonic characterisation.

This technique measures the variation of the damping of forced mechanical vibrations in a sample, with temperature and with oscillation frequency. Peaks in the damping response are produced by defects in the material. Analysis of these peaks can give defect energies and approximate concentrations. The technique has the advantage that it is sensitive to defects which may not be optically or electrically active (for example, non–radiative recombination centres). It has been used by several workers to analyse deep levels in GaAs (Laszig 502, Abe 503, Brozel 504).

Ultrasonic characterisation relies on the same principles as internal friction measurements but has probing frequencies in the ultrasonic range (Brophy 505)

3.13.3 Differential thermal analysis.

A Differential Thermal Analysis (DTA) spectrum gives the difference in the heating power needed to maintain a sample and a reference sample (ideally defect free) at the same temperature during a temperature scan. This difference is due to reactions of defects in the sample. The technique can be used to find total defect energies, approximate defect concentrations and can be used to study defect reactions, in particular, the temperatures at which they occur (Bourgoin 506, Lim 507).

3.13.4 Electron and optical beam induced current.

Electron Beam Induced Current (EBIC) is a recombination sensitive technique which gives similar results to CL (Bode 508 Jakubowicz 509). The EBIC image is a map of the current generated by an electron beam scanning over a Schottky barrier, on a sample surface, in a SEM. The requirement of contacts is often a disadvantage for an assessment technique, but in this case scanning DLTS can be carried out, using the same contacts, in the same apparatus (Ikuta 323, Wosinski 431, Breitenstein 434, Sporon–Fiedler 435).

Optical Beam Induced Current (OBIC) is a similar technique to EBIC but has the advantages of being non–destructive and requiring a scanning optical microscope, which is less expensive than an SEM (McCabe 510).

3.13.5 Photothermal spectroscopy.

Photothermal spectroscopy is used to investigate non–radiative recombination centres in GaAs. It involves optical excitation of these centres, giving local heating. The local heating effect can then be detected in a variety of ways. One method, known as the Photo–Acoustic (PA) Technique, is to measure the acoustic waves set up by the fluctuations in local heating due to a chopped excitation beam. These vibrations can then be detected by using either a microphone, a piezo–electric transducer or a cantilever arrangement with a Michelson inteferometer (Suemune 511). Another method is known as Photothermal Beam Deflection (PBD). This uses a second beam reflected off the sample surface to measure the surface distortion due to the local heating (Sawada 512). A third method, known as the Photo–Thermal Radiation (PTR) technique, is to use an infrared detector to detect the radiation produced by the local heating (Nakamura 513, Mikoshiba 280, 514, Amer 515). A fourth technique, known as photothermal deflection spectroscopy monitors the deflection of a beam due to the change in refractive index of the air above the surface, caused by the local heating (Amer 515).

Thermal Wave Microscopy (TWM)is a similar technique which uses the blanked electron beam of an SEM to set up thermal waves in a sample which are then detected by a piezo–electric transducer. The thermal waves interact with lattice defects. Hence, an image of the distribution of these defects can be produced (Strausser 516, Brandes 517).

3.13.6 Micro–wave assessment.

Microwave absorption is used to map photo–excited free carriers in SI GaAs. The technique is non–destructive and does not require contacts. Microwave assessment can be used either for photoconductance mapping or can be used to characterise defects using spectral studies similar to DLTS. To produce photo–conductance maps either the illumination source (Abernathy 252, 275, Look 452, Cummings 518) or the antenna (Borego 519, Gutmann 520) can be scanned. Also, either intrinsic or extrinsic light excitation can be used (Borego 519, Gutmann 520). Intrinsic (below band gap) excitation must be used to give information on deep levels (Usami 521). The photoconductivity decay transients produced by recombination at emptied deep levels can give similar information to the photocapacitance transients in DLTS. Hence, trap concentrations and cross sections can be calculated using either the entire transient (Ohyama 522) or by sampling it with various rate windows (Fujisaki 333, 523, Usami 521, Ferenczi 524, Jantsch 525, Tamura 526). This technique is sometimes known as Microwave Absorption Spectroscopy, or MAS (Jantsch 525), alternately as Optically Stimulated Microwave Absorption, or OSMA (Fujisaki 333, 523).

3.13.7 Photorefractive imaging.

This technique optically measures the decay rate of a refractive index grating set up from the interaction of an optical interference pattern, produced by two coherent laser beams, with carriers in the sample. By altering the spacing of the grating and the intensity of a third monitering beam, which is used to probe the grating, the decay mode can be changed. Different decay modes can give information on different material properties. Using this technique the spatial variation of dark conductivity, photo–conductivity and deep level absorption coefficient can be calculated (Bylsma 527, 528, Cheng 529).

3.13.8 Photoreflectance and thermoreflectance.

The use of Photo–Reflectance (PR) and Thermo–Reflectance (TR) to assess deep levels in SI GaAs was recently demonstrated by Shen et al (530). In PR, carriers are photo–injected using a chopped laser beam. This results in a modulated electric field in the material through recombination of the photo–injected carriers with traps. This field modulation yields a change in reflectance which is monitored by a second beam. By changing the wavelength of the second beam a PR spectrum is produced. By monitoring the dependence of this spectrum on chopping frequency and temperature, details on traps in the material can be obtained, in a similar manner to DLTS, without the requirement of contacts. The authors also produced a TR spectrum on the same sample to demonstrate the correspondence of the two techniques. This technique examines changes in reflectance due to modulated local heating, generated in this case by a square wave current passing through a conducting strip on the sample surface. Because of the requirement for contacts the TR technique is less useful.

3.13.9 Electrochemical techniques.

Electrolyte Electro–Reflectance (EER) is used to measure antisite (point defect) densities and inhomogeneous local strain, from separate fitting parameters to the EER lineshape (Raccah 531, 532). Electrolyte Photo–Capacitance (EPC) can be used to measure EL2 concentrations (Raccah 532, Haak 533). The results were consistent with the antisite concentrations given by EER.

When a GaAs sample is used as an anode in an electrochemical cell, and is illuminated, a photoelectrochemical current is produced. Markov et al (534) used extrinsic illumination to investigate photocurrent variations across samples. Otsubo et al (535) developed a more advanced system where spectroscopic as well as spatial information can be obtained. This technique which can use either intrinsic or extrinsic light, gives a current output known as the Spectroscopic Photo–Electrochemical Current (SPEC). Using this technique, an approximate map of EL2 variations across a sample can be produced, from the EL2 photo–response.

Anodisation can be used to map carrier concentrations in SI GaAs (Young 324). For a particular voltage, anodisation only occurs when the carrier concentration in a region of the substrate exceeds a certain value. The thickness of the anodised layer produced (as measured by its thin film interference colour) is also a function of the carrier concentration.

3.13.10 Ballistic phonon transmission.

The anisotropy of phonon transmission can be used to assess the symmetry of point defects in a sample. Anisotropic phonon transmission, thought to be due to EL2, was demonstrated by Culbertson et al (180).

3.13.11 Cyclotron resonance.

The temperature dependence of time resolved far infrared laser cyclotron resonance of electrons excited from the EL2 level, can be used to evaluate the capture cross section of EL2 (Ohyama 522).

3.13.12 Spectral photo-quenching studies.

Various workers have been interested in the spectral photo-quenching efficiencies of photocapacitance (Taniguchi 149, 150, Hasegawa 451, Zhou 536, Mochizuchi 537, 538), photo-conductivity (Jimenez 210, Hariu 212, 539), or optical absorption (Fuchs 540, Dischler 541, 542). This is because photo-quenching is one of the most important properties of EL2 and also because of the distinctly different results obtained on material with ostensibly the same deep level concentrations. The mechanism for these differences is not yet clear, two leading theories being that an EL2 family exists, or that defects in the vicinity of EL2 affect its photoquenching efficiency in some way. Whatever the mechanism, this technique is clearly a highly sensitive method of distinguishing materials which have similar properties under most other forms of assessment. Other related studies include spectral photoconductance enhancement (Jimenez 210) and the photothermal recovery characteristics from the metastable state (Mita 211, 543, Fisher 544).

4. ASSESSMENT TECHNIQUES USED IN THIS WORK.

4.1 Introduction.

This chapter gives the experimental details of the assessment techniques used in this work. Samples were mainly supplied by ICI Wafer Technology Ltd. Sample details are given in the relevant sections of chapter 6 (6.3.1) and chapter 7 (7.2). The more general aspects of these techniques are discussed in chapter 3.

The experimental details are described here in three separate sections: The first deals with the Near Infra–Red (NIR) assessment of EL2, carried out at Nottingham Polytechnic, in association with M.R.Brozel; the second describes the A/B etching characterisation, carried out at Plessey Research (Caswell) Ltd., with D.J.Stirland; and the third section details the other techniques which have been utilised by various co–workers at Plessey, ICI Wafer Technology Ltd., and the Royal Signals and Radar Establishment.

4.2 Near–Infrared Assessment.

The optical assessment of EL2, as described below, is based on the characteristic EL2 absorption band in the near infra–red, which was discussed in section 2.3.3. The two main types of NIR assessment, which have been used, are described; these are: spectrophotometer line–scans and CCTV imaging. Next, the relative merits of the two techniques are discussed. This comparison leads to the conclusion that some form of quantifying the CCTV images is desirable, in order to obtain EL2 concentrations from them. The [EL2] line–scan system, which was developed to achieve this aim, will be discussed in the chapter 5.

4.2.1 The spectrophotometer.

A Pye–Unicam SP700 double beam spectrophotometer was used for near infra–red EL2 assessment (Stirland 236, Brozel 405). Its response extends from the ultra–violet out to beyond 2μm in the NIR, but, aside from the use of visible wavelengths for alignment purposes, only the NIR region between 0.8μm and 2.μm was utilised.

Absorption versus wavelength scans are carried out, at room temperature, from a wavelength of 0.8μm, which is above the GaAs bandgap (0.878μm), increasing to a wavelength of 2μm, where the contribution of EL2 to the absorption coefficient is negligible. This procedure is carried out to ensure that the absorption spectrum of the sample matches that of the characteristic absorption of uncompensated EL2 ($EL2^{o}$). Aside from EL2 absorption the spectrum may show absorption by free carriers (at the high wavelength end), absorption from the compensated EL2 ($EL2^{+}$), or absorption from other deep level centres such as EL3 and chromium (see section 2.3.3). However, if the absorption spectrum shows the presence of only $EL2^{o}$, then the absorption coefficient in the 1.1 to 1.0μm range can be converted to EL2 concentrations using Martin's calibration (131) with the following equation:

$$[EL2] = f.\alpha = f.\ln(T_2/T_1)/d$$

where, α is the sample absorption coefficient, d is the sample thickness and T_2 is the sample

transmissions at a wavelength where EL2 absorption is negligible, T_1 is the sample transmission, taken at a calibrated wavelength in the EL2 absorption band. The values of the calibration factor, f, at the wavelengths of 1μm (1.24eV) and 1.1μm (1.13eV) are $7x10^{15}$ and $12.5x10^{15}cm^{-3}$ respectively.

In this work T_2 is taken at a wavelength of 2μm and T_1 at a wavelength of 1μm. Therefore, the 1um calibration factor of $7x10^{15}cm^{-3}$ is used.

The change in absorption across a sample was investigated by mounting samples normal to a probing beam and then moving the sample horizontally through the beam, at a slow rate (about 1cm/minute), using a simple scanning mechanism. The technique depends on the high spatial resolution of the spectrophotometer beam. This is achieved by focusing the light emitted from the monochromator to a narrow line at the sample surface. In the visible region this line has approximate dimensions of 5mm hight and 0.2mm width. In the NIR region the beam width is reduced further by the automatic narrowing of the monochromator slits to about 0.1mm. Provided the scanning speed is not too fast, such that the electronic damping in the servo system distorts the output signal, the horizontal resolution will be limited by this beam width. The scanning rail can be raised and lowered to alter the vertical position of the scan. This position can easily be monitored visually by adjusting the beam wavelength into the visible region. Two consecutive absorption scans at 1μm and 2μm are taken in order to obtain the EL2 concentration, as described above. The 2μm scan is necessary as it clearly shows the position of scratches and other surface blemishes which could otherwise be mistaken for variations in EL2 absorption.

4.2.2 Vidicon imaging.

Two dimensional imaging was performed using either a silicon vidicon or an Extended Red Newvicon, close–circuit television (CCTV) camera (Skolnick 054, Stirland 236, Brozel 405). A schematic diagram of the system is shown in fig.4.1. The sample can be illuminated with light from a variety of sources. Usually an array of tungsten lamps with back reflectors is used. A diffusing screen can be placed between the light source and the sample in order to obtain uniform sample illumination. In some cases, a Fresnel lens is placed next to the diffusing screen, in order to increase the incident light intensity, on the CCTV target, at low illumination levels. The CCTV camera was equipped with a variety of lens and extension tubes to obtain different magnifications, focal lengths and depths of focus as required. The maximum magnification possible with the available lenses and extension tubes is about x200. The video signal from the camera was then displayed on a TV monitor, where the variations of grey levels on the screen give a qualitative measure of EL2 (absorption) fluctuations in the sample. The images on the monitor were photographed directly for permanent records.

4.2.3 Comparison of spectrophotometer and imaging.

Comparisons of various aspects of the vidicon and spectrophotometer NIR assessment techniques are given in table 4.1. It can be easily seen from the table that the spectrophotometer has the advantage of being quantitative and allowing spectral investigations, whereas the vidicon technique has much better resolution, flexibility and speed of measurement. Also, the spectrophotometer cannot be used for microscopic investigations (of,

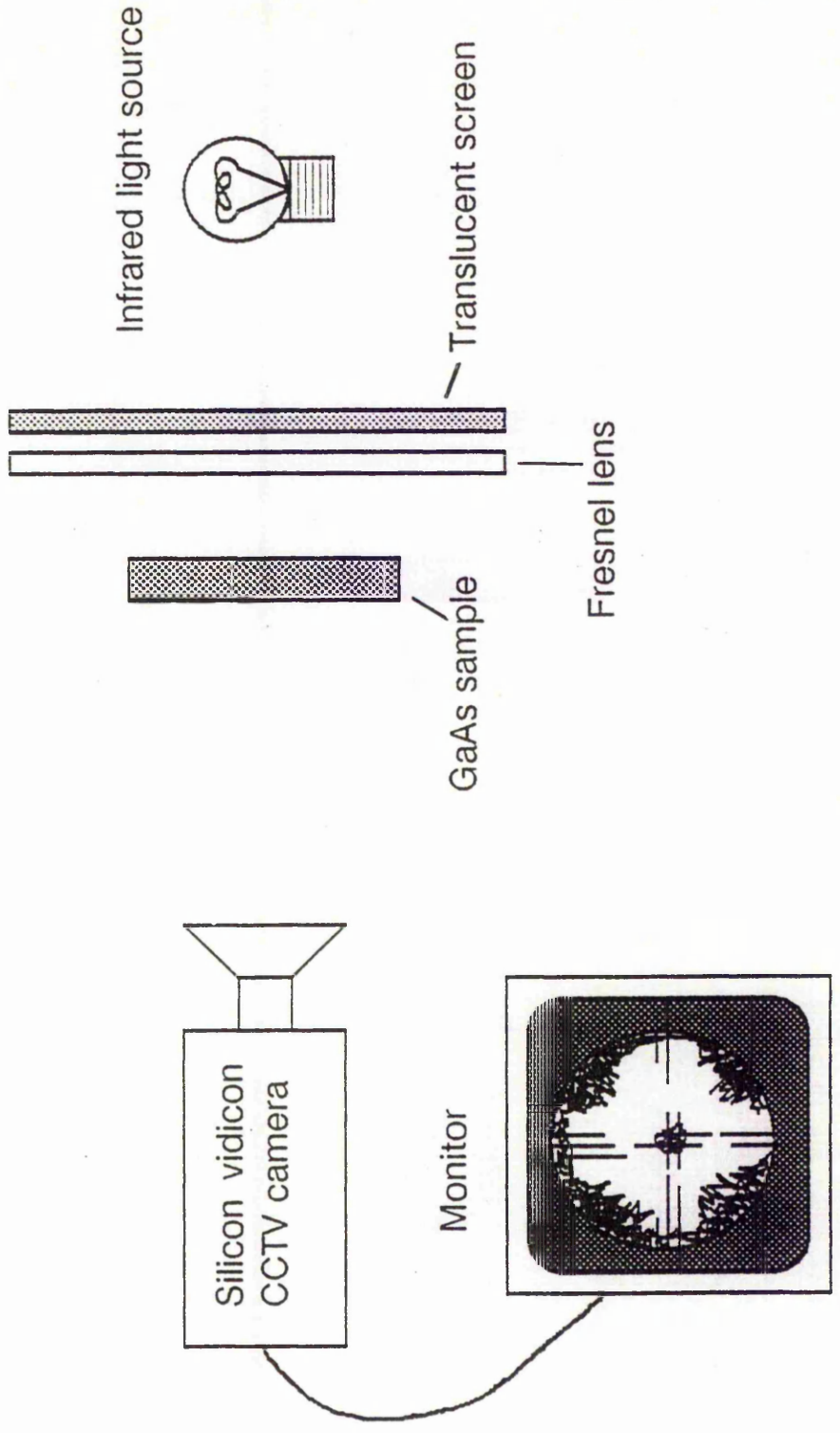

Fig.4.1. Schematic of near infrared imaging system

for example, the EL2 cloud around single dislocations in In doped GaAs). Another problem of the spectrophotometer system is that it does not give a direct [EL2] output. To produce an [EL2]–scan, from the transmission–scans taken at two different wavelengths, a laborious point by point calculation is required (which involves taking logarithms). In fact [EL2]–scans presented from this type of system are often just a scan of sample absorption with a calibrated logarithmic scale. However, a spectrophotometer measurement is required in order to check the NIR absorption spectra, to ensure that contributions from other than $EL2^{o}$ are negligible.

It is clear that a method of quantifying the CCTV imaging system would be advantageous. It would enable the measurement of microscopic fluctuations of [EL2] and would give advantages in the measurement of macroscopic fluctuations, due to the flexibility of the vidicon; in particular the ability to tilt, translate and rotate the specimen. A system to achieve this aim will be discussed in the next chapter.

Table 4.1

A Comparison of the Vidicon and Spectrophotometer methods of NIR Assessment

Spectrophotometer	**Vidicon**
Quantitative for [EL2]	Qualitative for [EL2]
Adjustable and calibrated wavelength selection	Wavelength is adjustable by the use of filters within the range of the wavelength response of the detector.
Spectral scan facility	No spectral scan facility
1D linescan	2D image (psuedo 3D with sample tilting)
Resolution limited by the width of the beam to 0.1mm	Variable magnification from x1 to x 200 with a maximum resolution of 2.5µm.
Moderate horizontal (~0.1mm) and poor vertical (~10mm) resolution	High resolution limited by magnification and screen resolution (up to 4µmx4µm)
No depth resolution	Depth resolution with high f number optics and high magnification
Slow acquisition time (~15 mins for 3" samples)	Very fast acquisition giving 'real time' sample adjustment

4.3 A/B Etching

The A/B etch, devised by Abrahams and Buiocchi (369) and developed by Stirland and co–workers (Stirland 367, 370), was used to study dislocation behaviour at the surface region of GaAs samples. This etch was compared with other available etches in section 3.2.1. The etch

consists of a mixture of silver nitrate solution (13g/ml) chromic acid (456 gm/l) and hydrofluoric acid (40%) in the volume ratio 1:3:2.

Before etching the mechano-chemically polished surfaces of the samples were chemically polished for 5 minutes in 3:1:1 H_2SO_4:H_2O_2:H_2O at 45°C, to remove residual work damage. The A/B etching is then carried out at room temperature, typically for 5 minutes, with an etch rate of approximately 2.5µm/minute (Stirland 370). The etched surface was examined with a Nikon, Nomarski interference contrast microscope and photographs of the surface were taken at various magnifications between x33 and x537. Dislocation densities were measured from the photographic images using the grid intersection method (Clark 039). In addition, surface profiles were taken, after A/B etching, using a Tencor surface profile instrument. Surface profiles were taken at Plessey Research (Caswell) by D.J Stirland.

4.4 Other Assessment Techniques.

4.4.1 X-ray topography.

X-ray topography was used, in the study of dislocations in In-doped material, described in chapter 6. Reflection and transmission X-ray topographs were taken, from various lattice planes, with a conventional Lang camera (Lang 388). Reflection topographs were taken using Cu(Ka) and transmission topographs were taken using Mo(Ka) radiation. More details on the specific topographs, including the lattice planes selected, are given in section 6.4.1. X-ray topography was carried out at Plessey in association with D.G.Hart.

4.4.2 Cathodoluminescence.

Low temperature (approximately 10K) Cathodoluminescence (CL) measurements were carried out on a modified Cambridge instruments S150 SEM, in the wavelength-dispersive CL mode. The SEM was operated between 10 and 20 kV. An S20ER photomultiplier was used in conjunction with the scanning facility of the SEM to obtain micrograph like maps of near band edge luminescence. The work was carried out at RSRE by C.A.Warwick.

4.4.3 Electrical assessment.

Two types of Hall effect measurement were used to electrically assess the substrate material in this work:

Firstly conventional Hall effect measurements were carried out at room temperature (Grant 548). Resistivities, carrier concentrations and mobilities were calculated from the data. The work was carried out by I.Grant and Y.Hokino at ICI Wafer Technology.

Secondly, temperature dependent Hall effect measurements were carried out, in order to gain information on the activation energy of the centres controlling the electrical properties of the material (Blunt 549). Carrier concentrations, resisitivities and moblities were also evaluated. Results were taken at temperatures in the range of 100°C to 150°C. The data was extrapolated back to room temperature to enable comparison with the earlier room temperature results. This work was carried out by R.T.Blunt at Plessey Research, Caswell.

5. THE EL2 LINE-SCAN SYSTEM.

5.1 Introduction.

The advantages of quantifying the vidicon imaging system to produce a map of [EL2] fluctuations were discussed briefly at the end of the last chapter. In practice this is not easy to achieve (see section 5.3), and so a compromise solution to the problem has been chosen. Firstly, in order to reduce the computational effort, data storage requirements and cost, a line–scan rather than a full screen approach has been taken. Secondly, the spectrophotometer must be used to calibrate the digitiser for each new sample (since the samples Near Infra–Red (NIR) absorption spectra must be checked against the EL2° "signature" for the absorption calibration to be validated, this is not a great limitation).

The system can be used to produce NIR absorption line–scans across GaAs samples. These are then converted to [EL2] line–scans using the calibration. An additional feature allows the production of background scans which contain information on non–uniform sample illumination. By dividing the absorption line–scans by the relevant background scans, true sample absorption line–scans can be obtained with the effect of non–uniform illumination removed. [EL2] scans are usually obtained from these "processed" line–scans.

The layout of this chapter is as follows: firstly the system will be described, with separate sections on the hardware, software and on its operation; secondly, the procedure for calculating [EL2] line–scans from absorption line–scans will be discussed with particular emphasis on the calibration method and its limitations.

5.2 System Outline.

5.2.1 General description.

The system is based around the vidicon NIR imaging set–up described in section 4.2.2. A video line, containing information on the variation in NIR absorption across a GaAs sample, is extracted from the CCTV camera output. It is then digitised, using a 10 MHz Analogue to Digital (A/D) converter and the digital data is stored in external RAM. In the time taken for the video signal to cycle back to the selected line, data is transferred, from the external RAM, to a BBC microcomputer. This entire process is repeated a chosen number of times (usually 256), with the line–scans being averaged in the BBC; the averaging is necessary as vidicon cameras tend to be rather noisy. The resulting averaged absorption line–scan can be stored on disc, displayed on a monitor, or printed out. It then can be processed and converted to an [EL2] line–scan with the aid of a point calibration (using a measurement from a spectrophotometer). The [EL2] line–scan can then be displayed, stored and printed as described above for the absorption line–scan.

5.2.2 Hardware.

The circuits to be described are housed in three die cast boxes. The line selector box holds the sync–separation, line selection and frame counter circuits. The digitiser box contains the analogue input, A/D converter, sync–generation, multiplexer and external RAM circuits. Finally

the mixer box holds the video mixer circuit which enables the line selected to be highlighted on the near infra–red (NIR) image. A block diagram of the system is given in fig.5.1 and the corresponding circuit diagrams are given in appendix 5.1. Each circuit will be discussed in turn below.

CCTV camera and synchronisation.

The Hitachi, silicon–vidicon CCTV camera was used in the NIR imaging apparatus (as described in section 4.2.2), to provide the video input signal for the system. The camera was synchronised to the clock of the digitiser, using a Ferranti ZNA134J TV synchronising pulse generator, which produces line and field drive signals for the camera's external synchronisation facility. The external synchronisation circuit diagram is given in appendix 5.1.1.

Line selector.

This can be divided into several sub–circuits:

The first circuit separates the line drive and field drive signals from the video output of the camera. These signals could have been derived from the ZNA134J synchronising pulse generator but this would have greatly reduced the flexibility of the system as it would not operate with an unsynchronised camera. With the present circuit the system can be configured to run from any standard video output, synchronised or not. The circuit diagram is given in appendix 5.1.2(a and b).

The second circuit enables the user to select a line number from either field of the video frame. A high pulse is generated for the duration of this line which will be referred to as "line" in the text. The "line" pulse starts and finishes on consecutive leading edges of the negative going video line sync–pulses. The "line" signal is used to control the multiplexer for the external RAM, generate an interrupt in the BBC User port and to indicate the selected line on the display monitor. The circuit diagram is given in appendix 5.1.3(a).

The third circuit enables a selection of the number of frames to be averaged. This can be set to 9, 90, 900 or infinite (that is no frame end–number requested). When the counter reaches the selected number the output disable goes low and the "line" signal is disabled (note that the output disable will be permanently low unless the ON/OFF switch is in the ON position). The "line" signal can be enabled again by pressing the RESET button (note that after switching on, RESET must be pressed as "line" will be initially disabled). In this work, the frame setting "infinite" is usually selected and the number of frames the line–scan is averaged over is then chosen in software. The circuit diagram is given in appendix 5.1.3(b).

Analogue input.

The analogue input circuit is based around a TDC1048 video flash A/D converter. Its features are: 8 bit resolution, 20 megasamples per second with 1/2 LSB linearity and low power consumption. Although the A/D, RAM and multiplexer could be operated at 20 MHz, for ease of operation and circuit construction a clock speed of 10 MHz was chosen. Note that the gain and offset potentiometers are used as a fine adjust for the input signal range seen by the A/D converter and should not normally be altered once set for a specific input. The A/D is free running with the digital output only being transferred to external RAM when "line" is high. The

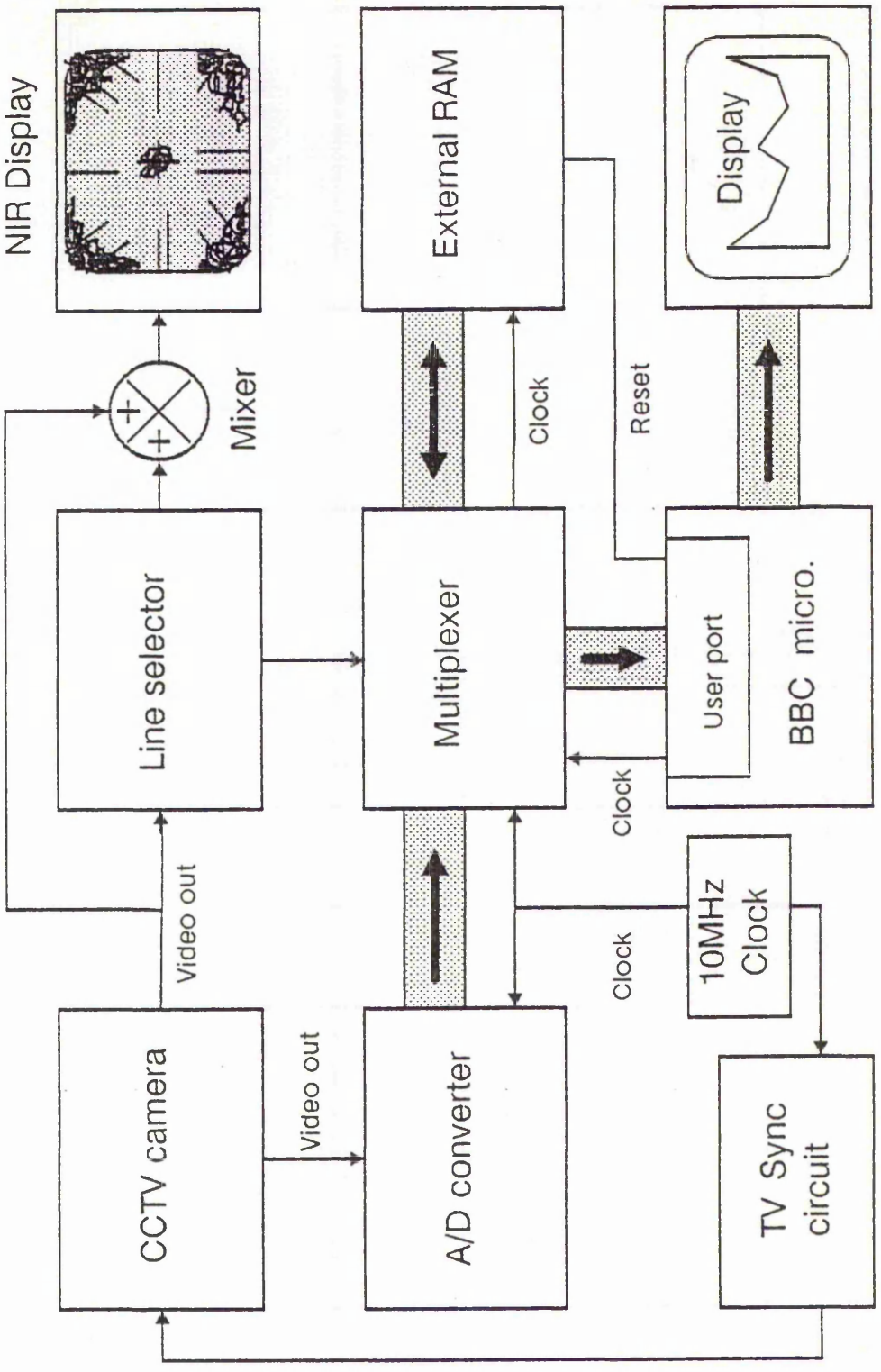

Fig.5.1 [EL2] line-scan system electronics block diagram.

circuit diagram is given in appendix 5.1.4.

Multiplexer and external RAM.

Two 74LS442 tri–directional latches control the 8 bit data flow for the RAM between (input from) the A/D converter ("line" high) and (output to) the BBC User port ("line" low). In addition one 74LS442 latch determines whether the clocking and control of the RAM arises from the 10 MHz clock on the A/D board ("line" high) or the low frequency clock in the BBC microcomputer, via the User port ("line" low). The RAM was required to operate at at least 10 MHz and store up to 640 bytes (time between consecutive lines is 64us) of 8 bit data. A CY7C128 2kx8bit static RAM with a 45ns access time was chosen. This allows for a possible alteration to a 20 MHz clock at some future date. The circuit diagram is given in appendix 5.1.5 and the timing diagram for the RAM is given in appendix 5.2.

BBC Microcomputer and VIA.

A microcomputer based rather than a microprocessor based, system is required because of the need for the data to be displayed on a monitor, stored in RAM (or on disc) and recorded on a printer. The BBC microcomputer was selected because of its low cost, flexibility for external control and adequate programming and data storage facilities. The microprocessor system included an NEC PC–8023BE–N printer and an LVL duel 5.25" disc drive with double density, double sided, floppy discs.

Input from the external RAM and external control are carried out through the BBC user port which is based around a 6522 Versatile Interface Adaptor (VIA). The configuration of the VIA is given in appendix 5.3. Briefly, data is accepted, in parallel as 7 bit bytes, along 7 of the 8 data lines of the User port. The least significant (8th) bit of the data stored on external RAM is discarded (because the noise level exceeds the magnitude of the least significant bit of the 7 bit byte, this does not create any problems). The eighth "data" line is used to reset the external RAM address counter. The two User port control lines (CB1 and CB2) are respectively set as an interrupt (which is generated from the inverted "line" signal) and a clock for the RAM address counter.

Video mixer box

This circuit mixes the video output of the CCTV camera with the "line" signal from the line selector box. The output provides the video signal for the display monitor which then shows the line selected from the video signal highlighted on the NIR image. The highlighted line can be removed or replaced, on a toggle basis, by pressing the reset button on the line selector box. The circuit diagram is given in appendix 5.1.6.

5.2.3 Software.

The system software is based around a main menu which is given in fig.5.2. Each menu selection will be described in turn after preliminary sections on the main program/menu and the screen dump (which can be called from both of the display routines). Schematic flowcharts for some of the menu selections and program listings are given in appendix 5.5. A memory map for the BBC is given in appendix 5.4.

MENU

R	RUN data acquisition program
D	DISPLAY linescan
G	Display GRAPH of [EL2]
M	MODIFY display
S	SAVE linescan on disc
L	LOAD linescan from disc
C	CATALOGUE
N	Drive NUMBER
A	AVERAGE 8 scans
B	Remove BACKGROUND
E	Calculate [EL2]
F	Calculate [EL2] FLUCTUATIONS

Fig.5.2. The main menu display for the [EL2] line-scan system software.

Main programme and menu.

The main program which includes the menu, display, and all of the call routines for the subprograms, is stored as "DIGIT" on the "linescan software" disc. The program, which is written in BASIC, is listed in appendix 5.5.1.

Screen dump.

The screen dump machine code subroutine, which is stored on disc as "MCDPNEC" cannot be called from the main menu. On entering either of the two display routines, a request "Do you want a hard copy Y/N?" occurs. If "Y" is typed in answer to this question, the screen dump routine is automatically loaded after the absorption line–scan (or [EL2] line–scan) is displayed and the screen will then be copied to the printer. A listing of the assembler routine is given in appendix 5.5.2. The program is written for an NEC PC8023BE–N printer and the print format is vertically condensed by a factor of two, from the screen format, to reduce printing time.

Data acquisition.

The machine code data acquisition program, is stored as "MCLOAD2". The assembler listing is given in appendix 5.5.3 and a flow diagram for the program is given in fig.5.3. The program consists of three subroutines.

The first is an initialisation routine in which the VIA status is set (as shown in appendix 5.3) and the memory space used to store the data from the absorption line–scan is cleared.

The second routine is called on interrupt; if the interrupt came from the VIA then the interrupt variable is set to indicate this.

The third routine contains the main bulk of the program. Firstly, the interrupt variable is checked. If an interrupt has occurred, since the last time the program was entered, then the remainder of the subroutine is executed; otherwise it is skipped. Next, the address counter of the RAM is set to zero, by a reset pulse via the user port, and the (seven bit) data bytes are clocked into the BBC RAM on (hex) pages &29 to &2E. After the data input is complete, the address counter is reset to zero again and the machine waits for another VIA interrupt before loading the next line of data. The input process is usually repeated 256 times (to give a signal to noise ratio improvement of a factor of 16 for stochastic noise) with each data point being added to a running total (within a two byte format) to give a 13 bit result. After this, the VIA interrupt is disabled and the main menu is re–loaded.

Display line–scan.

This routine is part of the main BASIC program. It provides a display of the current absorption line–scan (stored in memory on pages &29 to &2F) on the screen of the BBC monitor. On entry to the routine there is an option of selecting a copy of the screen to the printer, as described in the screen dump section above. This is followed by the option of giving the linescan a title, after which the absorption line–scan will be displayed (and printed if a screen dump was selected). [EL2] line–scans can be displayed with this routine but no concentration axes will be provided. More details on this routine, the [EL2] line–scan display, the "modify display" routine and the

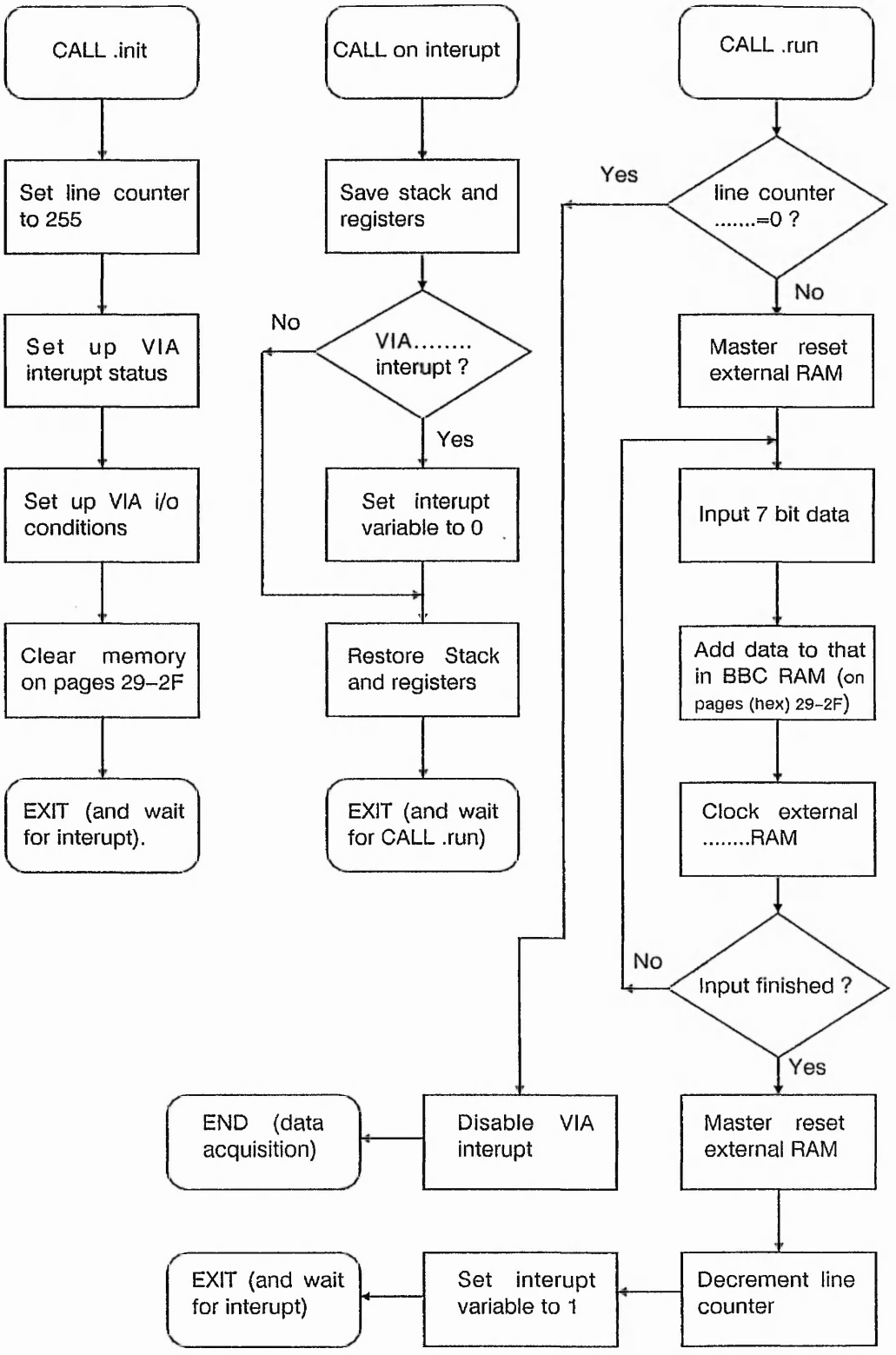

Fig.5.3. Flow diagram of the data acquisition program for the [EL2] line–scan system. The .run routine is called from the main program if the interupt variable =0. Note that the absorption line–scan data is stored in (hex) pages 29 to 2F of the BBC RAM. The line counter is used to count the number of full sets of line–scan data that have been taken into the BBC (where they are averaged). Master reset causes the external RAM address to be set to 0 (either for data input from the A/D convertor, or data output to the BBC)

screen layout, are given in appendix 5.6.

Display graph of [EL2].

This routine is part of the main BASIC program. It uses much of the software of the display line–scan routine but the axes are labelled with EL2 concentrations. It follows that only [EL2] line–scans can be usefully displayed in this mode. Fig.5.4 shows an example of this display.

Modify display.

This routine is part of the main BASIC program. It allows an absorption line–scan (or an [EL2] line–scan) to be enlarged and offset in both horizontal (x) and vertical (y) axes; to enable details of the scans to be seen more clearly. The standard screen image, with x and y magnifications of 1 and with x and y offsets of 0, is altered in accordance with the values selected in this routine. The resultant image is displayed in the format (absorption line–scan or [EL2] line–scan) last selected from the menu. Note that a unit of offset in both x and y directions corresponds to one eighth of the screen.

Save linescan on disk.

This allows an absorption line–scan or [EL2] line–scan to be stored on disc. The filename for the scan has a maximum length of 7 characters. Pages &29 to &2F will be stored on disc using a *SAVE operation with the selected filename. The routine is part of the main BASIC program.

Load linescan from disc.

This allows a named absorption line–scan or [EL2] line–scan to be loaded from disc, to pages &29 to &2F of the BBC RAM. The routine is part of the main BASIC program.

Catalogue.

This routine is part of the main BASIC programme. It allows you to perform a "*CAT" (catalogue) operation, to investigate the contents of a chosen drive without having to exit and re–enter the programme.

Drive number.

This routine is part of the main BASIC program. The drive number selected will be the current disc drive on which absorption line–scans or [EL2] line–scans will be saved and loaded. A choice of drive number from 0 to 7 is possible using the LVL disc filing system with double sided, double density discs. Drives 1 to 7 are usually used to store the absorption line–scans and [EL2] line–scans and drive 0 is used to store the system programme. On switching on the BBC the drive selected will default to drive 0.

Average 8 scans.

This calls the program "AVERAGE", which takes 8 absorption line–scans (or [EL2] line–scans), adds them together and divides the result by 8. The routine can also be used to average 4 or 2 lines by entering the relevant scans twice or four times each, respectively. This program is particularly useful when comparing absorption line–scans from the digitiser with those from the spectrophotometer. This will be discussed in more detail in section 5.3. The program listing is given in appendix 5.5.4.

Remove background.

This calls the program "DIVIDE" which takes the unprocessed absorption line–scan and divides it by its corresponding background scan. This program is used to produce an absorption line–scan without the effects of non–uniform sample illumination and blemishes on the CCTV camera detector. An example of its application is given in fig.5.4. The unprocessed scan is shown in fig.5.4(a) and its corresponding background scan in fig.5.4(b). The processed absorption line–scan obtained using the "DIVIDE" program is shown in fig.5.4(c). The main problem with this process is obtaining a "true" background scan.

Different methods of obtaining the background scan and the implications for the accuracy of the [EL2] line–scans obtained from the processed line–scans, are discussed in section 5.3. The program listing is given in appendix 5.5.5.

Calculate [EL2].

This calls the program "EL2" which calculates an [EL2] line–scan from the current absorption line–scan in memory. The program requires the sample thickness and transmission coefficients at 1μm and 2μm (obtained from the spectrophotometer) at the calibration point to be typed in, on request. The calibration is achieved by moving a cross to the corresponding point on the line–scan, and then pressing RETURN. This equates the y coordinate of the cross with the 1μm transmission calibration and intensity fluctuations of the line–scan are then assumed to correspond to fluctuations of 1μm transmission about this value. EL2 concentrations are then calculated from the line–scan in the usual manner. An example of an [EL2] line–scan is given in fig.5.5, it was calculated from the processed absorption line–scan shown in fig.5.4(c).

The calibration, its assumptions and consequences will be discussed in more detail in section 5.3. The program listing is given in appendix 5.5.6

Calculate [EL2] fluctuations.

This calls the program "FLUCTS" which calculates fluctuations of EL2 concentration about a line on an [EL2] line–scan. The line in this case is determined by a linear regression between two points on the scan (selected by moving the cursor keys and pressing RETURN for the right and left hand end points respectively). The standard deviation (or root mean square fluctuation) about this line is printed on the screen in the units of $[EL2]x10^{14}cm^{-3}$. the program listing is given in appendix 5.5.7.

5.2.4 Operating the system.

This section gives a brief description of the usual method of operating the system, note that it is not intended to be the only method as the design deliberately includes a degree of flexibility.

The system is best initialised in the configuration described in section 5.2.2 and which is illustrated by the block diagram in fig.5.1. The ON/OFF switch on the line selector box should be set to ON, the frame counter switch should be set to "infinity" and the reset button should be pressed. A highlighted line will now be visible on the NIR image corresponding to the selected line.

The main BASIC program, DIGIT, can be loaded from the linescan software disc by either a

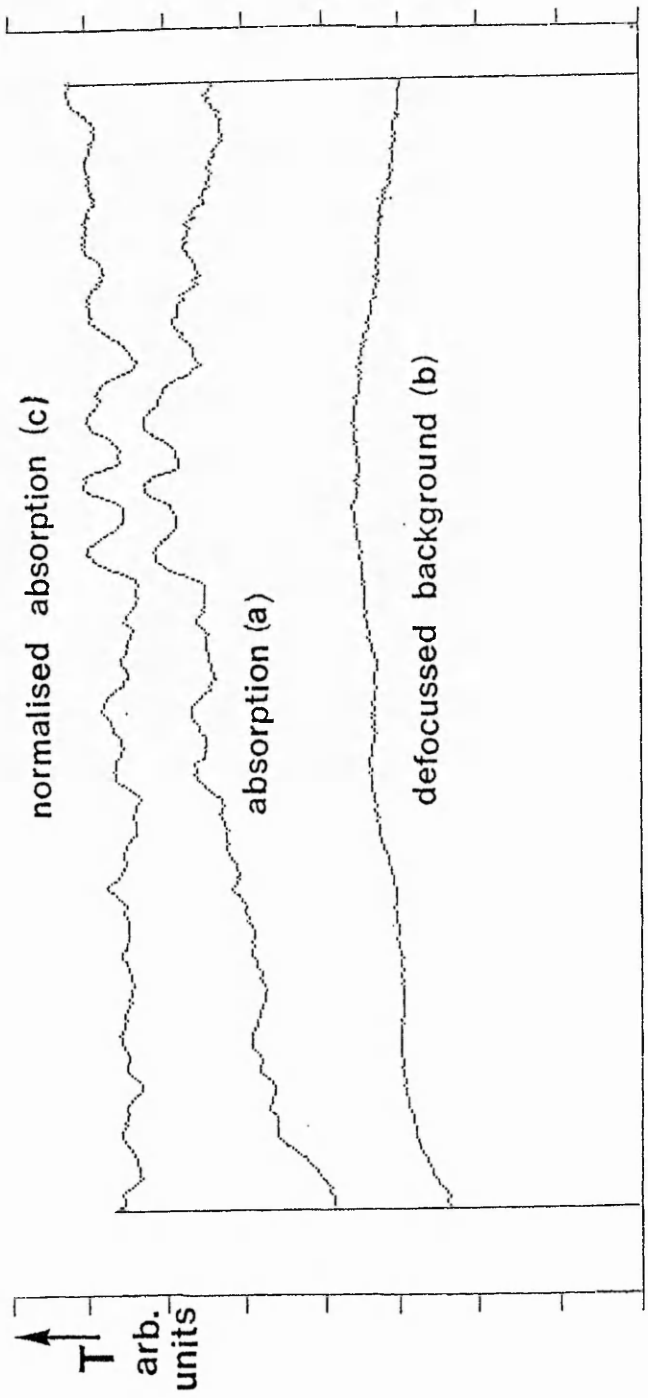

Fig.5.4. Example of an absorption line–scan across an undoped SI LEC GaAs sample (a) together with a defocused background line–scan showing the illumination profile for the sample (b). The absoption line–scan is divided by the background line–scan on a point by point basis to give the normalised (or processed) absoption line–scan (c), which gives the true sample absorption profile.

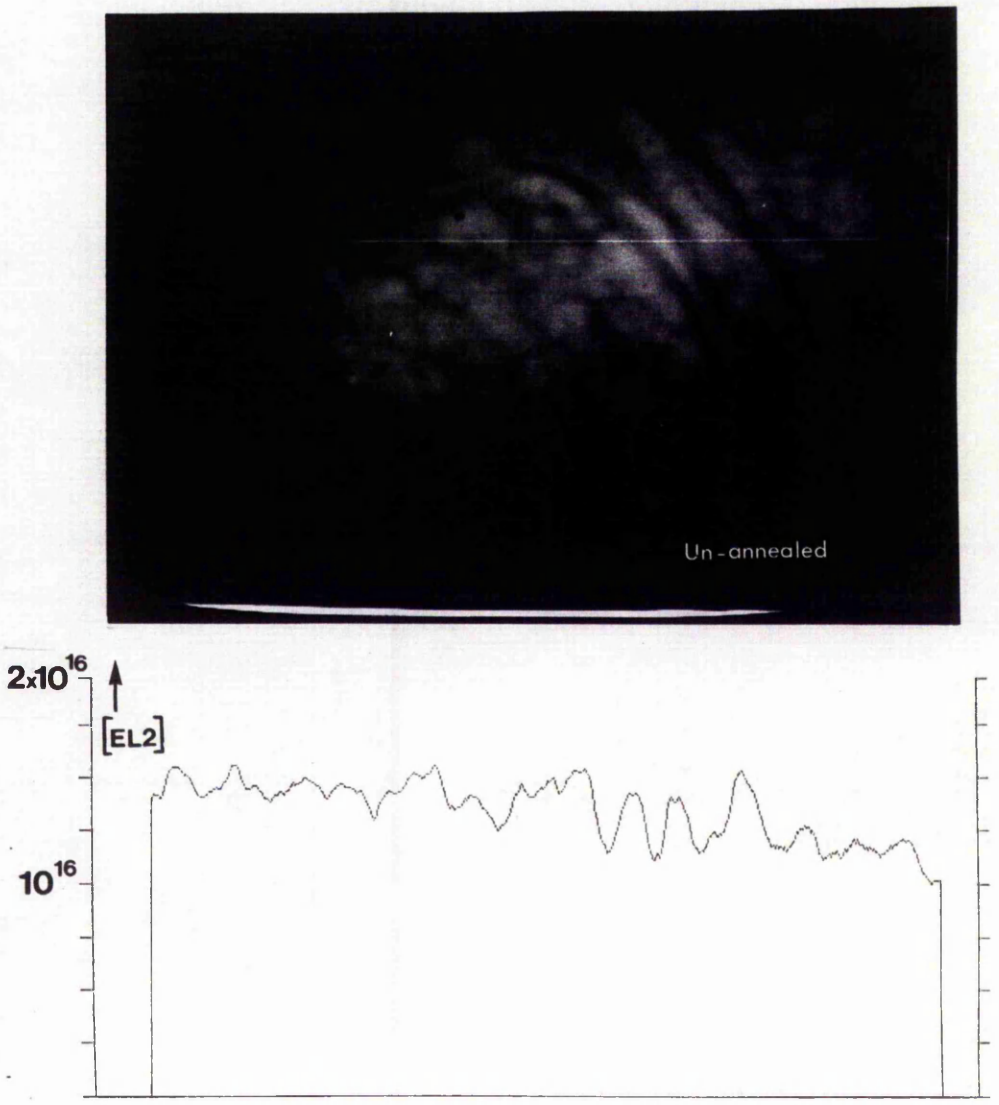

Fig.5.5. An example of an [EL2] line–scan together with the NIR absorption image from which it was obtained. The [EL2] line–scan was calculated from the normalised (or processed) absorption line–scan in Fig.5.4(c). Note that the fall off in transmission at the edge of the NIR image is mainly due to the non–uniform sample illumination. This feature is removed from the [EL2] line–scan by processing (dividing the raw absorption line–scan by the background).

"Boot" operation (press shift and break keys simultaneously) or by typing "LOAD "DIGIT" (RETURN) RUN (RETURN)". The menu (as shown in fig.5.2) will now be displayed on the screen. Next N should be pressed, the (disc) drive number it is wished to load and save line-scans to is typed and followed by RETURN. An absorption line-scan is now ready to be loaded by pressing R. After loading, the line-scan can be manipulated using the menu routines, as described in section 5.2.3. The selected line can be changed using the line counter switch bank, and the video field selection switch (EF/OF) which enables even or odd video fields to be chosen. This line selection procedure can be monitored using the line trace indicated on the NIR image.

5.3 [EL2] calibration.

5.3.1 Method of approach.

The principle behind the calibration is that intensity variations on a processed absorption linescan can be assumed to represent changes in transmission at a particular wavelength, within the optical band pass of the system (this assumption is discussed in more detail in section 5.3.5). This absorption linescan can then be calibrated by measuring, at a point on the sample intersected by the scan, the transmission, both at the calibration wavelength and at 2μm, using a spectrophotometer. The wavelength chosen for the calibration is not critical, as changes in absorption coefficient (α) are linear with changes in [EL2]. It follows that different wavelength calibrations will only differ by the constant used to convert the absorption coefficient to [EL2]. For convenience the "standard" wavelength of 1μm is used.

5.3.2 Procedure.

The use of the "EL2" program to calibrate the processed absorption linescan and calculate the [EL2] line-scan is outlined in section 5.2.2. The calculation of the [EL2] line-scan occurs on line 440 of the program and is represented by the equation below, where the two byte (13 bit) data points are called DATA.

$$[EL2]=(114688 \times \ln\{T2 \times Tx32/(DATA \times T1)\})/d$$

Where d is the sample thickness in mm; T1 is the sample transmission at a wavelength of 1μm; T2 is the sample transmission at a wavelength of 2μm; and T is the screen graphics y coordinate of the calibration point on the absorption line-scan, obtained using the cursor. The multiplication by 32 (which is the ratio of the maximum values of DATA and T) is to ensure that the absorption coefficient is calculated correctly by normalising the logarithmic operation to ln(T2/T1). The multiplication by 114688 ensures that the top of the screen (maximum y coordinate) corresponds to an EL2 concentration of 2×10^{16} cm^{-3}. An absorption coefficient of $1cm^{-1}$, at a wavelength of 1μm, corresponds to an EL2 concentration of $7 \times 10^{15} cm^{-3}$, using Martin's calibration (Martin 131). The maximum y graphics coordinate is 1024; hence, an absorption of $1cm^{-1}$ should correspond to a graphics coordinate of 358.4. Also the sample thickness is entered in millimetres rather than in centimetres and the scan is plotted with a graphics vertical scale factor of 0.03125. Hence, the screen calibration factor will be 358.4x10/0.03125 = 114688.

5.3.3 Background subtraction.

The program which removes background effects, involves a point by point division of the raw absorption line–scan by a background scan. The background scan contains any blemishes on the silicon vidicon and non–uniformities in sample illumination, here referred to as the illumination profile. The most obvious method of obtaining the background scan is to remove the sample. Unfortunately, due to the high refractive index of GaAs (n=3.55 at 1μm), the illumination profile is altered by this process, particularly at the edges of the viewed sample. An alternative approach is to put the sample out of focus for the camera. This has the effect of blurring fine scale variations but maintaining larger scale changes (of the order of the size of the screen). These larger scale changes will then be removed by the background subtraction along with the illumination profile. Also, if the depth of focus is large, as is usually the case at low magnification, the illumination profile can be changed considerably by altering the focus. For example, an aperture used to prevent light passing round the edges of a sample will appear to blur at the edge, when viewed by the camera, as it goes out of focus. This results in a large degree of distortion in the processed image near the aperture edge. Hence, this second process is most useful for samples which are macroscopically uniform, have small "screen size" transmission changes and when apertures are not being used. It is also useful for viewing samples at high magnification, where the depth of field tends to be less and the effect on the illumination profile of defocusing is reduced. Both of these factors are usually satisfied when imaging threading dislocations in In–doped samples. The defocusing method is also useful when any macroscopic changes are to be ignored, for example when calculating the local [EL2] fluctuations across cell walls and lineage.

An example of background subtraction by defocusing was given in fig.5.4.

5.3.4 Comparisons with a spectrophotometer.

The typical beam size, and hence spatial resolution, of the Pye–Unicam SP700 spectrophotometer is 5mm by 0.1mm (see section 4.2.1) whereas the resolution of the digitiser is limited by the magnification, the bandwidth of the system and ultimately the quality of the optics. For a direct comparison of the two systems an effective aperture must be constructed for the digitiser, to match the spectrophotometer aperture.

Using the digitiser, a two inch GaAs wafer which fills the screen will have about 460 sampled points across it. This corresponds to a horizontal screen resolution of 0.1mm. For 625 lines vertical resolution, one line corresponds to approximately 0.08mm and 62.5 lines gives 5mm. Hence by taking eight lines at every fourth line in one field (a span of 56 lines) and using the AVERAGE routine (see section 5.2.3) a reasonable comparison with the spectrophotometer can be achieved.

A comparison between a spectrophotometer scan and a processed absorption line–scan obtained using the AVERAGE program, as described above, is given in fig.5.6. The correlation is seen to be good although differences will always exist because: the linescan is not a true scan of 1μm transmission (as discussed in section 5.3.5); the spectrophotometer scan is damped; and neither scans include an in–situ 2μm subtraction.

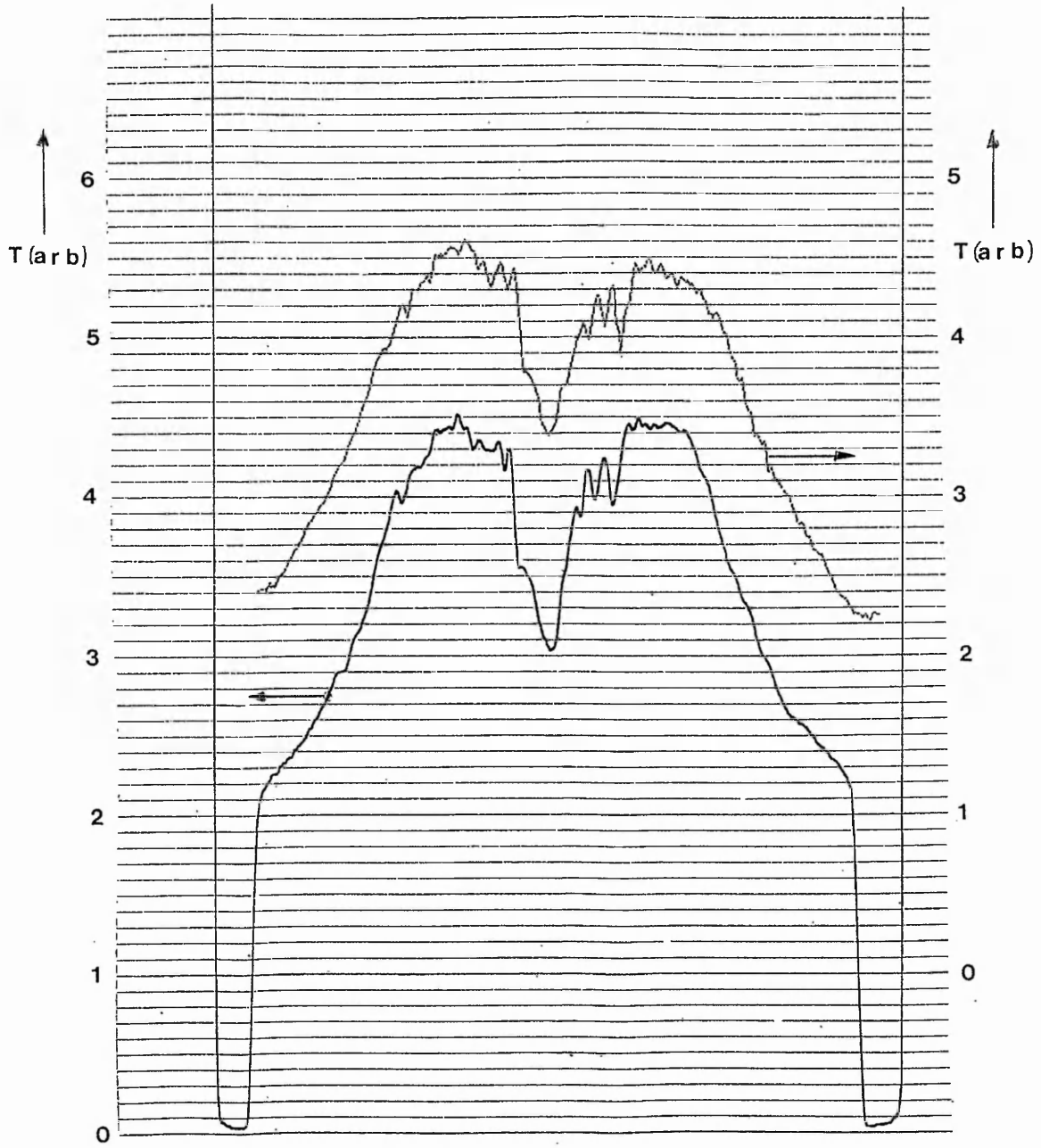

Fig.5.6. A comparison of absorption scans, across the same position of a 2" diameter GaAs sample, obtained using the spectrophotometer and the [EL2] line–scan system. The scale is measured in arbitrary units of Transmission (T) where 0 represents black for both scans.

The bottom absorption scan is taken directly from the spectrophotometer chart recorder. The top absorption scan is obtained from the [EL2] line–scan system. This has been processed (to remove non–uniform illumination effects) and averaged over 8 evenly spaced video lines (covering a span of 57 video lines in one field) in order to produce an aperture which matches the spectrophotometer beam. Note that the scale for the second absorption scan is shifted upwards by 1 Transmission unit in order to enable easy comparison.

5.3.5 Problems with the [EL2] calibration.

This discussion will be limited to problems with the digitiser system calibration rather than the inherent problems of measuring EL2 concentrations from NIR absorption. For a discussion of these problems see section 2.3.4.

Non–linear response of system.

This section is concerned with the non linear response of the digital output (of the A/D converter) to the light intensity input (incident on the vidicon tube). This is influenced by time dependent features such as the frequency bandwidth and slew rate, and time independent features such as the gamma factor of the vidicon target and any other non linear amplitude response of the camera electronics. These problems will be discussed in turn below.

The bandwidth of the system in this case is mainly determined by the analogue input circuit, (the video op–amp circuit). The frequency is chosen by adjusting a compensating capacitor (see appendix 5.1.4), which allows a trade off between lost system bandwidth and reduced overshoot (or ringing) at the video op–amp output in the analogue input circuit for the A/D. The frequency is set in this case to about 4 MHz. Note that the Nyquist limit of the A/D is 5 MHz with a 10 MHz clock, and the camera bandwidth is about 9 MHz.

Experimentally, the camera output signal shows noticeable distortion on black–white transitions, notably at the edge of an aperture. This slew rate type of effect is probably a feature of the camera tube but no details are available on its magnitude. This effect will distort the signal where contrast is high. Examples would be at dust specks, scratches and, less noticeably but more importantly, at lineage or at single dislocations in In–doped GaAs. This effect will obviously be of less importance as the magnification is increased.

The gamma factor (Γ) of the camera is defined as:

$$\log(I) = \Gamma.\log(L)+k$$

Where L is the incident light intensity, I is the detector output current and k is a constant. The current analysis depends on a unity gamma factor but by altering the [EL2] calculation program could be adapted for a camera with non unity gamma factor.

Monochromicity of the light detected by the camera.

The calculation of the [EL2] line–scan assumes that the intensity variations on the camera correspond to changes in transmission at one wavelength (in this case at 1μm). This can be achieved by using narrow band pass filters but in practice this makes little difference to the line scans obtained (see section 3.6.1) and results in a more noisy image.

Background subtraction.

The problem in obtaining a true background scan and its effect on the processed absorption line–scan were discussed in section 5.3.3. These problems produce distortions in the processed absorption line–scans and therefore in the corresponding [EL2] line–scans. Unfortunately, these distortions, although small in the line–scans, tend to be magnified in the [EL2] line–scans because of the logarithmic transformation involved in the calculation. For example, a 1% variation in intensity in the absorption line–scan for a 2mm thick sample with a

mean [EL2] of $10^{16}cm^{-3}$, gives approximately a 3.5% change on the [EL2] line–scan.

Depth of focus.

When taking an absorption line–scan, which will be converted to an [EL2] line–scan, the entire sample must be within the depth of focus of the camera for two reasons: firstly, the thickness entered in the calculation of the EL2 scan is that of the sample; secondly, out of focus contributions from the non–uniform [EL2] distribution will be included in the resulting scan, producing distortion. This factor puts a limit on the maximum magnification of an [EL2] line–scan which can be obtained from a sample using a lens with a particular f number.

2μm reference.

As described in section 4.2.1, [EL2] scans obtained from the spectrophotometer, rely on a 2μm background scan to remove the effects of sample reflectivity, dust, scratches and precipitates. There is no 2μm reference for the [EL2] line–scan system and hence the effects of dust, scratches and precipitates in particular could be included in the scan. Therefore, areas with these features should be avoided. If this is not possible, they should be documented by a photograph of the NIR absorption image, showing the intersection of the scan with the relevant feature. Reflectivity is assumed to be uniform across the sample.

In principle, using a camera sensitive to 2μm and 1μm wavelengths with filters would overcome the problems described above. Unfortunately, no such camera was available for this work. It would also be possible to use two cameras, one sensitive to each wavelength and interchange them to obtain the two scans. However identical alignment and optics would be difficult to achieve and the system would lose a great deal of its speed and flexibility of measurement.

5.4 System Applications.

The particular applications for which the system was designed are as follows:

1) Investigating the gettering of EL2 by single dislocations in In doped GaAs and the effects of annealing on this gettering.

2) Calculating the magnitude of [EL2] fluctuations at cell walls and lineage, to investigate the effect of heat treatments on these fluctuations.

3) Taking full slice scans, with improved speed of measurement and superior vertical resolution compared to the spectrophotometer system.

The first two of the above applications take advantage of the high resolution of the system. The last takes advantage of the direct [EL2] output. The spectrophotometer which gives a percentage absorption output on chart recorder paper which then must be converted, laboriously, by hand, to an [EL2] scan. This is a time consuming process which also involves loss of information.

In addition to the above applications, the system can be used as a general purpose video line scanner.

6 DEFECT ASSESSMENT IN In-DOPED MATERIAL.

6.1 Introduction.

This chapter contains the following sections: a brief review on the dislocation structures of In-doped GaAs; an outline of the sample details and the experimental procedures carried out in this work; the results of these experiments; and a discussion including the implications of the results for various aspects of In-doped and undoped material. The results and discussion presented here are concentrated on the [001] direction dislocations found in the central region of the ingot.

6.2 Dislocation Structures in In-doped Material.

Pichaud et al (550) divided dislocations in In-doped material into three groups: group A, which included tangled dislocations; group B, which included dislocations in non-crystallographic directions; group C, which included long straight dislocations. Group A usually occurred in bands, associated with growth striations. Group C was subdivided into several types: those with standard $a_o/2<110>$ burgers vectors in [001], <112> and <011> directions; and those with standard $a_o/3<111>$ burgers vectors in <112> directions.

Scott et al (551), investigating silicon-doped material as well as In-doped material, split dislocations into two groups:

> The first group consisted of the dislocations around the perifery. These fitted the standard <110>/{111} glide set, with standard $a_o/2<110>$ burgers vectors. They were probably introduced by thermal stress.
>
> The second group were found along [001] in the central region. They consisted of two types: straight dislocations and helices. The straight dislocations were of $a_o<010>$ burgers vector. The burgers vectors of the helices could not be determined as extinction was never observed for various diffraction vectors, presumably due to impurity decoration. These dislocations in the central region of the ingot were observed to propagate normal to the growth interface, as visualised by growth striations; the authors noted that this would be consistent with minimising dislocation strain energy. In addition to the dislocations described above, some dislocations with $a_o/3<111>$ burgers vectors were observed near the seed.

Matsui (552) classified dislocations into 4 types:

> Type A dislocations: grown in from the seed, propagating parallel to the [001] growth axis, and of edge character;
>
> Type B dislocations: grown in from the shoulder of the ingot, propagating parallel to the growth axis, of edge character;
>
> Type C dislocations: stress induced, and propagating normal to the growth axis in the four <110>/{111} slip systems;
>
> Type D dislocations: stress induced, and propagating inclined to the growth axis in the

eight <101>/{111} slip systems.

All dislocations observed were found to have the standard $a_o/2$<110> burgers vectors. In addition to the above classification, clear evidence of cross slip and dislocation climb (including helices) was given. Both of these effects were shown to have a strong bearing on the dislocation structures observed.

Nakajima et al (074) also classified dislocations into 4 types:

Type A dislocations (as Matsui's type A above);

Type B dislocations grown in from the seed, propagating inclined to the [001] growth axis along <013> or <011>;

Type C dislocations (as Matsui's type B above);

Type D dislocations (as Matsui's type C and D above).

The type A dislocations were thought to have burgers vectors along <1l0>, where l>1, from the lack of extinction for various XRT and TEM diffraction vectors. All other dislocations were found to have the standard $a_o/2$<110> burgers vectors. Evidence of climb was given for type A and B dislocations.

Ono et al (553) investigated slip dislocations in the perifery of the ingot. They split these dislocations into types A and B, consistent with Matsui's types C and D respectively.

Yamada et al (040) investigated grown–in dislocations. Dislocations were split into types A and B consistent with Nakajima's convention described above. To explain the lack of extinction for diffraction vectors other than the [00N] type, which was also noted by Nakajima et al (074), it was suggested that the dislocations were of composite nature. These grown–in dislocations were shown to arise from lattice mismatch between the seed and the growing crystal. Growth of a dislocation free crystal was demonstrated using a lattice matched seed.

Pichaud et al (554), in an extension to their earlier work (604), noted that not only did the dislocation density oscillate with [In] in growth striations, but also, the occurrence of helices was reduced by increased [In] as well. It was suggested that increasing [In] reduced the point defect super–saturations responsible for climb.

Ogawa (267) investigated dislocation structures using NIR scattering tomography. Dislocation reactions and evidence of climb were demonstrated.

6.3 Experimental Details.

6.3.1 Sample details.

The results presented here are taken from samples from 3 different 2" diameter In–doped GaAs LEC ingots, two of which had undergone a post–growth anneal. All samples were double polished using a chemo–mechanical bromine–methanol polish.

The unannealed ingot was grown from the melt, synthesised in–situ with about 1% added In. Growth was carried out under a dry boric oxide encapsulant in a Malvern MSR6/R high pressure puller. The crystal was cut in order to give two 3mm thick samples as illustrated in fig.6.1.

Sample #1 was a {110} slice from the cone of the crystal. The sample was cut across a diameter of the cone, down the [001] growth axis, in order to include the core region directly below the seed. Sample #2 was a (001) slice cut perpendicular to sample #1, from directly under the cone. A further (001) 3mm slice, sample #3, was cut from further down the ingot (at approximately g=0.4).

The annealed In–doped samples were obtained from ingots from two different suppliers. The first annealed sample was a 3mm {110} slice (similar to sample #1 from the unannealed ingot), from an ingot grown under identical conditions to the unannealed ingot described above. The ingot had subsequently been annealed for 5 hours at 950°C. The second annealed sample was a 3mm (001) slice from an annealed ingot, grown in a similar manner to the first. Details of the annealing treatment were not available.

6.3.2 Outline of assessment.

Electrical data were determined by room temperature Hall effect measurements. NIR assessment, including both the qualitative vidicon imaging system and the quantitative spectrophotometer system, was used to investigate the magnitude and distribution of the EL2 concentration ([EL2]). The [EL2] line–scan system described in chapter 5 was used to give an idea of the [EL2] distribution on a microscopic scale. Transmission and Reflection X–ray topography (TXRT and RXRT) were used to investigate the nature and distribution of dislocations. The samples were then A/B etched, primarily in order to further investigate dislocations and precipitates. Further details on experimental techniques can be found in chapters 4 and 5.

Investigations were concentrated on those dislocations, in the central region of the ingot, which lie approximately along [001]. The slight deviation of the directions of these axial dislocations from [001] was determined from NIR absorption images using two methods (Clark 555):

1) Using a low f number lens (f/1.2) with a limited depth of field, and focussing through a sample held perpendicular to the imaging axis. A section through the cylindrical enhanced [EL2] region associated with the dislocation is seen. As the depth of focus is altered from the front to the back of the sample, if the dislocation is not exactly parallel to [001], the angle of deviation from [001] can be calculated from the horizontal displacement of the EL2 cloud (for a known sample thickness). The angle from [100] can be measured directly from the direction of the horizontal displacement.

2) The (001) specimens were mounted on a stage which allowed two axis rotations and three axis translations. A high f number lens (f/16) was used such that the entire depth of the sample was in the focal plane. The angle from [001] was calculated by: tilting the sample, until the dislocation was seen "end on"; measuring the tilt angle; and subsequently correcting for the refractive index of GaAs, using Snell's law. The angle from [100] was measured directly from the aligned image with the sample perpendicular to the imaging axis.

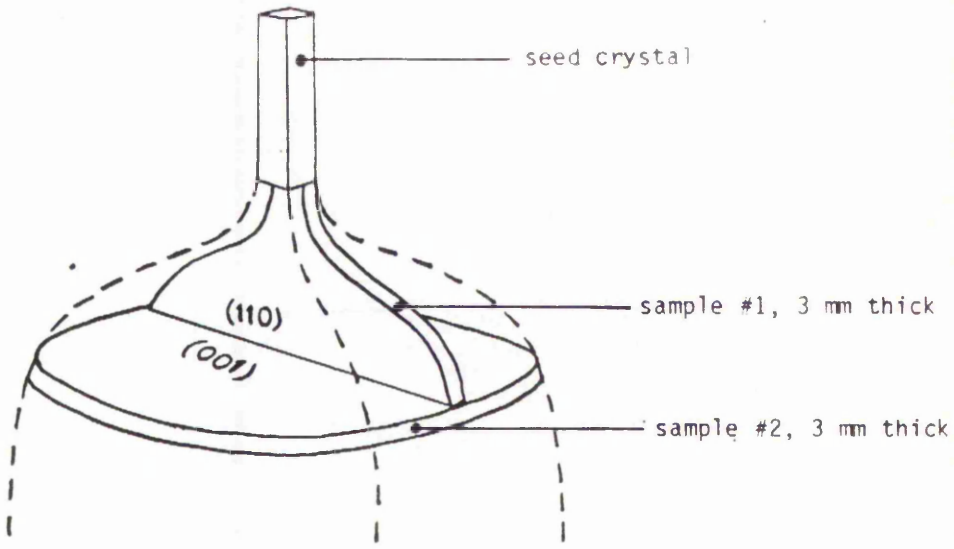

Fig.6.1. Location and orientation of samples at the shoulder region of the as-grown In-doped ingot.

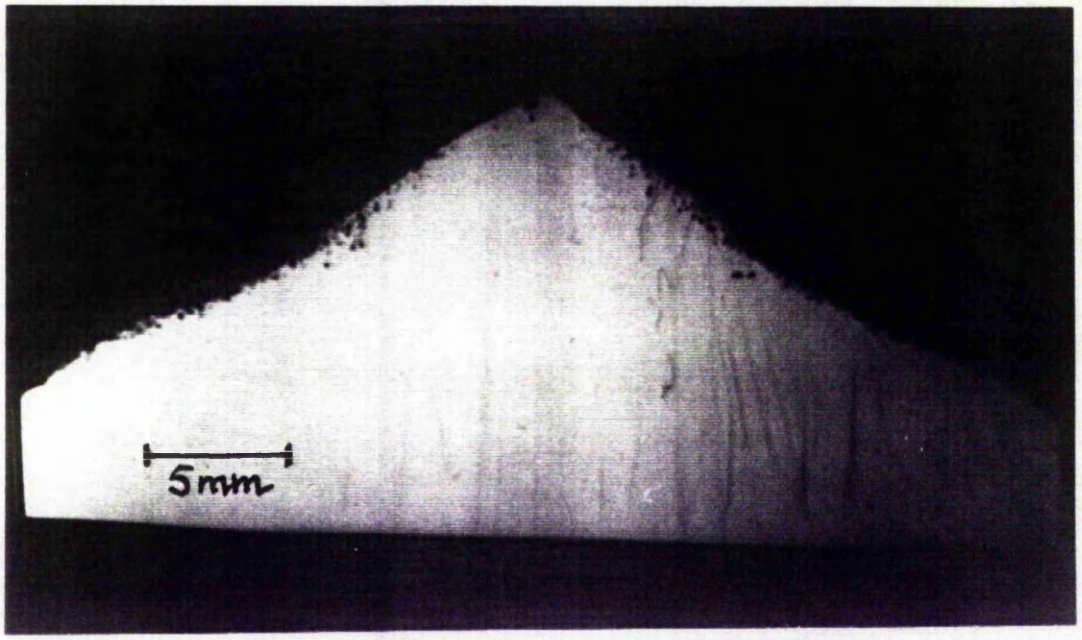

Fig.6.2. Transmission infrared macrograph of sample #1.

6.4 Results.

6.4.1 As-grown In-doped material.

Fig.6.1 shows the arrangement of samples cut from the as-grown In-doped LEC ingot. Fig.6.2 shows a transmission infrared macrograph of sample #1. Note the mass of absorbing features along [001] in the central region of the sample. These are known to be cylindrical rods of enhanced [EL2] surrounding individual dislocations (from their correspondence with dislocation etch pits (Stirland 556, 557) and also their characteristic photoquenching behaviour (Foulkes 558)). In addition, several other dislocation associated EL2 atmospheres are seen, originating from the shoulder region of the sample. The black dots along the edge of the sample at the shoulder are known to be gallium droplets (Brozel 066).

Fig.6.3 shows various X-ray topographs of sample #1 taken with different diffraction vectors. Fig.6.3(a) is a TXRT with an [004] diffraction vector. Note the near total extinction of the axial dislocations which lie along [001], indicating that they are all of edge character. The remaining faint traces are thought to be due to dislocation decoration. Various transmission and reflection topographs with diffraction vectors perpendicular to [001] were produced (TXRT of the <220> type and RXRT of the <620> type). Fig.6.3(b) shows a representative TXRT and fig.6.3(c) a representative RXRT. Extinction of all dislocations was not seen for any of these topographs. Unfortunately, due to the high density of dislocations in the central region it was difficult to judge the contrast (or extinction) of individual dislocations. Note also that the dislocations splay out slightly, from seed to tail, remaining approximately perpendicular to the growth front (as indicated by the growth striations); this is consistent with minimising the surface energy of the dislocation at the growth interface, during growth (Scott 262).

Fig.6.4 shows three NIR transmission topographs of sample #2 taken at three slightly different angles. The image is produced using a high f/number lens such that the entire thickness of the sample is within the depth of focus. Note again that the dislocations appear to splay out (from the seed towards the tail). Fig.6.5 shows an A/B etched surface of the same sample. There are of the order of a thousand dislocations in the central region of the crystal. Fig.6.6 shows the A/B etched surface at higher magnification. The dislocations appear as small pits (probably due to precipitates) which occur on top of mounds. The mounds are related to the dislocation defect atmospheres. Fig.6.6(a) shows dislocations from near the middle of the central region, whereas those in fig.6.6(b) are from the edge of the central region. Note the defect atmosphere associated with dislocations, as indicated by measurements from both etch and NIR images, are from 20 to 30μm across; being generally wider towards the edge of the central region.

Fig.6.7 is a series of NIR topographs, taken using a high f number lens, showing the appearance and relative position, at different focal planes through the sample, of the enhanced EL2 cloud surrounding five dislocations. The arrows indicate the projections of the dislocation directions on the (001) plane. Clearly the neighbouring dislocations in a particular region of the sample do not all have exactly the same direction. Other regions investigated also showed neighbouring dislocations with differing directions. Dislocation directions in several different regions of the core are given in Table 6.1.

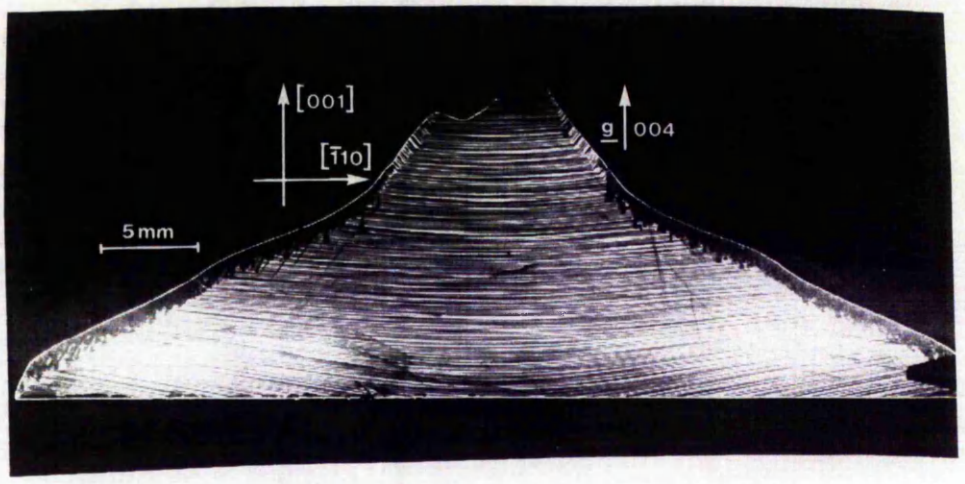

Fig6.3(a) TXRT of sample #1

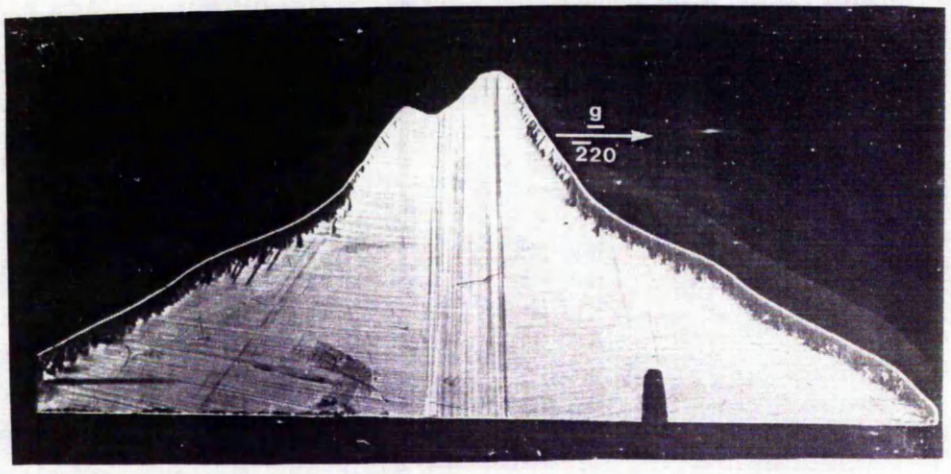

Fig6.3(b) TXRT of sample#1

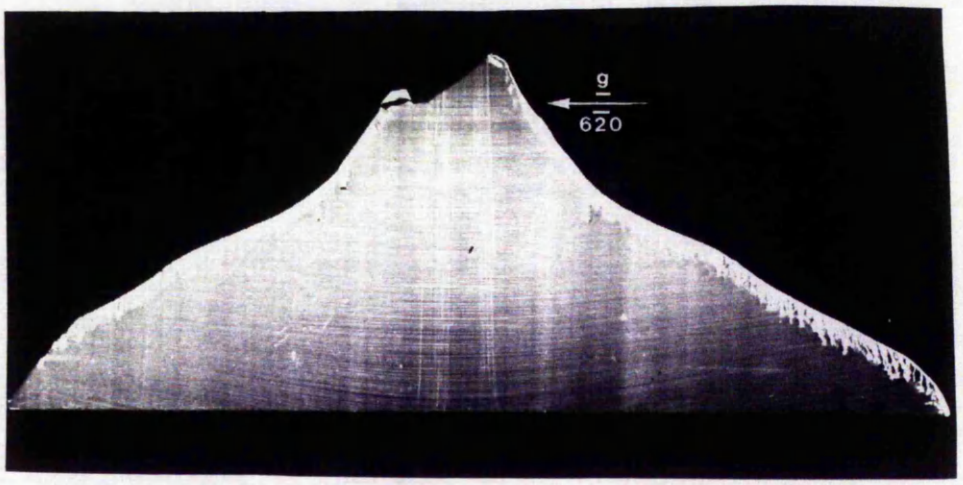

Fig6.3(c) RXRT of sample #1

Fig.6.4(a)

+10°

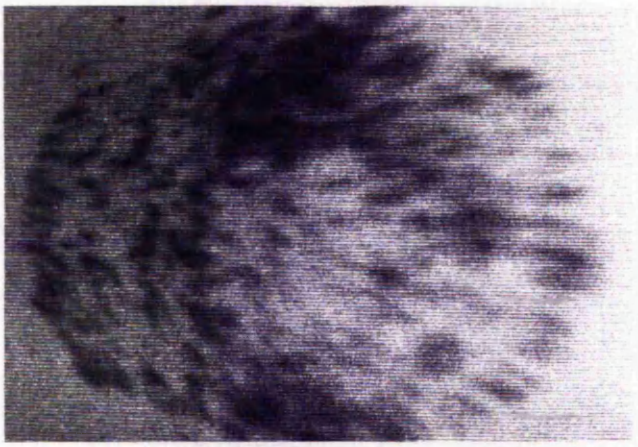

Fig6.4(b)

0°

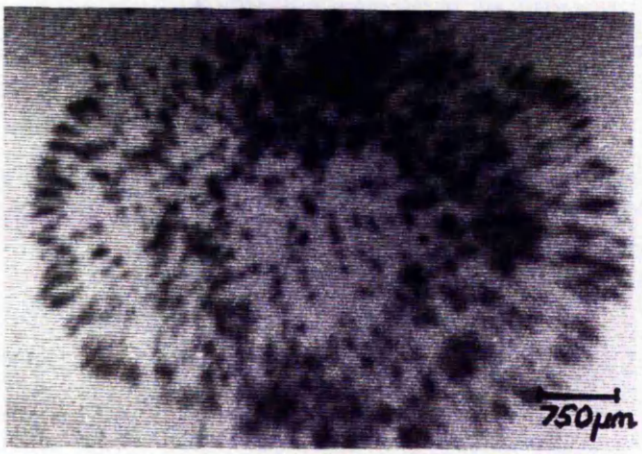

Fig6.4(c)

−10°

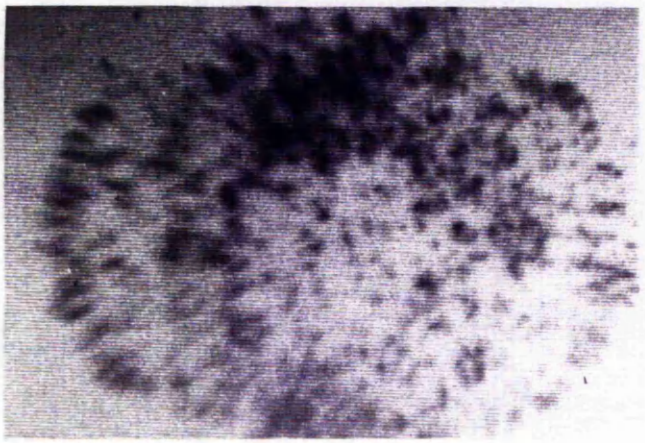

[110] ⟶

Fig 6.4. A series of NIR transmission topographs of the mass of dislocations in the central region of sample #2; taken with the sample tilted at three different angles.

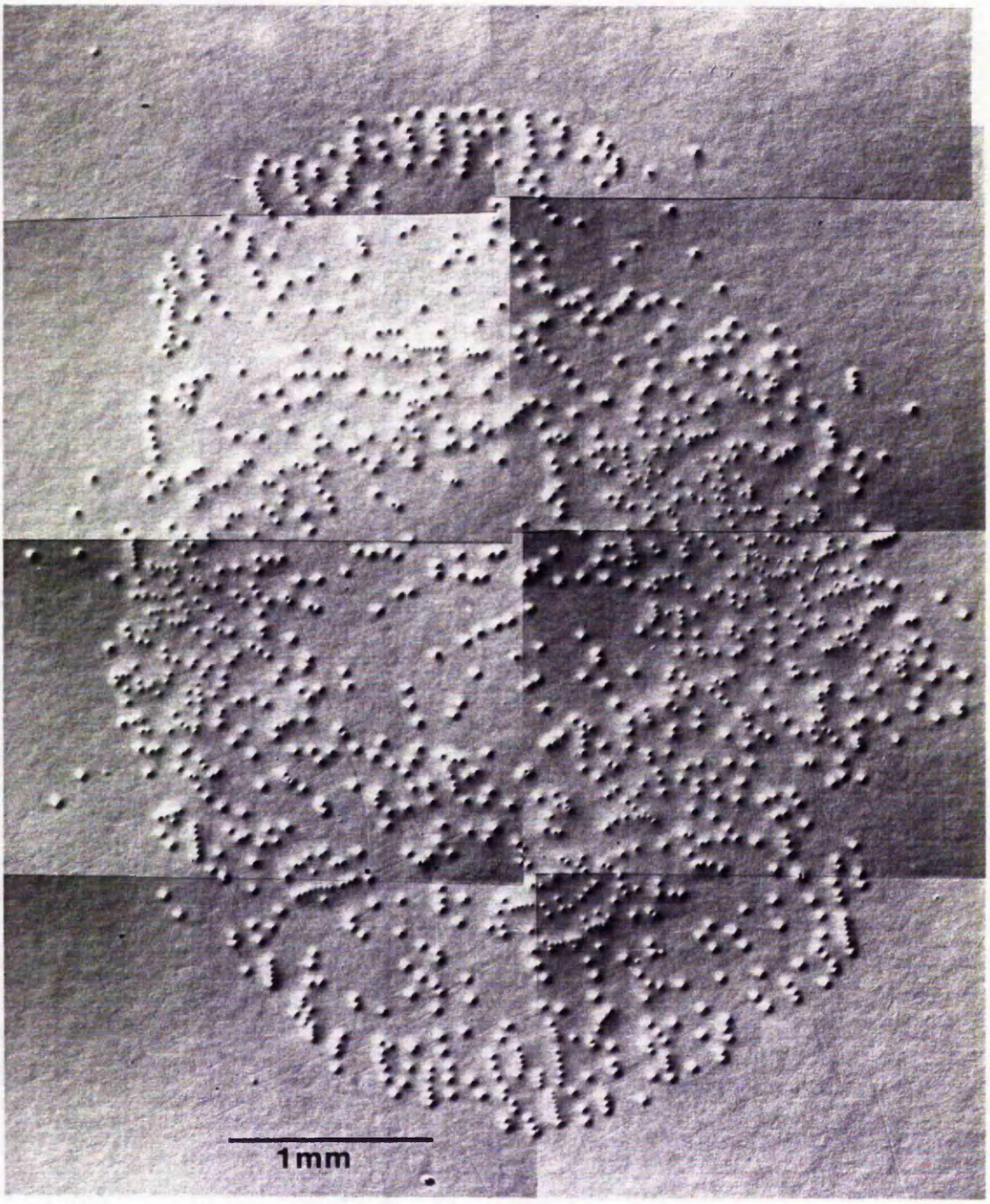

Fig.6.5. Nomarski micrograph of the A/B etched surface of the central region of sample#2.

Fig.6.6(a)

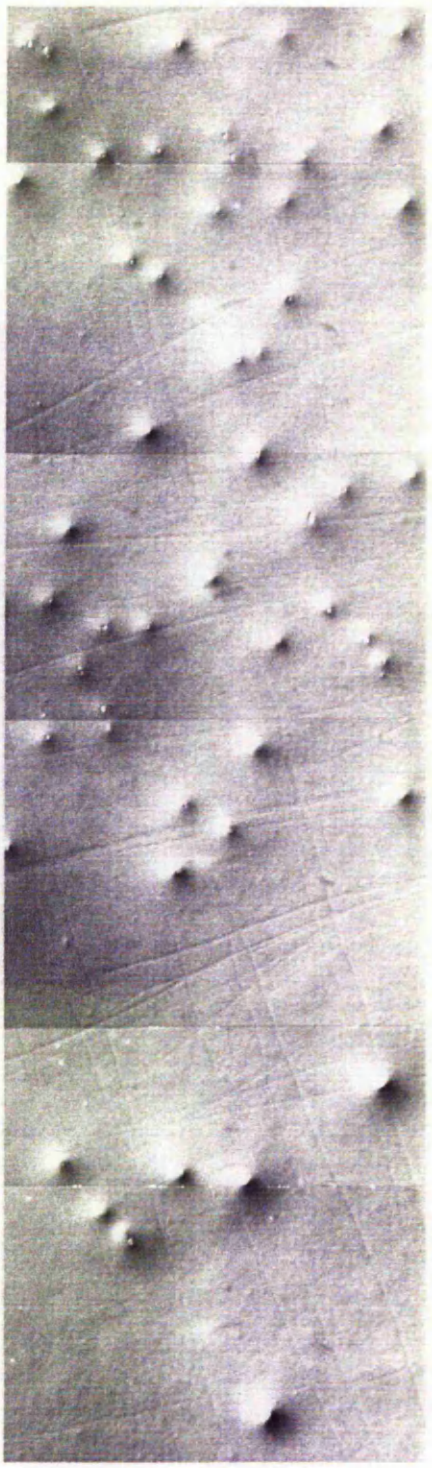

Fig.6.6(b)

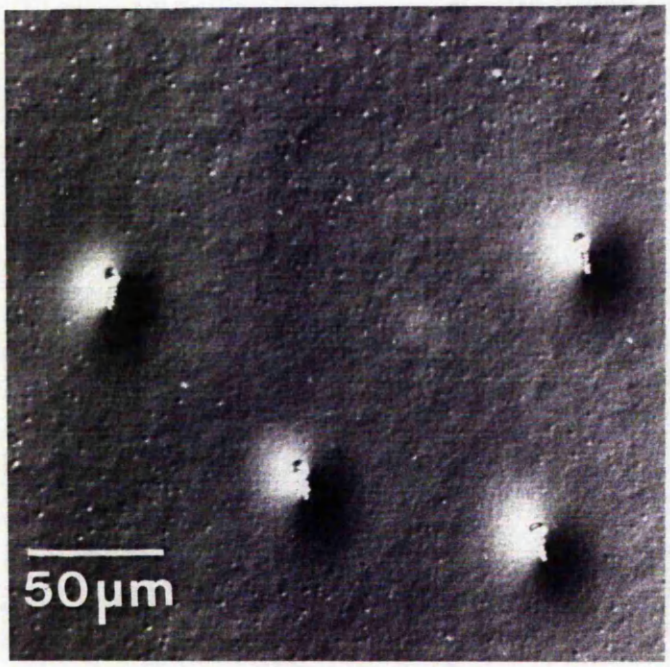

[110] ⟶

Fig.6.6. Two high magnification Nomarski micrographs of dislocations intersecting the A/B etched surface in the central region of sample #2.

Fig.6.6(a). A band from near the middle to near the edge of the central region (towards the top right hand side of fig.6.5.).

Fig.6.6(b). Four dislocations from the edge of the central region (just outside the area in fig.6.5.)

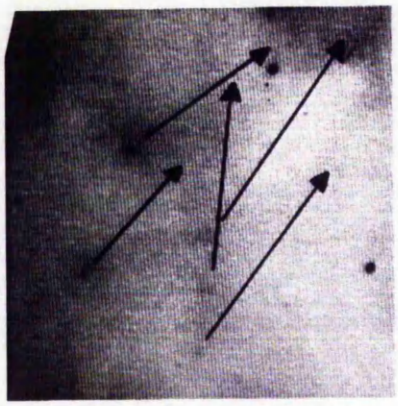

(a) Top surface (0mm depth)

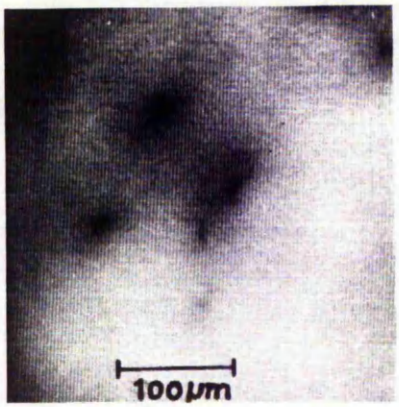

(b) 0.36mm depth

(c) 0.78mm depth

(d) 1.33mm depth

(e) 1.69mm depth

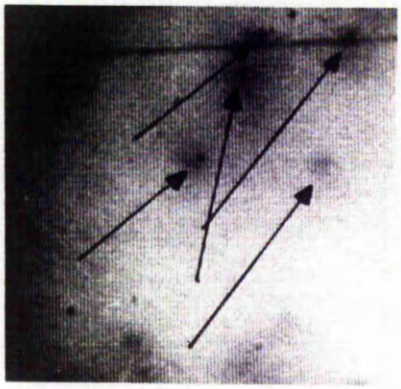

(f) Bottom surface (2.12mm depth)

Fig.6.7. A series of NIR topographs of an area of sample #2 using low f number optics. They show the change in lateral position of the dislocation–related EL2 cloud for 5 dislocations, through the entire depth of the sample. This technique is used to evaluate dislocation directions. The arrows on fig 6.7(a) and (f) show the full extent of this lateral shift.

Table 6.1.

Dislocation directions are given below for various dislocations selected from different areas of the central dislocated region. The numbering system of the dislocations is in the form X.Y where X represents the NIR image of the area which contains the dislocation and Y represents the dislocation reference number within that area. Note that area 4 corresponds to the series of images shown in fig.6.7. In the table below θ gives the angle of the dislocation from [110]. Φ gives the angle from [001], measured using both the high and low f number methods (note the good correlation between the results of these two methods).

Dislocation	θ°	Φ°(high f no.)	Φ°(low f no.)
1.1–1.10	70+/–1	5.8+/–0.4	5.7+/–0.2
2.1	277	7.3	7.1
2.2	277	7.8	7.9
3.1	217	1.4	1.6
3.2	217	2.5	2.6
3.3	182	1.1	1.3
3.4	165	4.7	4.6
3.5	150	2.0	2.0
3.6	150	2.0	2.1
3.7	217	2.5	2.9
3.8	217	2.5	2.9
4.1	325	5.5	5.5
4.2	325	5.3	5.2
4.3	351	5.5	5.7
4.4	311	3.6	3.4
4.5	311	3.6	3.4

Area 1 was at the edge of the central region at about 90 from [110]. It contained a series of 10 aligned dislocations with the same directions (within the acuracy of the measurement). Hence, the results above are shown as a group.

Area 2 was at the edge of the central region at about 270° from [110].

Area 3 was near the edge of the central region at about 180° from [110].

Area 4 was at about half way in from the edge at about 315° from [110].

In order to obtain more detailed information on the micro–structure of dislocations along [001] we used A/B etching. Figs.6.8, 6.9 and 6.10 show the A/B etched surface of (the {110} cut) sample #1 at high magnification. Dislocations etch as grooves, on a mound of width comparable to the enhanced EL2 zone. Dislocations appear as arcs, pinned at regular intervals, by precipitates. We have divided these dislocations into three types according to their A/B etching behaviour:

Type 1), display a prominent mound with complicated and often tangled dislocation grooves. These dislocations occur predominantly at the edge of the core region. An example of this type of dislocation is marked in fig.6.8.

Type 2), have less prominent etch mounds with dislocation grooves pinned regularly by precipitates at widely spaced intervals (30–50μm), for example dislocations a,c,h and i in fig.6.9.

Type 3), are similar to type 2 but have narrowly spaced precipitates (5–10μm), for example dislocations b,d,e,g and j in fig.6.9.

Fig.6.10 shows a region of fig.6.9 at higher magnification. Note the speckle effect, in the background, which is most prominent away from dislocations. Note also, that arcs for two of the dislocations (a and c) appear to have climbed in opposite directions, in the same region of the sample.

Results from dislocation in the core region of sample #3 (the second (001) slice from the as–grown ingot), are presented in fig.6.11. Fig.6.11(a) shows a NIR transmission image and fig.6.11(b) the A/B etched surface of the same region. The cell like features in the latter are thought to be due to constitutional supercooling arising from the increasing [In] towards the tail of the ingot, caused by segregation (Stirland 557). Note that the dislocation–related defect atmospheres seem to be unaffected by constitutional supercooling and are nearly 100μm across at this point in the ingot. The defect atmospheres are featureless on the NIR image (which is sensitive to [$EL2^{o}$]). However, they appear as a complicated mound–trough–mound structure on the A/B etched surface; which is thought to be sensitive to changes in fermi level (Brown 371). Fig 6.12 shows two A/B etched dislocations from sample #3 at higher magnification. Here the external mound appears to be very diffuse, due to a feature of the Nomarski imaging used. However, on the central mound, etch pits, which are probably due to precipitates, can be seen.

6.4.2 Annealed In–doped material.

Only preliminary annealing studies on In–doped material were made. These results give only an indication of the information available from annealing.

Fig.6.13 shows an NIR transmission image of the {110} slice from the first annealed ingot. The central region has a lower [EL2] than the rest of the ingot. Note also that there is a low [EL2] around slip bands at the edge of the sample. The values of [EL2] for the core region and dislocation free regions were $1.4x10^{16}cm^{-3}$ and $1.7x10^{16}cm^{-3}$ respectively. These values both exceed the [EL2] in unannealed ingots from the same crystal grower (typically 0.5 to $0.8x10^{16}cm^{-3}$)

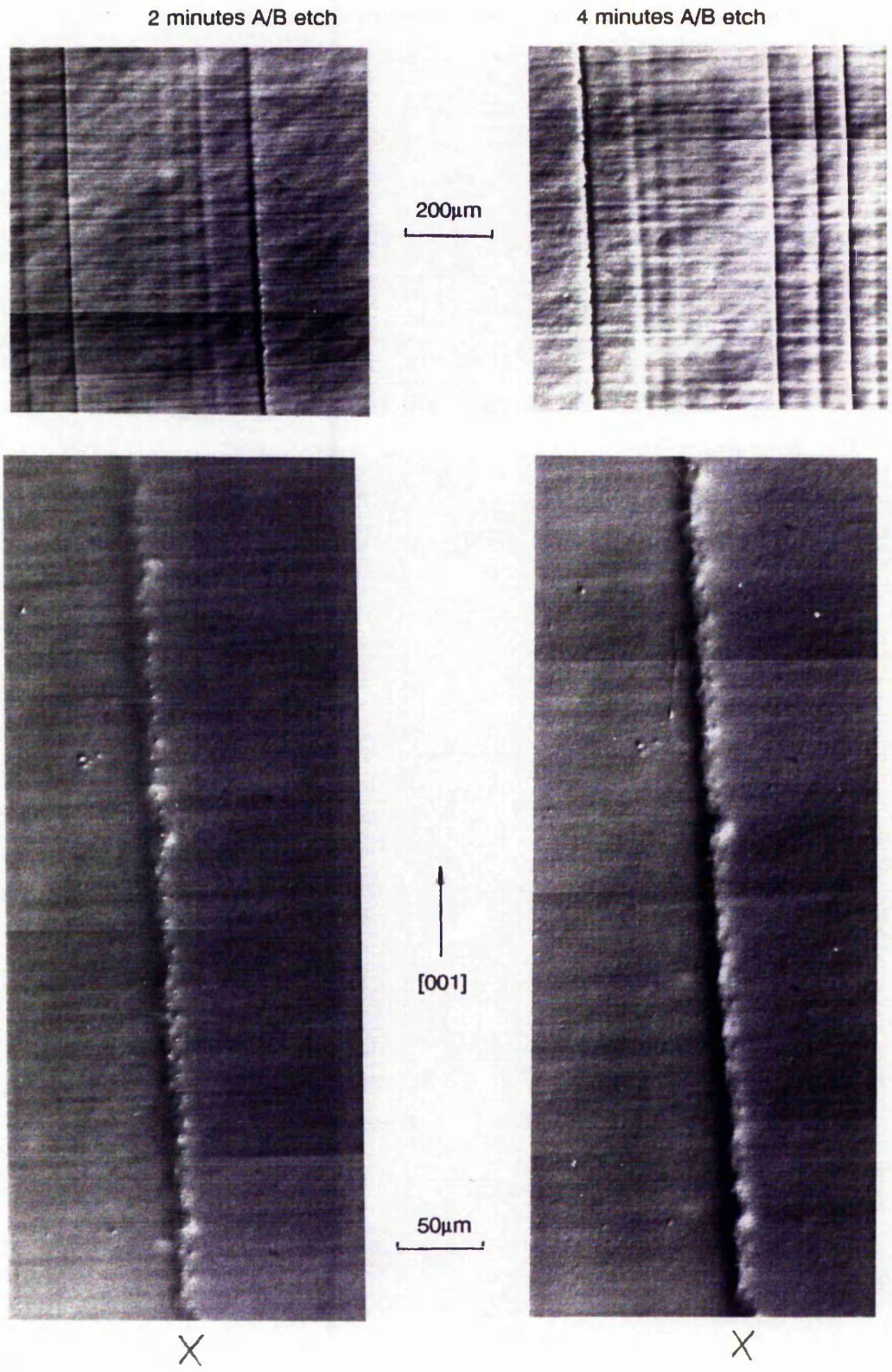

Fig.6.8. Nomaski micrographs of the A/B etched surface of the {110} sample #1 near the edge of the central dislocated region. The micrographs are taken at two different magnifications and after two different etch times: 2 minutes and 4 minutes, corresponding to etch depths of 50μm and 10μm respectively. Note the tangled appearance of the dislocation marked, X.

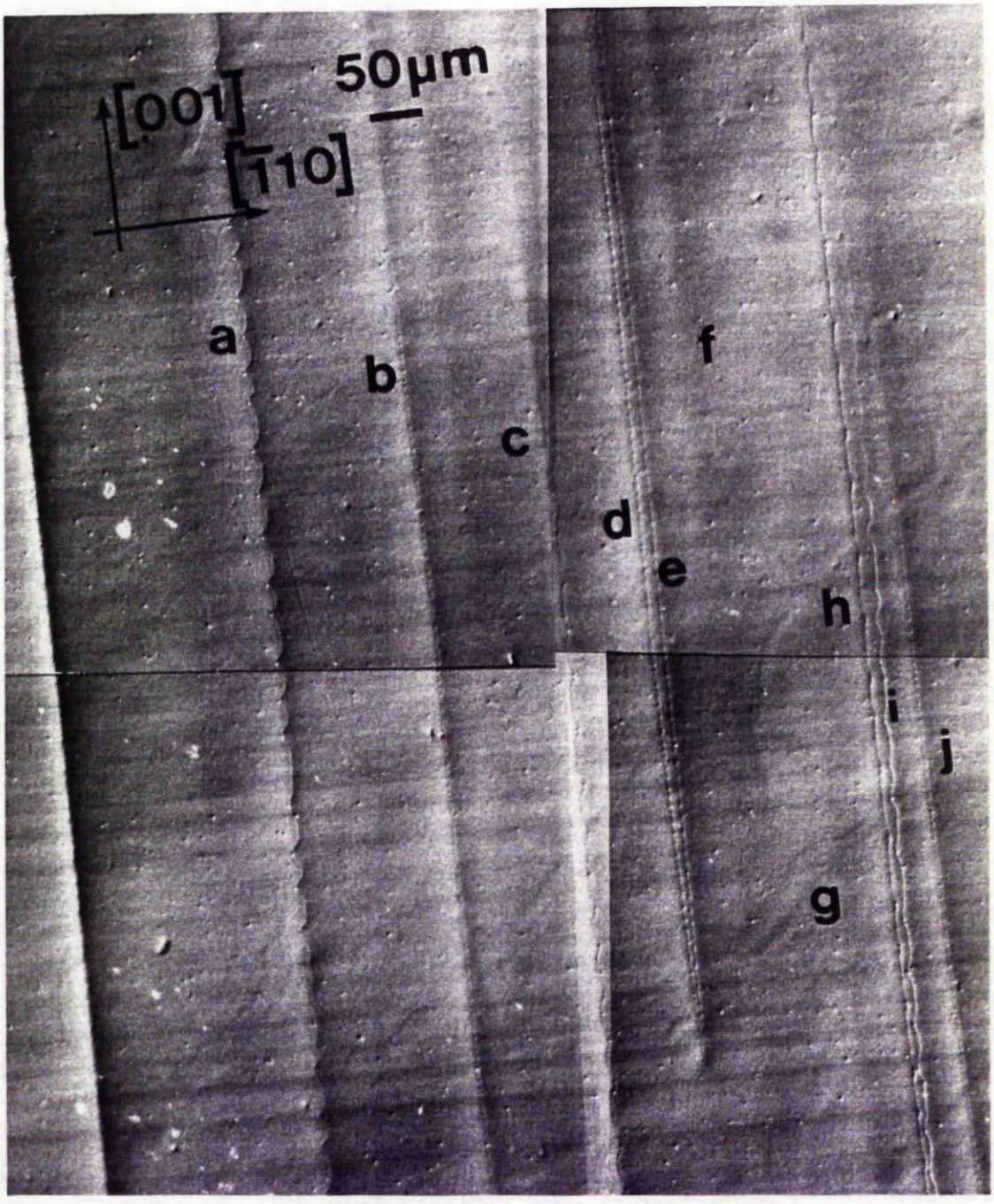

Fig.6.9. Nomarski micrograph of the A/B etched surface of sample #1, towards the middle of the central region.

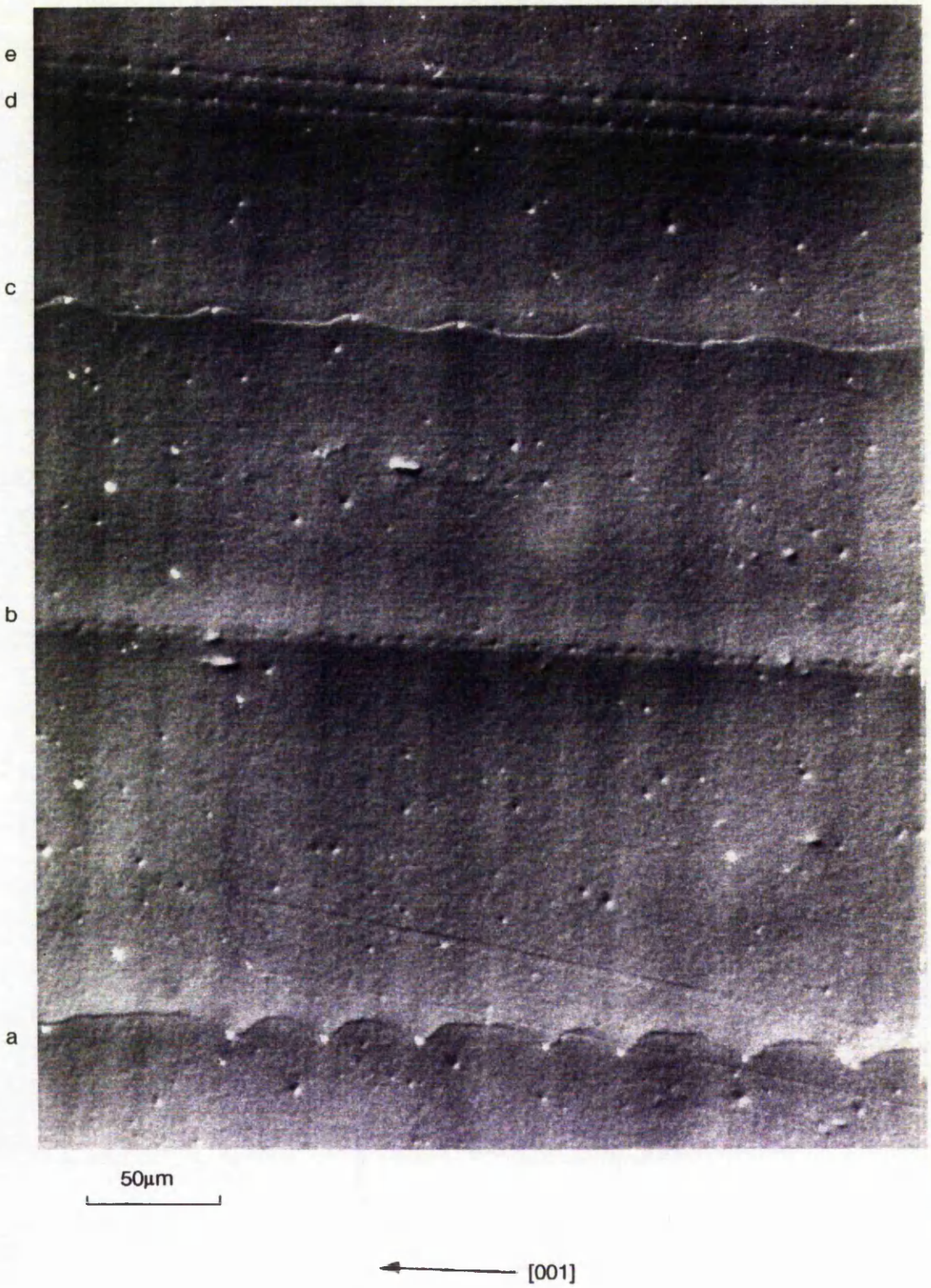

Fig.6.10. A region of fig.6.9. at higher magnification.

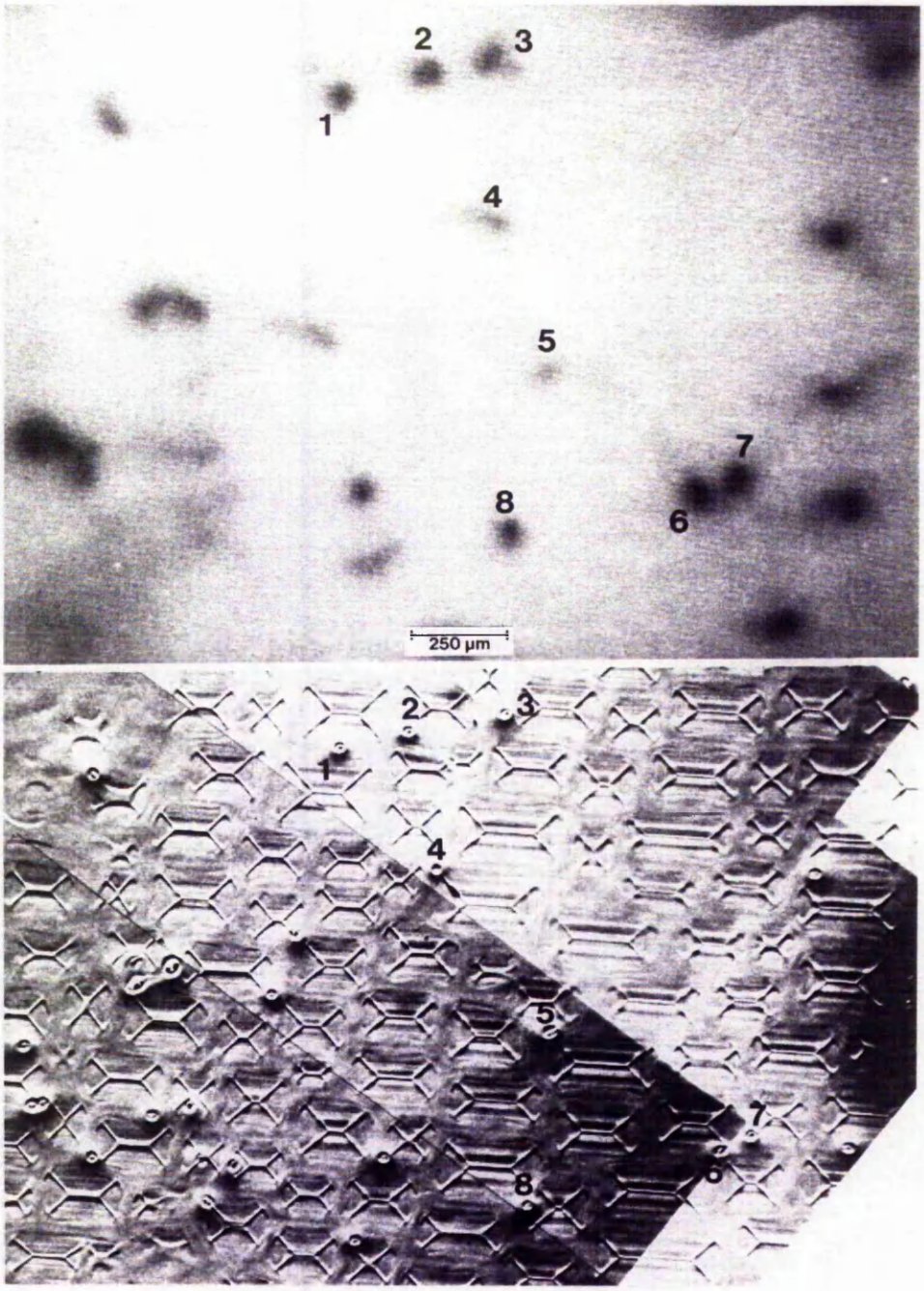

Fig.6.11. A comparison, for sample #3, of a NIR absorption image with the A/B etched (001) surface of the identical region.

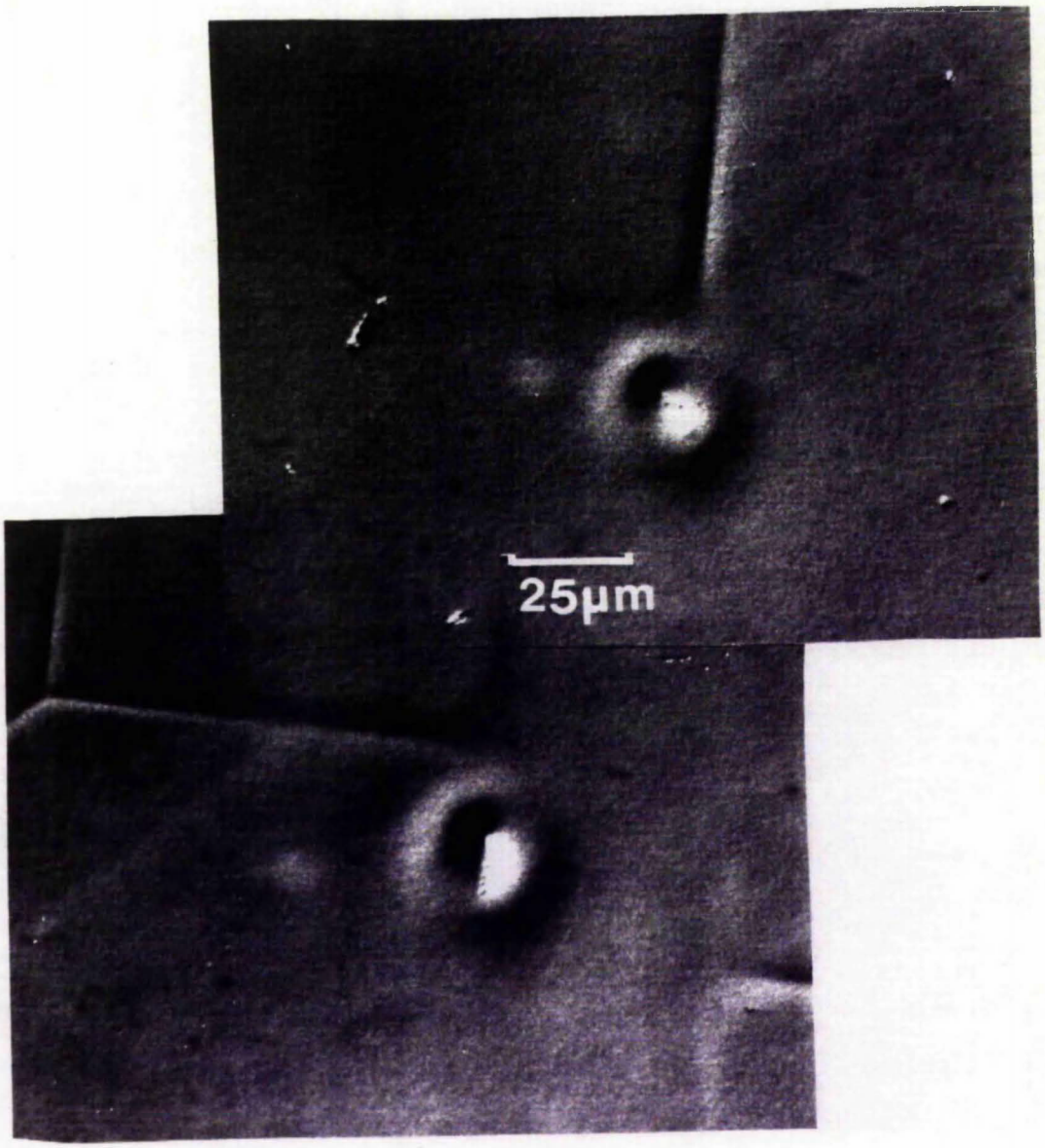

Fig.6.12. A region of fig.6.11. at higher magnification.

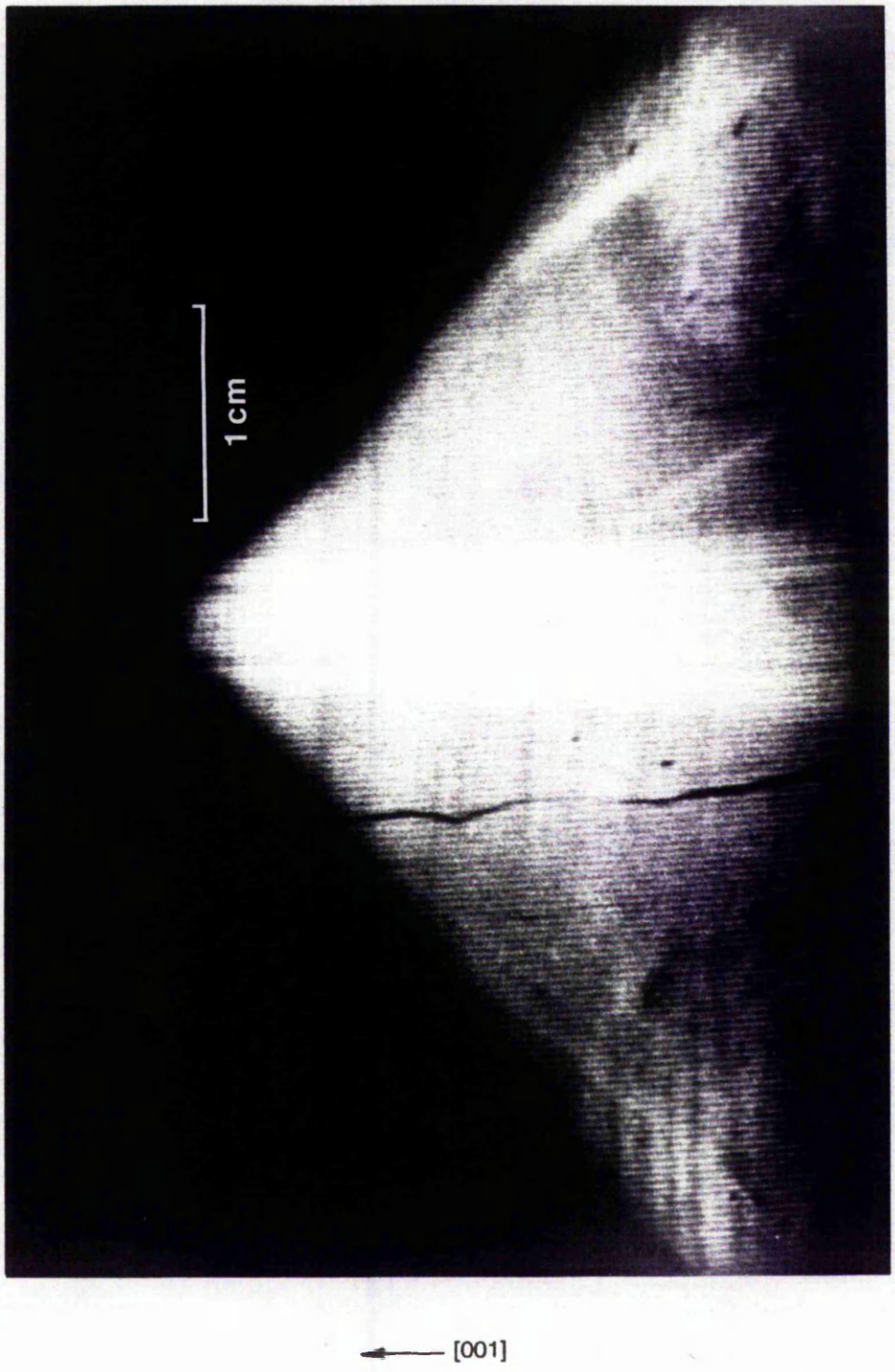

Fig.6.13. NIR absorption image of the {110} slice from the frirst annealed ingot.

Fig.6.14 and fig.6.15 show the A/B etched surface of the {110} slice from the first annealed ingot. Note that compared to the unannealed samples (figs.8, 9 and 10), the dislocation structure is far more complicated, indicating that a significant amount of climb has occurred during the anneal. Also dislocation mounds are now surrounded by a shallow trough of about 100um width. This can be seen particularly clearly in fig.6.15. Finally, it should be noted that there is still a pronounced background speckle in the sample after annealing.

The final set of results are from the second annealed ingot. As with the first annealed ingot described above, zones with low [EL2] are to be found in the central region of the ingot, or near slip bands. The typical [EL2] in the dislocation free matrix was found to be $0.93 \times 10^{16} cm^{-3}$, using the spectrophotometer. Fig.6.16 shows an NIR transmission image of the central region. The image displays a complicated structure where the dislocated regions display a higher [EL2] (peaking at dislocations) than the matrix, but are surrounded by bright denuded zones with lower [EL2] than the matrix. The [EL2] in the bright areas of the transmission image and at the dark dislocated regions were found to be typically 0.8 and $1.5 \times 10^{16} cm^{-3}$, respectively. These values should be regarded as approximate as they were obtained using the semi-quantitative [EL2] line-scan system. In addition to the above structure, some groups of aligned dislocations show an extra denuded zone, within the high [EL2] dislocated region. An example of this feature is given in fig.6.17.

6.5 Discussion.

6.5.1 Comments on dislocation structures.

The axial dislocations in our work are of edge type. The lack of contrast extinction for all diffraction vectors perpendicular to [001] could be explained by decoration (Scott 551), composite dislocations (Yamada 040) or by non-standard burgers vectors along <1l0> (Nakajima 074). However a fourth, much simpler, explanation also exists. For the $a_o/2$<110> burgers vector family, if dislocations of all possible combinations occur, only a fraction of the axial dislocations will exhibit extinction for a particular diffraction vector. Hence total extinction of all dislocations will not occur for any burgers vector perpendicular to [001]. The XRT method may lack the resolution to determine the extinction of individual dislocations, particularly at such high densities. The use of TEM would provide a clear indication which mechanism(s) is occurring.

On a macroscopic scale, the axial dislocations in this work are not quite straight. Their direction appears to be primarily influenced by the growth front (Scott 551). However, on a microscopic scale where the growth front would be expected to be flat, neighbouring dislocations do have different directions. Hence, there is clear evidence of some secondary effects on dislocation directions. These effects would include dislocation-dislocation interactions and post growth climb (climb features do exist in the material on a microscopic scale). Further evidence for dislocation interaction are the closely spaced parallel rows of dislocations appearing near the edge of the central region (for example, in fig.6.3 and fig.6.4). These look similar to classical low angle grain boundaries formed by several interacting parallel edge dislocations with the same burgers vector. Unfortunately, since the burgers vectors were not determined, this theory could not be confirmed.

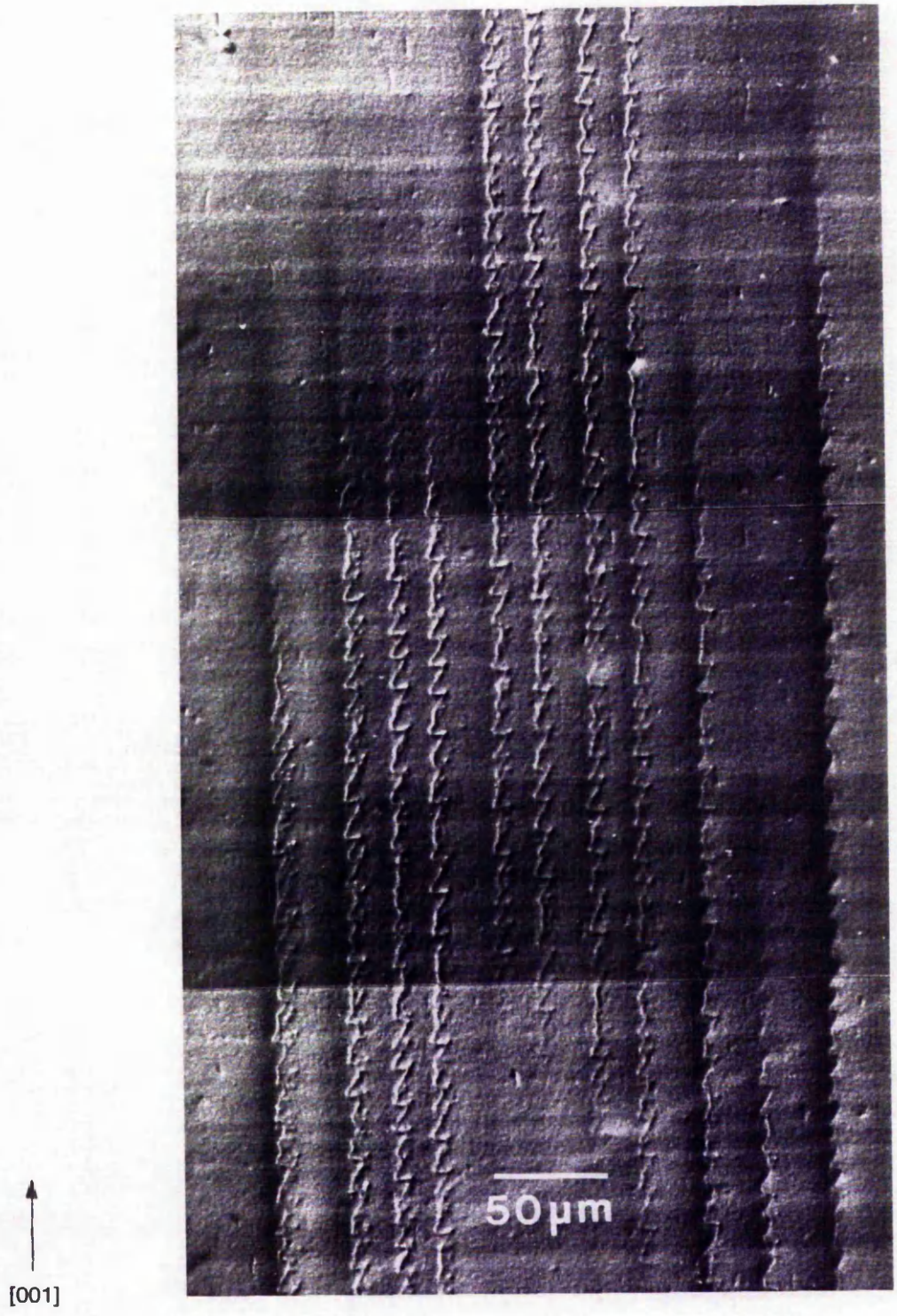

Fig.6.14. Nomarski micrograph of an area of the A/B etched surface (in the central dislocated region) of the {110} sample from the first annealed ingot.

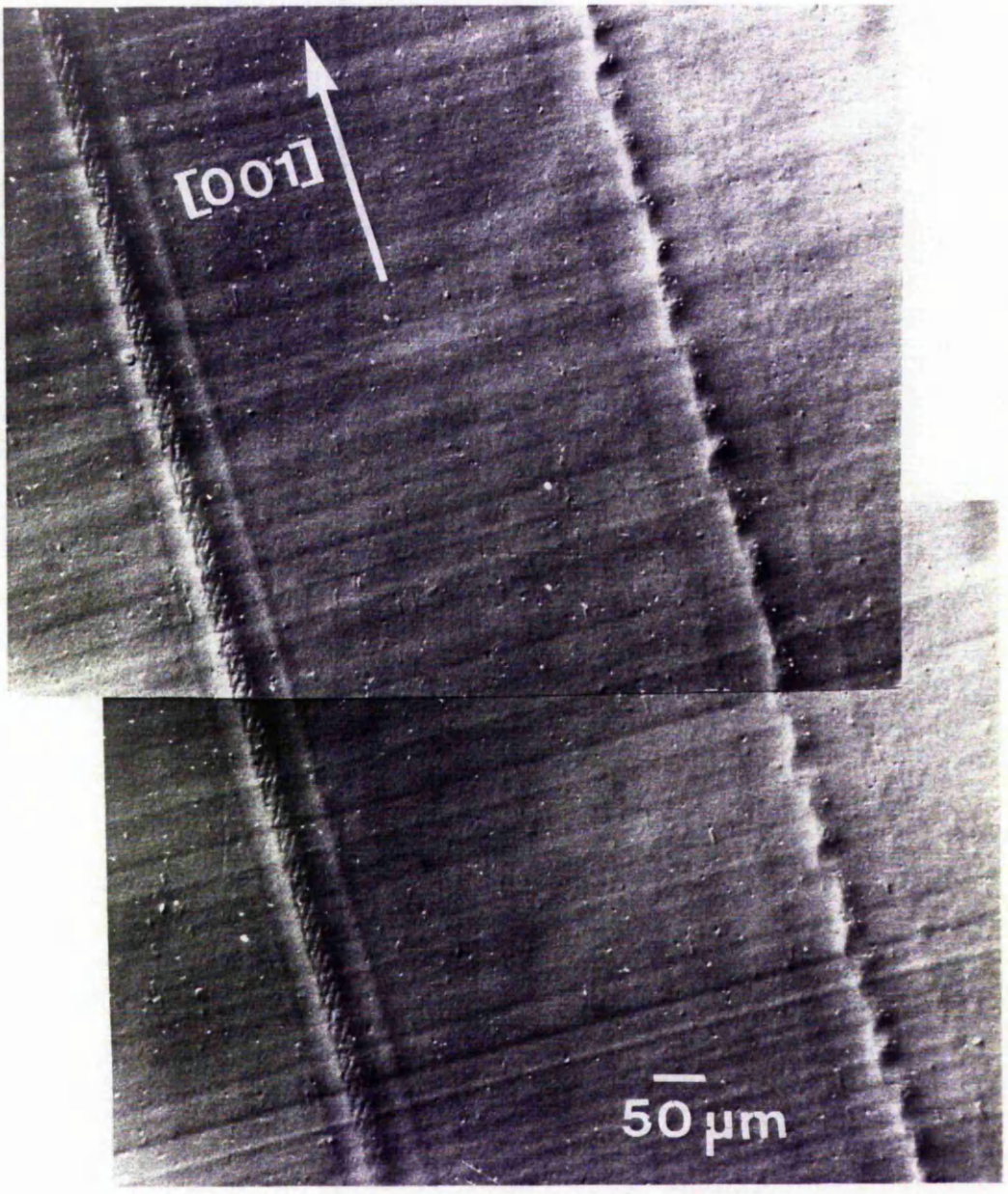

Fig.6.15. Nomarski micrograph of an area (in the central dislocated region) of tghe A/B etched surface of the {110} sample from the first annealed ingot.

Fig.6.16. NIR absorption image of the central dislocated region of the (001) sample from the second annealed ingot.

Fig.6.17. A region of fig.6.16 at higher magnification.

On a microscopic scale, the dislocation arcs pinned by precipitates give clear evidence of climb, as the dislocation loops do not lie on slip planes. This occurrence is not suprising, as many workers have seen helical dislocations in In-doped material (Ogawa 267, Scott 551, Matsui 552), which can only arise from climb processes. The complicated etching behaviour of Type 1 dislocations could arise from 2 or more, closely spaced, interacting dislocations. Type 2 and Type 3 appear to be single dislocations. The difference between them could arise from differences in their burgers vectors: If type 1 were, for example, an α type dislocation and Type 2 a β type dislocation. The different core structures of the dislocations, arising from the polarised nature of the lattice, could give rise to different diffusion rates of point defects along the dislocation core. This in turn could give rise to two distinct precipitate spacings, as is observed.

In some regions of the sample, dislocation loops on two neighbouring dislocations have climbed in different directions. This could be due to dislocations with identical burgers vectors with differences in climb arising from local changes in the dominant point defects (that is from (to) vacancy to (from) interstitial climb). However, it is more likely that the differences arise from dislocations having different burgers vectors. The situation could be further complicated if the predominant climb direction was out-of or into the {110} sample surface, as confusion then arises from the 2-D representation of the climb due to the A/B etch memory effect.

TEM investigations of burgers vectors would be required to confirm whether the dislocations with two distinct types of precipitate separations arise from the different core structures of α and β dislocations in GaAs. In addition, the type of climb (ie interstitial or vacancy) could be determined if both the burgers vector and climb direction were known.

6.5.2 Dislocation-defect interactions.

Individual dislocations in In-doped material have associated defect atmospheres. These could be formed by several mechanisms, including the following:

1) The defect atmospheres are grown-in, due to constitutional supercooling;

2) They form during cooling by the dislocation gettering point defects from the surrounding matrix;

3) They form from point defects produced by dislocation climb;

4) They form as a consequence of the growth of As precipitates on dislocations with a subsequent consumption and/or ejection of lattice point defects in the surrounding region.

The first mechanism is more unlikely than the others for several reasons. Firstly, constitutional supercooling is observed in In-doped material and appears to be independent of the presence or distribution of dislocations. Secondly, the defect atmospheres do not seem to be influenced by the growth cells which are genuinely formed by constitutional supercooling. Finally, the defect atmospheres can be altered considerably by annealing at relatively low temperatures (compared to the melting point of GaAs). Hence, we assume the defect atmospheres and precipitates are formed through a combination of gettering, climb and precipitate growth. However, the regularly spaced precipitates and uniform cylindrical defect atmospheres indicate

that the distribution of precipitates and other defects are also strongly affected by the presence of the dislocation itself. This is probably mainly controlled by rapid "pipe" diffusion of point defects along the dislocation.

As a guide to the number of defects involved in producing defect atmospheres by these mechanisms, the following approximate calculations have been carried out. They assume that approximately one atom in GaAs is contained in a volume given by the cube of the lattice constant (approximately 0.56nm). If a 1cm length of dislocation climbs on average 3μm (typically from 1μm to 10μm), it requires the production or absorption of about 10^{11} defects/cm on each sublattice. If an As–precipitate of 50nm width (typically from 10 to 100nm), is to be produced every 30μm (typically 5 to 50μm) along a dislocation it requires the production or absorption of about 10^{9} defects/cm on each sublattice. As a comparison, the enhanced [EL2] around dislocations is about $4x10^{15}cm^{-3}$ over an area of up to $(50\mu m)^2$, corresponding to about $10^{11}defects/cm^{-3}$. Clearly, the climb mechanism involves numbers of point defects of the correct order to have a significant effect whereas that of precipitate formation does not. However this result is highly sensitive to precipitate size which has been determined mainly in undoped material. If all precipitates in In–doped material were of the order of 400nm across (as the with the precipitate shown in the work of Nakajima et al; fig.5 in 074) with 20–30μm spacing, above 10^{11} defects/cm on each sublattice would be involved.

The increase in width of the defect atmosphere along the growth axis of the crystal (between sample #2 and sample #3) could be due to several reasons: the increase in defect concentrations because of the effective segregation of As or Ga defects in non–stoichiometric material; different cooling rates of different parts of the crystal, giving rise to different formation kinetics for the defect atmospheres; or a type of constitutional supercooling effect (again, this is unlikely for the same reasons as discussed above for the formation of defect atmospheres).

Extra information on the defect atmospheres surrounding dislocations can be obtained by luminescence studies (see section 3.9). Hunter and co–workers (470, 474, 475) found dislocations are associated with bright ring features, several hundreds of microns across. These bright rings contain dark circles, which in turn contain bright spots (at the dislocation). The authors suggest that the bright and dark rings could be caused by gettering of luminescence killer centres on one sublattice and the generation of others (perhaps by climb), with a different diffusion rate, on the other sublattice. The nature of these luminescent killers is still unknown. However, they must exist in very low concentrations ($<10^{15}cm^{-3}$), and have very large optical capture cross sections, if they are electrically active; since they do not greatly affect material resistivity. One set of possible candidates are the micro–defects which are known to exist in dislocation free regions of In–doped material (Hunter 475), as discussed in section 6.5.3 below). Another set would be larger concentrations of electrically inactive point defects (possibly vacancies or vacancy complexes). Luminescent efficiency is known to increase substantially after annealing In–doped material (Noto 277, Hunter 470). This indicates that the luminescent killer centres are not stable during the anneal.

Various reaction mechanisms involving point defects have been developed in order to explain the relationship between dislocation climb, the As precipitates formed on dislocations, EL2 distributions, and other defect atmospheres formed around dislocations (Osaka 299, Stirland

559, Brozel 560). The mechanism discussed here relies on the assumption of a supersaturation of As interstitials (As_i) in the matrix a negligible presence of Ga interstitials (Ga_i) and is also strongly related to As precipitate formation and dislocation climb:

> If the growth of As precipitates from a supersaturated As–rich matrix, during post–growth cooling, is conservative, then one atom of GaAs matrix is consumed to form one atom of As precipitate. In this case, if the supersaturation is mainly in the form of As, as is expected from stoichiometry studies (see section 2.2.1), then one of the two mechanisms below must be operation at the precipitate:
>
> As_i + GaAs ––> As_2(precipitate) + Ga_i
>
> As_i + V_{Ga} + GaAs ––> As_2(precipitate)
>
> The mass transport of the Ga away from the precipitate as it grows is an important if often neglected point. The Ga_i could then combine with a further As_i at the dislocation to give interstitial climb, or diffuse away from the dislocation. Alternately the following interstitial climb reaction could occur at the dislocation:
>
> As_i ––> GaAs (climb unit) + V_{Ga}
>
> The V_{Ga} produced in this way could then be consumed by precipitate growth or by diffusion into the matrix where it can combine with As_i to form As_{Ga}, the main component (?) of EL2. Since dislocations are surrounded by zones of enhanced [EL2] the production and out–diffusion of V_{Ga} defects is a strong possibility. The gettering of As_i at dislocations and production of a lesser amount of V_{Ga} (or Ga_i) on the other sublattice could also explain the strange multiple ring structures observed in luminecence and etching studies.
>
> The main alternative to the model above, that involving vacancy type climb, is unlikely if a supersaturation of mobile As_i exists. Hence determination of the type of climb in In–doped material could also be used to confirm this series of precipitate formation and climb driven reactions associated with the As_i.

6.5.3 Precipitates in In–doped material.

Dislocation–associated precipitates.

In the central region of In–doped ingots precipitates appear as regularly spaced pinning sites, at intervals of 5 to 50µm, with dislocation arcs, arising from climb, between them. In other regions of the crystal precipitates on dislocations are seen as near continuous lines, using NIR scattering (Ogawa 267); indicating decoration on at, or near, a micron scale.

Barrett (073) demonstrated that precipitates are As–rich GaAs using EDX; there was no evidence of In. Nakajima et al (074) also using EDX, detected only Ga and As and concluded that the precipitates are probably the same as those observed in undoped crystals.

Sizes of precipitates in In–doped material have been investigated by several workers using TEM. Results indicate that precipitates are typically up to 100nm across (Barrett 073, Yamada 075). However a precipitate of about 400nm across associated with a 300nm kink in a dislocation has been found (Nakajima 075). This is larger than any precipitate reported in undoped material. In addition, the clear association of a precipitate with a large kink may

indicate that kinks act as precipitate nucleation sites.

Micro–defects in In–doped material.

Various workers have seen some background speckle in the In–doped dislocation free matrix similar to that seen in this work. It is thought to arise from micro–precipitates or decorated dislocation loops, which are not necessarily associated with dislocations. Lessof (078) has shown that dislocation loop structures give rise to background speckle on an etched surface using a eutectic KOH–NaOH etchant. This was also seen by Moriya et al (264). Yamada et al (075) investigated the background speckle seen by NIR scattering in dislocation free regions of In–doped material (Osaka 299, Miyairi 382). The effect was very prominent in slowly cooled material and weak in quenched material. This is probably due to the defects (possibly precipitates) being smaller but more uniformly abundant in quenched material. Although the scattering intensity of Rayleigh type scatterers is proportional to the number of the precipitates, it is also, more critically, proportional to the square of their volume. Hence, scattering is more sensitive to fewer, larger precipitates, for the same total number of atoms contained in the precipitates. There may be a relationship between this speckle and the more dense micro surface roughness which has been reported in undoped GaAs (Miyazawa 012, Dobrilla 242, 380); usually occurring in cell centres of as–grown and annealed material.

To confirm the association of the background speckle observed in this work with that of others, a combined etching, TEM and NIR scattering would be required, similar to the work by Suchet et al (069) in undoped material.

6.5.4 The effects of annealing on In–doped GaAs.

Annealing In–doped material increases the average [EL2] from about 0.5–0.8x10^{16}cm^{-3} to 1.2–1.7x10^{16}cm^{-3}. However, the increase is not uniform, especially in dislocated regions. In particular, on a microscopic scale, strange effects occur in the locality of core dislocations.

Investigation of NIR images and A/B etched surfaces indicate that there are three zones surrounding dislocations in this work:

1) a very wide gettering zone of surrounding dislocations at about 50–100μm;

2) a defect generation and out diffusion zone of up to 50μm from dislocations;

3) a dislocation core influence zone of up to 5μm in the vicinity of dislocations.

These results are in agreement with the luminescent studies of Hunter et al (470, 474, 475), although the the thermal history of the crystals investigated are not necessarily the same. Hence it is reasonable to suggest that the features arise from the same fundamental mechanism: that is, the gettering of defects on one sublattice along with the generation and out–diffusion of defects on the other. The reason that EL2 absorption also displays features (described in section 6.4.2 above) similar to luminescent images could be that the As_{Ga} defect, which is contained in EL2, is being influenced by the differing concentrations of defect components on both sublattices (for example an As_i and a V_{Ga}). Further investigations of the strange effects which occur around individual dislocations when In–doped material is annealed may help to explain the more complicated defect interactions in undoped material.

7 BULK QUENCHING AND ANNEALING STUDIES.

7.1 Introduction.

This chapter details the effects of various heat treatments, in particular quenching, on bulk material uniformity. The specific effects of quenching on [EL2], dislocations, As precipitates and bulk electrical properties are investigated and discussed.

The main body of work was carried out on four quadrants cut from a cylindrical block taken from an undoped SI LEC GaAs ingot. Further quenching and annealing studies were carried out on quadrants cut from two blocks from another ingot. Finally, an undoped LEC ingot was specially grown to study the effect of whole ingot quenching.

7.2 Experimental details.

This section is split into three sub–sections. Firstly 7.2.1 gives the sample details and annealing and quenching procedures performed on quadrants. Secondly 7.2.2 details the samples and the quenching procedure for whole ingot quenching using "optimum" conditions obtained from the block quenches. Finally 7.2.3 gives an outline of the assessment techniques which have been used.

7.2.1 Block quenches.

Two ingots, #1 and #2, were used in the initial block quenching studies. Sample details, quenching treatments and assessment procedures are described below. Slices adjacent to these blocks were retained as reference samples.

A 5cm long cylindrical section (labelled block 1) was taken from the 2" diameter, <001> axis, undoped SI LEC GaAs ingot, #1 (fig.4.1). The block was cut into four quadrants. Each quadrant was then sealed inside an evacuated quartz ampoule at 10^{-6} torr. These ampoules had been previously out–gassed at 1200°C at a vacuum of 10^{-6} torr to reduced the possibility of transition metal contamination (Tin 315) during subsequent anneals. The ampoules were annealed for 5 hours at 700, 800, 900 and 1000°C before quenching, performed by rapidly withdrawing the ampoules from the furnace and plunging into cold water. The ampoules were then opened and a 2mm surface cut was removed from each quadrant. Subsequently a 1mm slice was taken for electrical measurements and a 2mm slice for NIR, etching and CL examinations. After initial results were obtained, the remaining quadrant material, now approximately 4.5cm long, was cleaned and re–sealed in out–gassed quartz ampoules for further quenching studies. The second set of anneals were for 5 hours at temperatures of 1100, 1150, 1180 and 1200°C. These samples were quenched and slices were taken for assessment as described for the lower temperature anneals. The remaining quadrant material, now approximately 4cm long, was cleaned and re–sealed in a quartz ampoule for a third set of anneals. These comprised of annealing all four quadrants for 5 hours at 850°C, followed by slow cooling. The thermal treatments given to the blocks from ingot #1 are summarised in fig.4.1.

Two 3cm <001> axis blocks from another 2" diameter undoped SI LEC GaAs ingot, #2, were

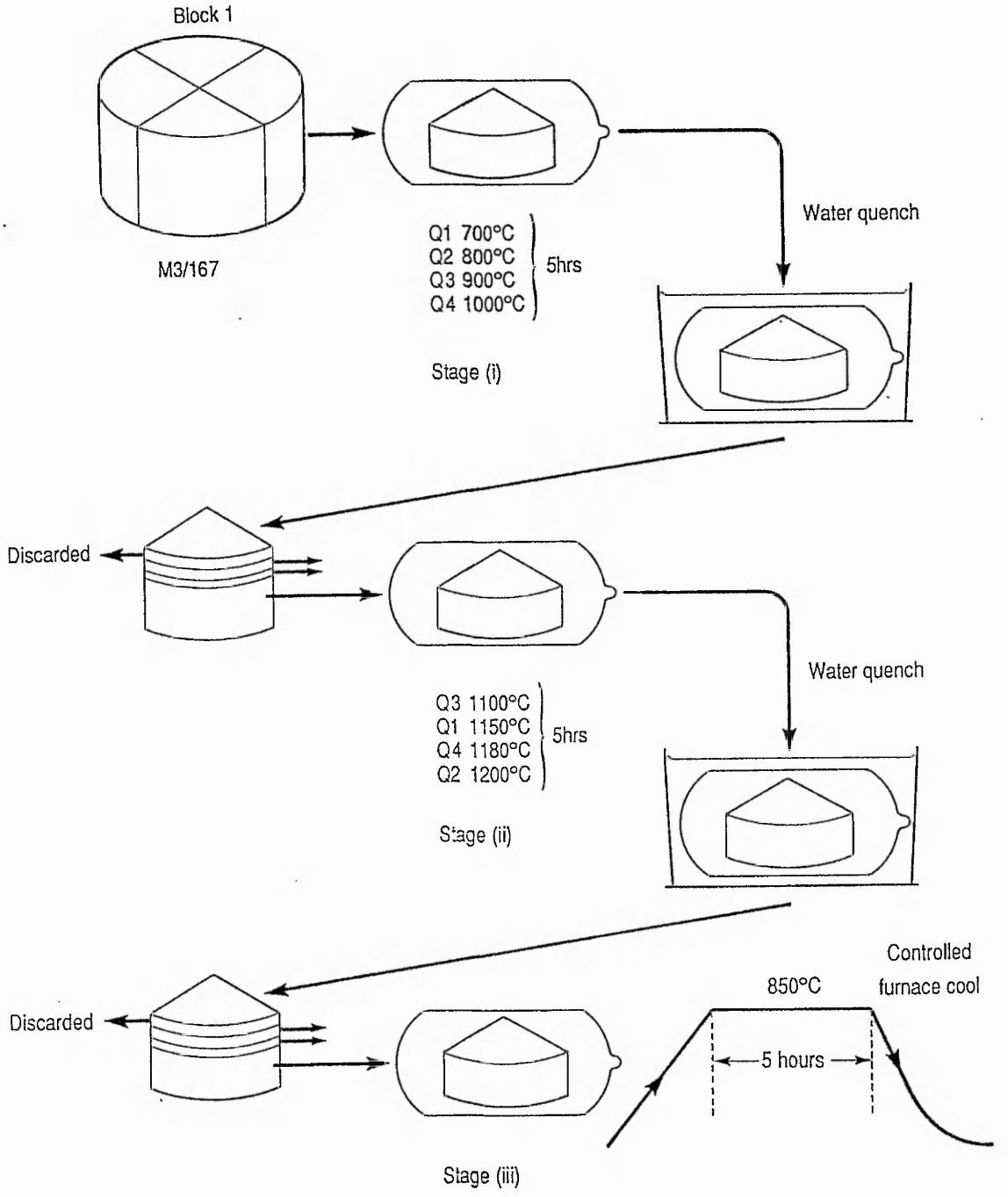

Fig.7.1. Schematic of the heat treatments given to the 4 quadrants from ingot #1.

used for further investigations. Blocks from ingot #2 were cut into quadrants before thermal treatments. The quadrants from the first block (Block 1) were used to study the effect of re–annealing samples quenched from 1100°C. The quenching procedure was identical to that carried out on the blocks of ingot #2. The first quadrant was re–annealed for 5 hours at 950°C, the second for 5 hours at 900°C and the third for 24 hours at 900°C. The forth quadrant was retained after quenching for use as an as grown reference. A second block (Block 2) was used to investigate the effect of conventional 5 hour anneals at 950 and 1000°C and also an air quench after a 5 hour, 1100°C anneal. The air quench was carried out by removing the ampoule from the furnace and allowing it to cool down naturally in air. The thermal treatments given to the quadrants from ingot #2 are summarised in fig.4.2.

7.2.2 Ingot quench.

Following favourable initial results from quenching quadrants, an entire ingot, #3, of about 5Kg in mass and nominally 2" diameter, was quenched and annealed. The ingot was air–quenched in its ampoule after being held at 1100°C for 5 hours. It was then annealed at 950°C for 5 hours, before cutting. Slices were taken from the top and the tail of the ingot for assessment. The thermal treatment given to the ingot #3 is illustrated in fig.7.3.

7.2.3 Outline of assessment.

Electrical data were determined by room temperature Hall effect and temperature dependent Hall effect measurements. NIR assessment, including the qualitative vidicon imaging system and the quantitative spectrophotometer system, was used to investigate the magnitude and uniformity of [EL2]. The [EL2] line–scan system described in chapter 5 was used to give an idea of the [EL2] on a microscopic scale. Samples were also taken for CL and A/B etching studies. The samples were A/B etched primarily in order to investigate dislocations and precipitates. In addition, information on etch rates were obtained by taking surface profiles of the samples after etching. Details of the experimental techniques can be found in chapters 4 and 5.

Uniformities were semi–quantitatively assessed using line–scans of the CL, [EL2] and A/B etch surface profiles. To enable comparisons between the uniformities of a scanned parameter, P, from sample to sample, a percentage uniformity parameter U(P) was defined. The percentage uniformity parameters U(P) for a quantity P is given by the quantity:

$$U(P)=[(P_{max}-P_{min})/P_{min}]\times 100\%$$

where P_{max} and P_{min} are the values of successive peaks and troughs on a profile of the quantity P. This is illustrated in fig.7.4. Normally several values of U(P) are taken from one profile. The mean value and standard deviation of the U(P) measurements are then given.

7.3 Results.

7.3.1 Initial quadrant quenches.

Fig.7.5 gives an example of the electrical data obtained from the temperature dependant Hall effect measurements. The activation energy for conduction is obtained from the slope of the graph of $\ln(n_s)$ versus 1000/T. Fig.7.6(a) summarises the electrical data calculated from the

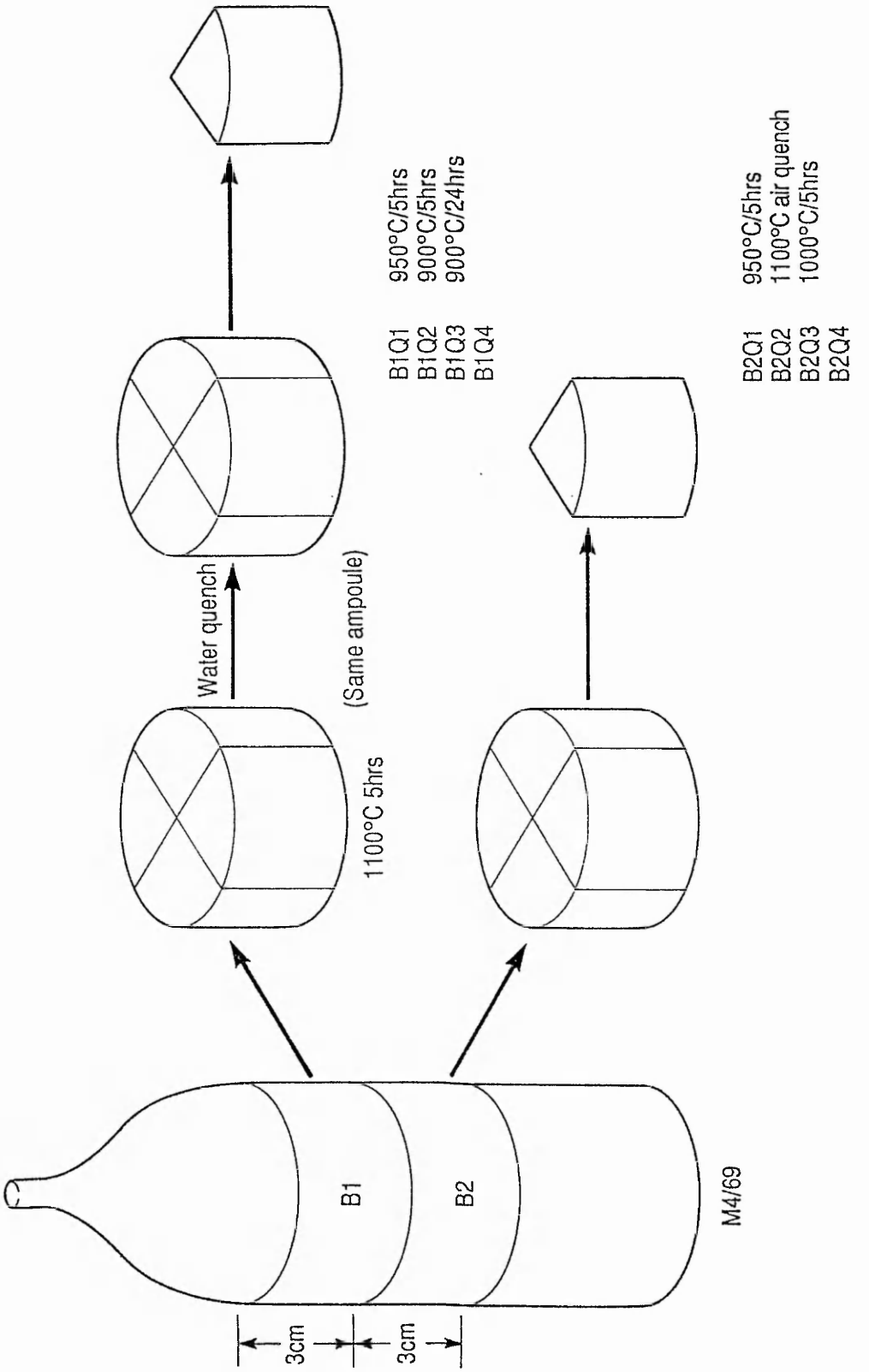

Fig.7.2. Schematic of the heat treatments given to the 8 quadrants from ingot #2

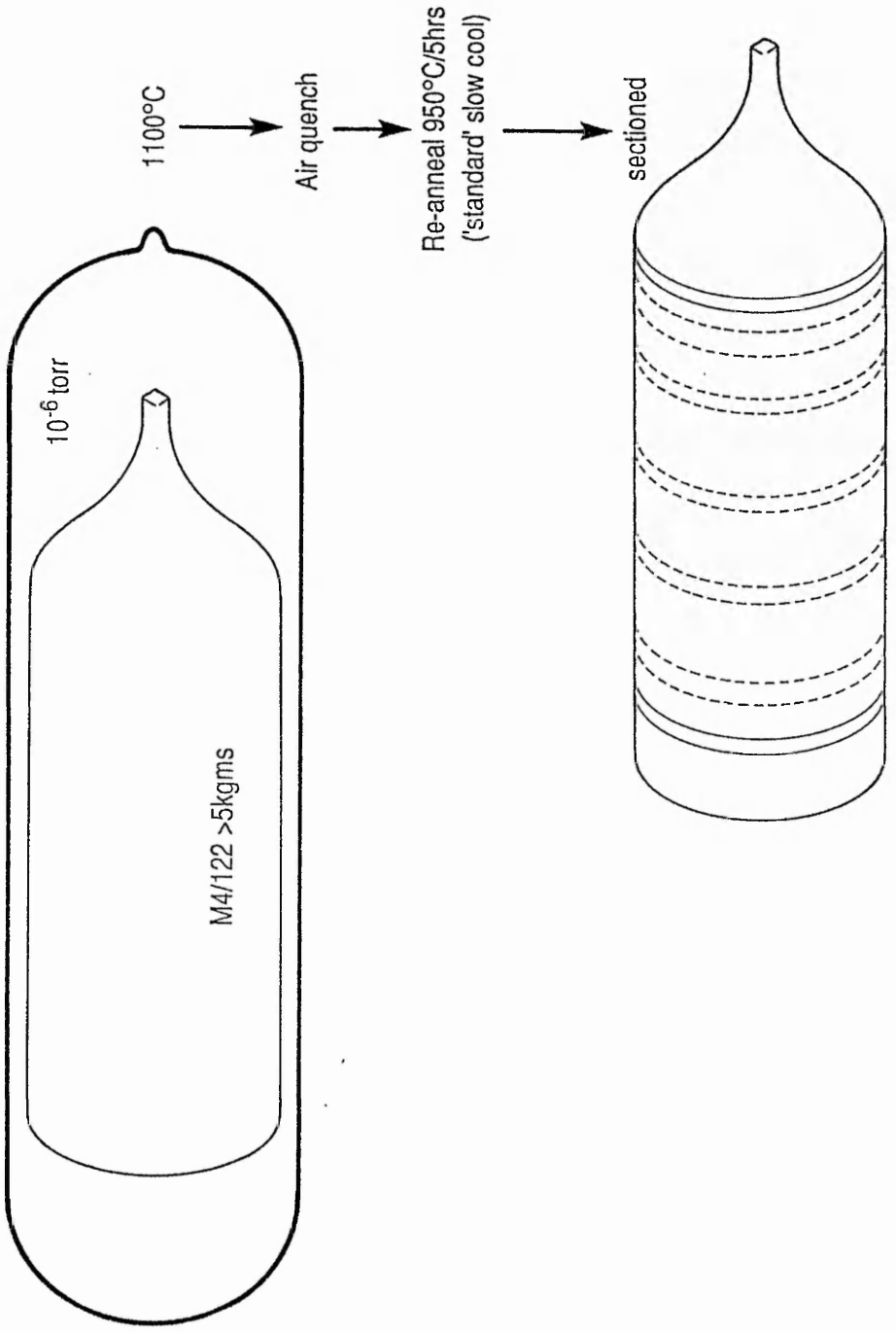

Fig.7.3. Schematic of the heat treatments given to ingot #3

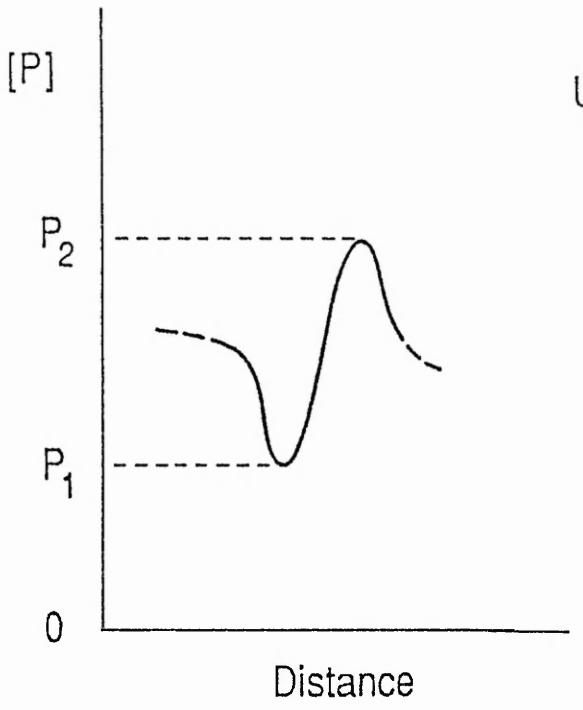

$$U(P) = \frac{P_2 - P_1}{P_1} \times 100\%$$

Fig.7.4. Defin-ition of the uniformity parameter U(P) for a measured parameter P.

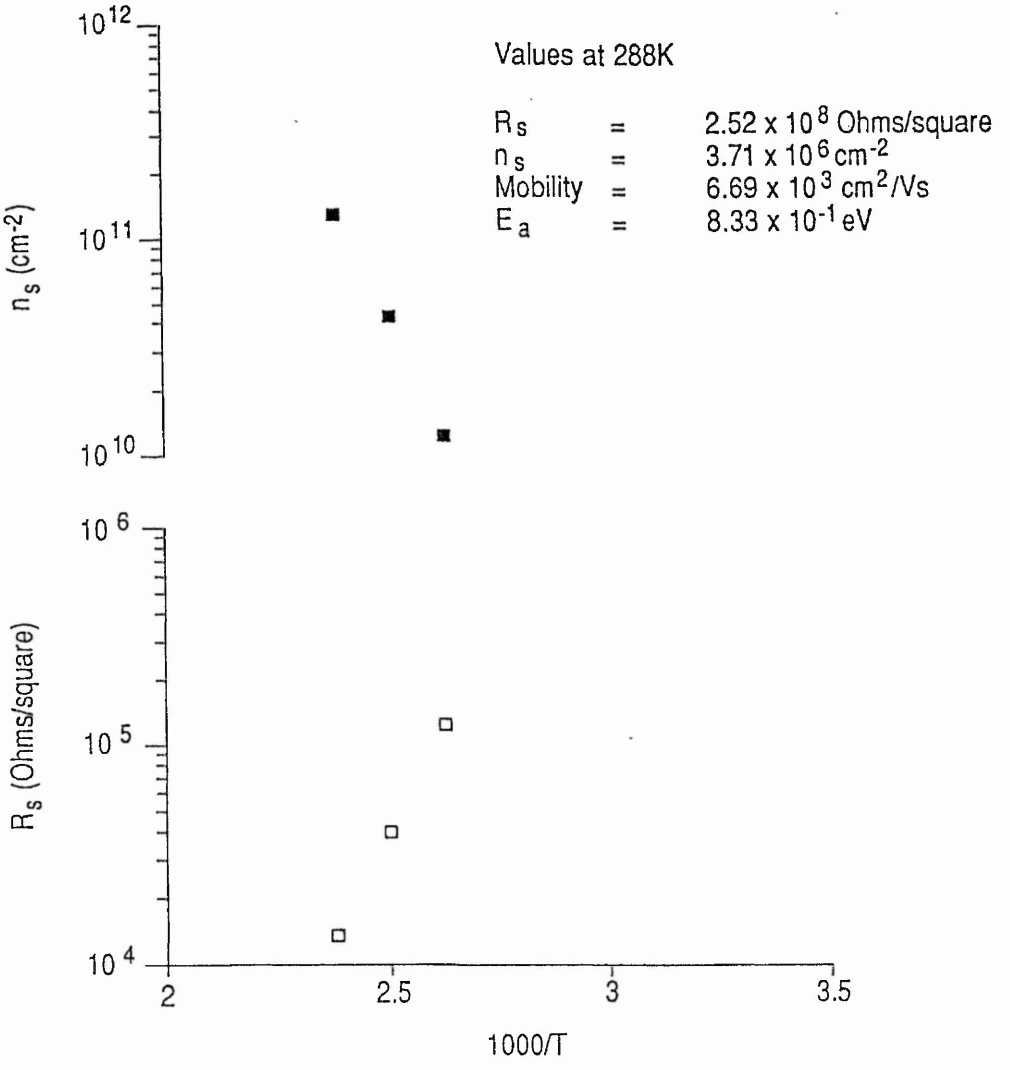

Fig.7.5. Sheet resistance and carrier concentration versus (reciprocal) temperature for an as-grown reference sample from ingot#1.

room temperature Hall effect measurements and the activation energy for conduction obtained from the temperature dependent Hall measurements. Several features are evident. Firstly the sheet resistivity, carrier concentration and electrical mobility values are all approximately maintained at the level of the unquenched reference sample, up to a quench temperature of 1100°C. Also the activation energy remains at a value of about 0.8eV which is consistent with EL2 controlled compensation. Above 1100°C, the electrical resistivity and mobility drops, the carrier concentration increases, and the activation energy falls. All of this is consistent with a move towards mixed and eventually p–type conduction.

Fig.7.6(b) gives [EL2] taken from the centre of the slices from the quadrants, along with a suitable uniformity parameter. This parameter, U(EL2), was calculated from the standard deviation of [EL2] which was in turn obtained from the [EL2] line–scan system; the analysis is detailed in appendix 7.1. The uniformity parameter was used in preference to a standard deviation value in order to be consistent with the uniformity parameters of the other measurements. Three examples of [EL2] line–scans from samples quenched from 900, 1000, 1100 and 1200°C are given in fig.7.7. These are to be compared with the [EL2] line–scan across an as–grown reference sample previously shown in fig.5.5. The images from which these [EL2] line–scans were taken are shown in fig.7.8 and fig.7.9 (a) (c) and (d). These images are discussed in more detail below. Fig.7.6(c) gives the mean value of the uniformity parameter for CL, U(CL) defined in the same way. This was obtained from the CL scans illustrated in fig.7.9(e)–(h). Error bars represent the standard deviation of the uniformity parameters data. Fig.7.6(d) gives the mean value of the uniformity parameter U(A/B) for the A/B etch surface profile measurements defined in the same way. Error bars represent the standard deviation of the uniformity parameter measurements. Some representative surface profiles are given in fig.7.10, together with microscopic images of A/B etched surfaces showing the profile positions in fig.7.11.

Fig.7.9. shows representative CL and EL2 images for the samples from ingot #1 which were quenched from 900, 1000 and 1200°C, together with an as–grown reference. Clearly, the uniformity improves with quench temperature. The best uniformities were achieved for quenches from 1100 and 1150°C. The CL intensities also dropped strongly with quench temperature although this is not evident from the scans, as the CL system gain is increased as the luminescent intensity drops. These CL images (in fig.7.9) also show scans of luminescent intensity across the images. The straight line under the scans is the signal baseline NOT the scan position. The unmarked scan positions are across the centre of the images. The EL2 images in fig.7.9 show the position of the scan line from which the EL2 absorption scans were taken. Background scans were taken by putting the camera out of focus. These scans are far more sensitive to microscopic fluctuations on the scale of cell structure than to macroscopic fluctuations (see section 5.3.3). In addition, the macroscopic fluctuations of [EL2] were investigated using the spectrophotometer. Fig.7.12 shows macroscopic fluctuations of [EL2] for the as–grown sample together with samples quenched from 800, 1000, 1100, 1150 and 1200°C. Note the strong improvement in macroscopic uniformity (flattening of the characteristic "W" shape variation of EL2 across a slice) up to 1100°C. Above this temperature the macroscopic uniformity is improved less by quenching.

Stability measurements of [EL2], as measured by optical absorption were carried out to see if

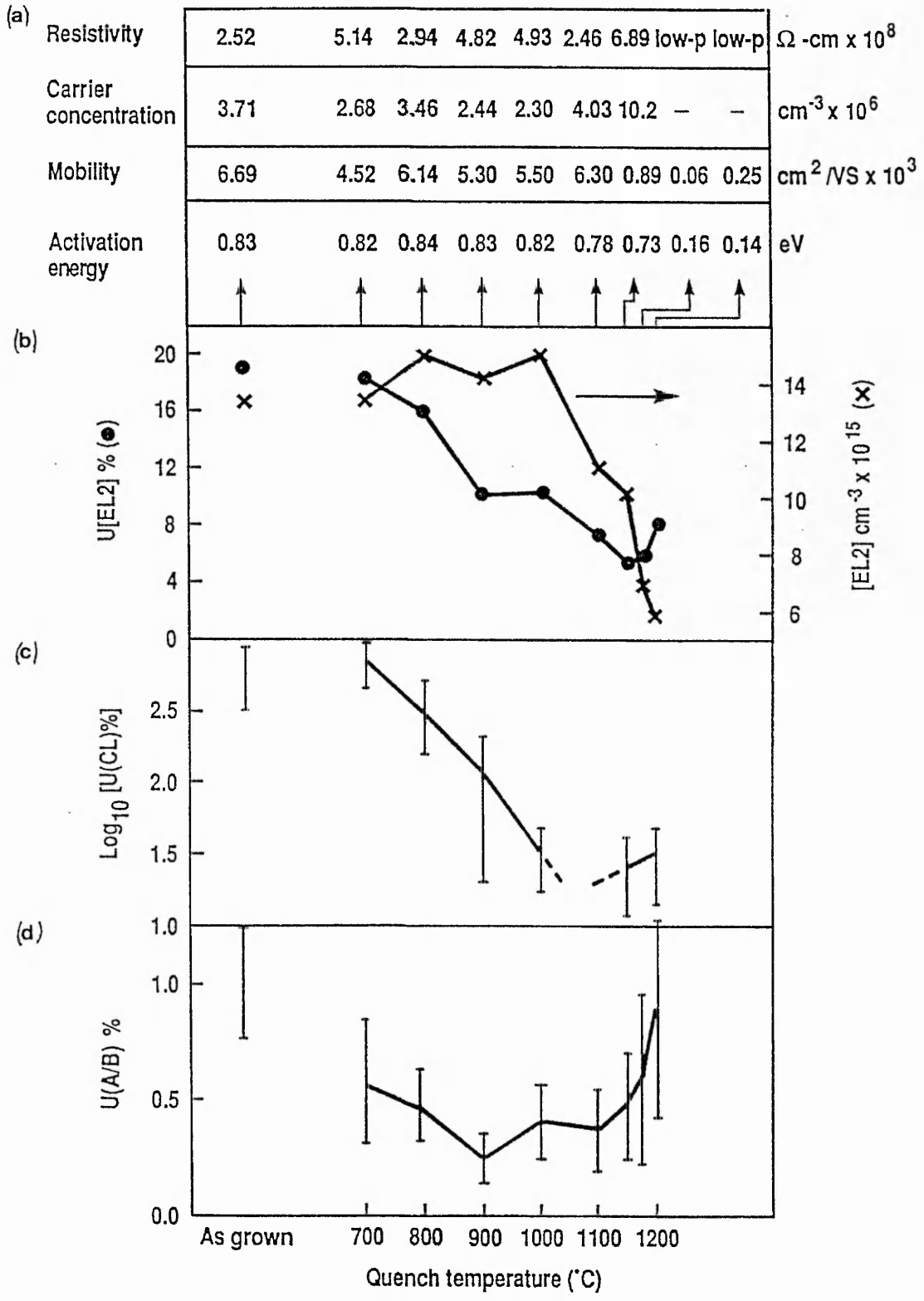

Fig.7.6. Variation of various material parameters with quench temperature for the quenched quadrant samples from ingot#1: (a) Electrical data; (b) [EL2] and U([EL2]); (c) U(CL); and (d) U(A/B).

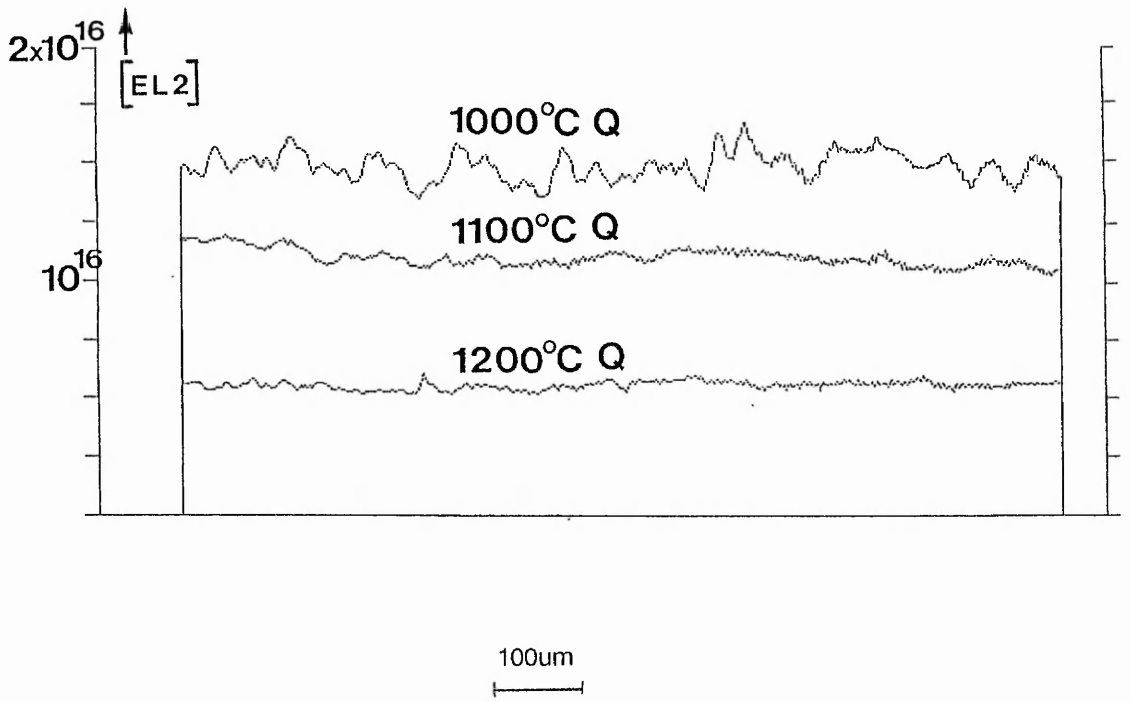

Fig.7.7 [EL2] line-scans for the samples quenched from 1000, 1100 and 1200°C

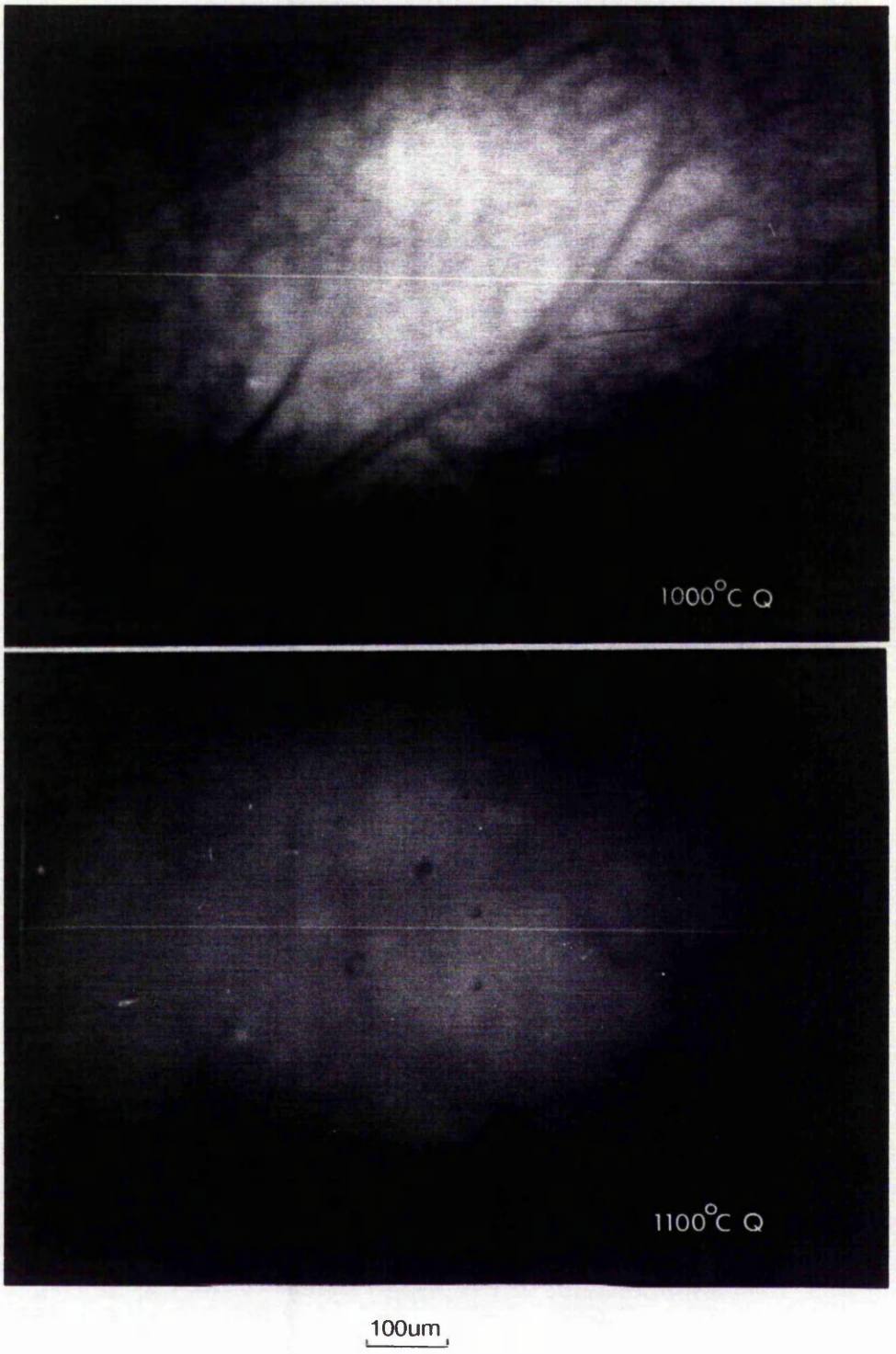

Fig.7.8. NIR absorption images for the samples quenched from 1000 and 1100°C, showing the position of the [EL2] line-scans.

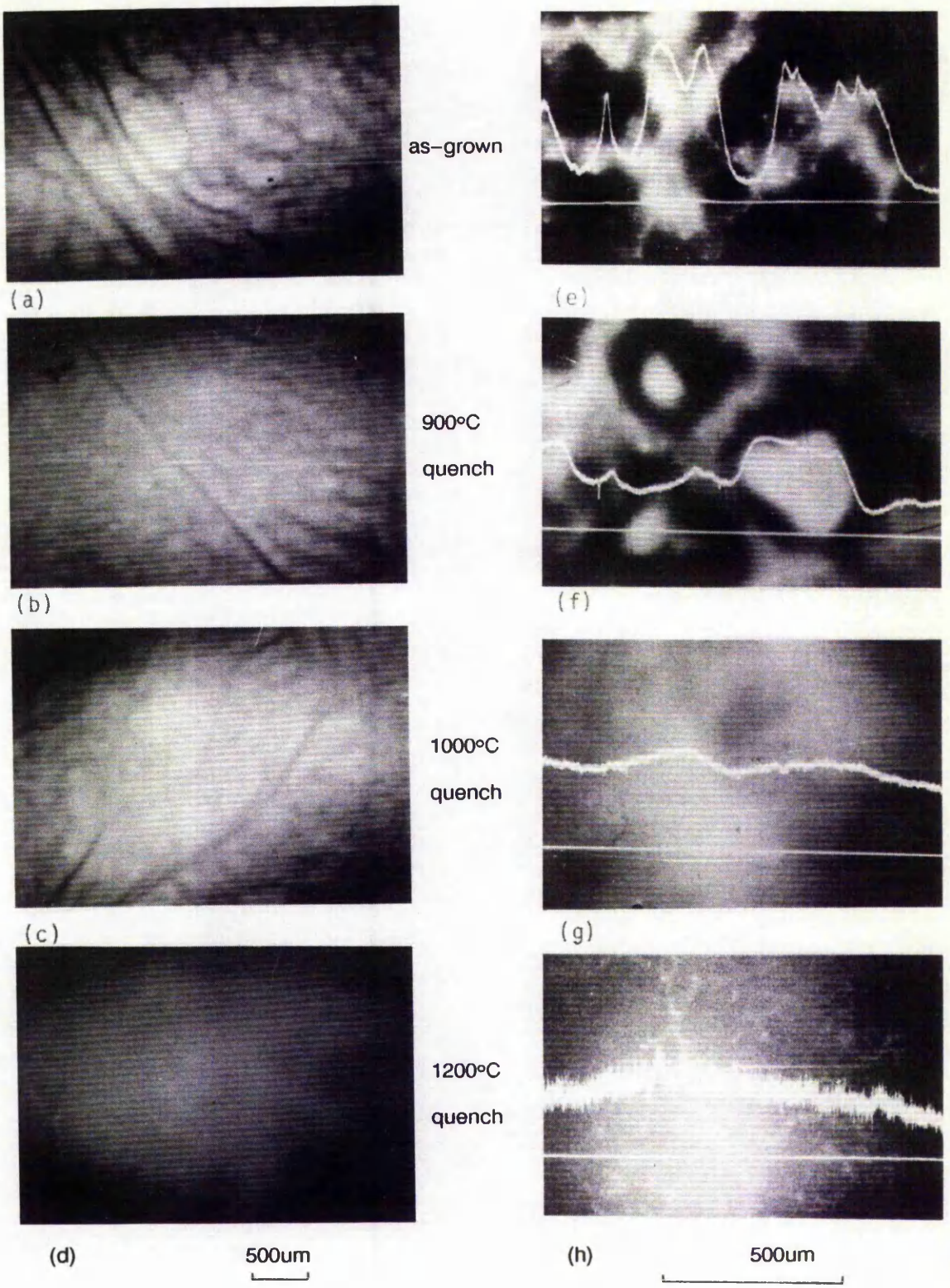

Fig.7.9. (a)–(d) NIR absorption images, (e)–(h) low temperature CL images with superimposed CL intensity scans.

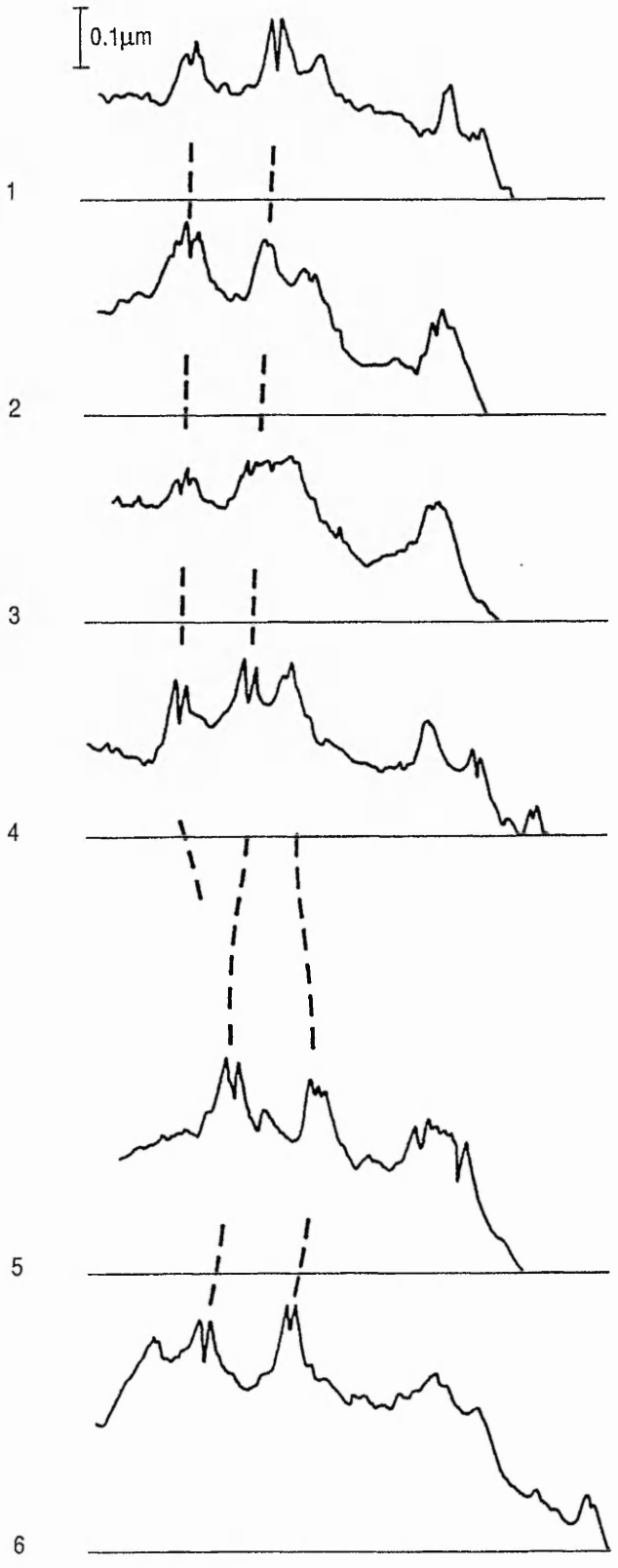

Fig.7.10. Surface profiles of the A/B etched surface of a quadrant quenched from 1000°C. A Nomarski micrograph showing the positions at which the scans were taken is given in fig7.11.

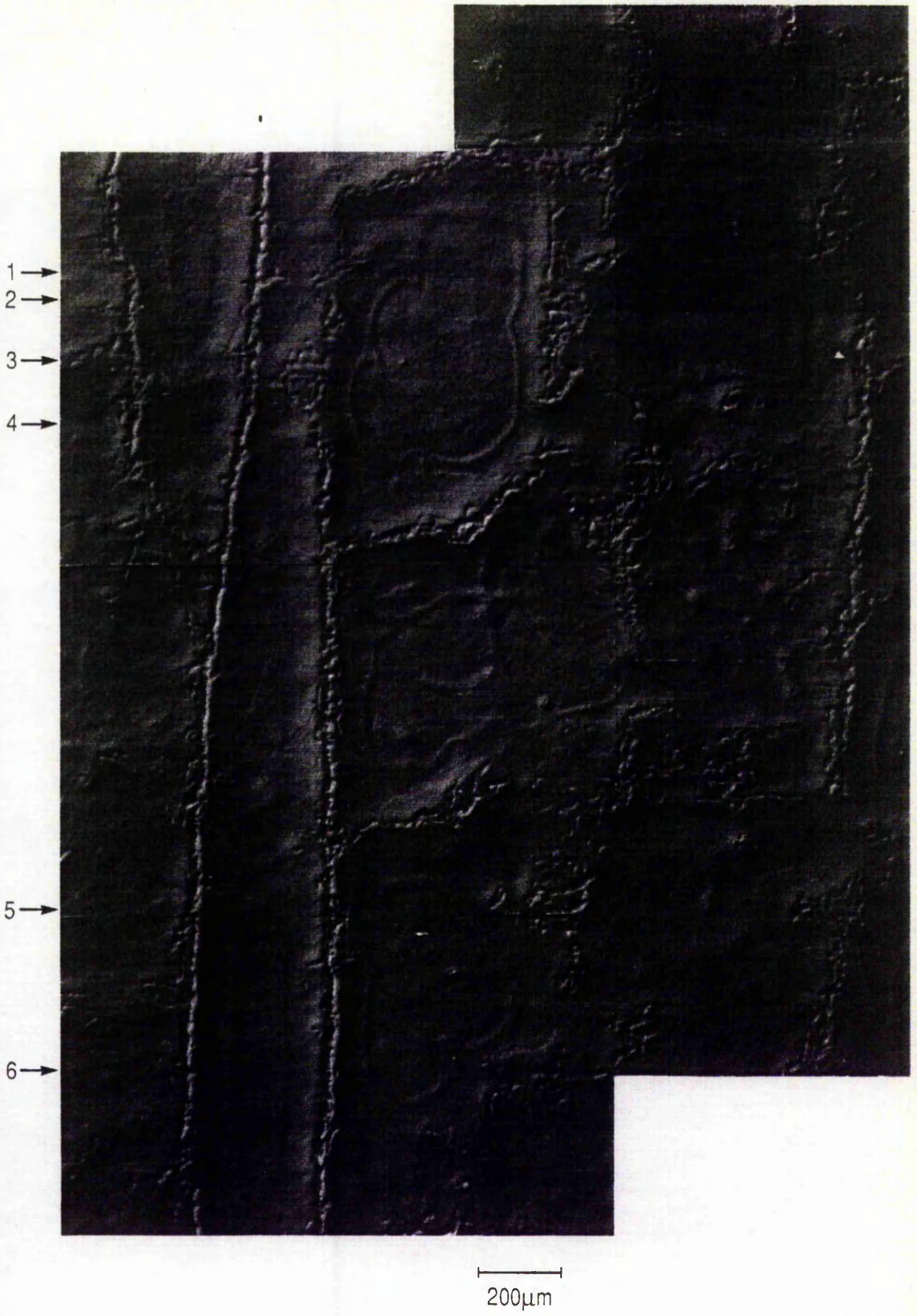

Fig.7.11. Nomarski micrograph of an area of the A/B etched surface of the quadrant quenched from 1000°C. The numbered arrows indicate the positions of the surface profiles in fig.7.10.

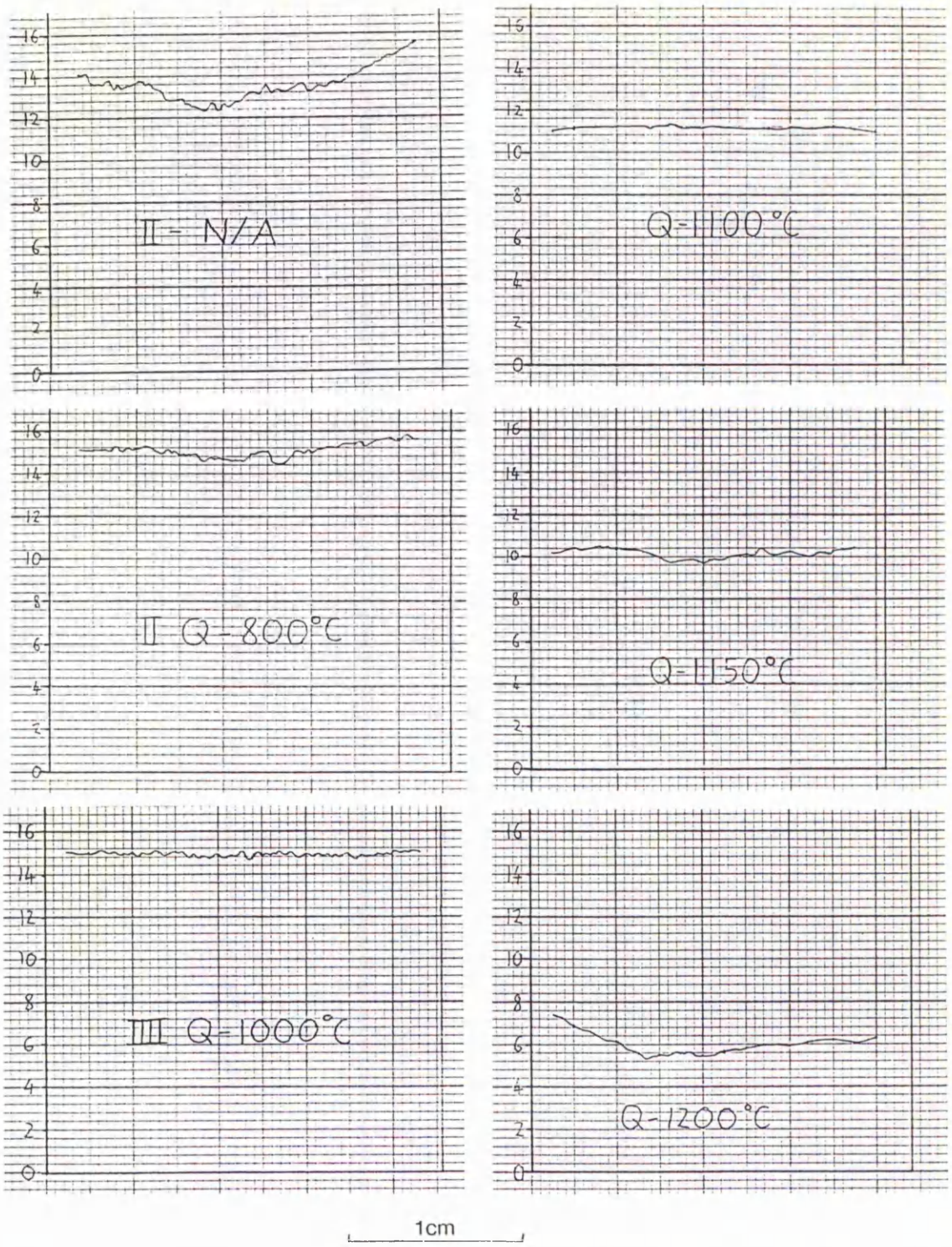

Fig.7.12. [EL2] profiles across quadrants from ingot #1 after being quenched (Q) from a series of temperatures (800, 1000, 1100, 1150, and 1200°C), together with [EL2] across an as-grown reference sample (indicated by N/A; Not Annealed). Profiles are taken along a <110> radius of the quadrant from a position near the centre of the ingot (left hand side) to near the edge (right hand side). Profiles are calculated from 1μm and 2μm spectrophotometer absorption scans and are plotted by hand. The scale indicates [EL2] in units of $10^{15}cm^{-3}$.

any changes occurred with time at room temperature. The experiment was carried out on the two samples quenched from 1000 and 1200°C. The samples were cut, polished and in place for measurements around 6 hours after the quench and were not physically moved in the spectrophotometer during the measurement period, which lasted for several weeks. An initial scan was used to investigate the absorption profile and select the measurement position. Within experimental errors, no change in [EL2] was observed for either of the samples. The data obtained from these measurements are given in appendix 7.2.

Dislocation densities taken from the same positions in the centre of the quenched blocks from ingot #1, are given below:

Quench temperature (°C)	Dislocation density ($x10^4 cm^{-2}$)
1200	78 +/– 21
1180	99 +/– 21
1150	77 +/– 9
1100	53 +/– 9
1000	5.4 +/– 0.9
900	8.2 +/– 2.3
800	4.8 +/– 2.4
As–grown	6.7 +/– 2.9

Dislocation densities are increased for the samples quenched from above 1000°C. Values given for the samples quenched from above 1100°C, are likely to be underestimates due to the difficulty in obtaining dislocation density counts in the tangled dislocation structure of the cell walls.

The main results taken from the microscopic Nomarski images of the A/B etched surfaces of quenched samples from ingot #1 are presented below:

Fig.7.13 shows an image of a sample quenched from 900°C. There are no major differences between this image and an image of an as–grown sample. The image shows dislocation cell structure. The cells appear fairly open as the "mounding" which normally occurs across the cell wall does not give strong contrast at this fairly high magnification. The cells are large, typically several hundreds of microns across. Dislocations appear as groves in the cell walls and as ridges in the cell centres. Dislocations are decorated with precipitates. One minor difference from as–grown samples is the prominence of micro–surface–roughness (Miyazawa 012, Dobrilla 242, 380), the pebbly texture in the central region of cells.

Fig.7.11 shows an image of the A/B etched surface of a sample quenched from 1000°C. The dislocation structure is still largely unchanged. The micro–surface–roughness is still present although less than in the sample quenched from 900°C. However a new ring feature just inside the edge of cells is now visible. Fig.7.10 gives A/B etched surface

Fig.7.13. Nomarski micrograph of the A/B etched surface of a quadrant (from ingot #1) quenched from 900°C. Dislocations in cell walls etch as grooves and in cell interiors as ridges. All dislocations are decorated with precipitates. Micro-surface-roughness occurs in cell interiors.

profiles, obtained at the positions 1 to 6 on fig.7.11, in the directions of the arrows. The lineage and cell walls are prominent whereas the ring feature is a barely visible dip just in from the cell walls. Fig.7.14 shows a higher magnification image of the A/B etched surface of the a sample quenched from 1000°C. This demonstrates that precipitates remain visible, although in considerably reduced numbers than in the samples quenched from lower temperatures.

Fig.7.15 shows an image of the A/B etched surface of a sample quenched from 1100°C. The dislocation density has increased substantially and now all dislocations appear as ridges. New cells have appeared within the centre of old cells resulting in the average size of cells dropping to a few hundred microns. Also, cells are more difficult to distinguish. Only faint micro–surface–roughness is seen. Fig.7.16 is an image at higher magnification. No precipitates are present on dislocations. The circular hollow features are believed to be caused by the etching procedure rather than the material properties.

Fig.7.17 is an image of the A/B etched surface of a sample quenched from 1150°C. The main features of this sample are the same as those of the sample quenched from 1100°C.

Fig.7.18 is an image from a sample quenched from 1200°C. All dislocations are seen as ridges and no precipitates are visible on the dislocations. Cell size is about a hundred microns. Only faint micro surface roughness is seen. There are a series of parallel dislocations across most of the sample surface with different orientations in different locations. They do not seem to interact strongly with the dislocations in the cell walls, and resemble newly created slip dislocations.

The changes described above are summarised in fig.7.19. A clear transition occurs between 900 and 1100°C. The as–grown, grove–ridge appearance of dislocations is transformed to an all–ridge appearance. No precipitates are seen for quenches from temperatures of 1100°C and above. Finally, the micro-surface-roughness is clearer than in as–grown material for quenches from 900°C but is faint for quenches from 1100°C and above.

7.3.2 Annealing of quenched blocks.

Fig.7.20 shows the effects of re–annealing quenched samples at 850°C for 5 hours on [EL2]. Error bars represent the standard deviations of the [EL2] line–scan data, and give an indication of microscopic [EL2] uniformity. Results are presented from the as–grown reference sample and the quadrants of M3/167 quenched from 1100, 1150, 1180 and 1200°C before and after annealing. [EL2] is almost restored to that of the as–grown sample by annealing and the high microscopic [EL2] uniformities of the quenched samples are maintained.

The inset in fig.7.20, gives the resistivities mobilities and Activation Energies taken from the Hall data. When compared with the electrical data in fig.7.6, it is found that electrical properties produced by quenching and annealing are superior to those of the as–grown sample.

Fig.7.21 shows the effect of the re–anneal on the macroscopic distribution of [EL2], as measured from the spectrophotometer. For the sample quenched from 1200°C the [EL2] has increased and the macroscopic uniformity is improved. However for the sample quenched from

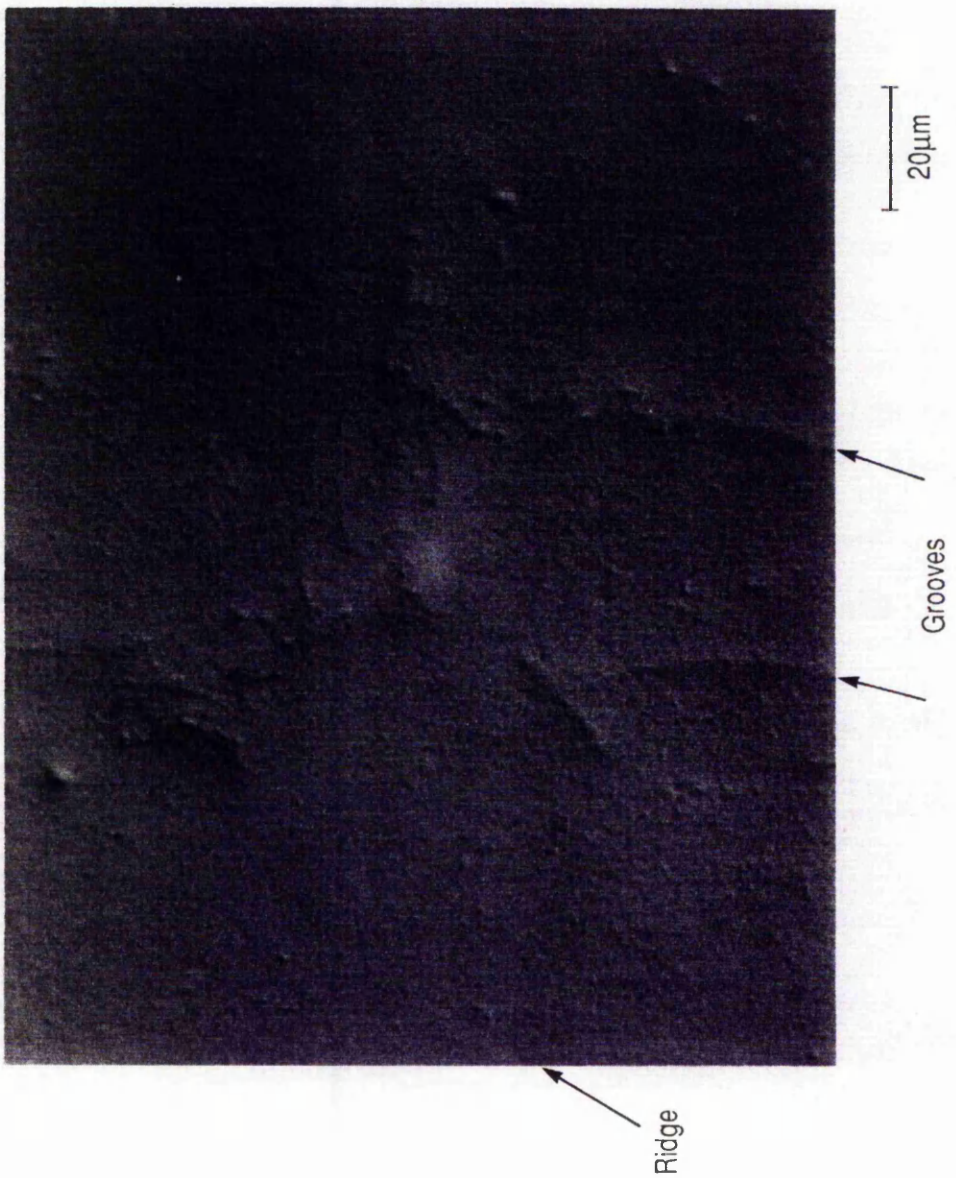

Fig.7.14 Nomarski micrograph of a region of fig.7.11 (quenched from 1000°C) at higher magnification; precipitates are still present, mainly associated with dislocations.

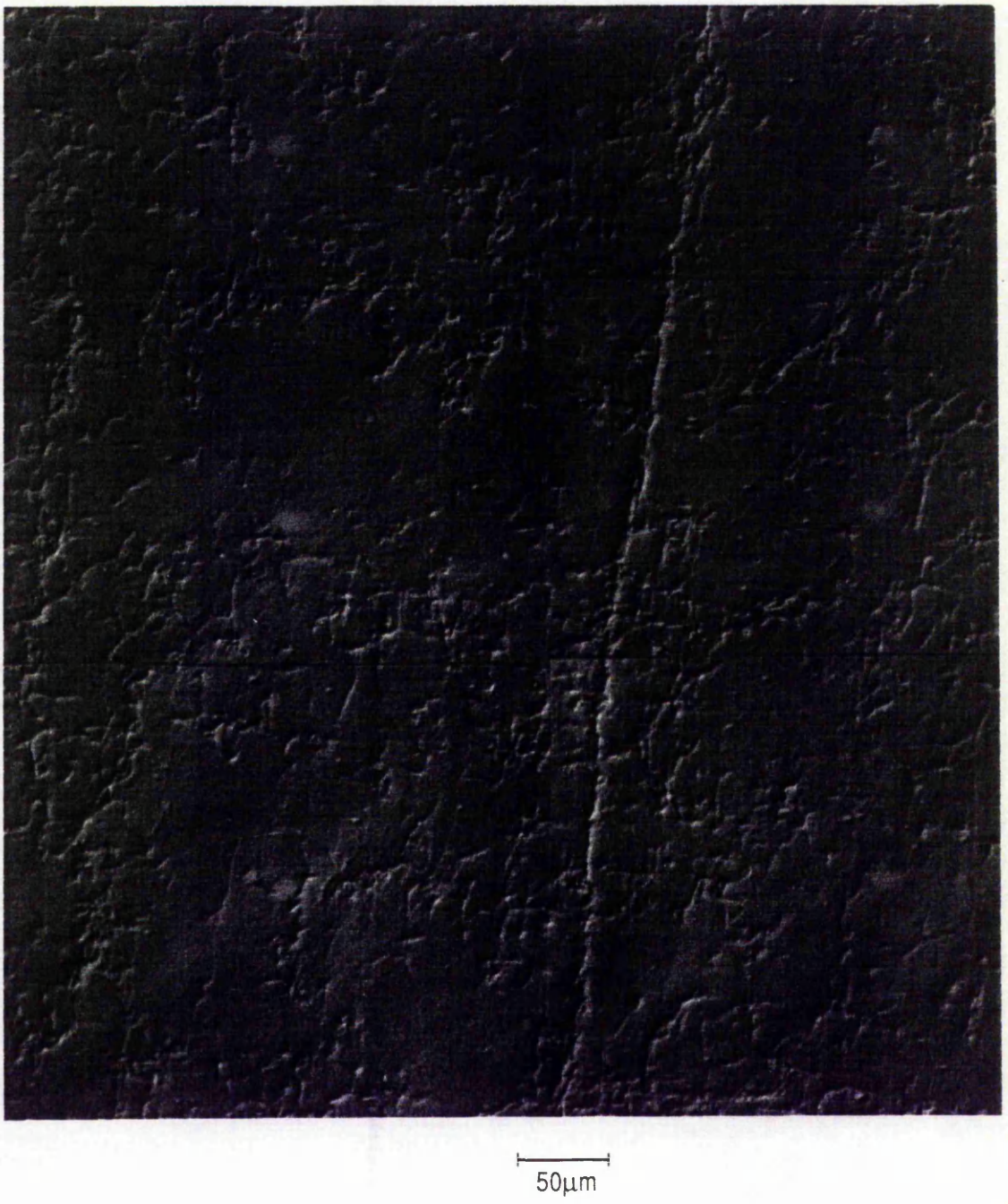

Fig.7.15. Nomarski micrograph of the A/B etched surface of a quadrant quenched from 1100°C. All dislocations etch as ridges and precipitates can no longer be found.

Fig.7.16. A region of fig.7.15. at higher magnification. Circular features are hollows, believed to be an artifact of the etch.

Fig.7.17 Nomarski micrograph of the A/B etched surface of a quadrant quenched from 1150°C. All dislocations etch as ridges and no precipitates are present.

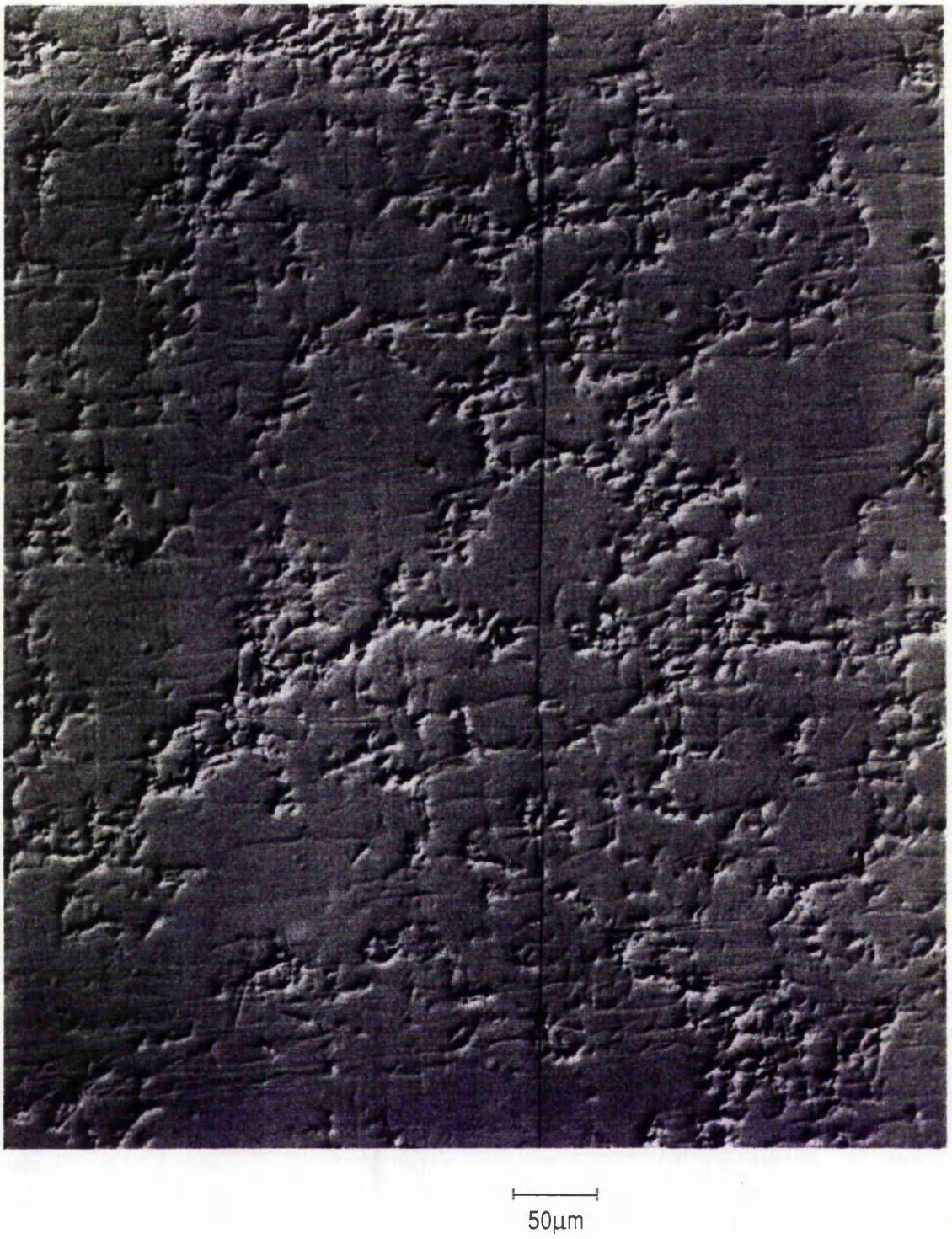

Fig.7.18. Nomarski micrograph of the A/B etched surface of a quadrant quenched from 1200°C. All dislocations etch as ridges, no precipitates are present.

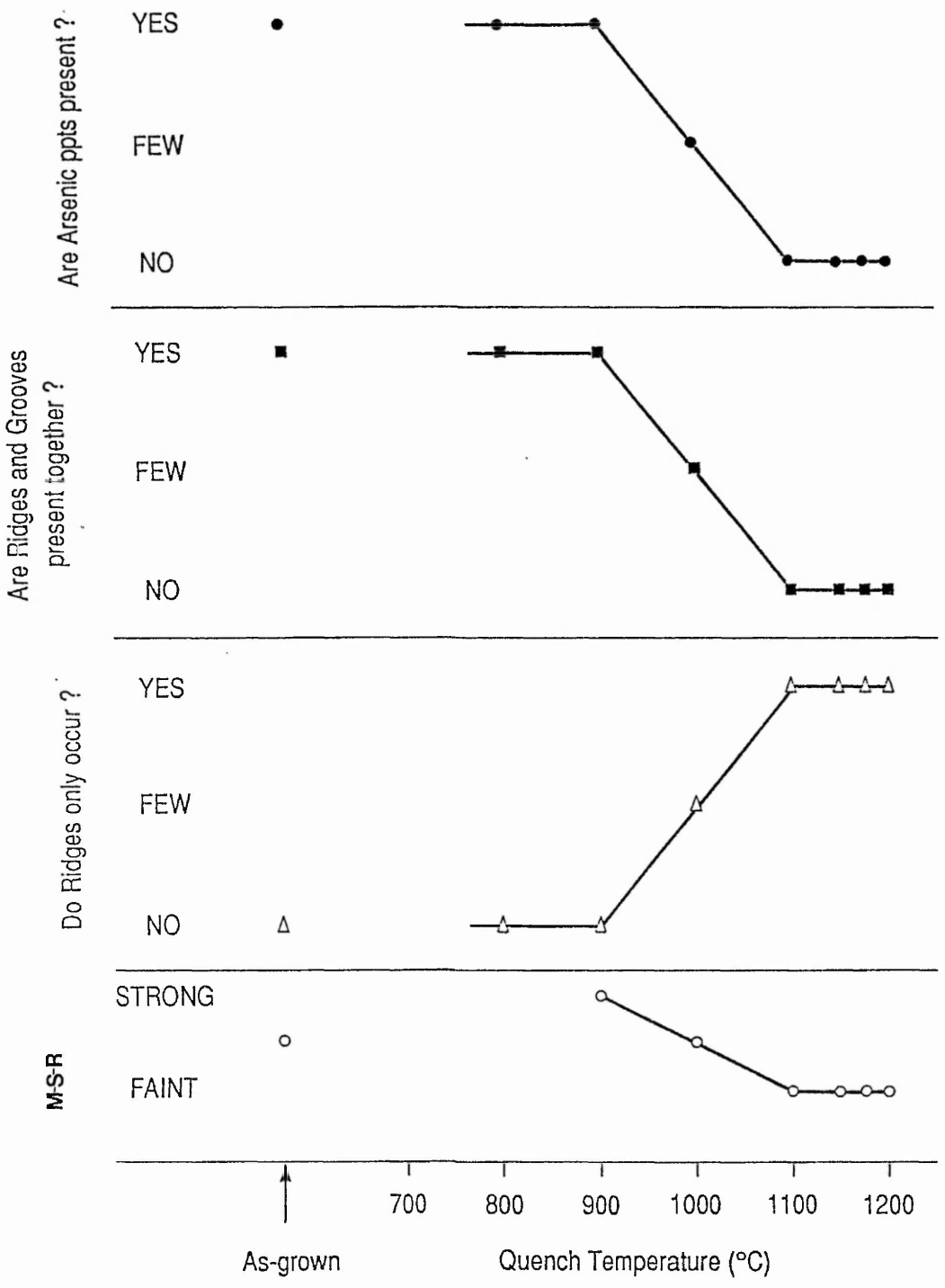

Fig.7.19. Changes in A/B etched surface characteristics, with quench temperature, for the quenched quadrants of ingot #1 (note that M–S–R is Micro–Surface–Roughness).

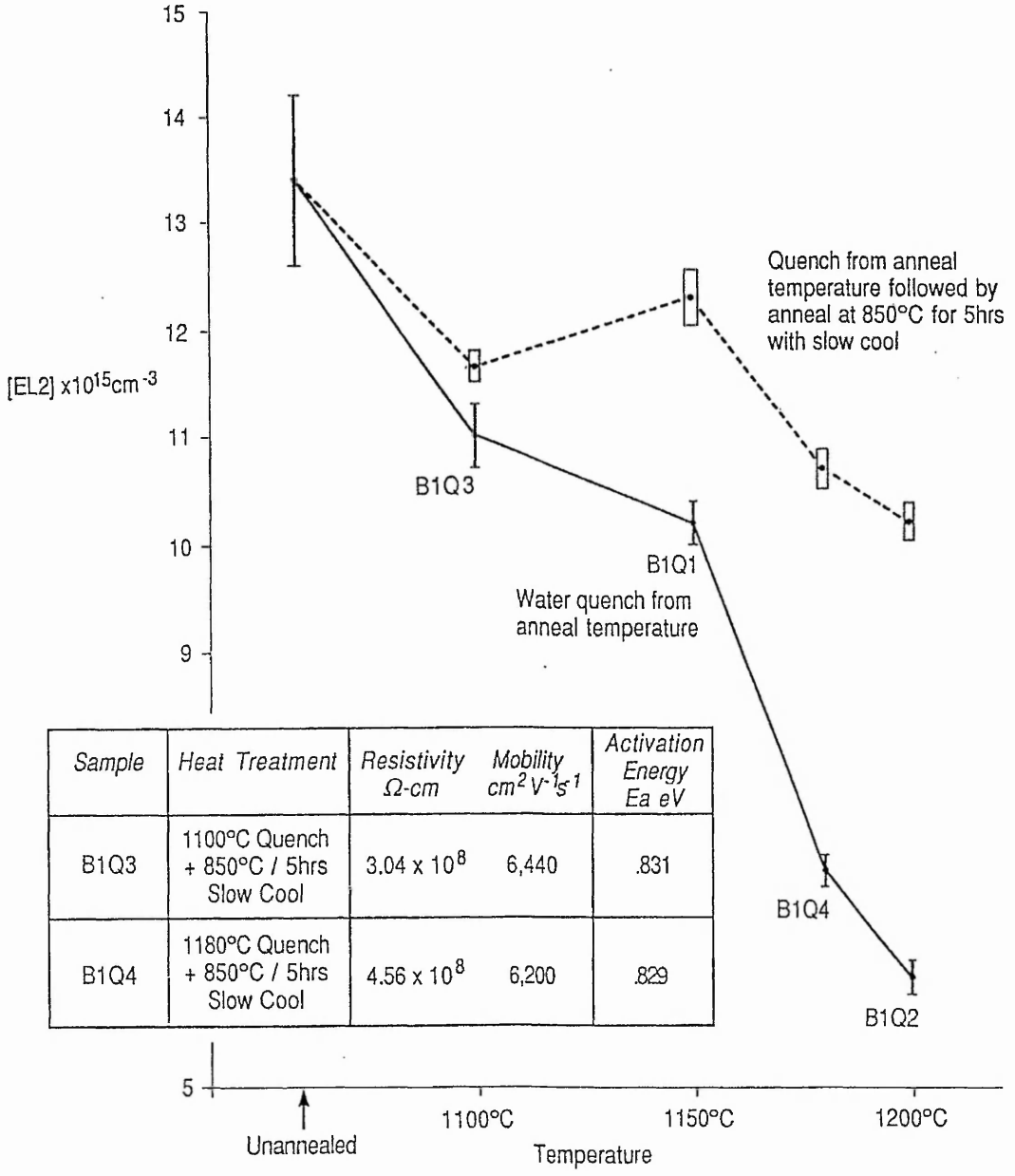

Sample	*Heat Treatment*	*Resistivity Ω-cm*	*Mobility $cm^2 V^{-1} s^{-1}$*	*Activation Energy Ea eV*
B1Q3	1100°C Quench + 850°C / 5hrs Slow Cool	3.04×10^8	6,440	.831
B1Q4	1180°C Quench + 850°C / 5hrs Slow Cool	4.56×10^8	6,200	.829

Fig.7.20. Comparison of [EL2] and the standard deviation of [EL2] (error bars) for the quadrant quenched samples from ingot #1 before and after re–annealing. The insert gives resistivity, mobility and activation energies for two of the quenched and re–annealed samples.

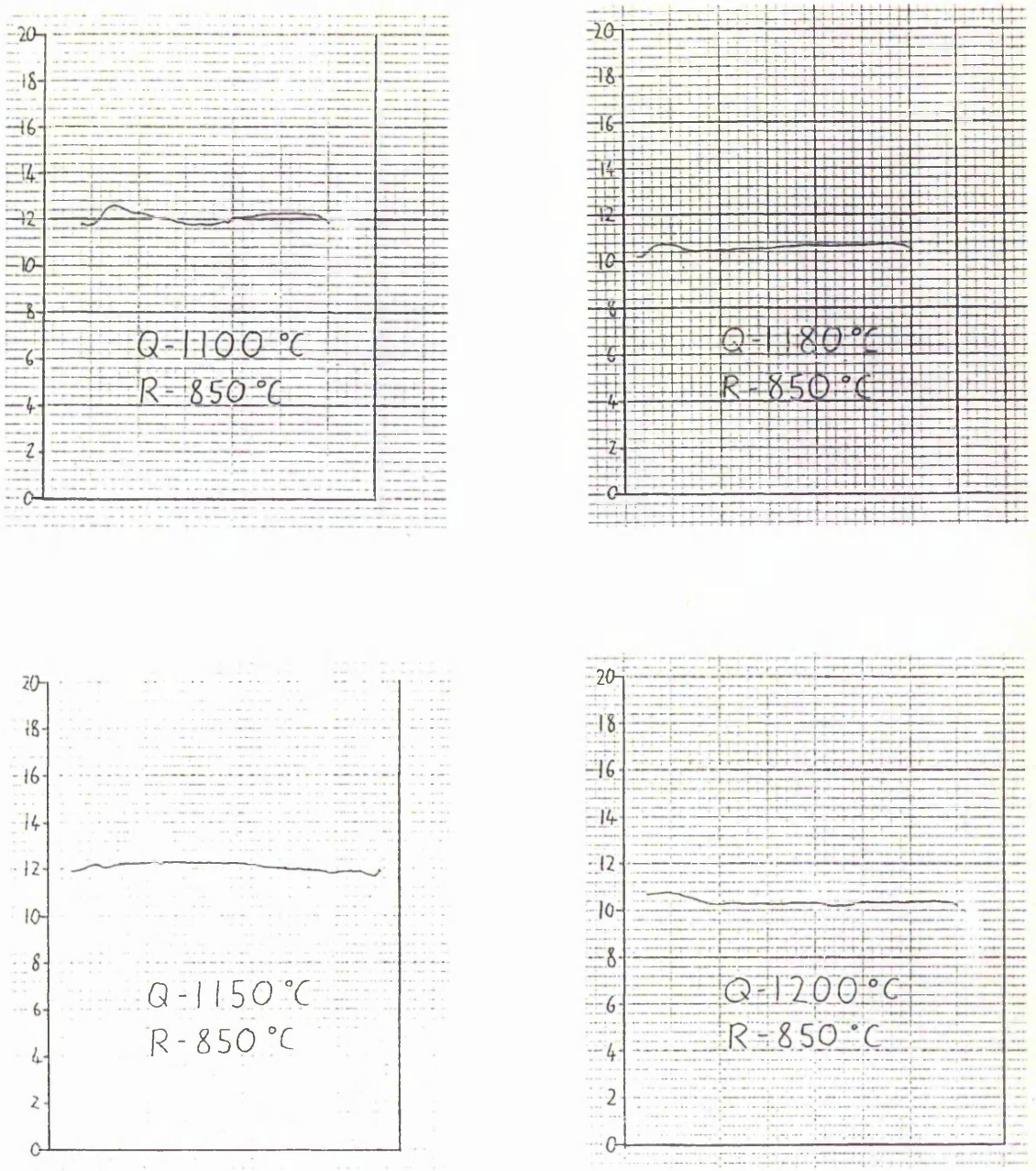

Fig.7.21. [EL2] profiles across quadrants from ingot #1, after being quenched (Q) from various temperatures (1000, 1100, 1150 and 1200°C) and re-annealed (R). Profiles are taken across a <110> radius, from a position near the centre of the ingot (left hand side) to a position near the edge (right hand side). Profiles are calculated from 1μm and 2μm spectrophotometer absorption scans and are plotted by hand. The scale indicates [EL2] in units of $10^{15}cm^{-3}$.

1100°C the macroscopic uniformity has worsened.

Fig.7.22 shows the A/B etched surface of the sample quenched from 1200°C and then re–annealed. The dislocation structure and density appears to be unchanged for all of the re–annealed samples. However, all dislocations now etch as grooves. In addition, some reformation of precipitates has occurred on dislocations. This is illustrated more clearly in fig.7.23, a region of the sample surface at higher magnification.

7.3.3 Further quadrant quenches and anneals.

Fig.7.24 summarises the effects of the various heat treatments on [EL2], resistivities and mobilities used on the quadrants from ingot #2. The error bars on [EL2] represent the standard deviation of the [EL2] line–scan data.

Annealing the as–grown sample increases the electron mobility and improves the microscopic [EL2] uniformity.

Quenching from 1100°C results in a strong drop in resistivity and mobility, associated with p–type conversion. [EL2] is largely unchanged but the microscopic EL2 uniformity is substantially improved compared to material given the standard anneal.

Annealing the quenched sample at 950°C for 5 hours gives substantial increases of resistivity and mobility, an [EL2] comparable with the standard anneal and a microscopic [EL2] uniformity comparable with the quenched sample.

Fig.7.25 shows a region of the A/B etched surface of a quadrant from ingot #2 quenched from 1100°C and annealed at 950°C for 5 hours. All dislocations appear as grooves and precipitates are present on dislocations. However the density of precipitates is far higher than seen in the samples from ingot #1. Fig.7.26 shows a region of the A/B etched surface from near the edge of the ingot. This shows a peculiar effect. At the edge, all dislocations appear as ridges and few precipitates are seen; towards the centre of the sample, dislocations appear as grooves and precipitates are present. The transition between these two regions is fairly sharp.

All annealed samples showed a flat featureless EL2 absorption profile from both spectrophot–ometer scans and vidicon imaging. This indicates high macroscopic as well as microscopic uniformity.

7.3.4 Ingot quench: bulk material properties.

The initial electrical results for the ingot #3 which was quenched and subsequently annealed are presented below:

Seed end:

Resistivity:	4.49×10^7 ohm.cm
Mobility:	$6.63 \times 10^3 cm^2/Vsec$
Carrier Conc:	$2.20 \times 10^7 cm^{-3}$, n–type

Fig.7.22. Nomarski micrograph of the A/B etched surface of a quadrant (from ingot #1) which has been quenched from 1200°C and re-annealed at 850°C for 5 hours. All dislocations etch as grooves.

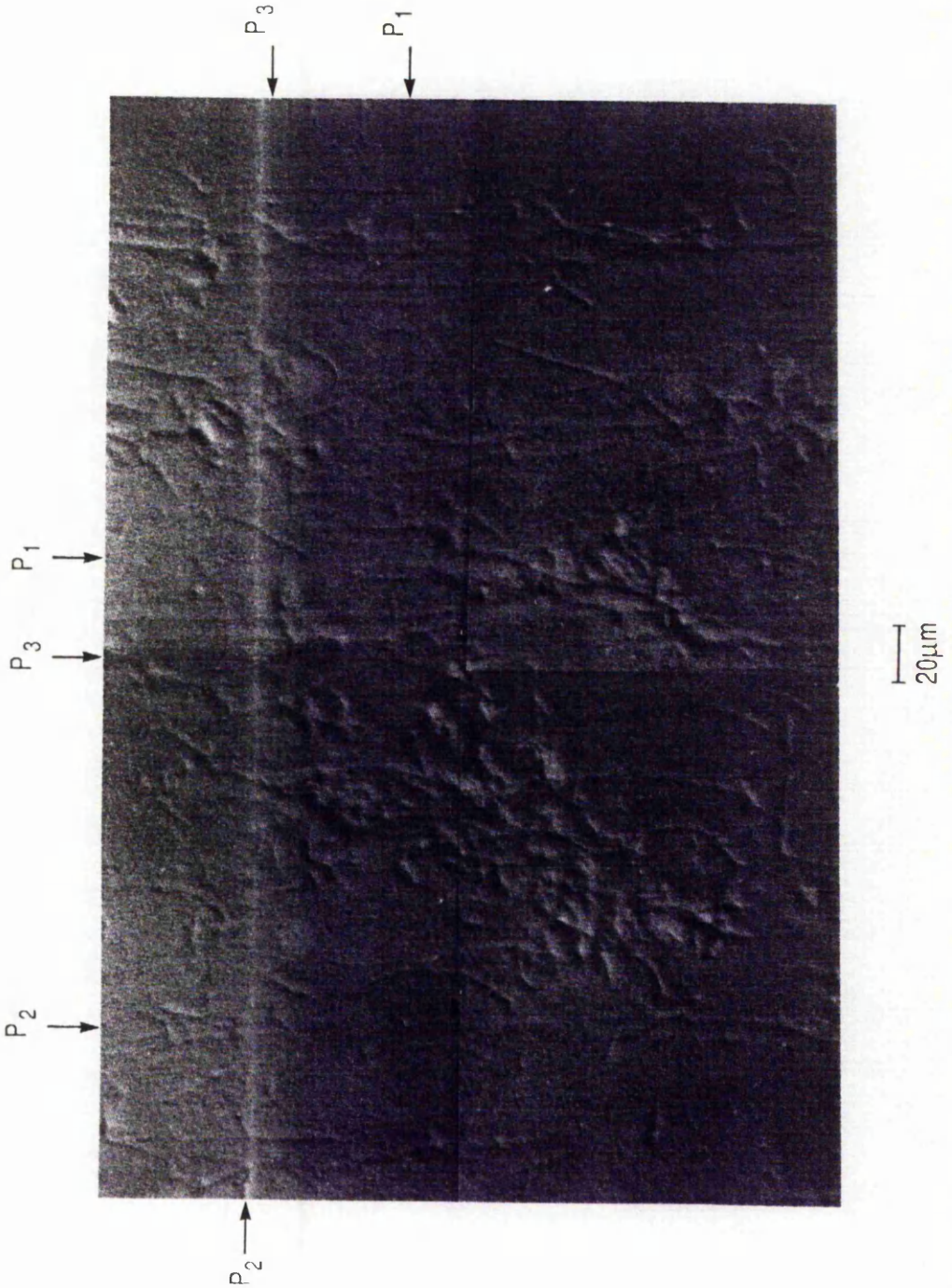

Fig.7.23. A region of fig.7.22. at higher magnification, some precipitates (arrowed are present).

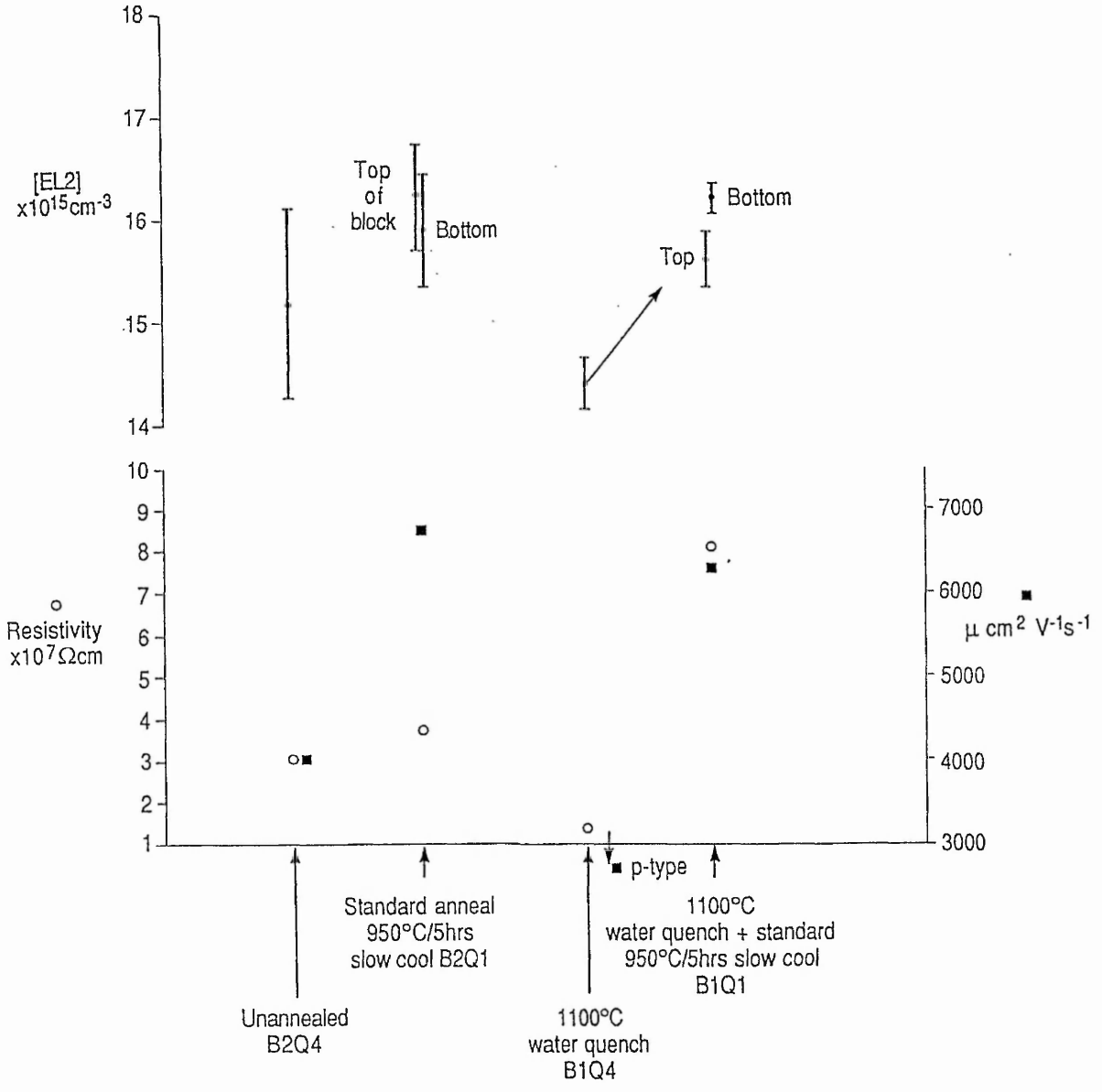

Fig.7.24. Changes in [EL2], the standard deviation of [EL2] (error bars), resistivity and mobility for the different heat treated quadrants of ingot #2.

Fig.7.25. Nomarski micrograph of the A/B etched surface of a quadrant (from ingot #2) which has been quenched from 1100°C and reannealed at 950°C for 5 hours. All dislocations etch as grooves and many precipitates are present.

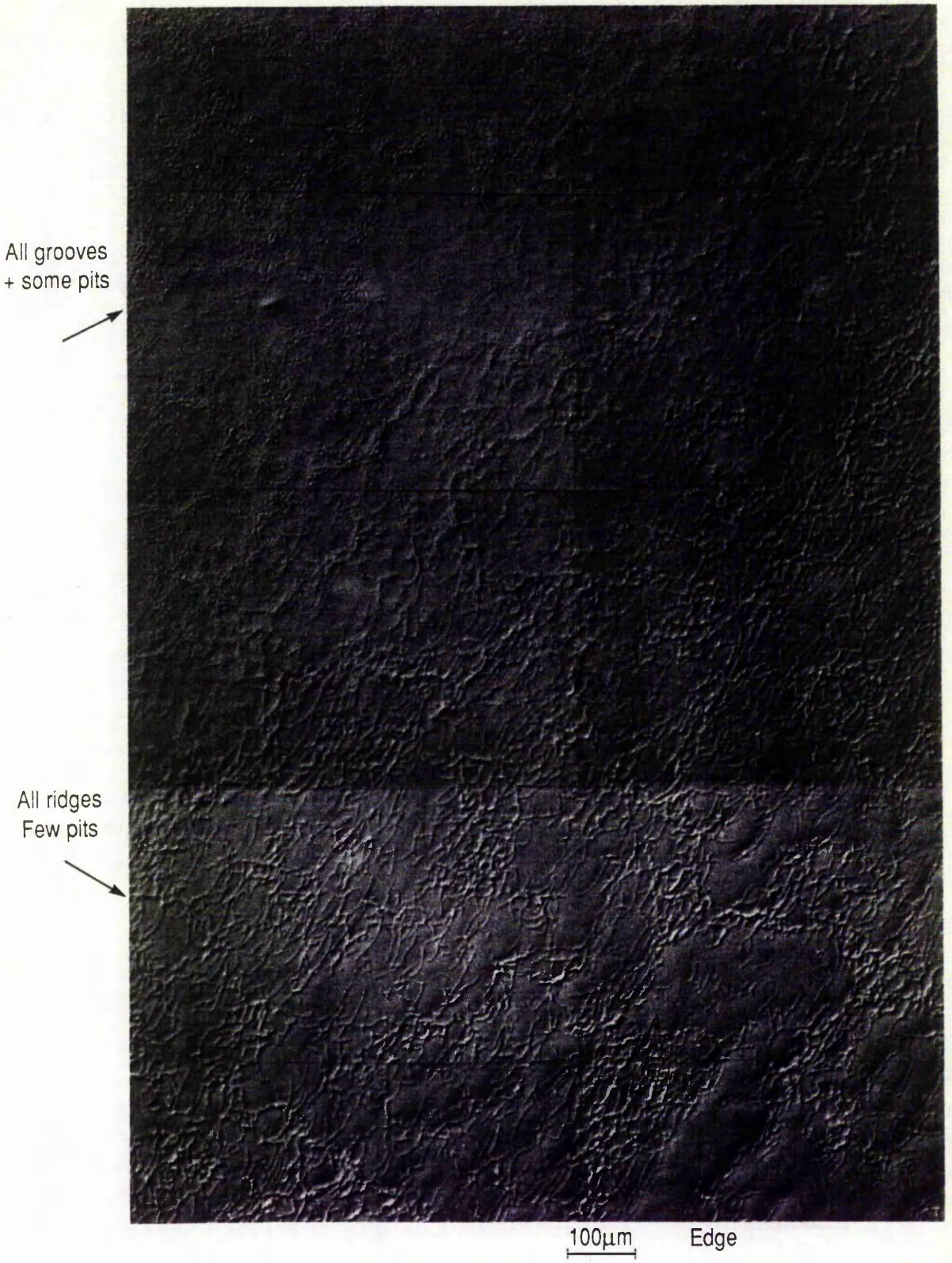

Fig.7.26. Nomarski micrograph of the A/B etched surface of a region near the edge of the sample shown in fig.7.25. As before, towards the centre of the sample, dislocations etch as grooves and precipitates are present. However, near the edge, dislocations etch as ridges and no precipitates are present.

Tail end:

Resistivity: 6.81×10^{7}ohm.cm

Mobility: $6.84 \times 10^{3}cm^{2}/Vsec$

Carrier Conc: $1.34 \times 10^{7}cm^{-3}$, n–type

EL2 absorption scans from the spectrophotometer are given in fig.7.27. The profiles are macroscopically flat. Values of the [EL2] at the seed and tail, were the same at $1.28 \times 10^{16}cm^{-3}$. The [EL2] data is summarised in fig.7.28 and compared with that obtained from the block quenches and anneals of ingot #2, error bars represent the standard deviation of [EL2] line–scan data. The standard deviation of [EL2] is small indicating high microscopic uniformity. The higher value obtained at the slice centre from the seed end is partially due to polishing artefacts. Microscopic [EL2] uniformity values are comparable with those from the quenched and annealed quadrants. The absolute values of [EL2] for the ingot are slightly less than those of the quadrants.

Fig.7.29 is a sketch of the dislocation arrangements of the quenched ingot #3. The thin parallel lines represent slip and the thickened lines represent pronounced lineage. Cell structure is prominent at low magnification but less so at high magnification due to the high dislocation densities. Fig.7.30 and fig.7.31 shows the A/B etched surface in the regions (a) and (b) of fig.7.29. Extensive slip is clearly visible. Fig.7.32 shows region (c). The dislocation density at the centre of the slice was $22.5 \times 10^{5}cm^{-2}$ with a standard deviation of $1.94 \times 10^{5}cm^{-2}$. This is a factor of two higher than the value of dislocation density at the centre of the quadrant quenched from 1200°C.

7.3.5 Ingot quench: initial processing results.

Initial ion implantation data has been reported for slices from the seed and tail end of ingot #3 (Warner 561). Implant activation on both samples are regarded as "good". One of the key points to arise out of processing is that the quench–anneal procedure gives material which is thermally stable during subsequent processing. This is to be expected as the material was annealed at a higher temperature than that experienced during implant activation.

7.4 Discussion.

7.4.1 Choice of ingot quench temperature.

For the quench to be effective in improving the uniformities of [EL2] and CL, an anneal temperature at or above 1100°C is clearly required. Although the best uniformity occurred for the quench from 1150°C, the dislocation densities and thermal stresses were noticeably higher than those of the quench from 1100°C. The increased size of the ingot compared to the block samples increased the concern that excessive thermal stresses may lead to breakage. Hence, the conditions chosen for the experiment were; quenching from 1100°C, followed by annealing at 950°C for 5 hours before cutting.

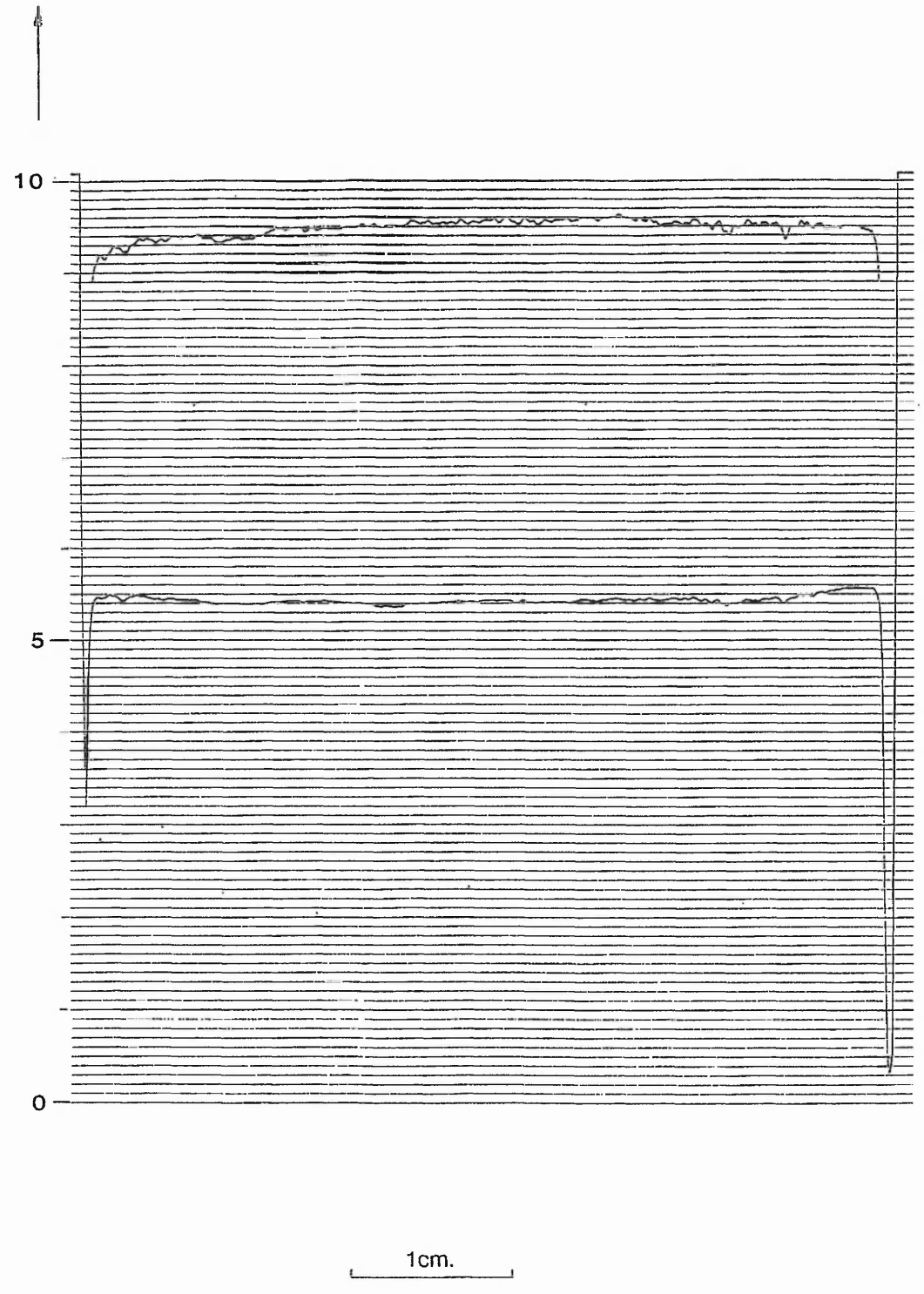

Fig.7.27. Spectrophotometer absorption scans at wavelengths of 1μm (bottom) and 2μm (top) for a 3mm slice from the tail end of the quenched and re-annealed ingot #3. (Note that 0 transmission corresponds to black)

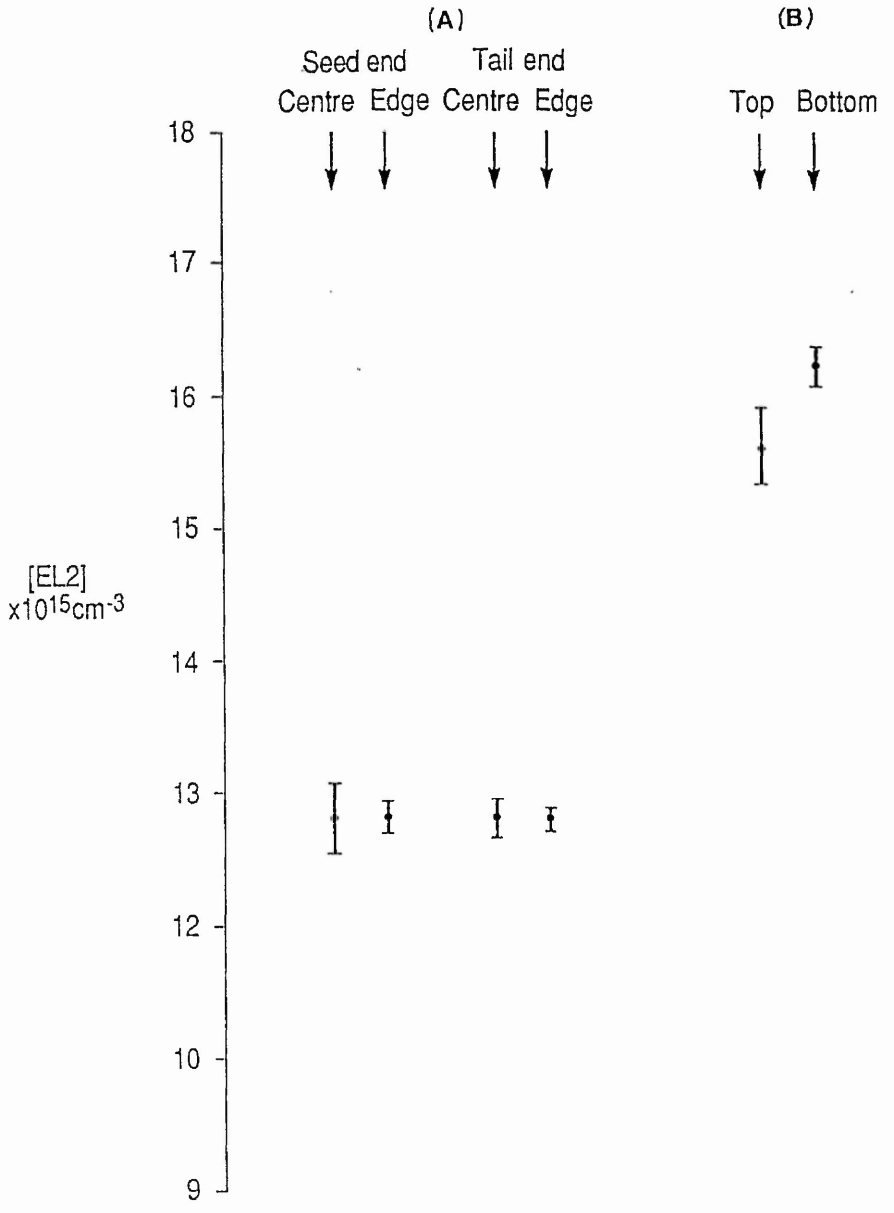

Fig.7.28. Comparison of [EL2] and the standard deviation of [EL2] (error bars) for ingot #3 (A) and a quadrant from ingot #2 (B), both quenched from 1100°C and re-annealed at 950°C for 5 hours.

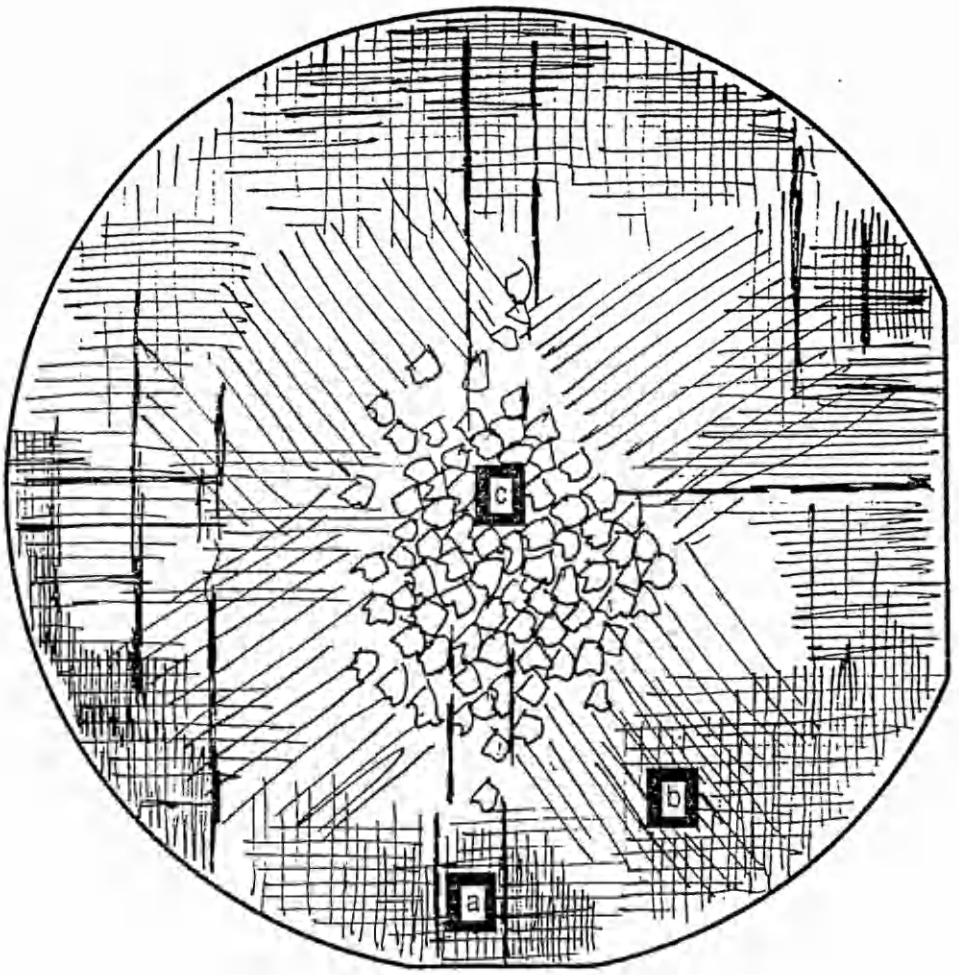

Fig.7.29. Sketch of the principal dislocation arrangements in ingot #3 (which has been quenched from 1100°C and re-annealed at 950°C). Nomarski micrographs of the A/B etched surface at (a), (b), and (c) are given in fig's: 7.30, 7.31 and 7.32.

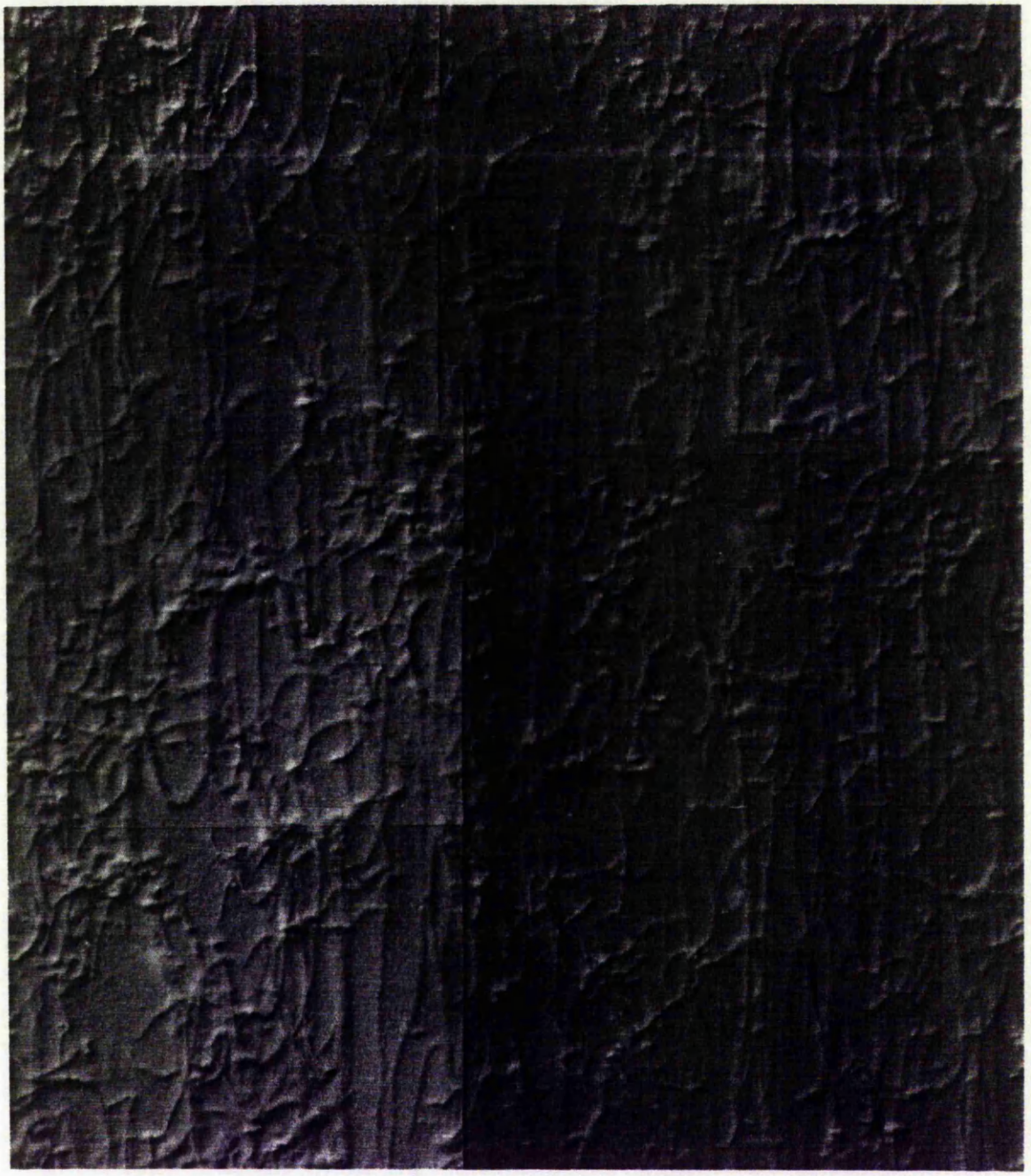

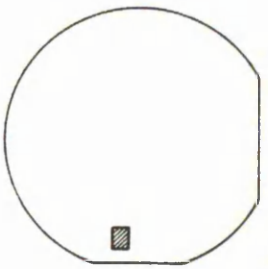

Fig.7.30. Nomarski micrograph of the A/B etched surface of a slice from ingot #3. All dislocations etch as grooves and few precipitates are present. The position of the micrograph on the slice (near the edge) is as indicated.

20μm

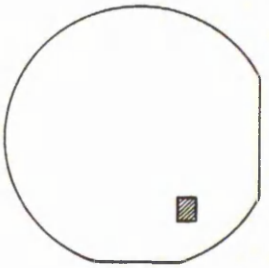

Fig.7.31. Nomarski micrograph of the A/B etched surface, at near the edge of a slice from ingot #3.

20μm

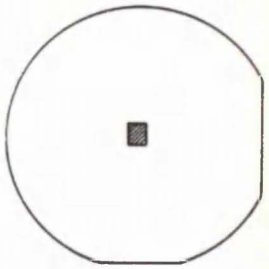

Fig.7.32. Nomarski micrograph of the A/B etched surface at the centre of a slice from ingot #3.

7.4.2 Cooling rates and thermal stresses.

It was not possible to measure the temperatures and cooling rates of samples in ampoules accurately. Estimates were taken of the time for the surface of samples to cool below red heat (at approximately 650°C). The readings can only be regarded as approximate as it took longer to remove some samples from the furnace than others. Also it was difficult to judge when the surface stopped glowing red. The recorded cooling times to this temperature for several of the quenched samples are given below:

Ingot quench;	3 minutes.
Quadrant quench from 1200°C;	60 seconds.
Quadrant quench from 1000°C;	50 seconds.
Quadrant quench from 900°C;	40 seconds.
Quadrant quench from 800°C;	30 seconds.

From the data given above, the following approximate cooling rates of the sample surfaces were obtained:

Sample	Cooling rate at 950°C	Cooling rate at 1100°C
Quadrant	10°C/sec	20°C/sec
Ingot	3°C/sec	6°C/sec

For samples in an evacuated ampoule the main mechanism of heat loss will be radiative from the sample surface, according to Stefan's law. Hence the cooling rate values given above can be regarded as upper limits for the cooling rate of the sample interior. In addition to radiative heat loss, some conduction through the sample holder or contact with the ampoule wall will occur; for the larger samples,radiative loss will dominate due to the relatively small contact area. Assuming that heat loss by conduction is negligible, larger samples will obviously cool more slowly than small samples, as the thermal mass increases faster than the surface area as sample size increases. This effect is exaggerated if the thermal conductivity is a limiting factor on the heat flow to the sample surface. This is likely to be the case for the size of samples we are to consider. The cooling rate also depends on the sample geometry as well as the size. For example, slices will cool faster than cubes of the same volume. Increasing cooling rates for a particular size and shape will also increase thermal gradients. Hence quenching will increase dislocation densities compared to slow cooling, providing that the Critically Resolved Shear Stress (CRSS) is exceeded. Thermal gradients are also increased if the annealing temperature before quenching is increased.

A full analysis of the cooling rate of samples and its effect on thermal stress was not undertaken. This type of thermo-elastic analysis, similar to that carried out by Jordan (Jordan 037, 080), is highly complicated. Thermal stresses arise from the temperature gradients induced in GaAs when it cools. Dislocations are generated when these stresses exceed the CRSS for a particular slip system. This is significant for crystals during growth, and is probably the main cause of the increase in dislocation density after quenching. If this is the case then a pattern of dislocations matching the stress conditions is to be expected. As during crystal growth, the

cooler outside of the sample would be in tension and the hot centre in compression. Hence increases in dislocation densities should be more significant near the edge and at the centre of the samples. This was indeed observed. However the quadrants are of unusual shape and the observed dislocation patterns were complicated. Further interpretation was not attempted.

A significant result was demonstrated by Kang et al (305). They quenched small samples (10x10x5mm) from 1200°C with no noticeable changes in dislocation densities. For our samples (typically, of the order of 25x25x40mm), clear increases in dislocation densities were noted for samples quenched from temperatures over 1000°C. Hence a critical condition, strongly related to sample size, must exist, which when exceeded results in stresses which exceed the CRSS, during quenching.

In addition to the generation mechanism of dislocations discussed above, the following mechanisms may also be important:

1) The contact points of the samples with the ampoules are likely to experience faster cooling due to heat conduction This will occur either at the corners or on the curved diameters of the quadrant samples. This has been supported in the present work by evidence of dislocation masses at these points.

2) When As precipitates dissolve at high temperatures, the supersaturation of As–rich point defects which arises can result in the condensation of dislocation loops; as is thought to occur in the growth of Bridgman material (see section 2.2.2).

3) Dislocation multiplication is likely to increase as the annealing temperature increases.

7.4.3 A/B etch features.

The appearance of dislocations on the A/B etched surface after various heat treatments can be explained by the fermi–level dependent etch rate model of Brown and Warwick (371). In that work SI (n–type) material was found to have a slower etch rate than conducting n–type and p–type material. For as–grown SI material, the fermi–level in the cell walls corresponds approximately to that which results in the minimum etch rate. The fermi–level in the matrix is nearer the valence band, resulting in a faster etch rate. The etch rate for dislocations was intermediate to the cell wall and matrix etch rates, but closer to that of the matrix. In the present work the shift from groove–ridge to ridge–only structure after quenching from high temperatures, is consistent with a drop in fermi–level, particularly in the cell wall regions. The shift to groove–only structures after annealing, indicates an upwards fermi–level shift for the entire sample, such that all of the surface etches in a similar way to the cell wall regions of as–grown material.

The micro–surface–roughness seen in fig.7.11 is probably due to defect clusters of very small precipitates or dislocation loops. Similar features have been previously been reported (Miyazawa 12, Dobrilla 242, 380) usually found in the cell centres of as–grown or annealed material. The sharply defined areas containing micro surface roughness correspond well to the bright regions in the cell centre seen in CL imaging (seen for example in fig.7.9(f) for the sample quenched from 900°C). The temperature dependence of micro–surface–roughness clarity, peaking for quenches from around 900°C, also correlates with the temperature

dependence of the appearance of bright CL zones in cell centres (see section 7.4.4). The clarity of micro–surface–roughness, after quenching from 900°C, is also consistent with the results of Suchet et al (069). They demonstrated the appearance of "milky way" scattering effects after annealing from similar temperatures (see section 2.4.5). In turn, this can be tentatively explained by suggesting that small micro–precipitates getter other defects from the matrix at this temperature.

If the larger, dislocation associated, As precipitates are present they usually appear on an etched surface as pits. For quenches from 1100°C and above, it cannot be stated definitely that As precipitates no longer exist, simply because they can no longer be observed on etched surfaces. This apparent disappearance could arise because either their size and/or density has dropped significantly.

7.4.4 Cathodoluminescence images.

The drop in CL intensity with increasing quenching temperature is almost certainly associated with a large increase in non–radiative recombination. This is probably associated with the dissolution of As precipitates into the lattice with a corresponding increase of As–rich point defects.

Strong changes occur in luminescent contrast in the centres of cells for the samples quenched from around 900°C. This is also associated with the increasing prominence of the micro–surface–roughness after A/B etching (as discussed in section 7.4.3). This indicates that non–radiative recombination centres are somehow denuded in the centre of cells, probably by gettering to the defects associated with micro–surface–roughness. The gettering and subsequent enlargement (or decoration) of the micro–defects, at this temperature, would give rise to their increased prominence on the A/B etched surface. A second possible explanation for these features is that the point defects responsible for non–radiative recombination cluster at about 900°C. These clusters, which give rise to the surface roughness, are then frozen in by the quench.

7.4.5 Compensation in quenched material.

Impurity concentrations are too low to indicate impurity induced changes in compensation (Grant 561) and it would be difficult to explain the change to p–type conduction after quenching and reversion to SI (n–type) after annealing. Changes in native defect concentrations are probably involved. Several possibilities exist which are detailed below:

1) The concentration of the deep donors shallower than EL2 such as EL3 or EL6 drops after quenching and this is followed by their regeneration after an anneal. This mechanism relies on a (constant) acceptor concentration exceeding the [EL2].

2) On quenching, [EL2] falls below the constant background acceptor concentration. Regeneration of EL2 occurs after annealing.

3) The acceptor concentration increases after quenching due to the creation of native acceptors and these are subsequently removed by annealing.

The first mechanism in the list above is highly unlikely for the following three reasons:

firstly, significant native donor concentrations are not normally seen in as–grown material (see section 2.5);

secondly a concentration of acceptors greater than the [EL2] would be required in the as–grown material; this is also not normally seen (see section 2.5);

finally, the recreation of these donors after annealing is required, when such anneals normally reduce their concentrations (see section 2.4.2).

The second mechanism is also unlikely to be the only mechanism, as [EL2°] (as measured by the infra–red absorption technique) has not dropped to near the native background acceptor impurity concentration. Moreover, native acceptors are not normally seen in as–grown material of this type (see section 2.5), although this should be investigated for these particular ingots. Hence, the third mechanism, with or without a contribution from the second, seems to be the most likely explanation.

Additional evidence can be obtained by comparing our results with those of other workers (also see section 2.4.4). Quenching experiments carried out by other groups can be divided into three sections according to the expected cooling rates of the samples.

Very fast cooling rates (Wafer Quenches):

Von–Bardeleben et al (125) demonstrated the effect of very fast quenching after 850°C annealing. Quenching was carried out by direct contact of an encapsulated slice with air. EL2 was found to separate into its components and could be regenerated by low temperature (around 100°C) anneals.

Fast cooling rates (Block Quenches):

Lagowski and co–workers (Lagowski 304, Kang 305) demonstrated p–type conversion of samples after quenching from 1200°C, with a return to SI n–type behaviour after annealing. This was explained by the destruction and re–creation of EL2 centres respectively. Kitagawara et al (308) quenched slices from 950°C which subsequently displayed thermal conversion from "conducting" n–type to SI n–type. This was caused by the removal of deep donors shallower than EL2. Kazuno et al (309) demonstrated the reduction of [EL2] and the creation of native acceptors in quenched material. Asom et al (250) demonstrated that a slow introduction of acceptors occurred in quenched samples which had previously been held at 950°C for more than 1 hour. The introduction rate increased with As over–pressure, with increasing temperature and with As–mole fraction.

Moderately fast cooling rates (Ingot Quenches):

Ford and co–workers (Ford 306, Look 307) quenched ingots from 950°C, which contained a high concentration of deep donors shallower than EL2. The as–grown, "conducting" n–type samples converted to SI n–type after the quench due to the creation of compensating native shallow acceptors. The samples became conducting n–type again after annealing due to the removal of these acceptors.

Since our results compare most closely with the third section above it would be expected that changes in compensation after quenching would mainly be related to the creation of native acceptors , with perhaps some contribution from [EL2] reduction. These acceptors are largely

removed and the original [EL2] is restored after annealing.

One problem with the above argument is that in the "p–type" material produced after quenching, [EL2°], as determined by NIR absorption, is still relatively high. At first sight this appears to be a major contradiction, especially since no major changes in the EL2 absorption spectra were seen. However, there are several possible explanations for this. The most obvious is that the Hall measurement is a surface technique and is being influenced by a surface region not typical of the bulk. However, this is unlikely as surface cuts were taken from the blocks before taking the samples for electrical measurements and were repeatable when the samples were thinned and re–polished (Blunt 563). A second explanation is that the spectrophotometer averages the absorption from quite a large area (typically 0.1mmx5mm) whereas the Hall measurements would be very sensitive to small p–type regions with relatively high conductivity. High resolution electrical assessment such as the three electrode guard technique or microwave photo–conductivity could be used to test this theory. Finally, a more pessimistic explanation would be that we still do not fully understand the compensation mechanism in GaAs, particularly after these new types of heat treatment.

7.4.6 Surface effects.

After quenching from high temperatures, free Ga metal was seen on sample surfaces. Also As deposition was visible on the inside of the ampoule; since no As was added to the ampoule this was clearly lost from the sample surface. This effect became more pronounced as the quenching temperature increased. It was assumed that the As loss from the surface was unlikely to affect the properties of the slices taken for assessment after a 2mm surface cut was removed.

Of more concern in these studies was the in–diffusion of transition metal impurities. This is due to the high diffusion rates of metals such as copper, from sources such as the ampoule (Tin 315). Care was taken to avoid such contamination by out–gassing the ampoules at 1200°C in a vacuum. Not all the ampoules used in the experiments were out–gassed but no difference was noticed between quenches under these different conditions. Even using out–gassed ampoules, the samples quenched from 1200°C may have suffered contamination from the quartz since ampoules were out–gassed at this temperature only.

The only assessment in which surface effects of any kind were observed was the boundary region in the A/B etch behaviour of some of the annealed quadrant samples (fig.7.26). In this sample, a region up to 2mm wide at the quadrant surface has ridge only dislocation structure. At greater depths, groove–only structure was apparent. Using the arguments based on the fermi–level dependent etch rate discussed above, this would indicate that the surface region has a lower fermi level and may even be p–type. It is difficult to say if this is due to surface As loss or in–diffusion some transition metal acceptor impurity or some other mechanism.

7.4.7 Mechanisms of uniformity improvement.

Mechanisms of uniformity improvement by quenching are probably associated with the dissolution into the lattice of point defects, at elevated temperatures. It has already been postulated that one of the effects of high temperature annealing is to dissociate the EL2 defect

into its components (Von–Bardeleben 125, Kang 305). Other effects could include the dissolution of As precipitates and other As–rich defects. Also the dissociated components of all these defects, would become homogenised. Quenching then prevents the reformation and the redistribution of the defects to form defect atmospheres around dislocations. This will ensure that the high uniformity of defects which exists at high temperatures is maintained. Hence quenching from high temperatures results in material with relatively low but uniform EL2 concentrations and no observable As precipitates.

Annealing the quenched material at a lower temperature, allows the reformation of As precipitates and EL2, but prevents the reformation of non–uniform EL2 distributions. One explanation for this is that the gettering mechanism is not operating at this temperature. Alternately the EL2 defect, or its components if they are present, are not mobile at this temperature.

7.4.8 Implications for defects properties in GaAs.

Unlike the work of Von Bardeleben and co–workers (125), the quench was not fast enough to separate the majority of EL2 into its components. In particular the thermal stability at room temperature would indicate that the mechanism that gave rise to changes in [EL2] after 100°C anneals in their work was not a significant factor in this study. The changes in [EL2] are small compared to the disappearance of As precipitates and the large increase in non–radiative recombination (from the CL results). These indicate that the primary defects responsible for non–stoichiometry are not the same as those involved in EL2 formation. This provides support for the Hurle model discussed in section 2.2.1, where non–stoichiometry arises through imbalance on the As sublattice, and EL2 arises from the lesser imbalance on the Ga sublattice.

The formation of precipitates is thought to occur at or below 1000°C during cooling after crystal growth (Suchet 069). Hence high temperature quenches are likely to remove precipitates. Since precipitates are seen again after annealing at 850 or 950°C, precipitate growth must occur at or below these temperatures. This is most probably due to the reformation of the As precipitate from the supersaturated As–rich matrix although a defect gettering mechanism, as discussed by Suchet et al (069), may also occur.

The micro–surface–roughness and high CL efficiency seen in cell centres in material quenched from around 900°C are clearly related. The identity of the defects responsible for the surface roughness is unknown, very small As related precipitates or decorated dislocation loops being two possibilities. It is probable that the high CL efficiency is due to the gettering of non–radiative recombination centres, at this temperature, to these defects, which occur in high concentrations.

8 CONCLUSIONS AND FURTHER WORK.

8.1 Conclusions.

8.1.1 Introduction.

The main conclusions of the work detailed in this thesis are presented below. The conclusions are presented in a chapter by chapter form with cross reference where relevant.

Chapter 2 and 3 contained reviews on the properties of SI GaAs and the assessment of SI GaAs respectively. Chapter 4 detailed the experimental techniques used in this work. Chapter 5 described a new [EL2] line–scan system developed from a NIR vidicon imaging apparatus. The main body of new experimental work and discussion is contained in chapter 6 and chapter 7. In chapter 6 results from the assessment of In–doped material are presented and discussed. In chapter 7 the effects on undoped SI material of heat treatments, especially those followed by rapid cooling (quenching), are described and discussed.

8.1.2 The properties of semi–insulating GaAs.

A wide ranging review on the present state of knowledge of GaAs substrate material has been given in chapter 2. The most important points from the review are summarised below.

Stoichiometry and the phase diagram.

Much experimental work and theoretical modelling has been carried out in an attempt to describe the different behaviour of various materials properties with stoichiometry. The most advanced of these models to date is the Hurle model (discussed in section 2.2.1), as it is the only model which satisfactorily explains the variation of electrical properties, [EL2], lattice parameter and stoichiometry with melt composition, in a manner consistent with the predicted phase diagram. The main assumption of the model is that the crystal stoichiometry is controlled by a dominant As Frenkel reaction whereas the EL2 concentration and electrical properties are controlled by a Ga Frenkel reaction.

Dislocations and precipitates.

The understanding of dislocations and their interactions with point defects and precipitates has much improved recently, largely through the use of In–doped material as a scientific tool. In–doping reduces dislocation densities and reveals their individual interactions. Dislocations are largely produced by thermal stress during cooling but other mechanisms such as point defect condensation are also likely to be important. Dislocations also interact strongly with each other, and with point defects, during cooling to give the characteristic features of lineage and cell structure seen in undoped material.

Much work has been carried out in the investigation of precipitates in stoichiometric or As–rich material. The majority are likely to be hexagonal As, of sub–micron size, occurring in concentrations which depend on thermal history and stoichiometry. It appears that the majority of the non–stoichiometry in As–rich material is taken up in As precipitates, which form from the aggregation of As interstitials at dislocations, during cooling. Similar precipitates are seen in In–doped material.

Crystal growth and isoelectronic doping

The LEC technique is the main growth technique at present for SI substrates. Its advantages are that no dopant is required to give SI properties, it produces circular cross section ingots and the technology is well developed and understood. Unfortunately, as–grown LEC wafers due not give the device uniformities required by device manufacturers. Hence there has been strong interest in either adapting the LEC technique, the use of other growth techniques or heat treating LEC ingots, to improve subsequent device performance. The best reports of device uniformity to date, come from devices with dislocation free, In–doped substrates where the crystals were grown under a strong magnetic field (MLEC), with a lattice matched seed. Unfortunately, crystals grown using this method are expensive (amongst other problems) and hence interest is increasing in methods of heat–treating conventional undoped crystals, or in other growth techniques (such as Gradient Freeze methods), which produce nearly comparable device results.

The growth of 4" diameter LEC GaAs crystals has been reported. As well as increasing the useable area on a slice this has the significant advantage that readily available 4" Si production equipment can be adapted for processing.

EL2 and the optical properties of SI GaAs.

Recent years have seen some development in elucidating the nature and properties of EL2, but an absolute identification has still not been made (despite the claims of some authors!). At present the isolated As antisite (As_{Ga}), or the As antisite–As interstitial (As_{Ga}–As_i) pair, look to be the most likely candidates for the atomic structure of EL2.

One of the most important properties of EL2 is its characteristic Near Infra–Red (NIR) absorption band. The use of this band to provide a calibration for evaluating [EL2] from absorption measurements has been discussed with particular emphasis on the pitfalls of the technique. The distribution of EL2 in SI LEC ingots was also discussed in relation to the causal mechanisms. Finally a brief discussion on other NIR absorption and NIR scattering mechanisms was given.

Annealing and defect dynamics.

Bulk and wafer annealing was discussed with reference to improvement of the uniformity of substrate properties and subsequently, the improvement of device uniformity. There has been strong scientific interest recently in anneals followed by fast cooling, or quenching. Quenching GaAs led to novel types of material such as ITC GaAs where the electrical properties of the final material are tailored, within limits, to specification, by re–annealing. Quenching studies have clearly emphasised the significance of cooling rate after annealing. Also, the importance of native defects other than EL2 in compensation and the importance and nature of electrical stability has been considered. In addition, the effects of annealing on As precipitates was reviewed.

Finally defect dynamics and diffusion in GaAs were briefly discussed. The improvements seen in the uniformity of substrate properties after ingot annealing are thought to be due to local redistribution of point defects. Surface effects are only significant for wafer anneals.

Electrical properties and compensation.

The traditional view of compensation in undoped SI GaAs is that of EL2 compensating an excess of shallow acceptors (predominantly C) over shallow donors. This view is now being seriously questioned. This is mainly due to the reduced impurity levels (especially that of C) but also because of the increasing importance of post–growth heat treatments. In particular, native defects other than EL2, both donors and acceptors, can play an important part in the compensation mechanism of GaAs substrates.

Device results.

Substrates clearly have an effect on device performance. This applies particularly to the properties of ion implanted FET's which must be highly uniform if VLSI digital GaAs circuits are to be developed. The uniformity of these properties is related to the dislocation distribution but this is probably an indirect effect due to the influence of dislocations on the surrounding point defect atmospheres. Breaking the association of dislocations with point defects, particularly EL2, seems to be the key factor in improving this uniformity. Hence the best device results at present come from dislocation free, In–doped material, closely followed by annealed, conventional dislocated material where EL2 and/or other defects have been rendered uniform.

8.1.3 Assessment of SI GaAs substrates.

There are many different assessment techniques in use for SI GaAs substrates and more are developed every year. The most important techniques were briefly reviewed in Chapter 3 under the headings of: dislocation assessment, precipitate assessment, stoichiometry assessment, crystal strain assessment, NIR assessment, DLTS and related space charge techniques, Electrical assessment, luminescence techniques, FET mapping, spin resonance techniques, impurity analysis and other assessment techniques.

Due to the large number of assessment techniques available questions should be asked as to the appropriateness of the techniques selected. In addition, care should be taken when making elaborate claims on material which may be unrepresentative of the current market when using only a few techniques. This particularly applies if the interpretation of the results is not clear, which for SI GaAs assessment seems to be the norm rather than the exception.

8.1.4 Assessment techniques used in this work.

The methods used in the work for this thesis, together with the reasons for their selection, were discussed in chapter 4. These techniques include:

NIR absorption assessment of EL2 using a video imaging system to give qualitative information on EL2 distributions and a spectrophotometer for quantitative results;

Investigations of dislocations and precipitates using A/B etching, X–Ray topography and NIR microscopy;

Luminescence of defect distributions using CL;

Electrical assessment using Hall measurements;

The main assessment carried out by the author was the investigation of EL2 and the use of A/B

etching. The NIR assessment of EL2 is a very powerful technique. It provides a cheap method of monitoring EL2 uniformity using room temperature vidicon imaging or spectrophotometer linescans. It is easy to use and quantitative, when using the spectrophotometer. It can also be used to spot cracks, twins, large precipitates, scratches, and striations. The A/B etchant, used extensively in this work, has several advantages over the industrial standard etch, molten KOH. It avoids undercounting of dislocations and provides information on impurity atmospheres.

8.1.5 The [EL2] line-scan system.

The development of the [EL2] line-scan system in order to produce semi-quantitative results from the NIR vidicon imaging system was discussed in Chapter 5. The system produces an absorption line-scan from a NIR topograph on the vidicon screen. The effects of non-uniform sample illumination can be easily removed by taking a background scan. The absorption line-scan is converted to the [EL2] line-scan, using a calibration of the absorption at a particular point on the sample at wavelengths of 1 and 2μm. The 2μm absorption is assumed to be constant while the variations in intensity on the vidicon are assumed to be proportional to changes in 1μm absorption. The proportion of EL2 in the ionised charge state is assumed to be negligible. These assumptions are unlikely always to be true, hence the description of the system as semi-quantitative.

In addition, the system provides a good measure of microscopic uniformity of EL2 based on the standard deviation of the [EL2] line-scan fluctuations. This can be used to reveal the effectiveness of annealing procedures in improving substrate uniformity. The system has great potential as a general method to assess substrate uniformity. Reducing local fluctuations is of primary importance for the realisation of VLSI GaAs technology. Although this system lacks the processing power of many commercial image processors, it has the advantage of being cheaper while still providing much of the same information.

8.1.6 Defect assessment in In-doped material.

In Chapter 6 new results and discussion from the assessment of In-doped material were presented. Emphasis was placed on the investigation of axial dislocations in In-doped material and their associated defect atmospheres. The effects of annealing on these dislocations were investigated. Assessment involved NIR EL2 absorption, A/B etching and X-ray topography of these dislocation structures.

These dislocations, which are grown-in from the seed, lie approximately along [001]. A slight curve is visible on the dislocations. This is due to the dislocations remaining approximately perpendicular to the curved growth front (as visualised by growth striations), consistent with minimising surface energy at the dislocation during growth. Small deviations from the expected direction are observed which are due to dislocations interaction or the effect of climb.

The dislocations are of edge character but an unambiguous determination of their burgers vector could not be made. On a microscopic scale, dislocations consist of a series of arcs pinned by precipitates. These arcs are produced by dislocation climb. The dislocations in the central region were divided into three types depending on their arc structure after A/B etching:

Type 1) These dislocations have highly tangled structures on prominent etch mounds

associated with defect atmospheres. They are mainly found at the edges of the central region.

Type 2) These have a periodic pattern of arcs pinned by precipitates at intervals of 30–50μm. Etch mounds associated with their defect atmospheres are less prominent than those of Type 1.

Type 3) These are similar to Type 2 but with a much smaller precipitate separation, typically of 5–10μm.

Differences between Type 2 and 3 structures could be due to core structures of α and β dislocations in the GaAs lattice. Type 1 dislocations may arise from two or more closely spaced interacting dislocations.

After annealing, it was found that the average [EL2] is increased from a typical value of $0.5–0.8x10^{16}cm^{-3}$ in as–grown material to $1–1.5x10^{16}cm^{-3}$. A zone of low [EL2] is seen surrounding the dislocated central region and surrounding groups of slip dislocations at the edge of the ingot. However, these "denuded" zones still have [EL2] exceeding that of typical as–grown material. The [EL2] is much higher in the immediate vicinity of dislocations. Dislocation structures on a microscopic scale are highly complicated, indicating that extensive dislocation climb has occurred during the anneal.

8.1.7 Bulk quenching and annealing studies.

In Chapter 7, novel results of heat treatments terminated by quenching, on undoped SI GaAs, were presented. These results were then discussed, together with their potential for the uniformity improvement of undoped SI GaAs substrate material for ion implantation.

Initial results were produced from block samples quenched from different temperatures. These results indicated that a critical temperature occurred between 1000 and 1100°C. The blocks quenched from above this temperature displayed:

some p–type conversion;

lower resistivity;

lower mobility;

lower [EL2];

more uniform EL2 distribution;

much higher dislocation densities (up to 10^6cm^{-2});

a change in A/B etching behaviour of dislocations (from groove–ridge to ridge only);

no As precipitates;

low CL intensity;

more uniform CL intensity.

This information was largely summarised in fig.7.6

In material quenched from around 900°C well defined regions with micro–surface–roughness

were seen in the centres of cells after A/B etching. It was postulated that this roughness was due to the etching of high density of micro–precipitates or decorated dislocation loops. In addition, these regions displayed high CL efficiency indicating that non–radiative recombination centres had been gettered by these micro–defects.

After re–annealing the quenched material in a conventional manner (950°C, 5 hours, slow cool), the [EL2] returned almost to the level in as–grown material but its superior quenched uniformity was retained. The resistivity and mobility levels were restored to as–grown values. The dislocations now all appeared as grooves on an A/B etched surface, and precipitates could be seen again on dislocations.

In quenched material, the improved homogeneity of EL2, CL and A/B etch profiles is probably due to the dissolution of defects such as EL2 and As precipitates into the lattice at high temperatures. Quenching prevents the reformation of precipitates and non–uniform point defect distributions. A second anneal at a lower temperature with a slow cooling rate is then required to restore good SI properties. This does not alter the superior uniformities obtained in quenched material.

It was later demonstrated that whole ingot quenching can be achieved. The ingot was re–annealed before cutting to reduce the possibility of breakage. The main problem with the quenched material is liable to be the high "quenched in" thermal stress and high dislocation densities.

This SI ingot quenched and re–annealed material, with improved uniformity over as–grown or conventional annealed material, has potential as substrate material for ion implanted FETs. However, it is worth noting that this material would fail most production quality control specifications on the excessive dislocation density. Despite this, initial assessment stages in device production are promising. It follows that the present specifications of maximum dislocation densities for substrate material should be questioned.

8.2 Further Work.

8.2.1 Work planned or in progress.

Device Results.

The most important piece of further work is to assess the commercial potential of the quenched ingots. Devices should be produced on these substrates, with emphasis given to the uniformity of FET properties. In addition, any unusual behaviour of the FETs should be investigated as this may be related to the unconventional nature of the substrate material. This work is in progress at Plessey Caswell.

Quenching of 3" Ingots

At present the largest ingot quenched is of 2" diameter. Clearly the procedure should be repeated for a 3" ingot.

Cathodoluminescence of quenched and re–annealed material

At present CL results have only been obtained on quenched blocks. Much useful information may be obtained from comparing these initial results with further CL investigations of quenched

and re–annealed material. This technique is particularly sensitive to the density and distribution of non–radiative recombination centres. At present, we have no information in this area, on samples which have been annealed after quenching.

8.2.2 Other further work.

Assessment of quenched material.

Due to the unconventional nature of this material and the difficulties associated with the assessment of SI GaAs, the material is not yet fully characterised. In particular, the nature of the native acceptor levels in the material requires investigation. In addition a large amount of A/B etch data exists which has not been fully investigated. This may provide useful information if examined more carefully. Finally no CL work has been carried out on quenched and annealed material.

Further work on annealing conditions for quenched material.

Re–annealing of quenched material at different temperatures should be investigated in order to optimise the conditions which may be different from those of an as–grown ingot. Re–annealing of quenched material at lower temperatures may also be useful in elucidating the degree to which thermodynamically unstable defects are frozen–in by quenching. Also the annealing times both before the quench and during the re–anneal should be varied. Finally the effect of high temperature anneals without quenches should be investigated.

Development of the line digitiser.

Upgrading the [EL2] line–scan system could provide many benefits if the funding was available to purchase a full frame image processor and frame storage facilities. This would enable more sophisticated image analysis than is possible on a small non–dedicated system based around the BBC microcomputer. In particular it would be possible to produce full screen [EL2] maps from the vidicon image.

TEM investigations of dislocations in In–doped GaAs.

A TEM study of the [001] grown–in dislocations in the central region of In–doped ingots would be useful for several reasons. It would enable the burgers vectors to be determined without ambiguity. The type of climb (interstitial or vacancy) could be determined. Also the nature of precipitates in In–doped material, together with their relationship with dislocations, could be investigated.

Annealing of In–doped material.

The results presented on In–doped material are a little sketchy. In particular the effects of annealing, on defect atmospheres around threading dislocations seen near the axis of In–doped crystals, are still unclear and require further investigation. Bearing in mind the resemblance of the strange features on the NIR transmission images, in the central regions of annealed In–doped ingots, to CL images, it may be useful to instigate CL investigations. Hopefully, these may reveal more information on the relative importance of the various mechanisms of formation of defect atmospheres as discussed in Chapters 2 and 6.

Investigation of micro–defect structure.

The nature of the defects responsible for both the micro-surface-roughness seen in material quenched form around 900°C, and the background speckle seen in dislocation free regions of In-doped material, after A/B etching, are still unknown. Due to the high density of the defects in the quenched material, it should be possible to investigate their nature in a TEM. Despite lower densities of "speckle" defects in In-doped material, they may not be difficult to locate, since some investigations have been carried out on these types of defect by other workers (see section 6.5.3).

Further investigation of the correlation of micro-surface-roughness with regions of high CL efficiency, in quenched material, may give useful information on the gettering of non-radiative recombination centres.

9. ACKNOWLEDGEMENTS

I would like to thank and acknowledge the following, for their help at various stages of the project:

My supervisors, Derek Stirland, Mike Brozel and Peter Holmes, for their help, support, advice and patience.

My collaborating establishment: Plessey Research Caswell (now a branch of GEC Siemans), for use of facilities.

The staff at Caswell, especially: Derek Stirland, Roy Blunt for electrical measurements, Derek Hart for X-ray topography, and Dave Warner for device processing.

The staff at ICI Wafer Technology (now MCP Wafer Technology), especially Ian Grant, for provision of samples, useful discussion and help with the heat treatments.

Colin Warwick at the Royal Signals and Radar Establishment (RSRE), Malvern, for CL measurements.

Don Hurle at RSRE, Malvern, for useful discussions.

The lecturers, research students, secretaries and technicians of the department of Electrical and Electronic engineering, Nottingham Polytechnic, for their help in various areas on numerous occations.

The excellent library services (before the cuts) at Nottingham Polytechnic, especially Richard Mathews and Fiona Williams, for obtaining most of the references.

Brian O'Neill, for the loan of the Atari wordprocessor and lessons on the Desk Top Publisher.

John Savage, for the photocopying at short notice.

My family and friends, for all of their tolerance and support.

Some of this work has been supported by the Procurement Executive, Ministry of Defence (Royal Signals and Radar Establishment).

10 REFERENCES

001. (835) Spadero J.J., Electronic Products (June 1988) p.30.

002. (837) Gagnon M.P., Electronic Products (June 1988) p.43.

003. (497) Ohmori M., GaAs and Related Compounds, 11 (Biarritz, 1984) Inst.Phys.Conf.Ser. 74 (1985) p.647.

004. (797) Cole B.C., Electronics (June 1988) p.65.

005. (819) Tomasetta L., EDN 33 (1988) p.243.

006. (836) Schappacher J., Electronic Products (June 1988) p.37.

007. (834) Lewis S., Electronic Products (June 1988) p.15.

008. (215) Eden R.C., SI III–V Mats., 4 (Hakone, 1986) p.553.

009. (342) Sugeta T., Mizutani T., Ino M and Horiguchi S., IEEE GaAs IC Symp. CH 2372–1/86 (1986) p.3.

010. (305) Sealy B.J., J.IERE 57 (1987) p.52.

011. (103) Blunt R.T., Sol.Stat.Dev. (1985) p.133.

012. (___) Miyazawa S., Watanabe K., Osaka J and Ikuta K., Revue Phys Appl 23 (1988) p.727.

013. (___) Koyama R.Y., SI III–V Mats., 5 (Malmo, 1988), p.203.

014. (264) Hurle D.T.J., J.Phys.Chem.Solids 40 (1979) p.613.

015. (___) Hurle D.T.J., SI III–V Mats., 5 (Malmo, 1988) p.11.

016. (376) Terashima K., Nishio J., Okada A., Washizuka S and Watanabe M., J.Crys.Growth 79 (1986) p.463.

017. (263) Logan R.M and Hurle D.T.J., J.Phys.Chem.Solids 32 (1971) p.1739.

018. (720) Van–Vechten J.A., J.Electrochem.Soc. 122 (1975) p.419.

019. (107) Dannefaer S and Kerr D., J.Appl.Phys. 60 (1986) p.591.

020. (149) Nakajima M., Sato T., Inada T., Fukuda T., Ishida K., Appl.Phys.Lett 49 (1986) p.1251.

021. (225) Nakajima M., Sato T., Inada T., Fukuda T., Ishida K., SI III–V Mats., 4 (Hakone, 1986) p.181.

022. (180) Terashima K., Ohmori O., Okada A., Watanabe M and Nakanisi T., SI III–V Mats., 4 (Hakone, 1986) p.187.

023. (223) Takano Y., Ishiba T., Fujisaki Y., Nakagawa J and Fukuda T., SI III–V Mats., 4 (Hakone, 1986) p.169.

024. (224) Okada Y and Tokumaru Y., SI III–V Mats., 4 (Hakone, 1986) p.175.

025. (___) Bublik V.T., Karataev V.V., Kulagin R.S., Mil'vidskii M.G., Ovenskii V.B., Stolyarov O.G and Kholoduyi L.P., Sov.Phys. Crystallog. 18 (1973) p.218.

026. (679) Aref'ev I.S., Bublik V.T., Morozov A.N., Karataev V.V., Koval'chuk I.A., Mil'vidskii M.G and Morozova O.Y., Sov.Phys.Crys. 32 (1987) p.267.

027. (445) Pons D and Bourgoin J.C., J.Phys.C. Sol.Stat.Phys. 18 (1985) p.3839.

028. (498) Baraff G.A and Schluter M., Phys.Rev.Lett. 55 (1985) p.1327.

029. (657) Morrow R.A., J.Mater.Res. 2 (1987) p.681.

030. (800) Morrow R.A., J.Appl.Phys. 63 (1988) p.5863.

031. (381) Holmes D.E., Chen R.T., Elliott K.R., Kirkpatrick C.G and Yu P.W., IEEE Trans. on Microwave theory and Techniques, Vol. MTT–30 No.7 (1982) p.949.

032. (578) Holmes D.E., Chen R.T., Elliott K.R and Kirkpatrick C.G., Appl.Phys.Lett. 40 (1982) p.46.

033. (240) Elliott K.R., Chen R.T., Greenbaum S.G and Wagner R.J., SI III–V Mats., 3 (Kah–nee–ta, 1984) p.239.

034. (559) Elliott K.R., Appl.Phys.Lett. 42 (1983) p.274.

035. (681) Elliott K.R., Chen R.T., Greenbaum S.G and Wagner R.J., Appl.Phys.Lett. 44 (1984) p.907.

036. (683) Elliott K.R., Holmes D.E., Chen R.T and Kirkpatrick C.G., Appl.Phys.Lett. 40 (1982) p.898.

037. (116) Jordan A.S., Von–Neida A.R and Caruso R., J.Crys.Growth 70 (1984) p.555.

038. (375) Jordan A.S and Parsey–Jr J.M., J.Crys.Growth 79 (1986) p.280.

039. (024) Clark S and Stirland D.J., Inst.Phys.Conf.Ser. 60 (1981) p.339.

040. (290) Yamada K., Kohda H., Nakanishi H and Hoshikawa K., J.Crys.Growth 78 (1986) p.36.

041. (036) Stirland D.J., DRIP II (Monterey, 1987) p.73.

042. (556) Parsey–Jr J.M., Nanishi Y., Lagowski J and Gatos H.C., J.Electrochem.Soc. 128 (1981) p.936.

043. (557) Parsey–Jr J.M., Nanishi Y., Lagowski J and Gatos H.C., J.Electrochem.Soc. 129 (1982) p.388.

044. (603) Lagowski J., Gatos H.C., Aoyama T and Lin D.G., Appl.Phys.Lett 45 (1984) p.680.

045. (523) Lagowski J and Gatos H.C., ICDS 13 (Coronado, 1984), Metallurgical Soc. of AIME (1985) p.73.

046. (___) Hirth J.P and Lothe J., "Theory of dislocations", second edition (Wiley, N.Y, 1982)

047. (166) Hornsta J., J.Phys.Chem.Solids 5 (1958) p.129.

048. (667) Sumino K., Defects and Properties of Semiconductors: Defect Engineering, Eds Chikawa J., Sumino K and Wada K., (KTK Scientific Publishers, Tokyo 1987) p.3.

049. (815) Sumino K., Proc. 2nd GADEST. Garzau DDR, Ed. Richter H., (1987) p.218.

050. (525) Feuillet G and Cherns D., ICDS 13 (Coronado, 1984), Metallurgical Soc. of AIME (1985) p.343.

051. (489) Jimenez–Melendo M., Djemel A., Riviere J.P., Castaing J., ICDS 14 (Paris, 1986), Mat.Sci.Forum 10–12 (1986) p.791.

052. (007) Stirland D.J., Augustus P.D., Brozel M.R and Foulkes E.J., SI III–V Mats., 3 (Kah–nee–ta, 1984) p.91.

053. (251) Weyher J.L and Van de Ven J., J.Crys.Growth 78 (1986) p.191.

054. (015) Skolnick M.S., Brozel M.R., Reed L.J., Grant I., Stirland D.J and Ware R.M., J.Electron.Mat. 13 (1984) p.107.

055. (410) Chin A.K., Caruso R., Young M.S.S and Von–Neida A.R., Appl.Phys.Lett. 45 (1984) p.552.

056. (537) Leigh P.A., Hall I.P., Elliott C.R., Wakefield B and Lyons M.H., SI III–V Mats., 3 (Kah–nee–ta, 1984) p.214.

057. (117) Kamejima T., Shimura F., Matsumoto Y., Watanabe H and Matsui J., Jap.J.Appl.Phys. 21 (1982) p.L721.

058. (427) Kitahara K., Nakai K and Shibatomi S., J.Electrochem.Soc. 129 (1982) p.880.

059. (273) Kikuta T., Katsumata T., Obokata T and Ishida K., GaAs and Related Compounds, 11 (Biarritz, 1984) Inst.Phys.Conf.Ser. 74 (1985) p.47.

060. (588) Bonnet M., Visentin N., Gouteraux B., Lent B and Duchemin J.P., IEEE. GaAs IC Symp. (1982) p.54.

061. (736) Bourret E.D., Guitron J.B and Haller E.R., J.Crys.Growth 85 (1987) p.290.

062. (018) Brozel M.R., Grant I., Ware R.M., Stirland D.J and Skolnick M.S., J.Appl.Phys. 56 (1984) p.1109.

063. (255) Weber E.R., Ennen H., Kaufmann U., Windscheif J., Schneider J and Wosinski T., J.Appl.Phys. 53 (1982) p.6140.

064. (754) Wehyer J.L., Dang L.S and Visser E.P., Crete (1988) p.109.

065. (___) Wehyer J.L., SI III–V Mats., 5 (Malmo, 1988), p.499.

066. (009) Brozel M.R., Foulkes E.J and Stirland D.J., DRIP I (Montpellier, 1985) p.177.

067. (028) Cullis A.G., Augustus P.D and Stirland D.J., J.Appl.Phys. 51 (1980) p.2556.

068. (277) Cornier J.P., Duseaux M., Chevalier J.P., GaAs and Related Compounds, 11 (Biarritz, 1984) Inst.Phys.Conf.Ser. 74 (1985) p.95.

069. (762) Suchet P and Duseaux M., GaAs and Related Compounds, 14 (Heraklion, 1987) Inst.Phys.Conf.Ser. 91 (1988) p.375.

070. (184) Duseaux M., Martin S and Chevalier J.P., SI III–V Mats., 4 (Hakone, 1986) p.221.

071. (818) Lee B.T., Gronsky R and Bourret E.D., J.Appl.Phys. 64 (1988) p.114.

072. (701) Lee B.T., Sands T., Gronsky R and Bourret E.D., Las Vegas (1987) p.51.

073. (102) Barrett D.L., McGuigan H.M., Hobgood H.M., Eldridge G.W and Thomas R.N., J.Crys.Growth 70 (1984) p.179.

074. (567) Nakajima M., Fujii T and Ishida K., J.Crys.Growth 84 (1987) p.295.

075. (783) Yamada K and Osaka J., J.Appl.Phys. 63 (1988) p.2609.

076. (235) Ponce F.A., Wang F.C and Hiskes R., SI III–V Mats., 3 (Kah–nee–ta, 1984) p.68.

077. (861) Lee B.T., Bourret E.D., Gronsky R and Park I., J.Appl.Phys. 65 (1989) p.1030.

078. (___) Lessof H., Tseng W and Gorman R., SI III–V Mats., 5 (Malmo, 1988), p.441.

079. (229) Willardson R.K., SI III–V Mats., 3 (Kah–nee–ta, 1984) p.96.

080. (372) Jordan A.S., Von Neida A.R and Caruso R., J.Crys.Growth 76 (1986) p.243.

081. (729) Hurle D.T.J., J.Crys.Growth 85 (1987) p.1

082. (___) Hollan L., Hallais J.P and Brice J.C., "The preparation of Gallium arsenide", Current Topics in Materials Science, Vol.5, ed E. Kaldis (North Holland 1980).

083. (259) Hunter A.T., Kimura H., Baukus J.P., Winston H.V and Marsh O.J., Appl.Phys.Lett. 44 (1984) p.74.

084. (285) Kikuta T., Emori H., Fukuda T and Ishida K., J.Crys.Growth 76 (1986) p.517.

085. (738) Emori H., Kikuta T., Inada T., Obokata T and Fukuda T., Jap.J.Appl.Phys 24 (1985) L.291.

086. (751) Baumgartner M., Lohnert K., Nagel G., Rufer H and Tomzig E., GaAs and Related Compounds, 14 (Heraklion, 1987) Inst.Phys.Conf. Ser. 91 (1988) p.97.

087. (730) Elliot A.G., Wei C.–L and Vanderwater D.A., J.Crys.Growth 85 (1987) p.59.

088. (699) Duncan W.M and Westphal G.H., GaAs and Related Compounds, 13 (Las Vegas, 1986) Inst.Phys.Conf.Ser. 83 (1987) p.39.

089. (340) Orito F., Seta Y., Yamada Y., Ibuka Y., Okano T., Hyuga F and Osaka J., IEEE GaAs IC Symposium, CH2372–1/86 (1986) p.33.

090. (109) Elliot A.G., Wei C.L., Ferraro R., Woolhouse G., Scott M and Hiskes R., J.Crys.Growth 70 (1984) p.169.

091. (457) Kohda H., Yamada K., Nakanishi H., Kobayashi T., Osaka J and Hoshikawa K., J.Crys.Growth 71 (1985) p.813.

092. (151) Shimada T., Terashima K., Nakajima H and Fukuda T., Jap.J.Appl.Phys. 23 (1984) L.23.

093. (418) Shimada T., Obokata T and Fukuda T., Jap.J.Appl.Phys. 23 (1984) L.441.

094. (840) Duseaux M., J.Crys.Growth 61 (1983) p.576.

095. (838) Jacob G., J Crys.Growth 58 (1982) p.455.

096. (___) Jacob G., SI III–V Mats., 2 (Evian, 1982) p.2.

097. (535) Mo P., Wu J., Zou Y., Yang J and Li S., S.I. III–V Mats., 3 (Kah–nee–ta, 1984) p.134.

098. (534) Osaka J and Hoshikawa K., SI III–V Mats., 3 (Kah–nee–ta, 1984) p.126.

099. (697) Kawase T., Kawasaki A and Tada K., GaAs and Related Compounds, 13 (Las Vegas, 1986) Inst.Phys.Conf.Ser.83 (1987) p.27.

100. (373) Kimura T., Katsumata T., Nakajima M and Fukuda T., J.Crys.Growth 79 (1986) p.264.

101. (175) Terashima K., Washizuka S., Nishio J., Shimada H., Yasuami S and Watanabe M., SI III–V Mats., 4 (Hakone, 1986) p.59.

102. (613) Kimura T., Obokata T and Fukuda T., J.Crys.Growth 84 (1987) p.394.

103. (795) Gray M.L., Sargent L., Burke K.M., Grim K.A and Blakemore J.S., J.Appl.Phys. 63 (1988) p.4413.

104. (842) Khattak C.P., Lagowski J., Wohlgemuth J.H., Mil'shtein S., White V.E and Schmid F., GaAs and Related Compounds, (Karuizawa, 1985) Inst.Phys.Conf.Ser. 79 (1986) p.31.

105. (757) Khattak C.P., Di Gregorio S., Schmid F and Lagowski J., GaAs and Related Compounds, 14 (Heraklion, 1987) Inst.Phys.Conf.Ser. 91 (1988) p.133.

106. (627) Gray M.L., Clemens J.E and Grim K.A., DRIP II (Monterey, 1987) p.25.

107. (839) Gault W.A., Monberg E.M and Clemans J.E., J.Crys.Growth 74 (1986) p.491.

108. (___) Clemens J.E and Conway J.H., SI III–V Mats., 5 (Malmo, 1988), p.423.

109. (546) Reynolds C.L., Gibson W.C and Clemans J.E., Electron. Letts. 23 (1987) p.1222.

110. (299) McGuigan S., Thomas R.N., Barrett D.L., Eldridge G.W., Messham R.L and Swanson S.W., J.Crys.Growth 76 (1986) p.217.

111. (237) Hobgood H.M., Thomas R.N., Barrett D.L., Eldridge G.W., Sopira M.M and Driver M.C., SI III–V Mats., 3 (Kah–nee–ta, 1984) p.149.

112. (350) Ehrenreich H and Hirth J.P., Appl.Phys.Lett. 46 (1985) p.668.

113. (405) Kimura H., Afable C.B., Olsen H.M., Hunter A.T and Winston H.V., J.Crys.Growth 70 (1984) p.185.

114. (155) Tabache M.G., Bourret E.D and Elliot A.G., Appl.Phys.Lett. 49 (1986) p.289.

115. (735) Bourret E.D., Tabache M.G., Beeman J.W., Elliot A.G and Scott M., J.Crys.Growth 85 (1987) p.275.

116. (817) Jimenez–Melendo M., Djemel A., Riviere J.P., Castaing J., Thomas C and Duseaux M., Revue Phys.Appl. 23 (1988) p.251.

117. (732) Kimura H., Hunter A.T., Cirlin E.H and Olsen H.M., J.Crys. Growth 85 (1987) p.116.

118. (545) Martin G.M and Makram–Ebeid S., Deep Centres in Semiconductors Ch.6. Ed. S.Pantelides (Gordon & Breach – New York, 1985) p.399.

119. (554) Martin G.M and Makram–Ebeid S., ICDS 12 (Amsterdam, 1982), Physica 116B (1983) p.371.

120. (231) Makram–Ebeid S., Langlade P and Martin G.M., SI III–V Mats., 3 (Kah–nee–ta, 1984) p.184.

121. (501) Gatos H.C and Lagowski J., Mat.Res.Symp.Proc.46 (1985) p.153.

122. (523) Lagowski J and Gatos H.C., ICDS 13 (Coronado, 1984), Metallurgical Soc. of AIME (1985) p.73.

123. (502) Weber E.R and Omling P., FestkÖrperprobleme XXV (1985) p.623.

124. (710) Kaminska M., Physica Scripta T19 (1987) p.551.

125. (318) Von–Bardeleben H.J., Steivenard D.,Deresmes D., Huber A and Bourgoin J.C., Phys.Rev.B. 34 (1986) p.7192.

126. (393) Martin G.M., Mitonneau A and Mircea A., Electronics Lett. 7 (1977) p.191.

127. (496) Makram–Ebeid S and Lannoo M., Phys.Rev.B. 25 (1982) p.6406.

128. (592) Chantre A., Vincent G and Bois D., Phys.Rev.B. 23 (1981) p.5335.

129. (857) Lagowski J., Lin D.C., Chen T.P., Skowronski M and Gatos H.C., Appl.Phys.Lett. 49 (1985) p.929.

130. (787) Bencherifa A., Guillot G., Bremond G., Nouailhat A., Guivarc'h A and Regreny A., 18th Conf.Phys.Semicond. (Stockholm, 1986), Ed. O.Engstrom (World Scientific, 1987) p.817.

131. (128) Martin G.M., Appl.Phys.Lett. 39 (1981) p.747.

132. (118) Kaminska M., Skowronski M., Lagowski J., Parsey Jr. J.M and Gatos H.C., Appl.Phys.Lett. 43 (1983) p.302.

133. (573) Mochizucki Y and Ikoma T., Phys.Rev.Lett. 59 (1987) p.590

134. (158) Tsukada N., Kikuta T and Ishida K., Phys.Rev.B 33 (1986) p.8859.

135. (377) Vincent G., Bois D and Chantre A., J.Appl.Phys. 53 (1982) p.3643.

136. (778) Skowronski M., Lagowski J and Gatos H.C., Phys.Rev.B 32 (1985) p.4264. 805) Manasreh M.O., Phys.Rev.B 37 (1988) p.2722.

137. (687) Samuelson L and Omling P., Phys.Rev.B 34 (1986) p.5603.

138. (205) Tsukada N., Kikuta T and Ishida K. SI III–V Mats., 4 (Hakone, 1986) p.221.

139. (764) Lagowski J., Matsui M., Bugajski M., Kang C.H., Skowronski M., Gatos H.C., Hoinkis M., Weber E.R and Walukiewicz W., GaAs and Related Compounds, 14 (Heraklion, 1987) Inst.Phys.Conf.Ser. 91 (1988) p.395.

140. (500) Walukiewicz W., Lagowski J and Gatos H.C., Appl.Phys.Lett. 43 (1983) p.192.

141. (123) Kitagawara Y., Noto N., Takahashi T and Takenaka T., Appl.Phys. Lett. 48 (1986) p.1644.

142. (190) Kitagawara Y., Noto N., Takahashi T and Takenaka T., SI III–V Mats., 4 (Hakone, 1986) p.273.

143. (241) Kaufmann U., Windscheif J., Baeumler M., Schneider J and Kohl F., SI III–V Mats., 3 (Kah–nee–ta, 1984) p.246.

144. (245) Weber E.R., SI III–V Mats., 3 (Kah–nee–ta, 1984) p.296.

145. (239) Lagowski J., Lin D.G., Aoyama T and Gatos H.C., SI III–V Mats., 3 (Kah–nee–ta, 1984) p.222.

146. (272) Gatos H.C., Skowronski M., Pawlowicz L and Lagowski J., GaAs and Related Compounds, 11 (Biarritz, 1984) Inst.Phys.Conf.Ser. 74 (1985) p.41.

147. (422) Yahata A., Sato T., Kikuta T and Ishida K., Mat.Res.Soc.Symp. Proc. 46 (1985) p.179.

148. (438) Taniguchi M and Ikoma T., J.Appl.Phys. 54 (1983) p.6448.

149. (156) Taniguchi M and Ikoma T., Appl.Phys.Lett 45 (1984) p.69.

150. (236) Taniguchi M., Mochizuki Y and Ikoma T., SI III–V Mats., 3 (Kah–nee–ta, 1984) p.232.

151. (188) Mita Y., SI III–V Mats., 4 (Hakone, 1986) p.341.

152. (478) Parker J.C and Bray R., ICDS 14 (Paris, 1986), Mat.Sci.Forum 10–12 (1986) p.347.

153. (311) Vignaud D and Farvacque J.L., Sol.Stat.Comms. 60 (1986) p.527.

154. (723) Ikoma T and Mochizuki Y., Jap.J.Appl.Phys. 24 (1985) p.L935.

155. (___) Mochizuchi Y and Ikoma T., Revue Phys.Appl. 23 (1988) p.747.

156. (718) Zhong X., Jiang D., Ge W and Song C., Appl.Phys.Lett. 52 (1988) p.628.

157. (522) Weber E.R., ICDS 13 (Coronado, 1984), Metallurgical Soc. of AIME (1985) p.7.

158. (468) Kennedy T.A., ICDS 14 (Paris, 1986), Mat.Sci.Forum 10–12 (1986) p.283.

159. (___) Bourgoin J.C and Lannoo M., Revue Phys.Appl. 23 (1988) p.863.

160. (472) Meyer B.K., Hofmann D.M and Spaeth J.M., ICDS 14 (Paris, 1986), Mat.Sci.Forum 10–12 (1986) p.311.

161. (513) Meyer B.K., Hofmann D.M., Niklas J.R and Spaeth J.M., Phys. Rev.B 36 (1987) p.1332.

162. (317) Weber E.R., Sol.Stat.Coms. 60 (1986) p.871.

163. (145) Omling P., Weber E.R and Samuelson L., Phys.Rev.B 33 (1986) p.5880.

164. (569) Skowronski M., Lagowski J., Milshtein M., Kang C.H., Dabrowski F.P., Hennel A and Gatos H.C., J.Appl.Phys. 62 (1987) p.3791.

165. (243) Samuelson L., Omling P., weber E.r and Grimmeiss H.G., SI III–V Mats., 3 (Kah–nee–ta, 1984) p.263.

166. (665) Wosik J., Palczewska M and Kaminska M., Crystal Prop. & Prep. 12 (1987) p.239.

167. (804) Manasreh M.O., McDonald P.F., Kivlighn S.A., Minton J.T and Covington B.C., Sol.Stat.Coms. 65 (1988) p.1267.

168. (451) Kaminska M., Skowronski M and Kusko W., Phys.Rev.Lett. 55 (1985) p.2204.

169. (161) Wada K and Inoue N., Appl.Phys.Lett. 47 (1985) p.945.

170. (291) Makram-Ebeid S., Gautard D., Devillard P and Martin G.M., Appl.Phys.Lett. 40 (1982) p.161.

171. (678) Mauger A., Von-Bardeleben H.J., Bourgoin J.C and Lannoo M., Phys.Rev.B 36 (1987) p.5982.

172. (___) Dabrowski J and Scheffler M., SI III-V Mats., 5 (Malmo, 1988), p.37.

173. (845) Chadi D.J and Chang K.J., Phys.Rev.Lett. 60 (1988) p.2187.

174. (689) Gatos H.C and Lagowski J., Phys.Rev.B 36 (1987) p.7668.

175. (690) Von Bardeleben H.J., Bourgoin J.C and Steivenard D., Phys.Rev.B 36 (1987) p.7671.

176. (369) Martin S and Duseaux M., DHIP I (Montpellier, 1985) p.287.

177. (492) Matsui M and Kazuno T., Appl.Phys.Lett. 51 (1987) p.658.

178. (656) Dannefaer S., Mascher P and Kerr D., DRIP II (Monterey, 1987) p.313.

179. (466) Stucky M., Corbel C., Geffroy B., Moser P and Hautojarvi P., ICDS 14 (Paris, 1986), Mat.Sci.Forum 10-12 (1986) p.265.

180. (575) Culbertson J.C., Strom U and Wolf S.A., Phys.Rev.B 36 (1987) p.2962.

181. (514) Levinson M and Kafalas J.A., Phys.Rev.B 35 (1987) p.9383.

182. (335) Manasreh M.O and Covington B.C., Phys.Rev.B 35 (1987) p.2524.

183. (574) Manasreh M.O and Covington B.C., Phys.Rev.B 36 (1987) p.2730.

184. (399) Baraff G.A and Schluter M., Phys.Rev.B 35 (1987) p.5929.

185. (398) Baraff G.A and Schluter M., Phys.Rev.B 35 (1987) p.6154.

186. (781) Wosinski T., Semicond.Sci. & Technol. 3 (1988) p.411.

187. (562) Lagowski J., Gatos H.C., Parsey-Jr.J.M., Wada K., Kaminska M and Walukiewicz W., Appl.Phys.Lett. 40 (1982) p.342.

188. (826) Johnson E.J., Kafalas J., Davies R.W and Dyes W.A., Appl.Phys.Lett. 40 (1982) p.993.

189. (563) Walukiewicz W., Lagowski J and Gatos H.C., Appl.Phys.Lett. 43 p.112.

190. (___) Lagowski J., SI III-V Mats., 2 (Evian, 1982) p.41.

191. (203) Von-Bardeleben H.J., Steivenard D., Bourgoin J.C and Huber A., SI III-V Mats., 4 (Hakone, 1986) p.355.

192. (334) Von-Bardeleben H.J., Steivenard D and Bourgoin J.C., Appl.Phys.Lett. 47 (1985) p.970.

193. (765) Von-Bardeleben H.J., Bourgoin J.C., Steivenard D and Lannoo M., GaAs and Related Compounds, 14 (Heraklion, 1987) Inst.Phys.Conf.Ser. 91 (1988) p.399.

194. (471) Steivenard D., Von-Bardeleben H.J., Bourgoin J.C and Huber A., ICDS 14 (Paris, 1986), Mat.Sci.Forum 10-12 (1986) p.305.

195. (380) Zou Y., Zhou J., Lu Y., Wang K., Hu B., Lu B., Li C., Li L., Shao J and Sheng C., ICDS 13 (Coronado, 1984), Metallurgical Soc. of AIME (1985) p.1021.

196. (509) Zou Y., Matt.Lett. 5 (1987) p.203.

197. (510) Zou Y., Wang G and Wu J., Matt.Lett. 5 (1987) p.207.

198. (330) Wu J., Zou Y and Mo P., Matt.Lett. 5 (1987) p.29.

199. (808) Wu J., Mo P and Zou Y., Matt.Lett. 6 (1988) p.161.

200. (339) Wager J.F and Van-Vechten J.A., Phys.Rev.B 35 (1987) p.2330.

201. (829) Van Vechten J.A., J.Phys.C. Sol.Stat.Phys. 17 (1984) p.L933.

202. (822) Suezewa M and Sumino K., Jap.J.Appl.Phys. 27 (1988) p.L18.

203. (271) Goltzene A., Meyer B., Schwab C., Greenbaum S.G and Wagner R.J., GaAs and Related Compounds, 11 (Biarritz, 1984) Inst.Phys.Conf.Ser. 74 (1985) p.35.

204. (677) Figielski T., Kaczmarek E and Wosinski T., Appl.Phys.A 38 (1985) p.253.

205. (658) Figielski T., Acta.Physica.Polonica. A72 (1987) p.537.

206. (477) Figielski T., ICDS 14 (Paris, 1986), Mat.Sci.Forum 10–12 (1986) p.341.

207. (515) Figielski T and Wosinski T., Phys.Rev.B 36 (1987) p.1269.

208. (585) Figielski T., Phys.Stat.Sol. 102 (1987) p.493.

209. (275) Ikoma T., Taniguchi M and Mochizuki Y., GaAs and Related Compounds, 11 (Biarritz, 1984) Inst.Phys.Conf.Ser. 74 (1985) p.65.

210. (727) Jimenez J., Hernandez P., Gonzalez M.A., Sanz L.F and De Saja J.A., Cryst.Latt.Def.and Amorph.Mat. 17 (1987) p.199.

211. (745) Mita Y., GaAs and Related Compounds, 14 (Heraklion, 1987) Inst.Phys.Conf.Ser. 91 (1988) p.69.

212. (200) Hariu T., Komori H and Matsushita K., SI III–V Mats., 4 (Hakone, 1986) p.335.

213. (310) Hariu T., Sato T., Komori H and Matsushita K., J.Appl.Phys. 61 (1987) p.1068.

214. (___) Schneider J., SI III–V Mats., 2 (Evian, 1982) p.144.

215. (378) Levinson M., GaAs and Related Compounds, 14 (Heraklion, 1987) Inst.Phys.Conf.Ser. 91 (1988) p.73.

216. (431) Fillard J.P., Bonnafe J and Castagne M., Appl.Phys.A 35 (1984) p.149.

217. (579) Fillard J.P., Bonnafe J and Castagne M., J.Appl.Phys 56 (1984) p.3020.

218. (336) Kuszko W., Kaminska M and Baranowski J.M., Acta Physica Polonica A71 (1987) p.273.

219. (798) Silverberg P., Omling P and Samuelson L., Appl.Phys.Lett. 52 (1988) p.1689.

220. (___) Silverberg P., Omling P and Samuelson L., SI III–V Mats., 5 (Malmo, 1988), p.369.

221. (153) Skowronski M., Lagowski J and Gatos H.C., J.Appl.Phys. 59 (1986) p.2451.

222. (460) Lagowski J., Bugajski M., Matsui M and Gatos H.C., Appl.Phys. Lett. 51 (1987) p.511.

223. (113) Ishida K., Yahata A and Kikuta T., Jap.J.Appl.Phys. 24 (1985) p.L250.

224. (195) Tajima M., Yahata A., Kikuta T., Tsukada N and Ishida K., SI III–V Mats., 4 (Hakone, 1986) p.305.

225. (610) Blakemore J.S., J.Appl.Phys. 62 (1987) p.4528.

226. (606) Bahzhenov A.V and Krasil'nikova L.L., Sov.Phys.Sol.Stat. 26 (1984) p.356.

227. (___) Alt H.C., Schink H and Packeiser G., SI III–V Mats., 5 (Malmo, 1988), p.515.

228. (823) Alt H.C and Schink H., Appl.Phys.Lett. 52 (1988) p.1661.

229. (249) Katsumata T., Okada H., Kimura T and Fukuda T., J.Appl.Phys. 60 (1986) p.3105.

230. (238) Holmes D.E., Kuwamoto H. Kirkpatrick C.G and Chen R.T., SI III–V Mats., 3 (Kah–nee–ta, 1984) p.204.

231. (130) Martin G.M., Jacob G., Poiblaud G., Goltzene A and Schwab C., Inst.Phys.Conf.Ser. 59 (1981) p.281.

232. (111) Holmes D.E., Chen R.T., Elliot K.R and Kirkpatrick C.G., Appl.Phys.Lett. 43 (1983) p.305.

233. (100) Dobrilla P and Blakemore J.S., J.Appl.Phys. 60 (1986) p.169.

234. (257) Holmes D.E and Chen R.T., J.Appl.Phys. 55 (1984) p.3588

235. (206) Kuhn K.J and Sigmon T.W., SI III–V Mats., 4 (Hakone, 1986) p.373.

236. (050) Stirland D.J., Grant I., Brozel M.R and Ware R.M., Microsc. Semicond. Mats. Conf. (Oxford, 1987), Inst.Phys. Conf.Ser. 87 (1987) p.285.

237. (343) Figielski T., Appl.Phys.A 36 (1985) p.217.

238. (770) Figielski T., Crys.Res.Technol. 22 (1987) p.1263.

239. (293) Alt H.C and Packeiser G., J.Appl.Phys. 60 (1986) p.2954.

240. (347) Alt H.C and Packeiser G., 18th Conf.Sol.Stat.Dev.& Mat. (Tokyo, 1986) p.659.

241. (307) Dobrilla P and Blakemore J.S., J.Appl.Phys. 61 (1987) p.1442.

242. (655) Dobrilla P., DRIP II (Monterey, 1987) p.305.

243. (133) Miyari H., Inada T., Obokata T., Nakajima M., Katsumata T and Fukuda T., Jap.J.Appl.Phys. 24 (1985) p.L729.

244. (362) Katsumata T., Obokata T., Nakajima M and Fukuda T., DRIP I (Montpellier, 1985) p.149.

245. (316) Bray R., Sol.Stat.Comms. 60 (1986) p.867.

246. (625) Kuma S and Otoki Y., DRIP II (Monterey, 1987) p.1.

247. (644) Windscheif J and Wettling W., DRIP II (Monterey, 1987) p.195.

248. (653) Heinemann M., Meyer B.K., Spaeth J.M and Lohnert K., DRIP II (Monterey, 1987) p.289.

249. (763) Spaeth J.M., Hofmann D.M., Heinemann M and Meyer B.K., GaAs and Related Compounds, 14 (Heraklion, 1987) Inst.Phys.Conf.Ser. 91 (1988) p.391.

250. (776) Asom M.T., Parsey–Jr.J.M., Kimerling L.C., Sauer R and Theil F.A., Appl.Phys.Lett. 52 (1988) p.1472.

251. (654) Walukiewicz W., Bourret E.D., Yau W.F., McMurray–Jr.R.E., Haller E.E and Bliss D.F., DRIP II (Monterey, 1987) p.297.

252. (731) Abernathy C.R., Kinsella A.P., Jordan A.S., Caruso R., Pearton S.J., Temkin H and Wade H., J.Crys.Growth 85 (1987) p.106.

253. (724) Fillard J.P., Montgomery P., Baroudi A., Bonnafe J and Gall P., Jap.J.Appl.Phys. 27 (1988) p.L258.

254. (354) Castagne M., Bonnafe J., Zhang F, and Fillard J.P., DRIP I (Montpellier, 1985) p.35.

255. (483) Castagne M., Fillard J.P., Bonnafe J and Gall P., ICDS 14 (Paris, 1986), Mat.Sci.Forum 10–12 (1986) p.371.

256. (646) Gall P., Fillard J.P., Bonnafe J., Castagne M., Wheyer J and George A., DRIP II (Monterey, 1987) p.215.

257. (051) Skolnick M.S and Brozel M.R., Appl.Phys.Lett. 48 (1986) p.341.

258. (011) Skolnick M.S., Brozel M.R., Pitt A.D and Maguire J., SI III–V Mats., 4 (Hakone, 1986) p.139.

259. (331) Katsumata T., Okada H., Kikuta T and Fukuda T., Appl.Phys.A 42 (1987) p.103.

260. (177) Katsumata T., Okada H., Kikuta T., Fukuda T and Ogawa T., SI III–V Mats., 4 (Hakone, 1986) p.149.

261. (351) Ogawa T., DRIP I (Montpellier, 1985) p.1.

262. (645) Ogawa T and Kojima T., DRIP II (Monterey, 1987) p.207.

263. (178) Moriya K., SI III–V Mats., 4 (Hakone, 1986) p.151.

264. (353) Moriya K., DRIP I (Montpellier, 1985) p.27.

265. (352) Kuma S., Otoki Y and Kurata K., DRIP I (Montpellier, 1985) p.19.

266. (142) Ogawa T., Jap.J.Appl.Phys 25 (1986) p.L316.

267. (796) Ogawa T., J.Crys.Growth 88 (1988) p.332.

268. (017) Rumsby D., Ware R.M., Smith B., Tyjberg M., Brozel M.R and Foulkes E.J., IEEE GaAs IC Symposium (Phoenix, 1983) p.34.

269. (030) Rumsby D., Grant I., Brozel M.R., Foulkes E.J and Ware R.M., SI III–V Mats., 3 (Kah–nee–ta, 1984) p.165.

270. (274) Martin S., Duseaux M and Erman M., GaAs and Related Compounds, 11 (Biarritz, 1984) Inst.Phys.Conf.Ser. 74 (1985) p.53.

271. (369) Martin S and Duseaux M., DRIP I (Montpellier, 1985) p.287.

272. (189) Lohnert K., Wettling W and Koschek G., SI III–V Mats., 4 (Hakone, 1986) p.267.

273. (344) Obokata T., Sato T and Fujii T., Appl.Phys.Lett. 50 (1987) p.1146.

274. (172) Inada T., Ozawa S., Fujii T., Obakata T., Ishida K and Fukuda T., SI III–V Mats., 4 (Hakone, 1986) p.23.

275. (628) Abernathy C.R., Caruso R., Jordan A.S., Pearton S.J and Temkin H., DRIP II (Monterey, 1987) p.35.

276. (270) Yokogawa M., Nishine S., Matsumoto K., Morishita H., Fujita K and Akai S., GaAs and Related Compounds, 11 (Biarritz, 1984) Inst.Phys.Conf.Ser. 74 (1985) p.29.

277. (140) Noto N., Kitagawara Y., Takanishi T and Takenaka T., Jap.J. Appl.Phys. 25 (1986) p.L394.

278. (389) Obokata T., Matsumura T., Terashima K., Orito F., Kikuta T and Fukuda T., Jap.J.Appl.Phys. 23 (1984) p.L602.

279. (173) Hovel H.J., Albert M., Farrell E., Guidotti D and Becker J., SI III–V Mats., 4 (Hakone, 1986) p.97.

280. (518) Mikoshiba N., Akutsu Y., Nakamura H., Tsubouchi K and Hosokawa M., IEEE Ultrasonics Symp. (1986) p.481.

281. (703) Koteles E.S., Kafalas J., Zemon S and Norris P., GaAs and Related Compounds, 13 (Las Vegas, 1986) Inst.Phys.Conf. Ser. 83 (1987) p.63.

282. (346) Sekiguchi T and Sumino K., Jap.J.Appl.Phys. 26 (1987) p.L179.

283. (365) Dussac M., Dupuy M and Molva E., DRIP I (Montpellier, 1985) p.209.

284. (411) Chin A.K., Camlibel I., Caruso R., Young M.S.S and Von Neida A.R., J.Appl.Phys. 57 (1985) p.2203.

285. (192) Otoki Y., Nakamori M., Nakazono R and Kuma S., SI III–V Mats., 4 (Hakone, 1986) p.285.

286. (358) Bonnet M., DRIP I (Montpellier, 1985) p.105.

287. (408) Matsumoto Y and Watanabe H., Jap.J.Appl.Phys. 21 (1982) p.L515.

288. (170) Miyazawa S., SI III–V Mats., 4 (Hakone, 1986) p.3.

289. (494) Miyazawa S., ICDS 14 (Paris, 1986), Mat.Sci.Forum 10–12 (1986) p.1.

290. (217) Egawa T., Sano Y., Matsuura H., Nakamura H and Kaminishi K., SI III–V Mats., 4 (Hakone, 1986) p.567.

291. (216) Packeiser G., Schink H and Kniepkamp H., SI III–V Mats., 4 (Hakone, 1986) p.561.

292. (187) Ogawa O., SI III–V Mats., 4 (Hakone, 1986) p.237.

293. (147) Auret F.D., Leitch W.R and Vermaak J.S., J.Appl.Phys. 59 p.158.

294. (131) Martin G.M., Esteve E., Langlade and Makram–Ebeid S., J.Appl.Phys. 56 (1984) p.2655.

295. (212) Samitier J., Morante J.R., Cornet A., Perez A., Herms A., Giraudet L and Gourrier S., SI III–V Mats., 4 (Hakone, 1986) p.439.

296. (437) Samitier J., Morante J.R., Giraudet L and Gourrier S., Appl.Phys.Lett. 48 91986) p.1138.

297. (449) Samitier J., Herms A., Cornet A and Morante J.R., Physica Scripta 35 (1987) p.524.

298. (486) Samitier J., Morante J.R., Cornet A., Herms A., Roura P and Perez A., ICDS 14 (Paris, 1986), Mat.Sci.Forum 10–12 (1986) p.539.

299. (191) Osaka J., Hyuga F and Watanabe K., SI III–V Mats., 4 (Hakone, 1986) p.279.

300. (558) Osaka J., Hyuga F and Watanabe K., Appl.Phys.Lett. 47 (1985) p.1307.

301. (193) Kuzuhara M and Nozaki T., SI III–V Mats., 4 (Hakone, 1986) p.291.

302. (440) Hasegawa F., Yamamoto N and Nannichii Y., Appl.Phys.Lett. 45 (1984) p.461.

303. (186) Stoakes R.C., Willoughby A.F.W and Grant I.R., SI III–V Mats., 4 (Hakone, 1986) p.231.

304. (248) Lagowski J., Gatos H.C., Kang C.H., Skowronski M., Ko K.Y and Lin D.G., Appl.Phys.Lett. 49 (1986) p.892.

305. (586) Kang C.H., Lagowski J and Gatos H.C., J.Appl.Phys. 62 (1987) p.3482

306. (185) Ford W., Mathur G., Look D and Yu P., SI III–V Mats., 4 (Hakone, 1986) p.227.

307. (289) Look D.C., Yu P.W., Theis W.M., Ford W., Mathur G., Sizelove J.R., Lee D.H and Li S.S., Appl.Phys.Lett. (1986) p.1083.

308. (666) Kitagawara Y., Noto N., Takahashi T and Takenaka T., Appl,Phys.Lett. 52 (1988) p.221.

309. (743) Kazuno T., Takatsuka Y., Satoh K., Chino K and Chiba Y., GaAs and Related Compounds, 14 (Heraklion, 1987) Inst.Phys.Conf.Ser. 91 (1988) p.61.

310. (726) Palfrey H.D., Brown M and Willoughby F.W., J.Electron.Mat. 12 (1983) p.863.

311. 9455) Palfrey H.D., Brown M and Willoughby F.W., J.Electrochem.Soc. 128 (1981) p.2224.

312. (379) Newman R.C., ICDS 13 (Coronado, 1984), Metallurgical Soc. of AIME (1985) p.87.

313. (323) Ding J., Chang J.S.C and Bujatti M., Appl.Phys.Lett 50 (1987) p.1089.

314. (___) "Properties of GaAs", EMIS Datarevews Series No.2 (pub. INSPEC)

315. (512) Tin C.C., Teh C.K and Weichman F.L., J.Appl.Phys. 62 (1987) p.2329.

316. (129) Martin G.M., Farges J.P., Jacob G., Hallais J.P and Poiblaud G., J.Appl.Phys. 51 (1980) p.2840.

317. (425) Johnson E.J., Kafalas J.A and Davies R.W., J.Appl.Phys. 54 (1983) p.204.

318. (611) Chichibu S., Matsumoto S and Obokata T., J.Appl.Phys. 62 (1987) p.4316.

319. (___) Clegg J.B., SI III–V Mats., 2 (Evian, 1982) p.80.

320. (052) Brozel M.R in "Properties of GaAs", EMIS Datarevews Series No.2 (pub. INSPEC) sec.13.2.

321. (___) Wagner J and Windscheif J., SI III–V Mats., 5 (Malmo, 1988), p.507.

322. (541) Hunter A.T., Baukus J.P., Marsh O.J., Winston H.V., Young M.H and Hart R., SI III–V Mats., 3 (Kah–nee–ta, 1984) p.429.

323. (210) Ikuta K., Inoue N and Wada K., SI III–V Mats., 4 (Hakone, 1986) p.427.

324. (044) Young M.L., Hope D.A.O and Brozel M.R., Semicond.Sci. Technol. 3 (1988) p.292.

325. (719) Mitchel W.C., Brown G.J., Fischer D.W., Yu P.W and Lang J.E., J.Appl.Phys. 62 (1987) p.2320.

326. (673) Moore W.J., Hawkins R.L and Sharnabrook B.V., Physica 146B (1987) p.65.

327. (790) Wagner J., Seelwind H., Dischler B., Newman R.C and Maguire J., 18th Conf.Phys.Semicond. (Stockholm, 1986), Ed. O.Engstrom (World Scientific, 1987) p.951.

328. (426) Ta L.B., Hobgood H.M., Rohatgi A and Thomas R.N., J.Appl.Phys 53 (1982) p.5771.

329. (181) Wohlegemuth J.H., Khattack C.P., Lagowski J and Skowronski M., SI III–V Mats., 4 (Hakone, 1986) p.191.

330. (174) McGuigan s., Thomas R.N., Hobgood H.M., Eldridge G.W and Swanson B.U., SI III–V Mats., 4 (Hakone, 1986) p.29.

331. (755) Johannesen J.S., Harris J.S., Rensch D.B., Winston H.V., Hunter A.T., Kocot C and Bivas A., GaAs and Related Compounds, 14 (Heraklion, 1987) Inst.Phys.Conf.Ser. 91 (1988) p.113.

332. (403) Inada T., Fujii T and Fukuda T., J.Appl.Phys. 61 (1987) p.5483.

333. (384) Fujisaki Y and Takano Y., J.Appl.Phys. 61 (1987) p.2910.

334. (284) Dobrilla P., Blakemore J.S., McCamant A.J., Gleason K.R and Koyama R.Y., Appl.Phys.Lett. 47 (1985) p.602.

335. (360) Dobrilla P and Blakemore J.S., DRIP I (Montpellier, 1985) p.127.

336. (134) Miyazawa S and Wada K., Appl.Phys.Lett. 48 (1986) p.905.

337. (135) Miyazawa S., Honda T., Ishii Y and Ishida S., Appl.Phys.Lett. 44 (1984) p.410.

338. (136) Miyazawa S and Ishii Y., IEEE Trans.Electron.Dev. ED-31 (1984) p.1057.

339. (137) Miyazawa S., Ishii Y., Ishida S and Nanishi Y., Appl.Phys. Lett. 43 (1983) p.853.

340. (396) Miyazawa S and Hyuga F., IEEE Trans.Electron.Dev. ED-33 (1986) p.227.

341. (367) Nanishi Y., Miyazawa S and Matsuoka Y., DRIP I (Montpellier, 1985) p.225.

342. (414) Nanishi Y., Ishida S and Miyazawa S., Jap.J.Appl.Phys. 22 (1983) p.L54.

343. (415) Nanishi Y., Ishida S., Honda T., Yamazaki H and Miyazawa S., Jap.J.Appl.Phys. 21 (1982) p.L335.

344. (114) Ishii Y., Miyazawa S and Ishida S., IEEE Trans.Electron.Dev. ED-31 (1984) p.800.

345. (115) Ishii Y., Miyazawa S and Ishida S., IEEE Trans.Electron.Dev. ED-31 (1984) p.1051.

346. (333) Chen R.t., Holmes D.E and Asbeck P.M., Appl.Phys.Lett. 45 (1984) p.459.

347. (607) Takano Y., Ishiba T., Matsunaga N and Hashimoto N., Jap.J. Appl.Phys. 24 (1985) p.L239.

348. (___) Deconinck P., Pasqualini F., Maluenda J., and Schiller C., SI III-V Mats., 5 (Malmo, 1988), p.237.

349. (___) Fujisaki Y and Takano Y., SI III-V Mats., 5 (Malmo, 1988), p.247.

350. (246) Winston H.V., Hunter A.T., Olsen H.M., Bryan R.P and Lee R.E., SI III-V Mats., 3 (Kah-nee-ta, 1984) p.402.

351. (260) Winston H.V., Hunter A.T., Olsen H.M., Bryan R.P and Lee R.E., Appl.Phys.Lett. 45 (1984) p.447.

352. (281) Winston H.V., Hunter A.T., Kimura H., Olsen H.M., Bryan R.P., Lee R.E and Marsh D.J., GaAs and Related Compounds, 11 (Biarritz, 1984) Inst.Phys.Conf.Ser. 74 (1985) p.497.

353. (417) Yamazaki H., Honda T., Ishida S and Kawasaki Y., Appl.Phys.Lett. 45 (1984) p.1109.

354. (584) Anholt R and Sigmon T.W., J.Appl.Phys. 62 (1987) p.3995.

355. (447) Kasahara J., Arai M and Watanabe N., Jap.J.Appl.Phys. 25 (1986) p.L85.

356. (436) Suchet P., Duseaux M., Maluenda J and Martin G.M., J.Appl.Phys. 62 (1987) p.1097.

357. (626) Kuwamoto H and Holmes D.E., DRIP II (Monterey, 1987) p.15.

358. (450) Schink H., Packeiser G., Maluenda J and Martin G.M., Jap.J.Appl.Phys. 25 (1986) p.L369.

359. (446) Maluenda J., Martin G.M., Schink H and Packeiser G., Appl. Phys.Lett. 48 (1986) p.715.

360. (112) Hunter A.T., Kimura H., Olsen H.M and Winston H.V., J.Electron.Mat. 15 (1986) p.215.

361. (706) Rocher C., Maluenda J., Gabillard B., Ducourant T., Prost M and Rocchi M., GaAs and Related Compounds, 13 (Las Vegas, 1986) Inst.Phys.Conf.Ser. 83 (1987) p.509.

362. (230) Di-Lorenzo J.V., Jordan A.S., Von-Neida A.R and O'Conner P., SI III-V Mats., 3 (Kah-nee-ta, 1984) p.308.

363. (268) Martin G.M., Duseaux M and Maluenda J., GaAs and Related Compounds, 11 (Biarritz, 1984) Inst.Phys.Conf.Ser. 74 (1985) p.13.

364. (659) Blakemore J.S., J.Appl.Phys. 53 (1982) p.R123.

365. (___) Grabmair J.G and Watson C.B., Phys.Stat.Solidi. 32 (1969) K13

366. (421) Miyazawa S., Mizutani T and Yamazaki H., Jap.J.Appl. Phys. 21 (1982) p.L542.

367. (034) Stirland D.J., Rees G.J and Ritson A., J.Crys.Growth 79 (1986) p.493.

368. (033) Rees G.T., Stirland D.J and Bicknell R.W., Matt.Lett. 4 (1986) p.455.

369. (165) Abrahams M.S and Buiocchi C.J., J.Appl.Phys. 36 (1965) p.2855

370. (031) Stirland D.J., Inst.Phys.Conf.Ser. 33 (1977) p.150.

371. (605) Brown G.T and Warwick C.A., J.Electrochem.Soc. 133 (1986) p.2576.

372. (357) Wheyer J.L and Giling L.J., DRIP I (Montpellier, 1985) p.63.

373. (374) Gilling L.J., Weyher J.L., Montree A., Fornari R and Zanotti L., J.Crys.Growth 79 (1986) p.271.

374. (647) Bunod P., Molva E., Chabli A., Bertin F and Boveyron C., DRIP II (Monterey, 1987) p.257.

375. (769) De Raedt W., Van Hove M., Potter M.D., Van Rossum M and Weyher J.L., GaAs and Related Compounds, 14 (Heraklion, 1987) Inst.Phys.Conf.Ser. 91 (1988) p.685.

376. (661) Gleichmann R., Menniger H and Raidth H., Crystal Prop & Prep 12 (1987) p.17.

377. (390) Van de Ven J., Lourens A.F., Weyher J.L and Giling L.J., Chemitronics 1 (1986) p.19.

378. (830) Saitoh T., Matsubara S and Minagawa S., J.Electrochem.Soc. 122 (1975) p.670.

379. (832) Munoz–Yague A and Bafleur M., J.Crys.Growth 53 (1981) p.239.

380. (803) Dobrilla P and Miller D.C., J.Electrochem.Soc. 12 (1987) p.3197.

381. (233) Lessoff H and Gorman R., SI III–V Mats., 3 (Kah–nee–ta, 1984) p.83.

382. (298) Miyairi H., Ozawa S., Eguchi M and Fukuda T., J.Crys.Growth 76 (1986) p.388.

383. (635) Wang F.C., Rau M.F., Kurz J., Ehman M.F., Liao D.D and Carter R., DRIP II (Monterey, 1987) p.117.

384. (833) Schell H.A., Z.Metallke. 48 (1957) p.158. (in German)

385. (828) Richards J.L and Crocker A.J., J.Appl.Phys. 31 (1960) p.611.

386. (827) Abrahams M.S., J.Appl.Phys. 35 (1964) p.3626.

387. (355) Scott M.P., DRIP I (Montpellier, 1985) p.41.

388. (___) Lang A.R., J.Appl.Phys. 5 (1958) p.358.

389. (141) Tohno S., Shinoyama S and Katsui A., Appl.Phys.Lett 49 (1986) p.1204.

390. (157) Tohno S., Shinoyama S., Yamamoto A and Uemura C., J.Appl.Phys 54 (1983) p.666.

391. (632) Tohno S and Katsui A., DRIP II (Monterey, 1987) p.87.

392. (278) Matsui J., Kitano T., Kamejima T and Ishikawa T., GaAs and Related Compounds, 11 (Biarritz, 1984) Inst.Phys.Conf.Ser. 74 (1985) p.101.

393. (250) Sato T., Nakajima M., Fukuda T and Ishida K., Appl.Phys.Lett. 49 (1986) p.1599.

394. (419) Fujimoto I., Jap.J.Appl.Phys. 23 (1984) p.L287.

395. (528) Fujimoto I., ICDS 13 (Coronado, 1984), Metallurgical Soc. of AIME (1985) p.943.

396. (670) Fujimoto I., Defects and Properties of Semiconductors: Defect Engineering Eds Chikawa J., Sumino K and Wada K., (KTK Scientific Publishers Tokyo, 1987) p.71.

397. (234) Brown G.t., Skolnick M.S., Jones G.R., Tanner B.K and Barnett S.J., SI III–V Mats., 3 (Kah–nee–ta, 1984) p.76.

398. (608) Kitano T., Ishikawa T and Matsui J., Jap.J.Appl.Phys. 25 (1986) p.L282.

399. (356) Forman R.A., Bell M.I and Mayo S., DRIP I (Montpellier, 1985) p.55.

400. (631) Forman R.A., Hill J.R., Bell M.I., White G.S., Freiman S.W and Ford W., DRIP II (Monterey, 1987) p.63.

401. (636) Ananthanarayanan T.s and Trivedi S.B., DRIP II (Monterey, 1987) p.125.

402. (054) Brozel M.R., in "Properties of GaAs", EMIS Datarevews Series No.2 (pub. INSPEC) sec.13.1.

403. (053) Stirland D.J and Brozel M.R., (1987) to be published!

404. (010) Skolnick M.S., DRIP I (Montpellier, 1985) p.165.

405. (006) Brozel M.R., Grant I., Ware R.M and Stirland D.J., Appl.Phys.Lett. 42 (1983) p.610.

406. (388) Katsumata T and Fukuda T., Rev.Sci.Instrum. 57 (1986) p.202.

407. (383) Windscheif J., Baeumler M and Kaufmann U., Appl.Phys.Lett. 46 (1985) p.661.

408. (364) Windscheif J., Baeumler M and Kaufmann U., DRIP I (Montpellier, 1985) p.193.

409. (453) Windscheif J and Wettling W., GaAs and Related Compounds, 13 (Las Vegas, 1986) Inst.Phys.Conf.Ser. 83 (1987) p.197.

410. (283) Wettling W and Windscheif J., Appl.Phys.A 40 (1986) p.191.

411. (244) Dobrilla P., Blakemore J.S and Koyama R.Y., SI III–V Mats., 3 (Kah–nee–ta, 1984) p.282.

412. (385) Dobrilla P and Blakemore J.S., J.Appl.Phys. 58 (1985) p.208.

413. (276) Gouteraux B., Visentin N., Lent B and Bonnet M., GaAs and Related Compounds, 11 (Biarritz, 1984) Inst.Phys.Conf.Ser. 74 (1985) p.89.

414. (359) Visentin N., Gouteraux B., Bonnet M and Lent B., DRIP I (Montpellier, 1985) p.117.

415. (363) Silverberg P., Nielson L., Omling P and Samuelson L., DRIP I (Montpellier, 1985) p.157.

416. (652) Silverberg P., Omling P and Samuelson L., DRIP II (Monterey, 1987) p.281.

417. (327) Fillard J.P., Castagne M., Bonnafe J and Gall P., Mat.Res.Soc Symp.Proc. 69 91986) p.231.

418. (612) Suchet P., Duseaux M., Gillardin G., Le Bris J and Martin G.M., J.Appl.Phys. 62 (1987) p.3700.

419. (043) Kidd P., Booker G.R and Stirland D.J., Microsc. Semicond. Mats. Conf. (Oxford, 1987), Inst.Phys.Conf.Ser. 87 (1987) p.275.

420. (035) Kidd P., Booker G.R and Stirland D.J., Appl.Phys.Lett. 51 (1987) p.1331.

421. (041) Brozel M.R., GaAs and Related Compounds, 14 (Heraklion, 1987) Inst.Phys.Conf.Ser. 91 (1988) p.117.

422. (037) Brozel M.R., DRIP II (Monterey, 1987) p.225.

423. (168) Dobrilla P and Blakemore J.S., SI III–V Mats., 4 (Hakone, 1986) p.103.

424. (___) Winnacker A., Vetter Th. and Zack F.X., SI III–V Mats., 5 (Malmo, 1988) p.583.

425. (860) Lang D.V., J.Appl.Phys. 45 (1974) p.3023.

426. (444) Zhota Y and Watanabe M.O., J.Appl.Phys. 53 (1982) p.1809.

427. (439) Yahata A and Nakajima M., Jap.J.Appl.Phys.23 (1984) p.L313.

428. (529) Li G.P., Wu Y and Wang K.L., ICDS 13 (Coronado, 1984), Metallurgical Soc. of AIME (1985) p.951.

429. (424) Lagowski J., Lin D.G., Aoyama T and Gatos H.C., Appl.Phys.Lett. 43 (1984) p.336.

430. (750) Skowronski M., Lagowski J., Milshtein M., Kang C.H., Dabkowski F and Gatos H.C., GaAs and Related Compounds, 14 (Heraklion, 1987) Inst.Phys.Conf.Ser. 91 (1988) p.93.

431. (220) Wosinski T and Breitenstein O., Phys.Stat.Sol.(a) 96 (1986) p.311.

432. (601) Wada K., Ikuta K., Osaka J and Inoue N., Appl.Phys.Lett. 51 (1987) p.1617.

433. (623) Breitenstein O., Microsc.Semicond.Mats.Conf. (Oxford, 1987), Inst.Phys.Conf.Ser. 87 (1987) p.763.

434. (104) Breitenstein O and Diegner B., Phys.Stat.Sol.(a) 94 (1986) p.K21.

435. (302) Sporon–Fiedler F and Weber E.R., SPIE 623 (1986) p.72.

436. (253) Morante J.R., Samitier J., Perez A., Altelarrea H and Gorrier S., J.Appl.Phys. 60 (1986) p.1661.

437. (552) Kremer R.E., Arikan M.C., Abele J.C and Blakemore J.S., J. Appl.Phys. 62 (1987) p.2424.

438. (553) Abele J,C., Kremer R.E and Blakemore J.S., J.Appl.Phys. 62 (1987) p.2432.

439. (671) Tin C.C., Teh C.K and Weichman F.L., J.Appl.Phys. 63 (1988) p.355.

440. (785) Teh C.K., Tin C.C and Wiechman F.L., Can.J.Phys. 65 (1987) p.945.

441. (218) Yoshie O and Kamihara M., Jap.J.Appl.Phys. 24 (1985) p.431.

442. (676) Balland J.C., Zielinger J.P., Noguet C and Tapiero M., J.Phys.D: Appl.Phys. 19 (1986) p.57.

443. (853) Tapiero M., Benjelloun N., Zielinger J.P., El–Hamd S and Noguet C., J.Appl.Phys. 64 (1988) p.4006.

444. (211) Ikeda K and Ishii Y., SI III–V Mats., 4 (Hakone, 1986) p.433.

445. (792) Omeljanovsky E.M., Polyakov A.J., Raihstein V.I., Rytova N.S and Fridman V.A., 18th Conf.Phys.Semicond. (Stockholm, 1986), Ed. O.Engstrom (World Scientific, 1987) p.1007.

446. (542) Seabaugh A.C., Bell M.I., Larrabee R.D and Oliver–Jr. J.N., SI III–V Mats., 3 (Kah–nee–ta, 1984) p.437.

447. (473) Kuszko W., Walczak P.J., Trautman P., Kaminska M and Baranowski J.M., ICDS 14 (Paris, 1986), Mat.Sci.Forum 10–12 (1986) p.317.

448. (663) Walczac J.P., Trautman P., Kaminska M and Baranovski J.M., Crystal Prop. & Prep. 12 (1987) p.225.

449. (702) Von Neida A.R., Pearton S.J., Stavola M and Caruso R., GaAs and Related Compounds, 13 (Las Vegas, 1986) Inst.Phys.Conf.Ser. 83 (1987) p.57.

450. 520) Bencherifa A., Bremond G., Nouailhat A., Guillot G., Guivarc'h A and Regreny A., Revue Phys.Appl. 22 (1987) p.891.

451. (197) Hasegawa F., Tomozane M., Yamamoto N. and Nannichi Y., SI III–V Mats., 4 (Hakone, 1986) p.317.

452. (711) Look D.C., J.Electrochem.Soc. 134 (1987) p.2527.

453. (288) Anderson D.A and Aspley N., Semicond.Sci. & Technol. 1 (1986) p.187.

454. (420) Hyuga F., Jap.J.Appl.Phys. 24 (1985) p.L160.

455. (416) Honda T., Ishii Y., Miyazawa S., Yamazaki H and Nanishi Y., Jap.J.Appl.Phys. 22 (1983) p.L270.

456. (768) Tomizawa K., Sassa K., Shimanuki Y and Nishizawa J., Defects and Properties of Semiconductors: Defect Engineering, Eds Chikawa J., Sumino K and Wada K., (KTK Scientific Publishers, Tokyo 1987) p.25.

457. (027) Blunt R.T., Clark S and Stirland D.J., IEEE Trans. Microwave Theory & Tech. Vol MTT–30 No7 (July 1982) p.943.

458. (609) Kitahara K and Ozeki M., Jap.J.Appl.Phys. 23 (1984) p.1655.

459. (544) Wang F.C., SI III–V Mats., 3 (Kah–nee–ta, 1984) p.475.

460. (593) Look D.C and Pimental E., Appl.Phys.Lett. 51 (1987) p.1614.

461. (810) Pimental E and look D.C., J.Electron.Mat. 17 (1988) p.63.

462. (669) Tajima M., Defects and Properties of Semiconductors: Defect Engineering, Eds Chikawa J., Sumino K and Wada K., (KTK Scientific Publishers, Tokyo 1987) p.37.

463. (___) Tajima M., SI III–V Mats., 5 (Malmo, 1988) p.119.

464. (550) Samuelson L., Omling P and Grimmeiss H.G., Appl.Phys.Lett. 45 (1984) p.521.

465. (441) Yu P.Y., Phys.Rev.B 29 (1984) p.2283.

466. (539) Yu P.Y., SI III–V Mats., 3 (Kah–nee–ta, 1984) p.278.

467. (517) Tajima M., Jap.J.Appl.Phys. 26 (1987) p.L885.

468. (547) Tajima M., Iino T and Ishida K., Jap.J.Appl.Phys. 26 (1987) p.L1060.

469. (530) Paget D and Klein P.B., ICDS 13 (Coronado, 1984), Metallurgical Soc. of AIME (1985) p.959.

470. (576) Hunter A.T., Diffusion & Defect Data 48 (1986) p.1.

471. (412) Watanabe K., Nakanishi H., Yamada K and Hoshikawa K., Appl.Phys.Lett. 45 (1984) p.643.

472. (124) Kikuta T., Terashima K and Ishida K., Jap.J.Appl.Phys. 22 (1983) p.409.

473. (591) Tajima M and Okada Y., ICDS 12 (Amsterdam, 1982), Physica 116B (1983) p.404.

474. (300) Hunter A.T., SPIE Vol.623 (1986) p.36.

475. (637) Hunter A.T., DRIP II (Monterey, 1987) p.137.

476. (366) Kallel A., Lauret.N., Gall P., Brabant J.C., Brousseau M., Peyrade J.P., Duseaux M and Martin S., DRIP I (Montpellier, 1985) p.217.

477. (409) Chin A.K., Von Neida A.R and Caruso R., J.Electrochem.Soc. 129 (1982) p.2386.

478. (413) Warwick C.A and Brown G.T., Appl.Phys.Lett. 46 (1985) p.574.

479. (162) Wakefield B., Leigh P.A., Lyons M.H and Elliot C.R., Appl.Phys.Lett. 45 (9184) p.66.

480. (194) Spaeth J.M., SI III–V Mats., 4 (Hakone, 1986) p.299.

481. (485) Spaeth J.M., ICDS 14 (Paris, 1986), Mat.Sci.Forum 10–12 (1986) p.505.

482. (___) Gilason H.P., SI III–V Mats., 5 (Malmo, 1988) p.311.

483. (831) Wagner R.J., Krebs J.J., Strauss G.H and White A.M., Sol. Stat.Comms 36 (1980) p.15.

484. (348) Meyer B.K., Spaeth J.M and Scheffler M., Phys.Rev.Lett. 52 (1984) p.851.

485. (160) Von Bardeleben H.J., Bourgoin J.C and Miret A., Phys.Rev.B 34 (1986) p.1360.

486. (470) Von Bardeleben H.J., Bourgoin J.C and Miret A., ICDS 14 (Paris, 1986), Mat.Sci.Forum 10–12 (1986) p.299.

487. (527) Goltzene A., Meyer B and Schwab C., ICDS 13 (Coronado, 1984), Metallurgical Soc. of AIME (1985) p.937.

488. (742) Kaufmann U., GaAs and Related Compounds, 14 (Heraklion, 1987) Inst.Phys.Conf.Ser. 91 (1988) p.41.

489. (465) Kaczmarek E., ICDS 14 (Paris, 1986), Mat.Sci.Forum 10–12 (1986) p.253.

490. (499) Von Bardeleben H.J and Bourgoin J.C., Phys.Rev.B 33 (1986) p.2890.

491. (202) Von Bardeleben H.J and Bourgoin J.C., SI III–V Mats., 4 (Hakone, 1986) p.351.

492. (002) Brozel M.R., Clegg J.B and Newman R.C., J.Phys.D:Appl.Phys. 11 (1978) p.1331.

493. (844) Harris T.D., J.Crys.Growth 89 (1988) p.21.

494. (152) Skolnick M.S., RSRE Research Review (1985) p.125.

495. (294) Wagner J., Seelewind H., Koidl P., Appl.Phys.Lett. 49 (1986) p.1080.

496. (310) Wagner J and Ramsteiner M., Appl.Phys.Lett. 49 (1986) p.1369.

497. (766) Wagner J., Ramsteiner M., Jantz W and Lohnert K., GaAs and Related Compounds, 14 (Heraklion, 1987) Inst.Phys.Conf.Ser. 91 (1988) p.415.

498. (737) Mascher P., Kerr D and Dannefaer S., J.Crys.Growth 85 (1987) p.295.

499. (329) Dlubek G., Plazaola F., Makinen J., Hautojarvi P., Brummer O., Proc.7th Int.Conf. Positron Annihilation (1985) p.684.

500. (846) Dlubek G., Dlubek A., Krause R., Brummer O., Friedland K and Rentzsch R., Phys.Stat.Sol. (a) 106 (1988) p.419.

501. (476) Puska M.J., ICDS 14 (Paris, 1986), Mat.Sci.Forum 10–12 (1986) p.277.

502. (801) Laszig D and Haasen P., Phys.Stat.Sol. (a) 104 (1987) p.K105.

503. (761) Abe Y., GaAs and Related Compounds, 14 (Heraklion, 1987) Inst.Phys.Conf.Ser. 91 (1988) p.363.

504. (___) Brozel M.R., Private Communication.

505. (303) Brophy M.J and Granto A.V., SPIE 623 p.13.

506. (748) Bourgoin J.C., Von Bardeleben H.J., Lim H., Stievenard D and Bonnet A., GaAs and Related Compounds, 14 (Heraklion, 1987) Inst.Phys.Conf.Ser. 91 (1988) p.85.

507. (511) Lim H.J., Von Bardeleben H.J and Bourgoin J.C., J.Appl.Phys. 62 (1987) p.2738.

508. (639) Bode M., Jabubowicz A and Habermeier H.U., DRIP II (Monterey, 1987) p.155.

509. (622) Jakubowicz A., Bode M and Habermeier H.U., Microsc.Semicond. Mats.Conf. (Oxford, 1987), Inst.Phys.Conf. Ser. 87 (1987) p.763.

510. (638) McCabe E.M and Wilson T., DRIP II (Monterey, 1987) p.147.

511. (213) Suemune J., Yamamoto H., Uesugi N and Yamanishi M., SI III–V Mats., 4 (Hakone, 1986) p.445.

512. (150) Sawada T., Goshie Y., Watanabe T and Furuya K., Jap.J.Appl. Phys. 24 (1985) p.L938.

513. (139) Nakamura H., Tsubouchi K., Mikoshiba N and Fukuda T., Jap.J. Appl.Phys. 24 (1985) p.L876.

514. (148) Mikoshiba N., Nakamura H and Tsubouchi K., IEEE Ultrasonics Symp. 0090–5607/85 (1985) p.436

515. (543) Amer N.M., Haller E.E and Weber E.R., SI III–V Mats., 3 (Kah–nee–ta, 1984) p.460.

516. (228) Strausser Y.E and Rosencwaig A., SI III–V Mats., 3 (Kah–nee–ta, 1984) p.87.

517. (328) Brandes A.G., Tang C and Fillmore C., Mat.Res.Soc.Symp. Proc. 69 (1986) p.385.

518. (602) Cummings K.D., Pearton S.J and Vella–Coleiro G.P., J.Appl. Phys. 60 (1986) p.1676.

519. (642) Borrego J.M., Gutmann R.J., Lo C.S., Heimlich M and Paz O., DRIP II (Monterey, 1987) p.177.

520. (694) Gutmann R.J., Borrego J.M., Lo C.S., Heimlich M.C and Paz O., SPIE 794 (1987) p.128.

521. (179) Usami A., Matsuoka H., Wada T., Murai K and Umehara M., SI III–V Mats., 4 (Hakone, 1986) p.157.

522. (196) Ohyama T., SI III–V Mats., 4 (Hakone, 1986) p.311.

523. (222) Fujisaki Y., Takano Y and Ishiba T., SI III–V Mats., 4 (Hakone, 1986) p.163.

524. (643) Ferenczi G., Huber D and Jantsch W., DRIP II (Monterey, 1987) p.185.

525. (794) Jantsch W., Ferenczi G., Brunthaler G and Huber D., 18th Conf.Phys.Semicond. (Stockholm, 1986), Ed. O.Engstrom (World Scientific, 1987) p.1015.

526. (793) Tamura Y and Hamaguchi C., 18th Conf.Phys.Semicond. (Stockholm, 1986), Ed. O.Engstrom (World Scientific, 1987) p.1011.

527. (641) Bylsma R.B and Glass A.M., DRIP II (Monterey, 1987) p.171.

528. (740) Bylsma R.B., Olsen D.H and Glass A.M., Appl.Phys.Lett. 52 (1988) p.1083.

529. (851) Cheng L.J and Gheen G., SPIE 836 (1987) p.169.

530. (806) Shen H., Hang Z., Pan S.H., Pollak F.H and Woodall J.M., Appl.Phys.Lett. 52 (1988) p.2058.

531. (301) Raccah P.M., Garland J.W., Zhang Z., Mioc S., De Y., Chu A.H.M., McGuigan S and Thomas R.N., SPIE 623 (1986) p.40.

532. (854) Raccah P.M., Garland J.W., Zhang Z., Lee U., Xue D.Z., Abels L.L., Ugur S and Wilinsky W., Phys.Rev.Lett. 12 (1984) p.1958.

533. (856) Haak R and Tench D., J.Electrochem.Soc. 131 (1984) p.275.

534. (127) Markov A.V., Mil'vidsii M.G and Osvenskii V.B., Sov.Phys. Semicond. 20 (1986) p.403.

535. (581) Otsubo M and Morotani T., Jap.J.Appl.Phys. 22 (1983) p.L345.

536. (201) Zhou B.L., Hu B.H., Wu Z and Chen Q., SI III–V Mats., 4 (Hakone, 1986) p.347.

537. (198) Mochizuchi Y and Ikoma T., SI III–V Mats., 4 (Hakone, 1986) p.323.

538. (474) Mochizuchi Y and Ikoma T., ICDS 14 (Paris, 1986), Mat.Sci. Forum 10–12 (1986)

p.323.

539. (315) Hariu T., Sato T., Komori H and Matsushita K., J.Appl.Phys. 61 (1987) p.1068.

540. (199) Fuchs F., Dischler B and Kaufmann U., SI III–V Mats., 4 (Hakone, 1986) p.329.

541. (108) Dischler B., Fuchs F and Kaufmann U., Appl.Phys.Lett. 48 (1986) p.2204.

542. (480) Dischler B., Fuchs F and Kaufmann U., ICDS 14 (Paris, 1986), Mat.Sci.Forum 10–12 (1986) p.359.

543. (820) Mita Y., J.Appl.Phys. 64 (1988) p.797.

544. (392) Fisher D.W., Appl.Phys.Lett. 50 (1987) p.1751.

545. (247) Skolnick M.S., Hope D.A.O and Cockayne B., SI III–V Mats., 3 (Kah–nee–ta, 1984) p.446.

546. (577) Skolnick M.S., Reed L.J and Pitt A.D., Appl.Phys.Lett. 44 (1984) p.447.

547. (013) Brozel M.R and Skolnick M.S., SI III–V Mats., 4 (Hakone, 1986) p.109.

548. (___) Grant I. (Private communication)

549. (___) Blunt R.T. (Private communication)

550. (604) Pichaud B., Burle–Durbec N., Minari F and Duseaux M., J.Crys.Growth 71 (1985) p.648.

551. (262) Scott M.P., Laderman S.S and Elliot A.G., Appl.Phys.Lett 47 (1985) p.1280.

552. (587) Matsui J., Microsc. Semicond. Mats. Conf. (Oxford, 1987), Inst.Phys.Conf.Ser. 87 (1987) p.249.

553. (435) Ono H., Kitano T and Matsui J., Appl.Phys.Lett. 51 (1987) p.238.

554. (634) Pichaud B., Burle–Durbec N and Minari F., DRIP II (Monterey, 1987) p.109.

555. (025) Clark S., Brozel M.R and Stirland D.J., DRIP I (Montpellier, 1985) p.201.

556. (019) Stirland D.J., Brozel M.R and Grant I., Appl.Phys.Lett 46 (1985) p.1066.

557. (008) Stirland D.J., Brozel M.R and Grant I., Microsc. Semicond. Mats. Conf. (Oxford, 1985), Inst.Phys.Conf.Ser. 76 (1985) p.211.

558. (029) Foulkes E.J., Brozel M.R., Grant I., Singer P., Waldock B and Ware R.M., SI III–V Mats., 3 (Kah–nee–ta, 1984) p.160.

559. (042) Stirland D.J., Hart D.G., Grant I., Bozel M.R and Clark S., Microsc. Semicond. Mats. Conf. (Oxford, 1987), Inst.Phys.Conf.Ser. 87 (1987) p.269.

560. (014) Brozel M.R., Clark S and Stirland D.J., SI III–V Mats., 4 (Hakone, 1986) p.133.

561. (___) Warner D., private communication.

Details of relevant conference proceedings

Semi–Insulating III–V compounds:

SI III–V Mats., 2 (Evian, 1982) eds. S Makram Ebeid and B.Tuck (Nantwich: Shiva, 1982).

SI III–V Mats., 3 (Kah–nee–ta, 1984) eds. D.C Look and J.S Blakemore (Nantwich: Shiva, 1984).

SI III–V Mats., 4 (Hakone, 1986) eds. H Kukimoto and S Miyazawa (Tokyo: Ohmsha).

SI III–V Mats., 5 (Malmo, 1988) eds G Grossmann and L.Ledebo (Bristol: Adam Hilger, 1988).

GaAs and Related Compounds:

GaAs and Related Compounds, 11 (Biarritz, 1984) Inst.Phys. Conf.Ser. 74, ed. B De–Cremoux, (Bristol IOP, 1985).

GaAs and Related Compounds, 12 (Karuizawa, 1985) Inst. Phys.Conf.Ser. 79, ed M. Fujimoto (Bristol: IOP, 1986).

GaAs and Related Compounds, 13 (Las Vegas, 1986) Inst.Phys. Conf.Ser. 83, ed W.T Lindley (Bristol: IOP, 1987).

GaAs and Related Compounds, 14 (Heraklion, 1987) Inst.Phys. Conf.Ser. 91, eds A Cristou and H.S Rupprecht (Bristol: IOP, 1988).

Defect Recognition and Image Processing in III–V compounds:

DRIP I (Montpellier, 1985), Materials Science Monographs, 31, ed J.P Fillard (Amsterdam: Elsevier, 1985).

DRIP II (Monterey, 1987), Materials Science Monographs, 44, ed. E.R Weber (Amsterdam: Elsevier, 1987).

International Conference on Defects in Semiconductors:

ICDS 12 (Amsterdam, 1982), Physica 116B, ed C.A.J Ammerlaan (Amsterdam: North Holland, 1983).

ICDS 13 (Coronado, 1984), Metallurgical Soc. of AIME, 14, eds L.C Kimerling and J.M Parsey Jr (Warrendale: AIME, 1985).

ICDS 14 (Paris, 1986), Mat.Sci.Forum 10–12, ed H.J Von Bardeleben (Aedermannsdorf, Switzerland: Trans Tech, 1986).

Microscopy of Semiconducting Materials Conference:

Microsc. Semicond. Mats. Conf., (Oxford, 1985), Inst.Phys. Conf.Ser. 76, ed. A.G Cullis (Bristol: IOP, 1985).

Microsc. Semicond. Mats. Conf., (Oxford, 1987), Inst.Phys. Conf.Ser. 87, ed. A.G Cullis (Bristol: IOP, 1987).

Appendix 1.1

Acronyms and Abbreviations

"A" centre ..... 78meV/203meV double acceptor
A/B (etch) ..... Abrahams and Bouiochi (etch)
C–V (profile) ... Capacitance–Voltage profile
CCD ..... Configuration Coordinate Diagram
CCTV .....Closed Circuit Television (camera)
CL ..... Cathodoluminescence
CPAA ..... Charge Particle Activation Analysis
CRSS ..... Critically Resolved Shear Stress
D–FET ..... Depletion mode FET
DARC..... Digital Automated Rocking Curve (topography)
DLFS..... Deep Level Fourier Spectroscopy
DLOS..... Deep Level Optical Spectroscopy
DLTS..... Deep Level Transient Spectroscopy
DS(L) (etch) ..... Dilute Sirtl (with Light) etch
DTA..... Differential Thermal Analysis
E–FET..... Enhancement mode FET
E/D–FET..... Enhancement/Depletion mode FET
EBIC ..... Electron Beam Induced Current
EDX.....Energy Dispersive X–ray (analysis)
EDZ.....Extended Denuded Zone
EER..... Electrolyte Electro–Reflectance
EL2 (etc).....Electron Level 2
ENDOR..... Electron Nuclear Double Resonance
EPC..... Electrolyte Photo–Capacitance
EPR..... Electron Paramagnetic Resonance
ESR..... Electron Spin Resonance
FEC..... Fully Encapsulated Czochralski
FET ..... Field Effect Transistor
FTIR ..... Fourier Transform Infra–Red (spectrometer)
GDMS.....Glow Discharge Mass Spectrometer
GF.....Gradient Freeze
hf.....hyper–fine (spin interaction)
HB ..... Horizontal Bridgman
HEM.....Heat Exchanger Method
HGF.....Horizontal Gradient Freeze
HIL–PC (etch)...High Intensity Light–Photochemical (etch)

HL4 (etc) ..... Hole Level 4

HRTEM ..... High Resolution TEM

I_{DSS} ..... (FET) Drain Source Saturation Current

ITC ..... Inverted Thermal Conversion

LEC ..... Liquid Encapsulated Czochralski

LEK ..... Liquid Encapsulated Kryopoulus

LEF ..... Liquid Encapsulated Freeze

LPLEC .....Low Pressure LEC

LVM..... Local Vibrational Mode

MAS ..... Microwave Absorption Spectroscopy

MCD ..... Magnetic Circular Dichroism

MESFET ..... Metal–Semicondctor FET

MLEC..... Magnetic field LEC

MMIC ..... Monolithic Microwave Integrated Circuit

NIR..... Near–Infrared

OAIP ..... Optically Assisted Imperfection Profile

OBIC..... Optical Beam Induced Current

ODENDOR .....Optically Detected ENDOR

ODEPR .....Optically Detected EPR

ODESR .....Optically Detected ESR

ODLTS ..... Optical DLTS

OITS.....Optical Isothermal Transient Spectroscopy

OSMA ..... Optically Stimulated Microwave Absorption

OTCS ..... Optical Transient Current Spectroscopy

PA ..... Positron Annihilation

PA (PTS)..... Photo–Accoustic (PTS)

PBD ..... Photo–thermal Beam Deflection

PERS .....Photo–Electric Relaxation Spectroscopy

PICTS..... Photo–Induced Current Transient Spectroscopy

PITS ..... Photo–Induced Transient Spectroscopy

PL ..... Photoluminescence

PLE ..... Photoluminescence Excitation

PR ..... Photo–Reflectance

PR–DLTS..... Photo–Resistance DLTS

PTR.....Photo–Thermal Radiation

PTS ..... Photo–Thermal Spectroscopy

R–DLTS ..... Reverse (bias) DLTS

RC (etch)..... Richards–Crocker (etch)

RXRT..... Reflection X–Ray Topography

shf.....super hyper–fine (interaction)
SEM ..... Scanning Electron Microscope
SI..... Semi–Insulating
SIMS ..... Secondary Ion Mass Spectroscopy
SPEC ..... Spectroscopic Photo–Electrochemical Current
SSMS..... Spark Source Mass Spectroscopy
TEM ..... Transmission Electron Microscope
TR ..... Thermo–Reflectance
TSC..... Thermally stimulated Currents
TSCap..... Thermally stimulated Capacitance
TWM ..... Thermal Wave Microscopy
TXRT..... Transmission X–Ray Topography
V_{Th} ..... (FET) Threshold Voltage
V_{PO}..... (FET) Pinch–Off Voltage
VGF.....Vertical Gradient Freeze
VMFEC ..... Vertical Magnetic field FEC
VMLEC..... Vertical Magnetic field LEC
XRT ..... X–Ray Topography
YAG ..... Yttrium Aluminium Garnet (laser)
ZPL ..... Zero Phonon Line

APPENDIX 5.1.

Appendix 5.1.1.

CCTV camera external synchronisation circuit.

Appendix 5.1.2.

Sync. pulse separation circuits:

Appendix 5.1.2(a).

Line SYNC pulse separation

Appendix 5.1.2(b).

FRAME sync. pulse separation.

Appendix 5.1.3.

Line and frame number selection circuits;

Appendix 5.1.3(a).

LINE selection circuit.

Appendix 5.1.3(b).

Selection circuit for number of frames.

Appendix 5.1.4.

Analogue input circuit.

Appendix 5.1.5

Multiplexer and external RAM circuit.

Appendix 5.1.6.

Video mixer circuit.

Appendix 5.1.1

CCTV camera external synchronisation circuit

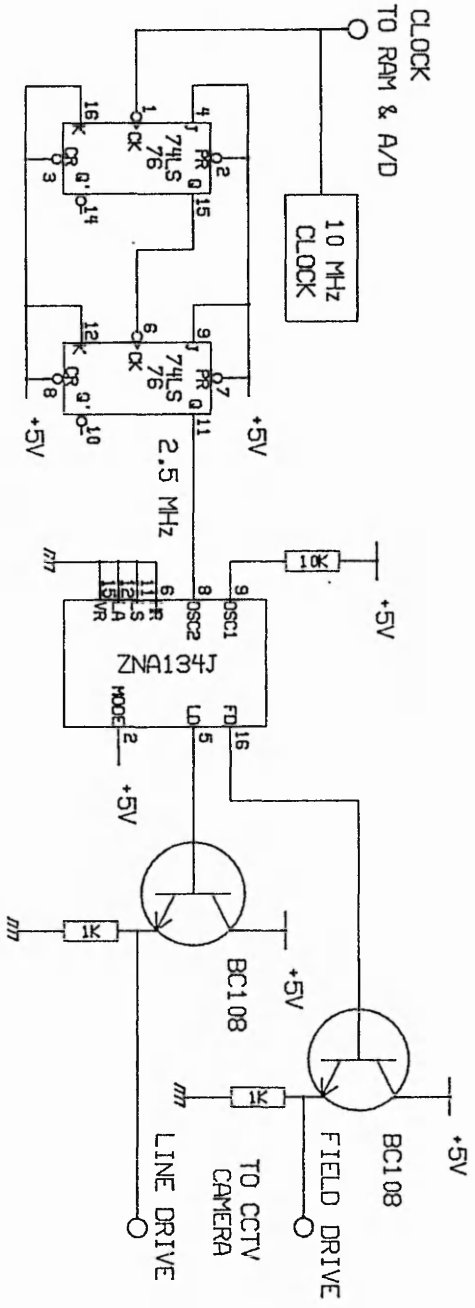

Appendix 5.1.2.

Appendix 5.1.2(a).

Line SYNC. pulse separation circuit.

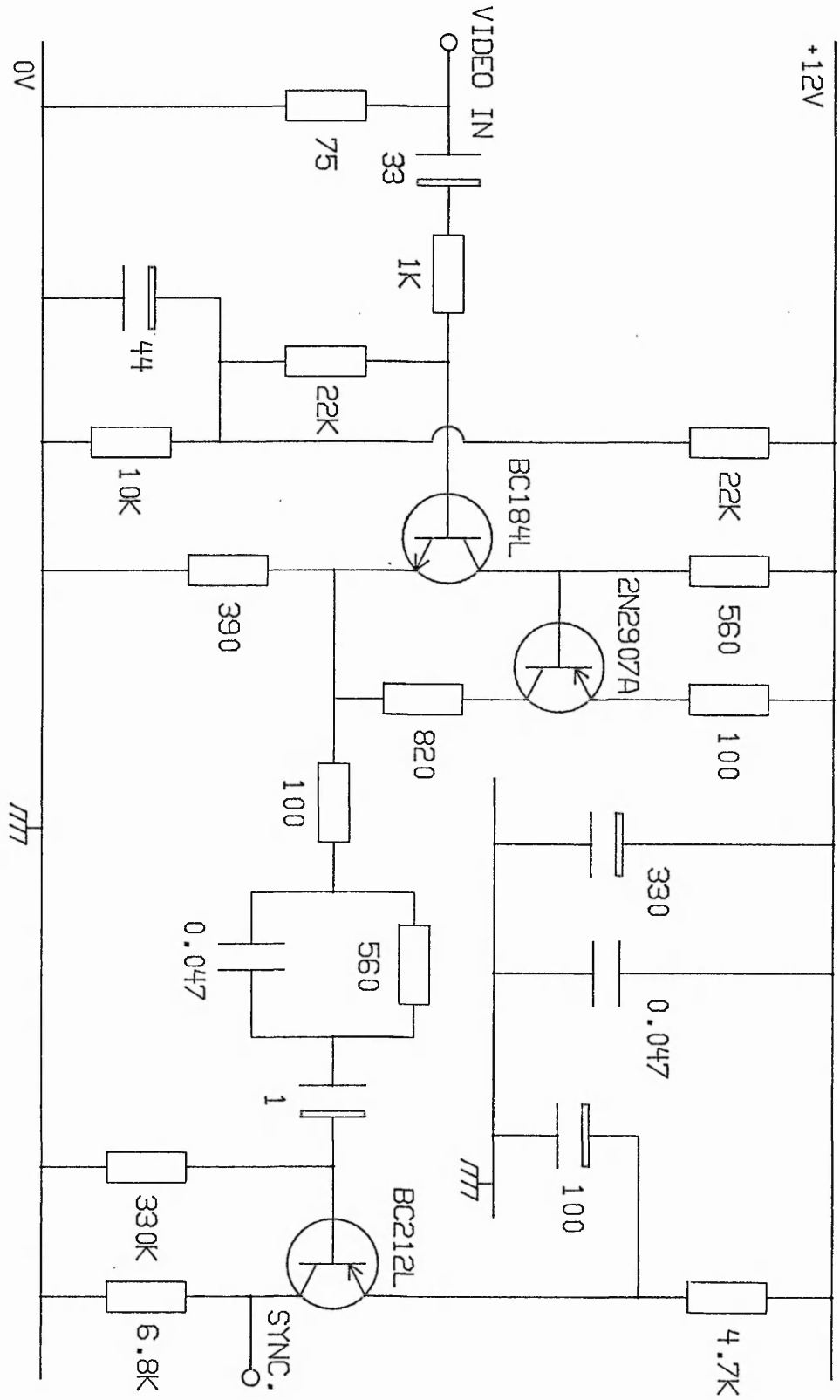

Appendix 5.1.2. (cont.)

Appendix 5.1.2(b).

FRAME sync. pulse separation circuit.

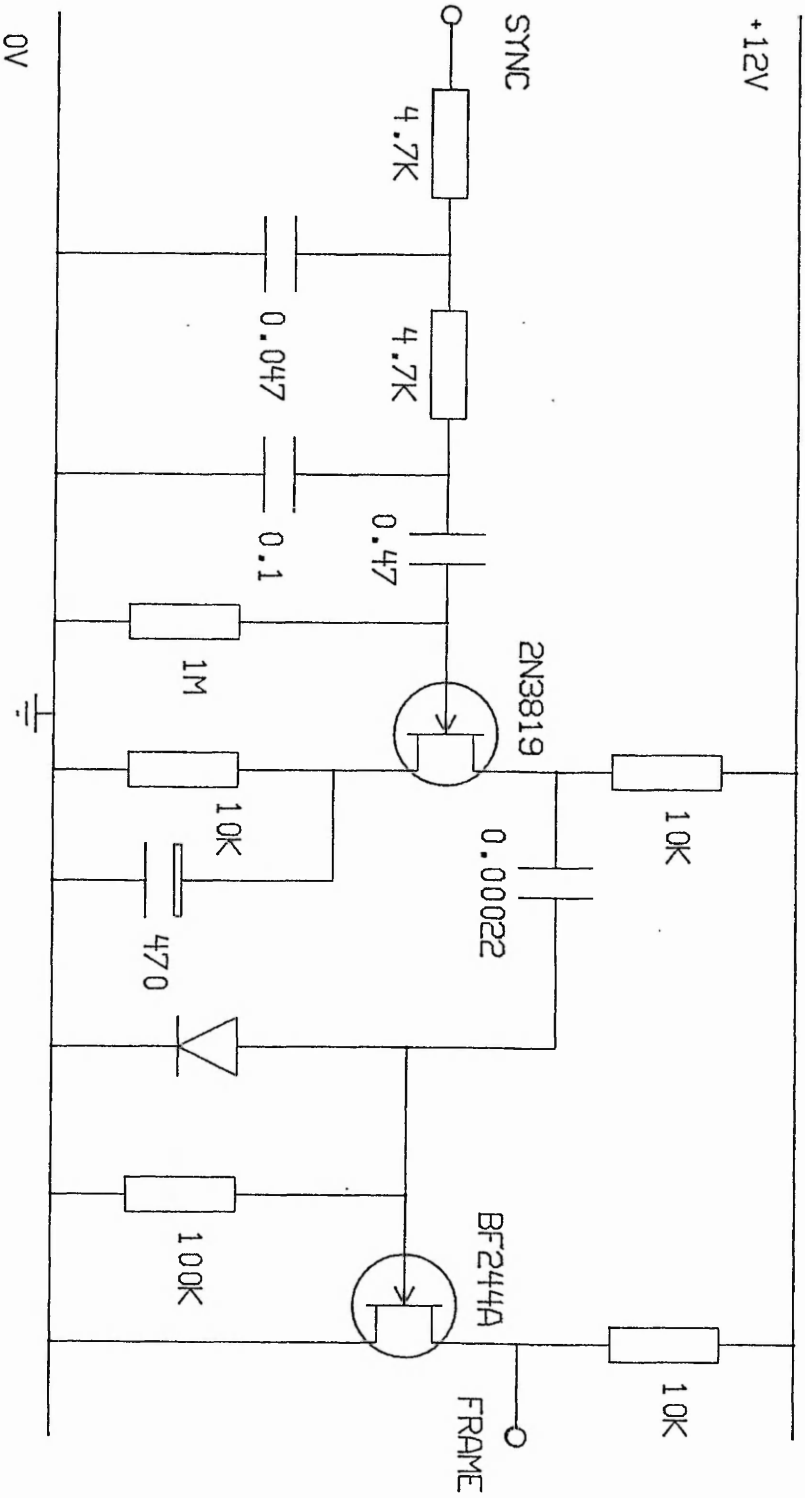

Appendix 5.1.3.

Appendix 5.1.3(a).

LINE selection circuit.

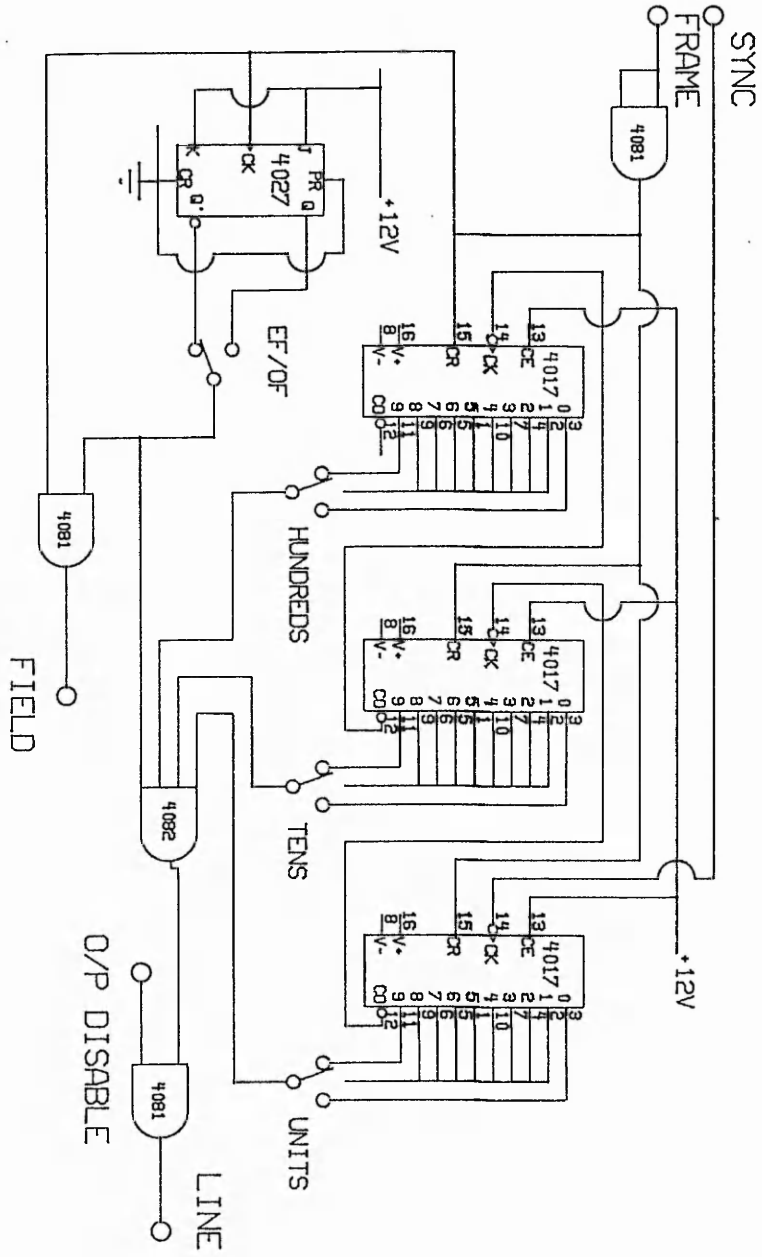

Appendix 5.1.3. (cont.)

Appendix 5.1.3(b).

Selection circuit for number of frames.

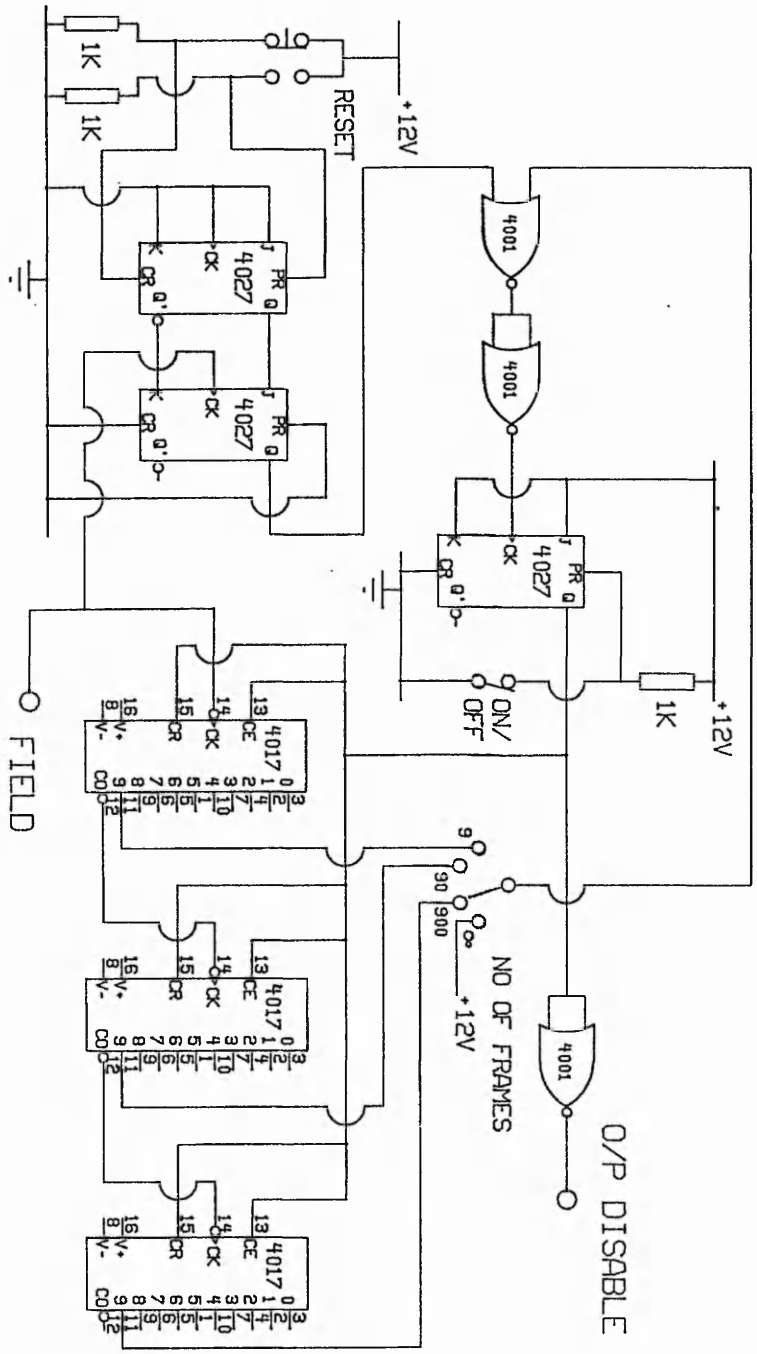

Appendix 5.1.4.

Analogue input circuit.

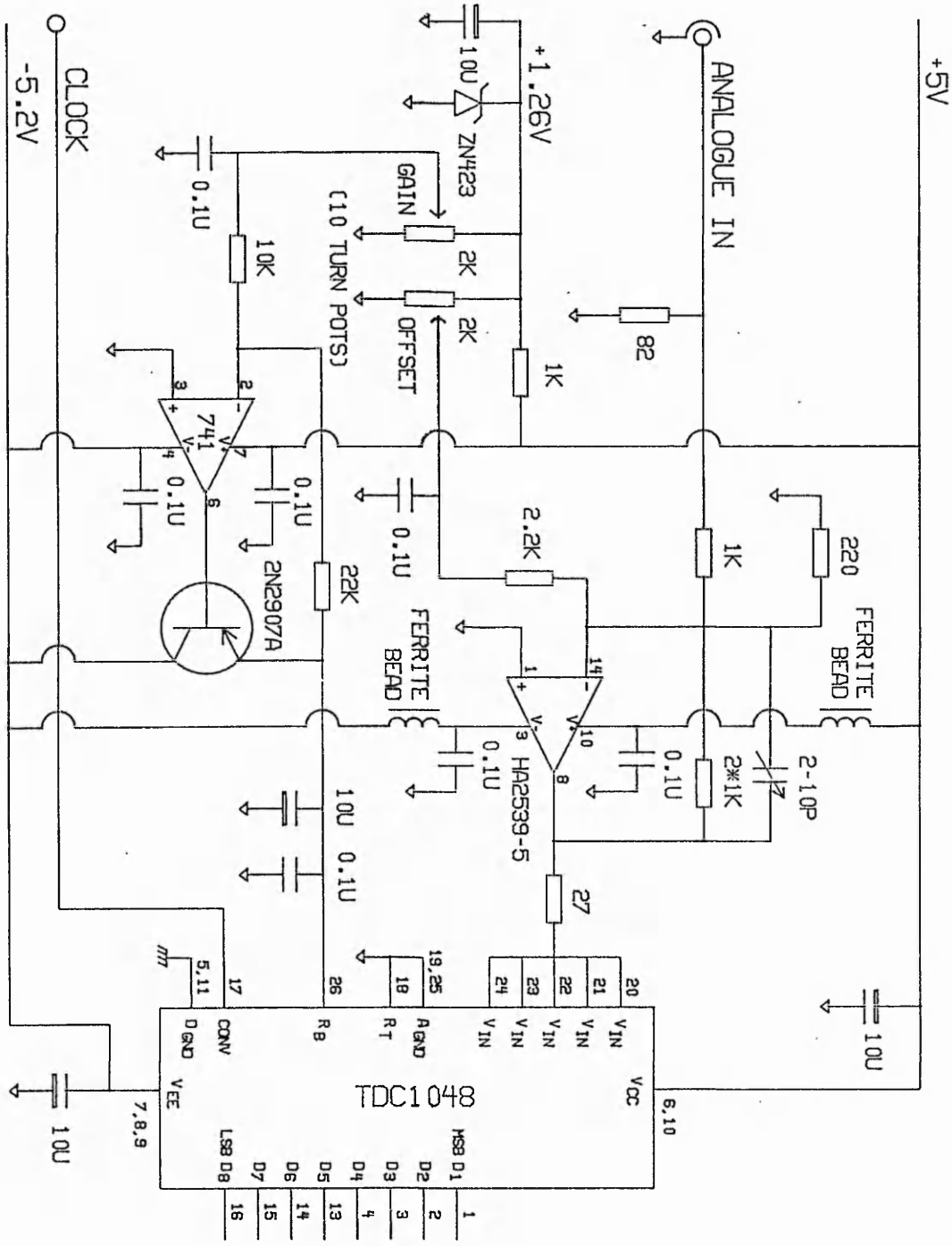

Appendix 5.1.5.

Multiplexer and external RAM circuit.

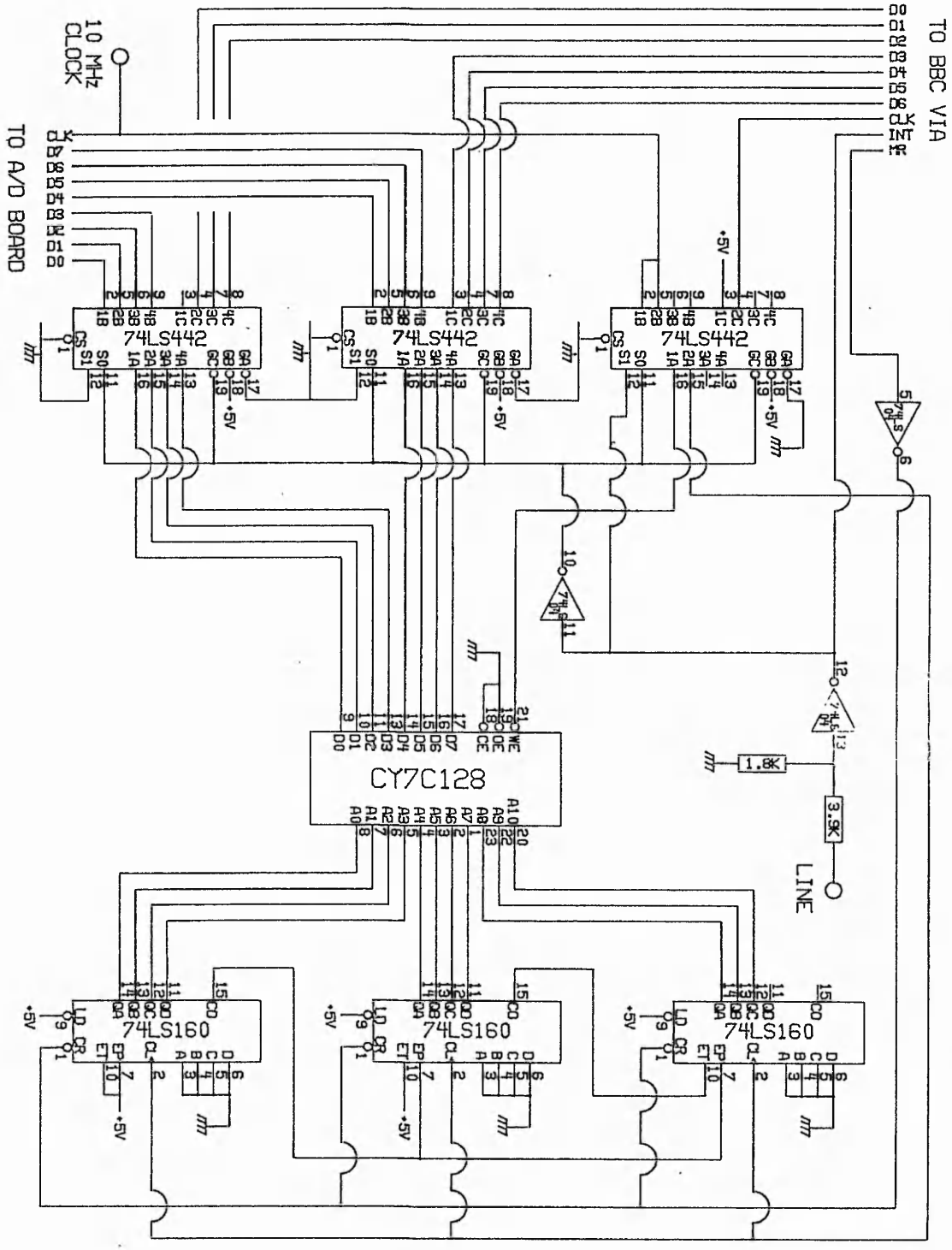

Appendix 5.1.6.

Video mixer circuit.

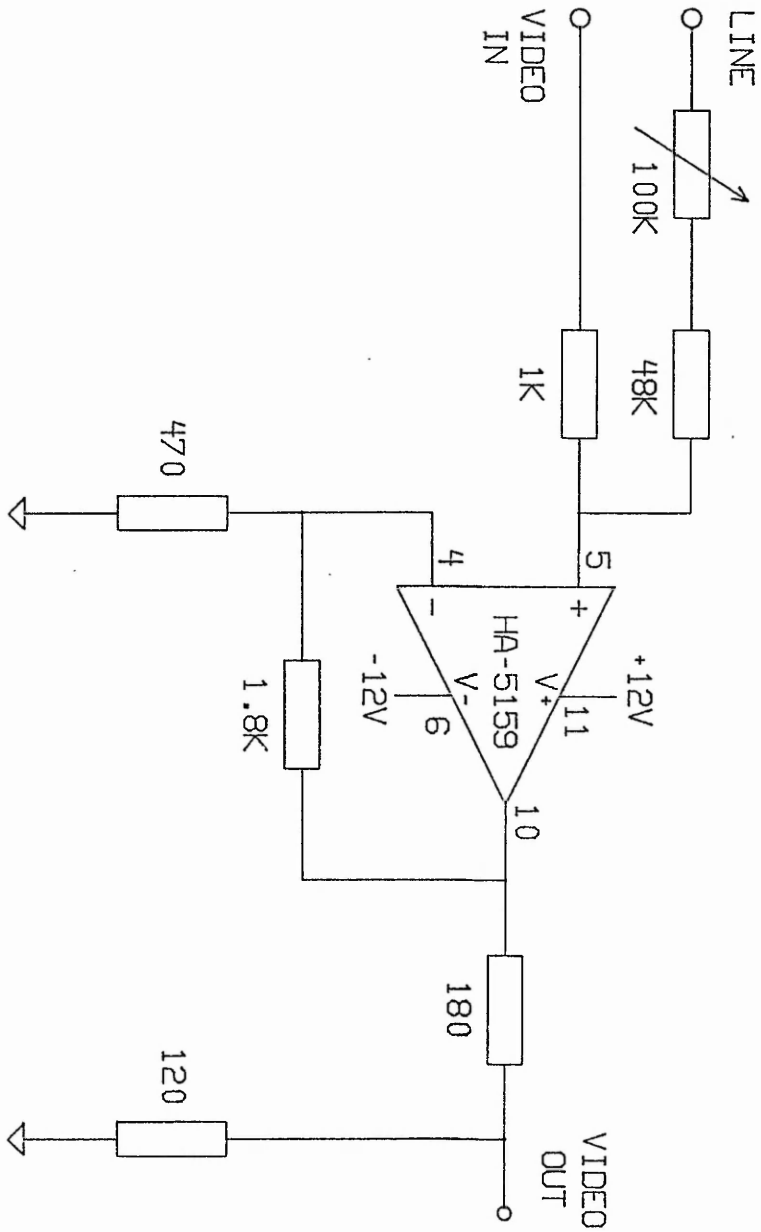

Appendix 5.2.

Timing diagram for RAM.

Read Cycle

Read from external RAM to BBC User port (VIA)

Control lines: $\overline{WE}$=1, $\overline{OE}$=0, $\overline{CE}$=0

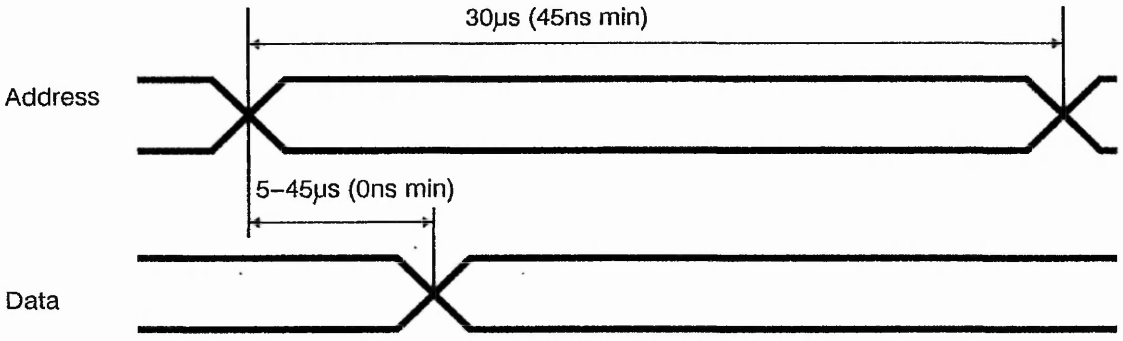

Write cycle

Write to external RAM from A/D convertor

Control lines $\overline{OE}$=0, $\overline{CE}$=0 ($\overline{WE}$ controlled)

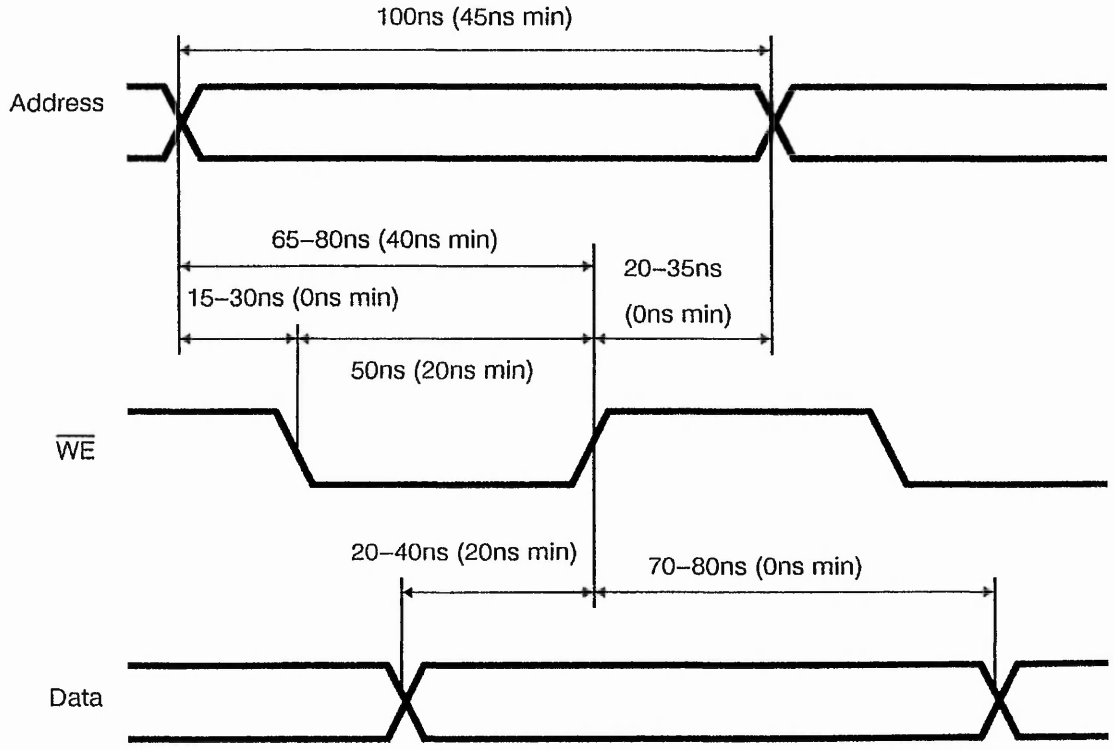

Appendix 5.3.

User Port (VIA) Status.

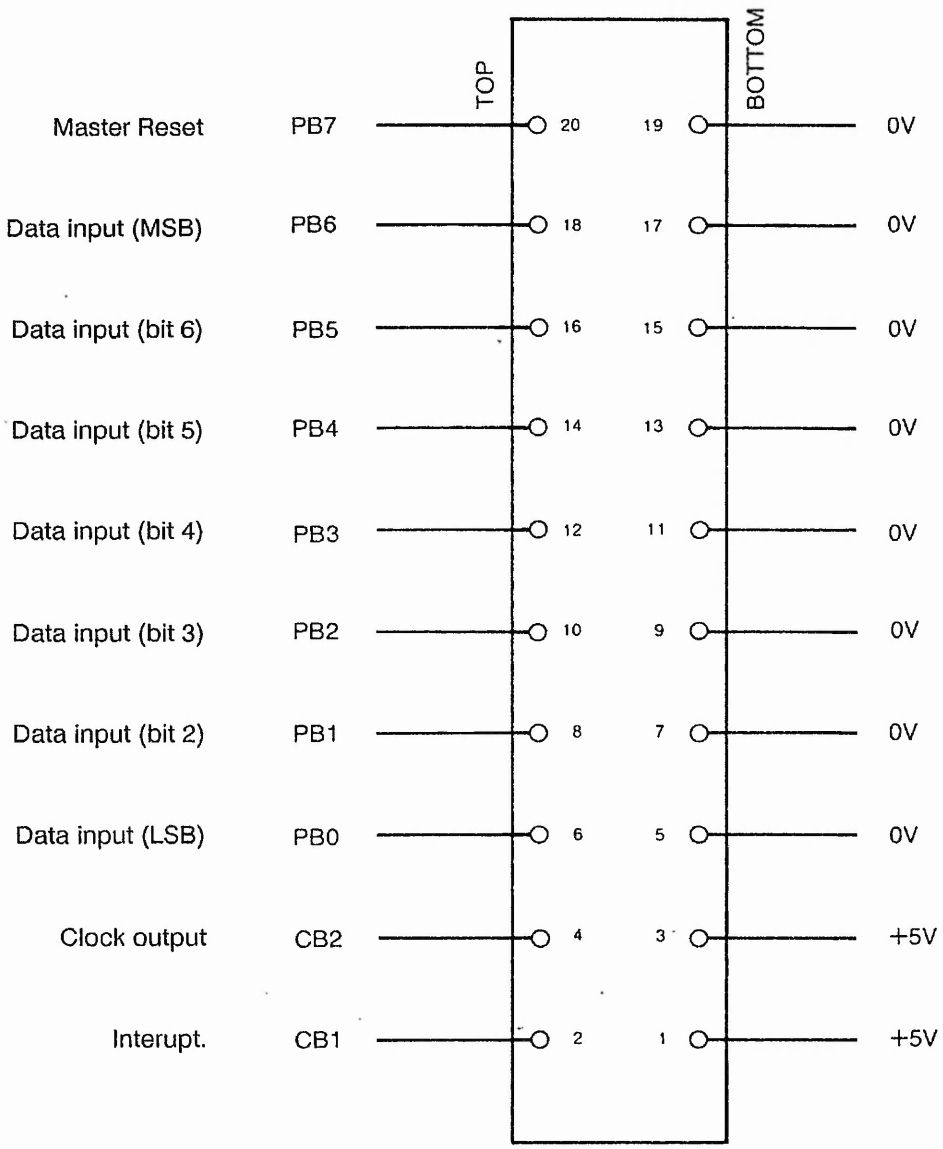

USER PORT CONNECTOR LOOKING INTO SOCKET MOUNTED ON THE MAIN CIRCUIT BOARD

Note—Pins 1 and 20 connect to the wires at the edge of the ribbon cable connected to the IDC header.

Appendix 5.4.

Memory map for BBC RAM.

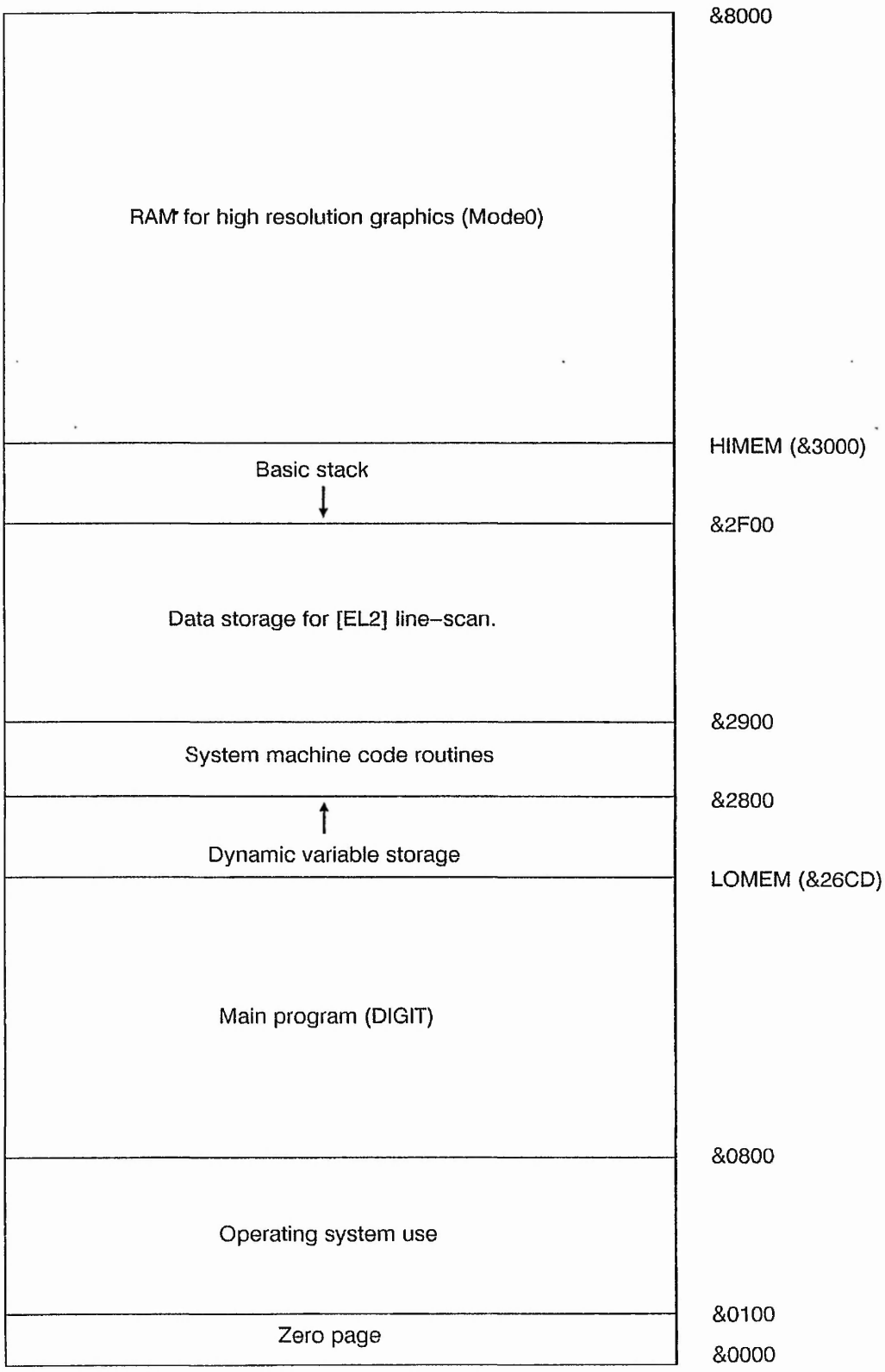

User locations in zero page.

Address	Routines using location	Usage
&70	LOAD2	Interupt variable
&71	LOAD2	Line counter
&72	ADD and LOAD2	00 – LSB of Start of data storage (2900 hex)
&73	ADD and LOAD2	29 – MSB of start of data storage (2900 hex)
&74	ADD and DIVIDE	00 – LSB of start of data storage (3000 hex)
&75	ADD and DIVIDE	30 – MSB of start of data storage (3000 hex)
&76	DIVIDE	Register
&77	DIVIDE	Register
&78	DIVIDE	Register
&79	DIVIDE	Register
&7A	DIVIDE	Register
&7B	DIVIDE	Register
&7C	DIVIDE	Register
&7D	DIVIDE	Register
&7E	DIVIDE	Loop counter
&7F		
&80	NSDUMP	LSB of 2FFF (hex) =FF
&81	NSDUMP	MSB of 2FFF (hex) = 2F
&82		
&83	NSDUMP	Temporary character store
&84	NSDUMP	Temporary character store
&85	NSDUMP	Temporary character store
&86	NSDUMP	Temporary character store
&87	NSDUMP	Temporary character store
&88	NSDUMP	Temporary character store
&89	NSDUMP	Temporary character store
&8A	NSDUMP	Temporary character store
&8B		
&8C		
&8D	NSDUMP	Bit mask
&8E	NSDUMP	Number of characters (counter)
&8F	NSDUMP	Number of lines (counter)

APPENDIX 5.5.

Appendix 5.5.1.

Program listing for "DIGIT"

Appendix 5.5.2

Program listing for "MCDPNEC"

Appendix 5.5.3

Program listing for "MCLOAD2"

Appendix 5.5.4

Program listing for "AVERAGE"

Appendix 5.5.5

Program listing for "DIVIDE"

Appendix 5.5.6

Program listing for "EL2"

Appendix 5.5.7.

Program listing for "FLUCTS"

Appendix 5.5.1.

Program listing for "REMDIG", a version of "DIGIT" with REM statements. "REMDIG" will not run as it takes up too much memory when loaded into the BBC RAM.

```
100 REM REMDIG 25.2.88
110 DIM SCALE(4)
120   REM Start of menu routine
130   REM
140 CLS:MODE4
150 PRINT"           MENU"
160 PRINT"           ----"
170 PRINT:PRINT
180 PRINT"  R  RUN data acquisition programme":PRINT
190 PRINT"  D  DISPLAY linescan":PRINT
200 PRINT"  G  Display GRAPH of [EL2]":PRINT
210 PRINT"  M  MODIFY Display":PRINT
220 PRINT"  S  SAVE linescan on disc":PRINT
230 PRINT"  L  LOAD linescan from disc":PRINT
240 PRINT"  C  CATALOGUE":PRINT
250 PRINT"  N  Drive NUMBER":PRINT
260 PRINT"  A  AVERAGE 8 Scans":PRINT
270 PRINT"  B  Remove BACKGROUND":PRINT
280 PRINT"  E  Calculate [EL2]":PRINT
290 PRINT"  F  Calculate [EL2] FLUCTUATIONS"
300 AN$=GET$
310 IF AN$="R" THEN 460
320 IF AN$="D" THEN 970
330 IF AN$="G" THEN 930
340 IF AN$="M" THEN 710
350 IF AN$="S" THEN 1440
360 IF AN$="L" THEN 1560
370 IF AN$="C" THEN 1770
380 IF AN$="N" THEN 1730
390 IF AN$="A" THEN 2000
400 IF AN$="B" THEN 2030
410 IF AN$="E" THEN 2060
420 IF AN$="F" THEN 2090
430 GOTO300
440   REM Data aquisition programme
450   REM
460 CLS:CLG
470 PRINT"Please wait"
480 REM Interupt variable "go", "set" when = 0
490 go=&70
500 REM Set to no interupt as yet
510 ?go=1
520 REM Counter "line" for number of scans averaged
530 line=&71
540 REM Number of scans =256
550 ?line=&FF
560 REM Set interupt vector to start of handling routine, &2842
570 ?&206=&42
580 ?&207=&28
590 REM Load "MCLOAD2" at &2800
600 *LOAD"MCLOAD2" 2800
610 REM Call start of initialisation routine .init (&2800)
620 CALL &2800
630 REM Call .run (adds scan to average if interupt has occured)
640 CALL &2861
650 REM If number of scans averaged = 256 then exit to menu
660 IF ?line=0 THEN 140
670 GOTO 640
680   REM Display Block
690   REM
700 REM Start of modify routine
710 CLS
```

Appendix 5.5.1. (cont.)

```
  720 REM Choose horizontal scale factor and offset
  730 INPUT"Horizontal Mag.=";HM
  740 PRINT
  750 REM SC= horizontal scale factor
  760 SC=2%HM
  770 PRINT"Horizontal Offset"
  780 INPUT"0 to 7 (eighths)";HO
  790 REM B%= data offset in RAM
  800 B%=(&2999)+HO%1152/8
  810 PRINT
  820 REM Select vertical scale factor and offset
  830 INPUT"Vertical Mag.=";VM
  840 REM VS= vertical scale factor
  850 VS=0.03125%VM
  860 PRINT
  870 PRINT"Vertical Offset"
  880 INPUT"0 to 7 (eighths)";VO
  890 REM H%= vertical screen offset
  900 H%=VO%1024/8
  910 GOTO 1010
  920 REM Set conditions for EL2 scan
  930 E%=1:CLS
  940 VM=1:VO=0
  950 GOTO 990
  960 REM Set conditions for linescan
  970 E%=0
  980 REM Full screen default values fo SC,H%,VS,B%
  990 SC=2:H%=0:VS=0.03125:B%=&2999
 1000 REM High resolution graphics 256 x 640
 1010 MODE0:CLS:CLG::M%=&70:P%=&60:N%=1152:Q%=&4F0:R%=&4FF
 1020 REM QUEST$="Y" will give screen dump
 1030 INPUT"DO YOU WANT A HARD COPY Y/N ";QUEST$
 1040 REM Hit RETURN if title not required
 1050 INPUT"TITLE";TITLE$
 1060 CLS: PROCgraph
 1070 REM Hit any key to return to menu
 1080 X=GET: GOTO 140
 1090   REM Plots linescan / EL2 scan with axes
 1100 DEF PROCgraph
 1110 CLG
 1120 REM Plot axes
 1130 MOVEP%,0:DRAWM%,0:MOVEP%,&80:DRAWM%,&80:MOVEP%,&100:DRAWM%,&100:MOVEP%,&18
0:DRAWM%,&180:MOVEP%,&200:DRAWM%,&200:MOVEP%,&280:DRAWM%,&280:MOVEP%,&300:DRAWM%
,&300:MOVEP%,&380:DRAWM%,&380:MOVEP%,&3FF:DRAWM%,&3FF:DRAWM%,0:DRAWR%,0
 1140 MOVEQ%,&80:DRAWR%,&80:MOVEQ%,&100:DRAWR%,&100:MOVEQ%,&180:DRAWR%,&180:MOVE
Q%,&200:DRAWR%,&200:MOVEQ%,&280:DRAWR%,&280:MOVEQ%,&300:DRAWR%,&300:MOVEQ%,&380:
DRAWR%,&380:MOVER%,&3FF:DRAWQ%,&3FF:DRAWQ%,0:MOVEM%,0
 1150 REM Plot linescan / EL2 scan
 1160 FORA%=0TON%STEP2:Y%=(?(A%+B%)%256+?(A%-1+B%)-H%%32)%VS:X%=(A%/2)%SC+M%:DRA
WX%,Y%:NEXT
 1170 REM Write text at graphics curser
 1180 VDU5
 1190 REM Do not print [EL2] scales for linescan
 1200 IF E%=0 THEN 1260
 1210 REM Calculate [EL2] scales
 1220FOR N=1 TO 4:SCALE(N)=(N/(2%VM))+VO/4:NEXT
 1230 REM Print [EL2] scales
 1240 @%=&20304:MOVE0,&3FF:PRINT SCALE(4):MOVE0,&30C:PRINT SCALE(3):MOVE0,&20C:P
RINT SCALE(2):MOVE0,&10C:PRINT SCALE(1):@%=10
 1250 REM If title$ is empty then do not print titles
 1260 IF TITLE$="" THEN 1330
 1270 REM Do not print [EL2] for linescan
 1280 IF E%=0 THEN 1310
 1290 REM Print titles
 1300 MOVE&90,&3FF:PRINT"[EL2]x10^16"
 1310 MOVE&200,&3FF:PRINT TITLE$
 1320 REM Write text at text curser
 1330 VDU4
 1340 IF QUEST$="Y" THEN PROCSDUMP
 1350 ENDPROC
 1360   REM NEC screen dump
 1370 DEFPROCSDUMP
 1380 REM Run machine code dump routine "MCDPNEC"
 1390 %RUN "MCDPNEC"
 1400 ENDPROC
```

Appendix 5.5.1. (cont.)

```
1410   REM Load/Save block
1420   REM
1430 REM Start of save
1440 CLS
1450 PRINT"              SAVE"
1460 PRINT"              ----"
1470 REM Do a %DRIVE(D%)
1480 PROCDRIVE
1490 REM Input filename to save
1500 INPUT" INPUT Filename (7 char max)"; file$
1510 REM Save &2900 to &2F00
1520 F$="SAVE "+file$+" 2900 2F00"
1530 REM Jump to PROCCLI
1540 GOTO 1650
1550 REM Start of load
1560 CLS
1570 PRINT"              LOAD"
1580 PRINT"              ----"
1590 REM Do a %DRIVE(D%)
1600 PROCDRIVE
1610 REM Input filename to load
1620 INPUT" INPUT Filename (7 char max)"; file$
1630 F$="LOAD "+file$
1640 REM Do a %LOAD/%SAVE
1650 PROCCLI
1660 REM Reset to drive 0
1670 %DRIVE0
1680 REM Return to main menu
1690 GOTO 140
1700   REM Drive number block
1710   REM
1720 REM D% contains current drive
1730 CLS : INPUT"INPUT DRIVE NUMBER 1-7";D%
1740 GOTO140
1750   REM Catalogue block
1760   REM
1770 CLS : INPUT"DRIVE NUMBER";N
1780 N$=STR$(N)
1790 F$="C."+N$
1800 REM Do a "%C.(N$)"
1810 PROCCLI
1820 REM Hit any key to return to menu
1830 X=GET : GOTO140
1840   REM Constructs F$ from "DRIVE(D$)"
1850 DEFPROCDRIVE
1860 drive$=STR$(D%)
1870 F$="DRIVE"+drive$
1880 PROCCLI
1890 ENDPROC
1900   REM Sends F$ to command line interpreter
1910 DEFPROCCLI
1920 DIM F 30
1930 $F=F$
1940 X%=F MOD 256
1950 Y%=F DIV 256
1960 CALL&FFF7
1970 ENDPROC
1980   REM Average block
1990   REM
2000 CHAIN"AVERAGE"
2010   REM Divide block
2020   REM
2030 CHAIN"DIVIDE"
2040   REM EL2 block
2050   REM
2060 CHAIN"EL2"
2070   REM Sigma block
2080   REM
2090 CHAIN"SIGMA"
```

Appendix 5.5.2.

Progam listing for "DUMPNEC" compiled as "MCDPNEC"

```
100 REM DUMPNEC 24.2.88
110 DIMGAP% 550:FORK=0TO2STEP2:P%=GAP%
120 [OPTK%
130 .DUMP
140       LDA£2:JSR&FFEE              \ VDU2
150       LDA£1:JSR&FFEE              \ Set line spacing to (16/144)"
160       LDA£27:JSR&FFEE
170       LDA£1:JSR&FFEE
180       LDA£84:JSR&FFEE
190       LDA£1:JSR&FFEE
200       LDA£&31:JSR&FFEE
210       LDA£1:JSR&FFEE
220       LDA£&36:JSR&FFEE
230       LDA£1:JSR&FFEE              \ Single directional print
240       LDA£27:JSR&FFEE
250       LDA£1:JSR&FFEE
260       LDA£62:JSR&FFEE
270       LDA£&FF:STA&80              \ Load &2FFF to &81,&80
280       LDA£&2F:STA&81              \ Screen start at &3000
290       LDA£32:STA&8F               \ Number of lines
300 .DN
310        LDA£80:STA&8E              \ Number of characters per line
320        LDA£1:JSR&FFEE             \ Dot image graphics
330        LDA£27:JSR&FFEE            \ 640 bytes of data
340        LDA£1:JSR&FFEE
350        LDA£83:JSR&FFEE
360        LDA£1:JSR&FFEE
370        LDA£&30:JSR&FFEE
380        LDA£1:JSR&FFEE
390        LDA£&36:JSR&FFEE
400        LDA£1:JSR&FFEE
410        LDA£&34:JSR&FFEE
420        LDA£1:JSR&FFEE
430        LDA£&30:JSR&FFEE
440        LDA£0
450        BEQDG
460 .DJ    BNEDN
470 .DG                                \ Character load loop
480         LDY£8
490 .DT
500          LDX£8
510          LDA£1:STA&8D              \ Bit mask
520 .DP
530           ASL&82,X                 \ Storage locations
540           LDA(&80),Y               \ Screen byte
550           AND&8D
560           BEQDQ
570           INC&82,X
580 .DQ
590           ASL&8D
600           DEX:BNEDP
610          DEY
620          BNEDT
630         LDX£0
```

Appendix 5.5.2. (cont.)

```
640 .DO                                 \ Character print loop
650           LDA#1:JSR&FFEE
660           LDA&83,X:JSR&FFEE
670           INX
680           CPX#8:BNEDO
690          CLC
700          LDA&80:ADC#8:STA&80        \ Next character
710          LDA&81:ADC#0:STA&81
720          DEC&8E:LDA&8E:BNEDG
730         LDA#1:JSR&FFEE
740         LDA#27:JSR&FFEE
750         LDA#1:JSR&FFEE
760         LDA#10:JSR&FFEE             \ Printer linefeed
770         LDA#1:JSR&FFEE
780         LDA#13:JSR&FFEE             \ Printer start of line
790         DEC&8F:BEQDZ:BNEDJ
800 .DZ
810        LDA#1:JSR&FFEE               \ Reset line spacing to (1/6)"
820        LDA#27:JSR&FFEE
830        LDA#1:JSR&FFEE
840        LDA#65:JSR&FFEE
850        LDA#3:JSR&FFEE               \ VDU3
860        RTS
870.FIN NOP
880 ]
890 NEXT
900 PRINT~DUMP:PRINT~FIN
```

Appendix 5.5.3.

Program listing for "LOAD2" compiled as "MCLOAD2"

```
100 REM LOAD2 24.2.88
110 MODE 3
120 REM Interupt variable "go" ( set when =0 )
130 go=&70
140 ?go=1
150 REM line counter "line"
160 line=&71
170 ?line=&FF
180 DIM M% 220
190 FOR opt%=0 TO 2 STEP 2
200 P%=M%
210 [
220 OPT opt%
230 .init SEI                   \ Disable interupts
240       LDA &FE6C             \ Set PCR for CB1,CB2
250       AND #&0F              \ CB1 Interupt positive edge
260       ORA #&D0
270       STA &FE6C
280       LDA #&90              \ Enable CB1 interupt
290       STA &FE6E
300       CLI
310       LDA #0                \ Set all outputs = 0
320       STA &FE60
330       LDA #&80              \ Set DDRB I/O conditions
340       STA &FE62             \ PB7 output
350       LDA #&29              \ Clear data memory space
360       STA &73               \ Data on pages &29-2F
370       LDA #0
380       STA &72
390       LDX #6
400       LDY #0
410 .loop   STA (&72),Y
420         INY
430         BNE loop
440        INC &73
450        DEX
460        BNE loop
470       LDA #&80              \ Master reset
480       ORA &FE60
490       STA &FE60
500       LDA #&7F
510       AND &FE60
520       STA &FE60
530       RTS                   \ Exit
```

Appendix 5.5.3. (cont.)

```
540 .int  LDA &FC          \ Do save....
550       PHA
560       TXA
570       PHA
580       TYA
590       PHA
600       LDA &FE6D        \ Get user VIA interupt status
610       AND #&90         \ Mask out bits not interested in
620       CMP #&90         \ Is it a CB1 interupt ?
630       BNE exit         \ If not, exit
640       STA &FE6D        \ Clear interupt
650       LDA#0
660       STA go
670 .exit PLA              \ Restore registers...
680       TAY
690       PLA
700       TAX
710       PLA
720       STA &FC
730       RTI
740 .run  LDA go
750       BNE end
760       LDA line         \ Has line count finished
770       BEQ end          \ If so end
780       LDA #&80         \ Master reset
790       ORA &FE60
800       STA &FE60
810       LDA #&7F
820       AND &FE60
830       STA &FE60
840       LDA #0
850       STA &72          \ Start of input routine
860       LDA #&29         \ Data on pages &29-2F
870       STA &73
880       LDX #6
890       LDY #0
900 .loop2  CLC
910         LDA &FE60      \ Load input
920         ADC (&72),Y    \ Add to existing data
930         STA (&72),Y    \ Store result
940         INY            \ Loop counter
950         LDA #0
960         ADC (&72),Y    \ Add carry to adjacent byte
970         STA (&72),Y    \ Store result
980         LDA &FE6C      \ Clock counter on RAM
990         ORA #&20
1000        STA &FE6C
1010        AND #&DF
1020        STA &FE6C
1030        INY            \ Loop counter
1040        BNE loop2
1050      INC &73          \ New page of memory
1060      DEX              \ 2nd loop counter
1070      BNE loop2
1080      LDA #&80         \ Master reset
1090      ORA &FE60
1100      STA &FE60
1110      LDA #&7F
1120      AND &FE60
1130      STA &FE60
1140      DEC line         \ Check line counter
1150      BNE end
1160      LDA #&10         \ Disable CB1 interupt
1170      STA &FE6E
1180 .end  LDA#1
1190       STA go
1200       RTS
1210 .fin  NOP
1220 ]
1230 NEXT opt%
1240 PRINT~init:PRINT~fin:PRINT~run:PRINT~int
```

Appendix 5.5.4.

Program listing for "AVERAGE"

```
100 REM AVERAGE 24.2.88
110 REM D% contains current drive number
120 D$=STR$(D%)
130 MODE4:CLS
140  REM Run assembler routine add
150 PROCADD
160  REM Clear pages &29 to &2F
170 CALL setup
180  REM Do a *DRIVE(D%)
190 G$="DRIVE"+D$
200 PROCCLI
210  REM Input the 8 scans to average
220 FOR X=1 TO 8
230  REM Input scan on pages &30 to &35
240 INPUT"INPUT FILENAME ";F$
250 G$="LOAD "+F$+" 3000"
260 PROCCLI
270  REM Call aver (average) machine code subroutine
280 REM Divides scan by 8 and stores result in &29 to &2F
290 CALL aver
300 NEXT
310 REM Reset to drive 0
320 *DRIVE0
330  REM Reload main programme
340 CHAIN"DIGIT"
350   REM
360 DEFPROCCLI
370 REM Send string G$ to command line interpreter
380 DIM G 30
390 $G=G$
400 X%=G MOD 256
410 Y%=G DIV 256
420 CALL&FFF7
430 ENDPROC
440   REM
450 DEFPROCADD
460 REM Assembler routine to add 8 scans
470 DIM M%150
480 FOR opt%=0 TO 2 STEP 2
490 P%=M%
500 [
510 OPT opt%
520.setup NOP
530 LDA#&29             \ Clear pages &29 to &2F
540 STA&73
550 LDA#0
560 STA&72
570 LDX#6
580 LDY#0
590.loop1 STA(&72),Y
600       INY
610       BNE loop1
620     INC&73
630     DEX
640     BNE loop1
650 RTS
```

Appendix 5.5.4. (cont.)

```
660.aver NOP
670 LDA£&29
680 STA&73
690 LDA£&30
700 STA&75
710 LDA£0
720 STA&72
730 STA&74
740 LDX£6
750 LDY£0
760.loop CLC
770      INY
780      LDA(&74),Y     \ Divide two byte data by two
790      LSR A
800      STA(&74),Y
810      DEY
820      LDA(&74),Y
830      ROR A
840      STA(&74),Y
850      INY
860      LDA(&74),Y     \ Divide two byte data by two
870      LSR A
880      STA(&74),Y
890      DEY
900      LDA(&74),Y
910      ROR A
920      STA(&74),Y
930      INY
940      LDA(&74),Y     \ Divide two byte data by two
950      LSR A
960      STA(&74),Y
970      DEY
980      LDA(&74),Y
990      ROR A
1000     CLC
1010     ADC(&72),Y     \ Add data divided by eight to running total
1020     STA(&72),Y
1030     INY
1040     LDA(&74),Y
1050     ADC(&72),Y
1060     STA(&72),Y
1070     INY
1080     BNE loop
1090    INC&73
1100    INC&75
1110    DEX
1120    BNE loop
1130    RTS
1140.fin NOP
1150 ]
1160 NEXT optX
1170 ENDPROC
```

Appendix 5.5.5.

Program listing for "DIVIDE"

```
100 REM DIVIDE 24.2.88
110 MODE4:CLS
120  REM Do a *DRIVE(D%)
130 REM D% contains current drive number
140 D$=STR$(D%)
150 G$="DRIVE"+D$
160 PROCCLI
170  REM *LOAD linescan and background
180 INPUT"INPUT BACKGROUND FILENAME";F$
190 REM Load to &3000
200 G$="LOAD "+F$+" 3000"
210 PROCCLI
220 INPUT"INPUT LINESCAN FILENAME";F$
230 REM Load to &2900 (default)
240 G$="LOAD "+F$
250 PROCCLI
260  REM Run division routine
270 PROCDIV
280  REM Call division routine
290 CALL start
300 REM Reset to drive 0
310 *DRIVE0
320  REM Reload main programme
330 CHAIN"DIGIT"
340 END
350   REM
360 DEFPROCDIV
370 REM Assembler routine to divide linescan by background
380 DIM M% 200
390 FOR opt%=0 TO 2 STEP 2
400 P%=M%
410 [
420 OPT opt%
430 .start LDA#0
440        STA&72            \ 0 to LSB data start (scan)
450        STA&74            \ 0 to LSB data start (back)
460        STA&78            \ 0 to X3
470        STA&7B            \ 0 to Y3
480        STA&7C            \ 0 to Z1
490        STA&7D            \ 0 to Z2
500        LDA#&29
510        STA&73            \ 0 to MSB data start (scan)
520        LDA#&30
530        STA&75            \ 0 to MSB data start (back)
540        LDY#0
550        LDX#6             \ 6 pages of data
560 .loop      LDA(&74),Y
570            STA&7A        \ LSB (back) to Y2
580            LDA(&72),Y
590            STA&77        \ LSB (scan) to X2
600            INY
610            LDA(&72),Y
620            STA&76        \ MSB (scan) to X1
630            LDA(&74),Y
640            CMP#0         \ If MSB (back)=0 then set to 1
650            BNE hop
660              LDA#1
```

Appendix 5.5.5. (cont.)

```
 670 .hop        STA&79          \ MSB (back) to Y1
 680             ASLA            \ Y1%2
 690             CMP&76
 700             BCS skip        \ If Y1%2>=X1 then skip
 710               LDA#&FF
 720               STA&7C        \ Otherwise set Z1=FF & save Z
 730               SEC           \ SEC ready for ROR Z
 740               JMP save
 750 .skip       LDA#16          \ Loop counter for divide
 760             STA&7E
 770 .loop2        CLC
 780               LDA&76
 790               CMP&79
 800               BCC jump          \ If X1<Y1 then jump
 810                 BNE setZ        \ If X1<>Y1 then setZ
 820                   LDA&77        \ If X1=Y1 then CMP X2 & Y2
 830                   CMP&7A
 840                   BCC jump      \ If X2<Y2 then jump
 850                   BNE setZ      \ If X2<>Y2 then setZ
 860                   LDA&78        \ If X2=Y2 then CMP X3 & Y3
 870                   CMP&7B
 880                   BCC jump      \ If X3<Y3 then jump
 890 .setZ             SEC
 900                   LDA&78    \ LSB     |
 910                   SBC&7B    \         |
 920                   STA&78    \         |
 930                   LDA&77    \         |
 940                   SBC&7A    \         | X-Y=Xnew
 950                   STA&77    \         |
 960                   LDA&76    \ MSB     |
 970                   SBC&79    \         |
 980                   STA&76    \         |
 990                   SEC
1000 .jump           ROL&7D       \ ROL Z
1010                 ROL&7C
1020                 LSR&79       \ ROR Y
1030                 ROR&7A
1040                 ROR&7B
1050                 DEC&7E       \ DEC divide loop counter
1060                 BNE loop2
1070               CLC
1080 .save         LDA&7C
1090               RORA           \ ROR to standardise plot
1100               STA(&72),Y     \ Store MSB of result
1110               DEY
1120               LDA&7D
1130               RORA
1140               STA(&72),Y     \ Store LSB of result
1150               INY
1160               INY
1170               BNE loop
1180             INC&73
1190             INC&75
1200             DEX
1210             BNE loop
1220           RTS
1230 ]
1240 NEXT opt%
1250 ENDPROC
1260   REM
1270 DEFPROCCLI
1280 REM Send sting G$ to command line interpreter
1290 DIM G 30
1300 $G=G$
1310 X%=G MOD 256
1320 Y%=G DIV 256
1330 CALL&FFF7
1340 ENDPROC
```

Appendix 5.5.6.

Program listing for "EL2"

```
  100 REM EL2 24.2.88
  110 MODE0:CLS
  120 REM Set default left and right edges
  130 XL=0:XR=1152
  140   REM INPUT calibration information
  150 REM D=Thickness of sample
  160 INPUT"D (mm)";D
  170 REM T1,T2 = 1um,2um transmission
  180 INPUT"T2";T2
  190 INPUT"T1";T1
  200   REM Calibrate linescan for [EL2]
  210 CLS
  220 PRINT"Place cross on calibration point"
  230 PROCGRAPH
  240 REM Disable curser
  250 *FX4,1
  260 PROCCROSS
  270 T=Y%
  280 INPUT"TRIM EDGES N";T$
  290 IF.T$="N" THEN 420
  300   REM Tidy left and right edges
  310 PRINT"Left edge"
  320 PROCCROSS
  330 XL=X%
  340 FOR N=0 TO (XL+2): ?(&2998+N)=0: NEXT
  350 PRINT"Right edge"
  360 PROCCROSS
  370 XR=X%
  380 REM Enable curser
  390 *FX4,0
  400 FOR N=(XR+2) TO 1536:?(&2998+N)=0:NEXT
  410   REM Calculate [EL2] scan from left edge to right edge
  420 X=XL
  430 REPEAT:X=X+2:IF ?(&2900+X)=0 THEN ?(&2900+X)=1
  440 EL2=(LN(T2*T*32/T((?(&2999+X)*256+?(&2998+X))*T1)))*114688/D:?(&2998+X)=EL2
MOD256:?(&2999+X)=EL2 DIV256:UNTIL X=XR
  450 CHAIN"DIGIT"
  460 END
  470   REM
  480 DEFPROCGRAPH
  490 REM Plots linescan on screen
  500 SC=2:H%=0:VS=0.03125:B%=&2999:M%=0:N%=1152
  510 MOVE M%,0
  520 FOR A%=0 TO N% STEP 2 :Y%=(?(A%+B%)*256+?(A%+B%-1))*VS: X%=(A%/2)*SC+M% :
DRAW X%,Y% : NEXT
  530 ENDPROC
  540   REM
```

Appendix 5.5.6. (cont.)

```
550 DEFPROCCROSS
560 REM Plots and moves curser on screen
570 X%=40:Y%=500
580 PROCPLOT
590 REPEAT
600 A=GET
610 IF A=136 THEN PROCBACK
620 IF A=137 THEN PROCFORWARD
630 IF A=138 THEN PROCDOWN
640 IF A=139 THEN PROCUP
650 UNTIL A=13
660 ENDPROC
670   REM
680 DEFPROCBACK
690 REM Moves cross to left (slow)
700 PROCPLOT
710 IF X%<-25 THEN X%=X%+1280
720 X%=X%-2
730 PROCPLOT
740 ENDPROC
750   REM
760 DEFPROCFORWARD
770 REM Moves cross to right (fast)
780 PROCPLOT
790 X%=X%+20
800 IF X%>1254 THEN X%=X%-1280
810 PROCPLOT
820 ENDPROC
830   REM
840 DEFPROCDOWN
850 REM Moves cross down (slow)
860 PROCPLOT
870 Y%=Y%-2
880 IF Y%<0 THEN Y%=Y%+1024
890 PROCPLOT
900 ENDPROC
910   REM
920 DEFPROCUP
930 REM Moves cross up (fast)
940 PROCPLOT
950 Y%=Y%+20
960 IF Y%>1023 THEN Y%=Y%-1024
970 PROCPLOT
980 ENDPROC
990   REM
1000 DEFPROCPLOT
1010 REM Plots cross at X%,Y%
1020 PLOT 4,X%,Y%
1030 PLOT 2,25,0
1040 PLOT 0,-25,25
1050 PLOT 2,0,-50
1060 PLOT 0,-25,25
1070 PLOT 2,25,0
1080 ENDPROC
```

Appendix 5.5.7.

Program listing for "SIGMA" refered to in the text as "FLUCTS"

```
  100 REM SIGMA 24.2.88
  110 MODE0:CLS
  120  REM Plot EL2 scan on screen
  130 PROCGRAPH
  140  REM Find left (XMIN) and right (XMAX) points for best fit line
  150 *FX4,1
  160 PRINT"Move cross to left hand point"
  170 PROCCROSS
  180 XMIN=X%
  190 PRINT"Move cross to right hand point"
  200 PROCCROSS
  210 REM Enable curser
  220 *FX4,0
  230 XMAX=X%
  240 REM N=Number of data points
  250 N=(XMAX-XMIN)/2
  260 REM SX,SY2,SXY=Sum of x,y squared,x.y etc
  270 SX=0:SY=0:SX2=0:SY2=0:SXY=0
  280  REM Calculate SX,SX2,SXY,SY,SY2 for data points
  290 X=XMIN
  300 REPEAT:X=X+2
  310 SX=SX+X:SX2=SX2+(X*X):Y=?(&2999+X)+(?(&2998+X)/256):SY=SY+Y:SY2=SY2+(Y*Y):
SXY=SXY+(X*Y):UNTIL X=XMAX
  320  REM Calculate standard deviation of [EL2] about best fit line
  330 REM Best fit straight line is A+Bx
  340 B=(N*SXY-SX*SY)/(N*SX2-SX*SX)
  350 A=(SY-B*SX)/N
  360 REM S2=Mean square deviation from best fit line
  370 S2=(SY2-2*A*SY-2*B*SXY+2*A*B*SX+N*A*A+B*B*SX2)/N
  380 REM S=Standard deviation of [EL2] about best fit line
  390 S=(SQR(S2))*1.5625
  400 PRINT "Standard deviation of [EL2] about best fit straight line =";S;" x10
E14"
  410 INPUT X
  420  REM Reload main programme
  430 CHAIN"DIGIT"
  440 END
  450   REM
```

Appendix 5.5.7. (cont.)

```
  460 DEFPROCGRAPH
  470 REM Plots EL2 scan on screen
  480 SC=2:HX=0:VS=0.03125:BX=&2999:MX=0:NX=1152
  490 MOVE MX,0
  500 FOR AX=0 TO NX STEP 2 :YX=(?(AX+BX)*256+?(AX+BX-1))*VS: XX=(AX/2)*SC+MX :
DRAW XX,YX : NEXT
  510 ENDPROC
  520   REM
  530 DEFPROCCROSS
  540 REM Moves cross
  550 XX=40:YX=500
  560 PROCPLOT
  570 REPEAT
  580 A=GET
  590 IF A=136 THEN PROCBACK
  600 IF A=137 THEN PROCFORWARD
  610 IF A=138 THEN PROCDOWN
  620 IF A=139 THEN PROCUP
  630 UNTIL A=13
  640 ENDPROC
  650   REM
  660 DEFPROCBACK
  670 REM Moves cross to the left (slow)
  680 PROCPLOT
  690 IF XX<-25 THEN XX=XX+1152
  700 XX=XX-2
  710 PROCPLOT
  720 ENDPROC
  730   REM
  740 DEFPROCFORWARD
  750 REM Moves cross to the right (fast)
  760 PROCPLOT
  770 XX=XX+20
  780 IF XX>1126 THEN XX=XX-1152
  790 PROCPLOT
  800 ENDPROC
  810   REM
  820 DEFPROCDOWN
  830 REM Moves cross down (slow)
  840 PROCPLOT
  850 YX=YX-2
  860 IF YX<0 THEN YX=YX+1024
  870 PROCPLOT
  880 ENDPROC
  890   REM
  900 DEFPROCUP
  910 REM Moves cross up (fast)
  920 PROCPLOT
  930 YX=YX+20
  940 IF YX>1023 THEN YX=YX-1024
  950 PROCPLOT
  960 ENDPROC
  970   REM
  980 DEFPROCPLOT
  990 REM Plots cross at XX,YX
 1000 PLOT 4,XX,YX
 1010 PLOT 2,25,0
 1020 PLOT 0,-25,25
 1030 PLOT 2,0,-50
 1040 PLOT 0,-25,25
 1050 PLOT 2,25,0
 1060 ENDPROC
```

Appendix 5.6.

Display routines and screen layout.

Screen layout (BBC graphics mode 0)

Number of vertical graphics points=500 (hex)

Number of horizontal graphics points=400 (hex)

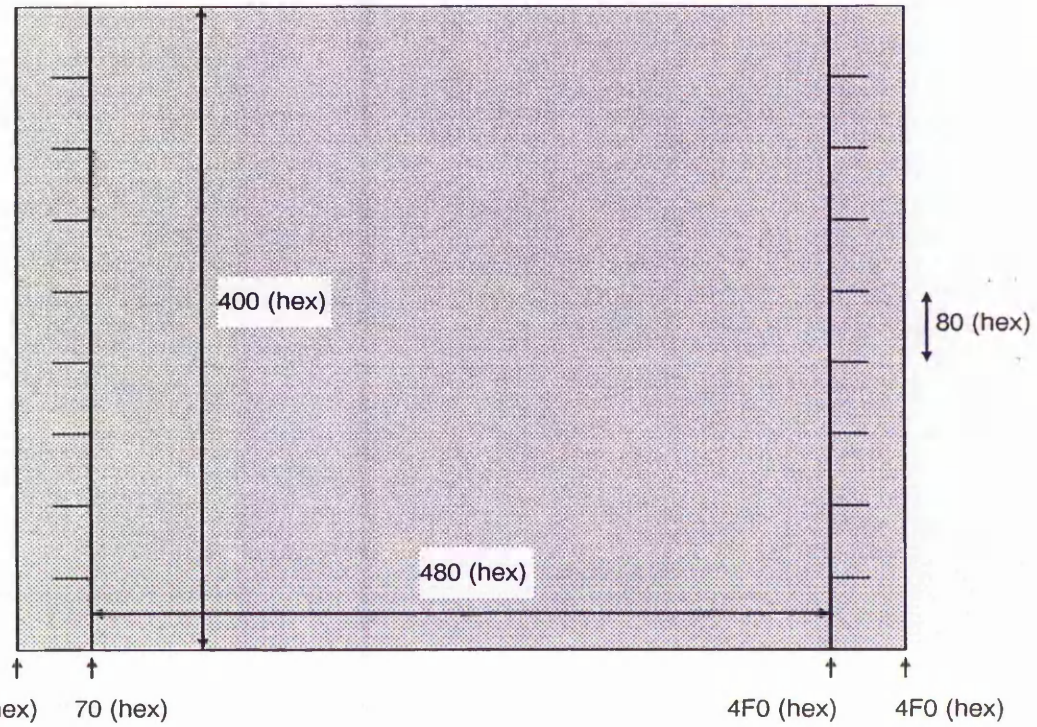

Data is stored on pages 29, 2A, 2B, 2C, 2D, 2E, and 2F (hex) in the BBC RAM. The 13 bit data is stored as pairs with LSB first (even no's) and MSB second (odd no's).

Screen width (480 hex) corresponds to 240 (hex) screen pixels and 240 (hex) data points.

Screen height (400 hex) corresponds to 100 (hex) screen pixels and 8 bit data resolution.

Display Parameters

Graph of [EL2]:

This routine uses the same layout as the standard display but the axes are marked with EL2 concentrations. The top of the screen represents [EL2]=$2 \times 10^{16} cm^{-3}$.

Modify Diplay:

The modify display routine enables sections of the screen to be enlarged using 4 variables

HM ..... Horizontal Magnification (default=1).

HO ..... Horizontal Offset (default=0), measured in eighths of the screen.

VM..... Vertical Magnification (default=1).

VO..... Vertical Offset (default=0), measured in eighths of the screen.

Other variables in display routine:

SC ..... Screen horizontal scale factor (SC=VMx2).

B% ..... Position in RAM of the first data point in the display (default 2999 hex).

N% ..... Number of RAM data locations used in the display (=2x no.of points).

M%..... Display start (default 70 hex).

Q%..... Display end (default 4F0 hex).

P%..... Start of left hand graph marker (end at M%), default 60 hex..

R% ..... End of right hand graph marker (start at Q%), default 4FF hex.

APPENDIX 7.1.

The relationship between U(EL2) and the standard deviation of [EL2] line–scan data

The "standard deviation" of the [EL2] line–scan data (σ[EL2]) is used to give a measure of the microscopic fluctuations of [EL2], on a scale of the order of the size of cell structure. It is calculated by taking the root mean square deviation of the data around a best fit line. The best fit line is calculated by linear regression and is used to avoid the influence of macroscopic fluctuations on the data.

Assuming that these fluctuations are sinusoidal about the best fit line, and that this best fit line is of constant [EL2] (there are no macroscopic fluctuations), then this "standard deviation" will correspond to the r.m.s. value of the sine wave. Hence the peak of the sine wave will be equal to this value $x\sqrt{2}$.

Therefore:

$$[EL2]_{max}=[EL2]+\sqrt{2}\sigma[EL2]$$

and

$$[EL2]_{min}=\overline{[EL2]}-\sqrt{2}\sigma[EL2]$$

where:

[EL2] corresponds to the value of [EL2] at the peak of a sine wave.

[EL2] corresponds to the value of [EL2] at the trough of a sine wave.

$\overline{[EL2]}$ is the mean value of [EL2] (the value of the best fit line).

σ[EL2] is the "standard deviation" of the [EL2] fluctuations..

Since:

$$U([EL2])=\frac{([EL2]_{max}-[EL2]_{min})}{[EL2]_{min}}\times 100\%$$

Then:

$$U([EL2])=\frac{2\sqrt{2}\sigma[EL2]}{(\overline{[EL2]}-\sqrt{2}\sigma[EL2])}\times 100\%$$

Appendix 7.2

The stabilty of [EL2], at room temperature, after a quench

Quench from 1000°C:

Sample removed from furnace and quenched:	Day0	1:10pm
Ampoule broken;	Day0	2:00pm
Cutting and polishing finished;	Day0	4:30pm
Sample mounted for first measurement;	Day0	6:30pm

Time from quench (hours)	T(1um)	T(2um)	[EL2]x10^{16}cm^{-3}
5:25	47.0	92.5	12.81
5:35	46.5	92.5	13.01
6:05	47.5	93.3	12.77
7:35	47.5	93.5	12.81
22:45	47.0	93.5	13.01
26:45	48.0	94.5	12.81
117:45	48.0	94.5	12.81
144:45	48.0	94.3	12.77
165:45	48.0	94.3	12.77

Quench from 1180°C:

Sample removed from furnace and quenched;	Day0	1:15pm
Ampoule broken;	Day0	2:30pm
Cutting and polishing finished;	Day0	6:00pm
Sample mounted for first measurement;	Day0	8:00pm

Time from quench (hours)	T(1um)	T(2um)	[EL2]x10^{16}cm^{-3}
6:45	7.70	9.48	5.49
7:15	7.87	9.71	5.55
7:30	7.85	9.66	5.48
8:00	7.85	9.60	5.31
9:30	7.88	9.61	5.24
19:15	8.00	9.84	5.47
23:15	7.97	9.84	5.47
26:45	7.94	9.74	5.40
29:15	7.85	9.62	5.37
96:45	7.96	9.80	5.49
167:45	7.79	9.61	5.55
310:45	7.85	9.76	5.75

Time from quench (hours)	T(1um)	T(2um)	[EL2]x10^{16}cm^{-3}
430:45	8.05	9.99	5.70
433:45	7.98	9.85	5.56
435:45	7.97	9.84	5.57
454:45	8.01	9.89	5.57
458:45	7.95	9.81	5.55
478:15	8.00	9.89	5.60
483:45	7.99	9.79	5.37
502:45	7.94	9.87	5.75
509:15	7.82	9.58	5.36
527:15	7.94	9.77	5.48
531:45	7.93	9.76	5.48
598:45	7.99	9.88	5.61
603:45	8.03	9.88	5.48
622:45	7.89	9.80	5.73
627:45	7.88	9.70	5.49
670:45	7.95	9.80	5.53
694:45	7.86	9.75	5.69
766:45	7.95	9.85	5.66